Improving estimation of spatial precipitation in a mountain region

Ronald Keith Shotton

School of Engineering

Newcastle University

A thesis presented for the joint degree of Doctor of Philosophy with Newcastle University and the University of Northumbria at Newcastle

September 2024

Abstract

Due to its importance for water resources, as well as flood and drought planning, an improved understanding of spatial precipitation patterns in mountain regions is needed. Precipitation gauge networks are sparse and traditional methods of interpolation yield inadequate precipitation fields for sparsely gauged mountain catchments. This work builds on a new method, Random Mixing, to generate multiple random spatial daily precipitation fields, conditioned on gauge observations. The Random Mixing algorithm has so far been tested on larger, densely gauged catchments. This project adapts the approach for a sparsely gauged, small 9.4 km^2 mountain catchment, Marmot Creek Research Basin (MCRB) in Alberta, Canada.

Three modifications have been made to the Random Mixing method in developing the new technique, which is referred to as RM-mountain: (1) improving spatial covariance, (2) introducing elevation dependence and (3) evaluating seasonal effects. Addition of each modification in turn increases the spatial variance of precipitation values across simulated fields. Leave-one-out cross-validation was used, and results compared with outputs from four deterministic spatial interpolation techniques. The best fit precipitation time series simulated by the RM-mountain generated ensemble members demonstrated improved precipitation estimates compared to the four deterministic techniques. Precipitation totals across the MCRB catchment generated by RM-mountain are higher than those from the other methods tested. Due to its random nature, RM-mountain enables generation of precipitation within the catchment on days when the gauges are dry. In contrast, deterministic spatial interpolation methods yield zero precipitation across the entire catchment on days with zero observed precipitation. Inclusion of modifications 1-3 in RM-mountain noticeably increased the likelihood of simulating more realistic precipitation values within the generated ensemble.

To optimise selection of the most plausible fields, ensemble hydrological simulations were run, using a modified spatially-distributed version of the HBV conceptual model, and the physically-based Cold Regions Hydrological Model (CRHM), with a 200-member ensemble of time series spatial precipitation fields generated on a 50 m x 50 m regular model grid. Optimisation involved the use of Nash-Sutcliffe Efficiency (NSE) and bias metrics, to identify a best constructed time series that most closely simulates the observed streamflows. The improvement in streamflow bias with HBV was from -20.94 to 0.14; with CRHM, bias was

improved slightly from 2.04 to 1.88. Increases in NSE values were from 0.76 to 0.96 with HBV and from 0.54 to 0.74 with CRHM. Some noticeable differences between catchment responses with HBV and CRHM were observed, relating to the complexity of the models, i.e., the relative simplicity of the conceptual HBV model in contrast to the more complex physically-based CRHM. Notable examples of these differences were snowmelt earlier in the year and much less variation in the streamflow ensemble with HBV. A much greater variety of streamflow hydrographs in the CRHM-generated ensemble were due to CRHM's much higher sensitivity to differences in observed meteorological input data, particularly wind speed.

This work demonstrates that modifying a random method, by adapting how it randomly samples from observed precipitation at a small number of gauges, includes elevation gradients and seasonal variation, improves estimation of spatiotemporal precipitation patterns for a small mountain catchment and improves hydrological simulations. The new method has the potential to be used to enhance precipitation datasets to improve water resource and flood modelling in other sparsely gauged mountain regions.

Acknowledgements

Firstly, I would like to give huge thanks to my amazing supervisors Liz Lewis, Stephen Blenkinsop, David Pritchard and Nick Rutter for their expertise, positivity, patience, enthusiasm and support throughout my research project. Their outstanding guidance has had an enormous impact over the last four years. I genuinely could not have got to this stage without them. Further thanks go to Liz for being such a great MSc dissertation supervisor, for teaching me to code and generally helping a former school teacher to become a hydrologist!

I would also like to thank the other PhD students and post-doctoral researchers in journal club and code club for being such great people and helping me get through some interesting challenges! Thank you also to Logan Fang at the University of Saskatchewan for his enthusiastic and insightful guidance in using the Cold Regions Hydrological Model.

Thank you to NERC for funding this research and also the OnePlanet DTP directors and administration team for providing opportunities to present my research at Residential Activity Centres and arranging writing retreats by the sea!

I'm very thankful too for the friends I made in OnePlanet cohorts 1 and 2, thank you especially to Becky, Sam, Natasha, Ryan and Emma for being such an important part of the PhD journey.

Finally, thank you so much to Gillian and Rosie for being such a brilliant, encouraging family, for always believing in me and for helping me to believe in myself.

Contents

List of figures

List of tables

Chapter 1. Introduction

1.1 Motivation

Mountain ranges play an important role in providing water resources for around 22% of the global population (Ragettli et al., 2016). Streamflows in spring and summer months are often dependent on snowmelt, which is then replenished during colder months. However, as the climate warms, patterns of precipitation and evapotranspiration are changing, with subsequent impacts on the timing and volume of water from mountains (Lutz et al., 2014). Changing precipitation patterns affect available water resources for communities living downstream of mountain ranges, alongside increased risk of flooding (Liu et al., 2016). Changes in snow cover and runoff are influenced by an increase in the proportion of precipitation falling as rain due to climate change effects. The depth and duration of snow cover are declining, particularly at lower elevations in mountain regions, and seasonal patterns are changing, for example earlier spring snowmelt and increased winter runoff due to rain-on-snow events at higher elevations (IPCC, 2019). Due to orographic precipitation effects, mountain regions seasonally produce greater surface runoff than lower lying areas. In addition to snowmelt, other strong seasonal effects, including snow and ice processes such as blowing snow redistribution and snowpack accumulation, are also often evident in mountain catchments (Viviroli et al., 2020; J.W. Pomeroy et al., 2022). Mountains also have greater sensitivity to climate change as temperatures are rising at a faster rate due to elevation-dependent warming (Immerzeel et al., 2020). The importance and complexity of precipitation patterns and variability in mountain regions means that developing a better understanding of precipitation patterns is essential for purposes such as evaluating anthropogenic hydrological impacts, water resource planning and forecasting of floods and droughts (Beck et al., 2017).

However, whilst high quality precipitation data is essential for simulating hydrological systems, it is notoriously difficult to obtain in mountain regions (Buytaert et al., 2006; Immerzeel et al., 2014; Wang et al., 2018), due to its high spatiotemporal variability (Herold et al., 2016). Precipitation gauges are widely regarded as the most reliable source of high-quality data, however they provide only a partial representation of spatial precipitation patterns. The problems associated with obtaining reliable spatial precipitation data is exacerbated in mountain regions, where precipitation is strongly influenced by topography, yet there are fewer gauges at higher elevations due to their relative inaccessibility (Henn, Newman, et al., 2018; Wang et al.,

2018). For distributed hydrological modelling, methods of spatial interpolation, for example Nearest Neighbour (Thiessen, 1911), Inverse Distance Weighting (Shepard, 1968), Kriging (Buytaert et al., 2006) or co-Kriging (Goovaerts, 2000) are typically used to infer precipitation totals between point measurements at gauge locations. Traditional interpolation methods yield inadequate precipitation fields for poorly gauged catchments (Wagner et al., 2012) and there is high uncertainty in spatiotemporal fields generated by these methods, with consequences for the accuracy and utility of outputs from hydrological modelling studies using this type of input data (Grundmann et al., 2019). Critically, these methods tend to underestimate precipitation amounts in mountainous areas (Henn, Clark, et al., 2018; Adam et al., 2006). Therefore, new approaches are needed to estimate precipitation patterns more accurately at high elevations to enable better understanding of water resources and flooding for populations dependent on water from mountain regions.

1.2 Random mixing

This thesis explores the development of the random mixing method of generating stochastic spatial precipitation fields (Bárdossy & Hörning, 2016; Grundmann et al., 2019; Haese et al., 2017; Hörning & Haese, 2021; Yan et al., 2021b), to evaluate its suitability for improving the representation of precipitation in sparsely gauged mountain catchments. The random mixing approach involves conditional simulation of random fields that respect gauge observations and their spatiotemporal relationships, whilst introducing realistic variability into the field. Due to its Monte Carlo framework approach, with repeated random sampling, random mixing provides an ensemble of possible estimates, unlike traditional interpolation methods which generate a single realisation of a precipitation field. Random mixing produces conditional spatial fields by combining multiple unconditional fields, i.e., spatial fields that are entirely random and not constrained by any observed datasets. A detailed explanation of the random mixing approach is provided later, in Section 4.3. The most plausible conditional fields are identified by using them as hydrological model inputs and evaluating simulated discharge against the observed streamflow hydrograph at the catchment outlet (Grundmann et al., 2019). Traditional interpolation methods tend to smooth out spatial variability (Hu et al., 2019); in contrast, the random mixing algorithm stochastically simulates spatial fields that can more realistically represent spatial variability (Hörning, 2016). The method uses spatial copulas (multivariate distribution functions), to describe the spatial dependence between gauge observations, with copula parameters estimated to give a best fit to the observations.

In a study by Grundmann et al. (2019), random mixing was applied to a synthetic 211 km^2 test site, with an elevation range of 100-1100 m above sea level (a.s.l.) and 10 virtual monitoring stations, and to a real-world arid test site, with an area of 257 km^2 and elevations from 600 m a.s.l. to higher than 2500 m a.s.l. Simulated ensemble fields resulted in improved model performance compared with that achieved with interpolated fields generated using the Inverse Distance (ID) method for both timing and magnitude of peak flows. However, the real-world part of the study, in which the method was tested on a catchment in Oman instead of on the synthetic test site, focused on only a single rainfall event for which there was no identifiable relationship between rainfall and elevation. Another application of the method was to a historical flood event in a data sparse region (Bárdossy et al., 2020), again with significant improvement in hydrological model performance. A key advantage of random mixing is that additional conditioning datasets can also be introduced in random field simulation, for example Commercial Microwave Link data and radar estimates (Haese et al., 2017; Hörning & Haese, 2021; Yan et al., 2021b). Furthermore, conditional random fields have been compared with those from a range of other interpolation methods, i.e., Ordinary Kriging, Kriging with External Drift, and Conditional Merging for gauge and radar data (Yan et al., 2021a). Random mixing outperformed these other methods, particularly when estimating extremes of precipitation. However, applying a random mixing technique in data-sparse mountain regions, accounting for the relationship between precipitation (rainfall and snowfall) and elevation, is a relatively unexplored area of research that is investigated in this study. The aim of this project is to adapt the Random Mixing Whittaker Shannon Python (RMWSPy) method (Hörning & Haese, 2021) from a large, densely gauged study area to a small, sparsely gauged mountain catchment. RMWSPy is modified in three ways to generate the new RM-mountain method: (1) a time series sampling technique is used in the spatial copula fitting approach to generate robust spatial covariance based on a small number of gauges; (2) elevation dependence is included so that precipitation amounts assigned to each model grid cell are related to its elevation; (3) to allow seasonal effects, such as snowmelt and its influence on surface runoff, which can be significant in mountainous cold regions, to be evaluated.

1.3 Research aims and objectives

The overall aim of this research project is to develop improved estimates of time series precipitation data for a mountain region. The key objectives were to:

O1. collect observed meteorological data, for the mountainous Marmot Creek Research Basin in the Canadian Rocky Mountains, including precipitation data that could be used as constraints for a stochastic spatial interpolation method;

O2. statistically characterise the observed precipitation data to better understand temporal and spatial precipitation patterns;

O3. develop a methodology for stochastic generation of spatiotemporal precipitation datasets for the selected mountain region based on a version of the random mixing technique;

O4. generate spatiotemporal precipitation datasets using the new method and evaluate the utility of the method by comparing observed and simulated precipitation amounts using a leave-one-out validation approach;

O5. select suitable hydrological models, both conceptual and physically-based models, capable of representing cold regions processes such as snow pack accumulation, blowing snow redistribution and snowmelt;

O6. set up and calibrate models of the chosen mountain catchment for the selected hydrological models;

O7. to use spatiotemporal precipitation datasets, generated using the new method and other deterministic spatial interpolation techniques, as inputs to the selected hydrological models to evaluate the performance of the precipitation datasets from the new stochastic generation method.

1.4 Thesis structure

The literature review for this research project is presented in Chapter 2. Chapter 3 describes Marmot Creek Research Basin, the hydrometeorological data obtained for the catchment, and the two hydrological models used: the conceptual Hydrologiska Byråns Vattenbalansavdelning (HBV) and the physically-based Cold Regions Hydrological Model (CRHM). Chapter 4 explains how the proposed RM-mountain method was developed from the Random Mixing Whittaker Shannon Python (RMWSPy) technique. Chapter 5 (for HBV) and Chapter 6 (for CRHM) then discuss the performance of RM-mountain generated spatial precipitation fields when used as inputs to the two hydrological models. Chapter 7 then provides a discussion of results and outlines potential further work.

Chapter 2. Literature Review

A range of topics must be considered to provide an appropriate context for this thesis, its methods and models used, and its results. This chapter provides an overview of literature most relevant to the subjects of mountain regions and mountain hydrology; available precipitation data in mountainous areas and its limitations; traditional spatial interpolation techniques and stochastic methods of generating spatial precipitation fields, considering their application and their limitations.

2.1 Mountain regions

High mountain ranges play an important role in providing water resources for many millions of people across the globe (Ragettli et al., 2016). Streamflows in spring and summer months are often dependent on snow and glacier melt which is then replenished during colder months. As the climate warms, patterns of precipitation, snowpack and glacier formation and melt are changing. These changes impact on available water resources for communities living downstream of mountain ranges, with increased risk of drought and flooding. The storage and supply of water from mountain regions to sustain environments and meet human demand can be described using the phrase 'water towers' (Immerzeel et al., 2020). Due to orographic precipitation effects, mountain regions seasonally produce greater surface runoff than lower lying areas. Water is stored upstream in snow and glaciers during winter which is then released as temperatures warm in spring. This 'buffer' effect maintains a comparatively constant flow of water as melt water compensates for lower precipitation amounts in downstream areas during the warmer months of the year. A Water Tower Unit (WTU) is defined according to major river catchments and mountain classification (Immerzeel et al., 2020). As water supply and demand are considered at catchment scale, a WTU can incorporate more than one mountain range providing a supply of water to a single river catchment that is hydrologically connected to the WTU. Examples include Saskatchewan-Nelson in North America, La Puna region in South America and the Po in Europe. Mountain hydrology has greater sensitivity to climate change than lower lying zones as temperatures are rising at a faster rate due to elevation-dependent warming. Future changes in the timing and volume of water from mountains will be affected by changes in snowmelt and precipitation patterns, as well as evapotranspiration, due to the warming climate (Immerzeel et al., 2020). An important feature of Immerzeel et. al.'s study is the global Water Tower Index (WTI) used to quantify and rank the global importance and vulnerability of water towers according to factors including water stress, governance and future

climatic and socioeconomic changes. A key conclusion indicates that the towers with the highest WTI values, i.e., the greatest global importance, include some of the most vulnerable water towers, hence action is needed to ensure future security of mountain water supply. The most recent synthesis report by the Intergovernmental Panel on Climate Change (IPCC) reports on several climate change impacts on mountain regions. Examples include: hydrological changes due to thawing of permafrost and glacier retreat; severe consequences for populations, economies and infrastructure in most mountain regions due to changes in water availability; and increases in localised pluvial flooding due to the projected rise in frequency and intensity of intense precipitation (Calvin et al., 2023).

Precipitation data is a key input in our understanding of hydrological systems and, to safeguard future water resources in key river catchments, developing a better understanding of precipitation patterns is essential for purposes such as evaluating anthropogenic hydrological impacts, water resource planning and forecasting of floods and droughts (Beck et al., 2017). In contrast to its high importance, precipitation is one of the most challenging meteorological variables to measure, due to its high spatiotemporal variability (Herold et al., 2016). Precipitation gauges are widely regarded as the likeliest source of high-quality data although these give information only at specific measurement locations, hence they provide only limited information on spatial distribution of precipitation. For distributed hydrological modelling, a method of spatial interpolation must be used to infer precipitation amounts between point measurements at gauge locations. Traditional interpolation methods yield inadequate precipitation fields for ungauged and poorly gauged catchments; dynamic, small-scale convective storms which are not reliably captured by gauges; and in catchments that are partly covered by rainfall (Grundmann et al., 2019). There exists high uncertainty in spatiotemporal fields generated by these methods, with consequences for the accuracy of outputs from hydrological modelling studies using this type of input data. Therefore, new approaches are needed to estimate precipitation patterns more accurately at high altitudes.

2.2 Precipitation data currently available and its limitations

High spatial variability in snowfall accumulation and precipitation patterns exist in mountain regions due to orographic processes (Roe, 2005), giving rise to greater uncertainty in water balance estimation (Wrzesien et al., 2019). Using current methods, the amount of precipitation falling on mountain catchments is systematically underestimated across parts of all major mountain ranges across the globe (Beck et al., 2020). It is possible to obtain information on the spatiotemporal distribution of precipitation from three primary data sources: satellite imagery, meteorological reanalyses and precipitation gauges. The reliability of all three of these data sources is diminished in mountainous terrain and regions dominated by high snowfall. Data retrieval by remote sensing from satellites is affected by snow and ice on land plus it is hard to detect snowfall using this method (Beck et al., 2017). Previous research indicates that all three observation methods show inaccuracy in mountainous, snow-dominated regions (Ma et al., 2019; Immerzeel et al., 2015; Mair et al., 2016). Globally, the number of precipitation gauges is small in comparison to the earth's total surface area. Based on the assumption that each precipitation gauge available to the Global Precipitation Climatology Centre (GPCC) is independent and represents precipitation measured within a 5 km radius of the gauge, it is estimated that the area covered is equivalent to only around 1% of the earth's surface. Added to this, the situation regarding snowfall is even poorer, due to higher measurement uncertainty (Kidd et al., 2017).

Measurements made using precipitation gauges, which are widely considered to be the highest quality data available, are far from error-free. The primary disadvantage of gauges is that they provide information only at specific locations, limiting spatial representation. Interpolating fields from gauge data can lead to significant biases in those fields, most notably in complex terrain. The main sources of systematic gauge error relate to evaporation from the gauge and aerodynamic effects, i.e., wind-induced gauge undercatch, where water droplets or snowflakes are blown across the top of the gauge orifice and not captured. Wind causes turbulent effects over the gauge orifice which increases non-linearly with wind speed (Pollock et al., 2018). Wind effects resulted in mean rainfall undercatch in a UK upland catchment (at an elevation of 440m) being more than 23% for a traditional cylinder-type gauge and 11.2% for an aerodynamic gauge, with gauges mounted at 0.5m above ground level. Raising the mount height to 1.5m caused mean undercatch for the aerodynamic gauge to increase to 17.5%. These mean undercatch percentage values were calculated by comparison with a reference gauge

consisting of a pit gauge, i.e., a gauge buried so that its orifice is at ground level. The phenomenon of wind-induced undercatch results in snowfall being frequently underestimated by 20% to 50% (Rasmussen et al., 2012). In addition to wind speed, wind bias is dependent on a number of factors including air temperature, precipitation characteristics and the configuration of the gauge, all of which can combine in extreme cases to result in undercatch as high as 100%. These problems are further compounded by large climatic variability. The density of gauge networks is another important feature: where density is low, sampling errors are greater (Schneider et al., 2014). Due to complex topography and reduced accessibility, gauge density is very low in mountain regions, with gauges concentrated in more populated valley locations, hence knowledge of precipitation patterns at the highest elevations is poor (Frei & Schär, 1998).

Perhaps the main advantage of remote sensed data retrieved from satellite observations is that satellites can instantaneously capture data from extensive global surface areas at high resolution. Considering the difficulties in measuring precipitation over the complex terrain of mountain regions with limited surface observations, access to precipitation estimates from satellites is useful in characterising hydrological, climatic and ecological conditions at high elevations (Ma et al., 2019). It must however be noted that satellite precipitation estimation is most reliable in regions where rainfall is highly heterogeneous, for example in the tropics (Beck et al., 2017). In mountainous regions such as the Canadian Rockies and northern Europe, where there is high spatiotemporal variability in precipitation patterns, the accuracy of satellite precipitation data is compromised by the presence of snow and ice, which are not identified as rainfall or snowfall, resulting in underestimation of precipitation in those areas (Beck et al., 2020; Kidd et al., 2012). Identifying snowfall is another challenge associated with satellite imagery, for example due to the difficulty in distinguishing ice hydrometeors from raindrops and the more complex radiative properties of snowflakes and ice crystals compared with water droplets (Levizzani et al., 2011). Situations in which satellite imagery can be particularly useful for hydrological purposes include measurements of snow cover on land and intercepted snow (Lv & Pomeroy, 2019).

Reanalysis of past observations of climatic variables is another method used to obtain estimates of precipitation for climate datasets for regions with sparse observations. Global datasets such as the Japanese 55-year Reanalysis JRA-55 (Kobayashi et al., 2015) and ERA5 (Guillory, 2017) are widely used at global and regional scales. However, their relatively low

spatial resolution of ≥ 0.25° (Beck et al., 2020), and use of parameters constrained only indirectly by observations, present a challenge for accurately representing orographic precipitation. Other methods of estimating precipitation are commonly used, including radar and Commercial Microwave Link (CML) data (Hörning & Haese, 2021). However, these are not applicable in mountain regions, hence they are not discussed here. Having identified the relative advantages and disadvantages of existing methods of identifying and generating spatial precipitation patterns, this study will go on to develop novel methods to generate improved time series of spatial precipitation fields for mountain regions.

2.3 Spatial interpolation methods and their limitations

Traditionally, a method of spatially interpolating point precipitation data, typically between gauge locations, is used to distribute precipitation values across an area of interest, such as a river catchment or region affected by flooding, to generate spatiotemporal precipitation fields that can be used as a time series input for hydrological modelling. This gives rise to significant uncertainty in modelling as these interpolation methods often result in underestimation of precipitation, particularly in sparsely gauged or ungauged catchments, such as those at higher elevations where spatial and temporal precipitation patterns are subject to increased variability.

A review of spatial interpolation methods (Wagner et al., 2012) identifies that most existing techniques provide a continuous, rather than discrete, smoothed spatial surface. One of the simplest methods for spatial interpolation of precipitation is the Thiessen (or Dirichlet) polygon technique, also known as the 'Nearest Neighbour' method. This involves drawing polygons, one per precipitation gauge, with the gauge located at the centre of the polygon. The precipitation value at each gauge location is attributed to the entire area within its polygon, making it an example of an 'exact' interpolation method. By applying a single value to each separate polygon, it results in abrupt transitions at polygon boundaries. In contrast, 'inexact' methods, such as regression models, assign values across space according to a mathematically derived relationship between precipitation and distance. More advanced methods combine regression analyses with distance-based weighted averages. Different interpolation procedures use different criteria for weighting precipitation values in relation to distance. These include straightforward distance relationships such as inverse distance methods; techniques like kriging and co-kriging that minimise variance; and applying smoothness criteria (splining). Some approaches are deterministic, i.e., they result in the same output each time they are applied, such as Nearest Neighbour and Inverse Distance Weighting (IDW). The Inverse Distance

Weighting (IDW) method calculates values at ungauged locations via linear combinations of observed values at gauged points. Weighting is a function of distance only, with heavier weighting given to points at closer proximity to gauged locations. No account is taken of spatial dependency in deriving the values of the weights. IDW gives more reliable estimates at sites closer to gauges but is less reliable for those further away. This method is not radically different to the Nearest Neighbour technique, but one key difference is that is smooths the transition from one zone to the next, giving gradual, rather than sudden, changes in the resulting precipitation field. Splining involves fitting a polynomial spline function, constrained at observation points, to describe the spatial surface. Methods such as kriging and co-kriging use linear combinations of weights at gauge points to estimate precipitation values at ungauged locations. This typically involves deriving a semi-variogram to describe the spatial correlation between precipitation and separation distance between pairs of gauges. Kriging methods assume stationarity in that the semi-variogram depends only on the distance between two points but not on their actual locations. Usually, a variogram model is fitted to the data, with the linear, spherical and exponential models being amongst the most commonly adopted. Previous studies have determined that, for hydrological applications, geostatistical interpolation methods, i.e., those that incorporate spatial dependence relationships such as kriging, outperform more traditional techniques that ignore spatial covariance, e.g. IDW (Mair & Fares, 2011).

While these methods of interpolation, both traditional and geostatistical, have their respective merits, alternative methods must be sought, particularly for data sparse regions, including mountainous areas with large changes in elevation over relatively short distances. The following section explores the development of some of these approaches.

2.4 Stochastic methods to generate spatial precipitation fields

Conditional simulation has considerable potential for estimating spatial precipitation patterns. Due to its Monte Carlo framework approach, with repeated random sampling, it results in an ensemble of possible estimates, unlike more traditional interpolation methods which generate a single realisation of a precipitation field. Key to the success of conditional simulation methods is accurately representing the marginal distribution function of the precipitation field (Yan et al., 2021b). Stochastic methods, i.e., those having a random variable, are widely used in hydrology to estimate precipitation. The simplest approaches, such as the Markov model, are used to predict a sequence of random variables where future rainfall depends only on the current state, i.e. wet day or dry day, using the conditional probability of moving from one state to the

other (Haan et al., 1976). More sophisticated methods, such as the Neyman-Scott Rectangular Pulses model (Cowpertwait et al., 1996), can generate higher order, i.e. hourly or sub-hourly rainfall estimates using a stationary spatial process (Burton et al., 2008).

The methods developed in this thesis can be traced back to a technique first developed for related geostatistical applications, for example subsurface hydrology (Hu, 2000). It describes the gradual deformation of multiple realisations of Gaussian-related stochastic models while also preserving their spatial variability. This method builds a stochastic process using an ensemble of the realisations of a spatial stochastic model, via an algorithm that combines independent Gaussian random functions to gradually deform those realisations. These unconditional Gaussian and Gaussian-related fields can be used to represent heterogeneous conditions, such as the variability of spatial precipitation patterns or pressure observations on a groundwater permeability field. To transform these unconditional fields to more plausible realisations, the Gaussian fields require conditioning to preserve the observed values in the available data. With linear data, such as point precipitation observations from gauges, honouring observed data is more straightforward than in non-linear situations, such as CML data (Hörning & Haese, 2021) or radar estimates (Yan et al., 2021b). One method of calibrating fields from a stochastic model to non-linear data is to adopt an optimisation approach, using an objective function to minimise the differences between observed values and those generated by the stochastic model. This kind of optimisation approach will be adopted in the development of the proposed method in this thesis.

A promising method for stochastic reconstruction of spatiotemporal rainfall patterns (Grundmann et al., 2019) involves using an inverse hydrological modelling approach combined with the random mixing method (Bárdossy & Hörning, 2016) in a Monte Carlo framework. This method generates multiple realisations of rainfall fields conditioned on point rainfall ground measurements which, crucially, are assumed to be accurate; and the observed streamflow hydrograph at a catchment outlet. These fields are also dependent on the optimised parameter values in a chosen hydrological model which, in Grundmann et al., (2019), is a 1 km x 1 km grid-based rainfall-runoff model, NAMarid. The random mixing algorithm represents an extension of the gradual deformation approach for geostatistical simulation (Hu, 2000) described above. It uses copulas which, in general, are multivariate distribution functions with each univariate marginal distribution uniformly distributed on the range [0, 1] as spatial random functions (Hörning, 2016). The spatial dependence between random variables, i.e.,

precipitation gauge observations, need to be described in such a way that it is independent of the marginal distributions of the data at each location. In other words, transforming the marginals, in this case to Gaussian fields in standard normal space, on the range $N(0, 1)$, does not affect the overall dependence structure. This is what spatial copulas are used to achieve, at each separate time step. As the selected copula needs to represent the spatial dependence structure of the observed data, copula parameters are estimated to fit the observations.

Traditional interpolation methods tend to smooth out spatial variability as they do not preserve spatial dependence. In contrast, copula-based interpolation affords a full conditional distribution at every unobserved location, i.e., each grid cell within a model domain, enabling identification of confidence intervals. Also, it depends on observed values and their marginal distributions, in addition to their spatial relationship. The random mixing method was applied to simulating high resolution daily precipitation fields for the Neckar catchment in the densely gauged Baden-Württemberg region of south west Germany (Hörning, 2016). A number of realisations was simulated over a period of 62 years, with a varying number of observation locations. For a given day, the marginal precipitation distribution is split into three components:

1. The discrete probability of zero precipitation p_0, as dry days have to be treated separately.
2. Wet day precipitation below a threshold L represented by an exponential distribution. These lower precipitation amounts occur frequently and are recorded with relatively high observation error; these two factors mean that values less than L can unduly impact the estimation of the entire distribution.
3. A distribution of higher precipitation values that exceed L which contribute less (in Germany) to total precipitation than values below L. These values tend to have a skewed distribution.

The method in Grundmann et al. (2019) differs in that the marginal distribution is split into only two parts: the discrete probability of zero precipitation p_0 and an exponential marginal distribution for all wet day precipitation values. The observed precipitation values are transformed to standard normal space; p_0 are not transformed in this way, instead they are treated as inequality constraints. Simulated spatial fields can then be backtransformed to real data space using the inverse marginal distribution. It is assumed that the precipitation distribution is the same at every location and time step. As the transformed spatial field is assumed normal, its spatiotemporal dependence can be described by a normal copula with a

correlation matrix based on the available observations. The spatiotemporal fields are conditioned on observed rainfall and observed streamflow at the catchment outlet for a synthetic case and a real-world catchment in an arid region in Yemen.

Another application of the random mixing method, this time in a data sparse environment, is presented by Bárdossy et al. (2020), in which precipitation fields are generated as hydrological model inputs to model a historical flood event, again in the relatively large Neckar catchment (current catchment area 2320 km^2) in south west Germany. A version of the spatially distributed conceptual Hydrologiska Byråns Vattenbalansavdelning (HBV) hydrological model (Bergström, 1992), calibrated and validated using recent data from a dense gauge network, was used to simulate a flood event in 1882, at which time the catchment area was smaller, at 1900 km^2 (the flow gauging station is now 8.5 km further downstream than it was in 1882) and the observation network was much more sparse. Using Ordinary Kriging for spatial interpolation of 1882 gauge data resulted in a large mismatch between observed and simulated hydrographs at the catchment outlet. To rectify this problem, high resolution daily precipitation fields were generated that would honour observed precipitation values at gauge locations; have values matching the marginal distribution of each day's observed precipitation; have spatial variability aligned to the observations, with a variogram for a typical day of the winter season (the flood occurred in December 1882); and that result in a good match between observed and simulated discharge when used as hydrological model inputs. As the focus was on high flows, spatial fields were simulated only for days with high precipitation. Fields for days with low precipitation were interpolated using inverse distance weighting (IDW). One aim of the study was to determine the relative impact on hydrological model uncertainty of model parameters and input data. Calibrating the model using data for the entire year of 1882 gave a good Nash-Sutcliffe Efficiency (NSE) value of 0.75 and a closely fitting hydrograph for that period. 100 spatial fields were generated, conditioned on observations from 20 gauges, a small number given the catchment size, resulting in the 100 fields being very different to each other. In spite of the uncertainty caused by these differences, results from HBV simulations using all 100 fields showed much improved model performance with a good hydrograph fit and NSE = 0.97 to 0.98. In contrast to the most common approach when evaluating uncertainty in rainfall runoff modelling, which is to attribute uncertainty to model parameters rather than input data (Bárdossy et al., 2022), it was concluded that initial poor model performance could be attributed more to precipitation data than to calibrated parameter values.

Yan et al. (2021) compares four techniques to simulate rainfall fields, including random mixing, using rain gauge observations and radar estimates to constrain model simulations. These are: Random Mixing (RM), Ordinary Kriging (OK), Kriging with External Drift (KED) and Conditional Merging (CM). Gauge data is more reliable than radar-based precipitation estimates; however, they are complementary in that radar data gives a better indication of spatial precipitation patterns. The sensitivity of the RM method to gauge density and random error in radar estimates was analysed by running simulations with different scenarios. Accuracy of estimation of extreme and mean precipitation fields was considered and the results compared with KED. This revealed that estimation of the extreme value of a precipitation field is improved by increasing the number of gauges and reducing radar estimate random error. Also, RM performed better than KED as indicated by evaluation of mean error and error interquartile range. For field mean estimation, RM was found to be less sensitive than KED to gauge density and random error in radar estimates.

Similar to Hörning & Haese (2021), Haese et al. (2017) also applied the random mixing method to generate spatial precipitation fields using a combination of point observations from precipitation gauges and rainfall estimates derived from CML data. Initially, a linear combination of unconditional spatial random fields is generated, i.e., without the use of any conditioning datasets such as gauge data. In the random mixing method, weights applied to these linear combinations are varied to produce fields that honour observed data and the observed spatial structure. The latter is achieved by fitting a spatial copula model to describe the spatial dependence relationship. In this way, an ensemble of potential reconstructions of spatial fields is generated. To evaluate these spatial fields, Haese et al. (2017) used both synthetic input datasets from an atmospheric model simulation of the Neckar catchment, and real-world observations for a neighbouring basin. A key recommendation from this paper was to explore further improvement of the method by incorporating topographic data into the spatial dependence structure, to better represent the relationship between topography and precipitation amount, an approach implemented in this research project. (Bárdossy & Pegram, 2013) developed methods for interpolating rainfall, at a range of time steps from daily to annual, using Gaussian copulas and unsymmetrical v-copulas, with a variety of ways used to consider altitude. A maximum likelihood approach was utilised to estimate spatial dependence and the copula method was evaluated by comparing it with Ordinary Kriging (OK) and Kriging with External Drift (KED) methods of interpolation. The study covered a large, well-gauged area of southern Germany, spanning the states of Rhineland-Palatinate (19,846 km^2), Baden-

Württemberg (35,751 km^2) and Bavaria (70,547 km^2); elevations range from around 50 m to 2600 m across the entire area, and daily precipitation data was available from a total of 1262 gauges covering the period 1961-2001. The mean gauge separation distances, for the three states respectively, are 9700 m, 11,100 m and 9500 m. Assuming that prevailing wind direction has a significant impact on accumulated gauge precipitation, but that local scale topography does not, Bárdossy & Pegram's study highlighted that, although there is a dependence on the direction of advection on a given day, precipitation in valleys and on peaks is similar. Also, due to orographic uplift on the first rising slope at higher elevations, a strong rain shadow effect is experienced. Alternative transformations of the topography were taken into account. For a given location, to allow for the effects of directional advection, a smoothed, shifted elevation, derived from original elevations from a Digital Elevation Map (DEM) was considered. In this way, the elevation model is shifted in the direction of the advection. For a given time interval, the vector representing the main advection flow direction and the distance between the original and shifted locations were changed progressively until the correlation between smoothed elevation and precipitation, for all observations, is maximised. It was noted that the correlation between topography and precipitation increases with increasing time aggregation, in numbers of days. Directional smoothing also increases the correlation. At shorter time steps, there is likely to be greater variation in the advection direction, hence the prevailing wind direction does not have a significant impact. However, for longer time steps, prevailing wind direction has more influence. A joint copula was constructed for both precipitation and elevation. However, this is complex as precipitation varies temporally whereas topography is time invariant. As a consequence, to interpolate precipitation at ungauged locations, a correlation model for precipitation and altitude was used that connected the elevation at a single location with precipitation values at a range of points. The modification introduced in this thesis to represent elevation dependence of precipitation is discussed in Section 4.4.1.

2.5 Hydrological modelling in mountain regions

Aspects of mountain hydrology, and the sensitivity of mountain regions to climate change, present unique challenges for hydrological modelling, for example sudden changes in air temperature and precipitation patterns over short distances due to steep land surface gradients, and differing exposure to wind. Hydrological models have an important role in understanding processes affecting mountain catchment water balance for water resource planning. Physically-based hydrological models which represent physical processes such as snow accumulation, snowmelt and runoff by solving partial differential equations are often considered to be valuable tools for environmental decision-making. However, comparison of different types of hydrological models is useful for evaluating model uncertainty (Morán-Tejeda et al., 2015). This can include not only process-based models but also conceptual models such as HBV (Caruso et al., 2013; Finger et al., 2015; Wang et al., 2019; Zhang et al., 2013), considering fully spatially distributed approaches and partially distributed or lumped models.

Chapter 3. Data and hydrological models

3.1 Introduction

Marmot Creek Research Basin (MCRB) is used in this thesis as the study area for development of the random mixing method for mountain regions, therefore it is essential to consider catchment characteristics and observed hydrometeorological data used in the developing the random mixing method for a mountain catchment. This chapter describes the catchment and a number of research studies conducted there. The collation and analysis of hydrometeorological data collected at three automatic weather stations is presented, including total precipitation, rainfall and snowfall, near-surface air temperature, relative humidity, wind speed, incoming solar radiation and soil temperature, as well as streamflow from a gauge downstream of the catchment. Analysis of monthly and annual patterns of observed rainfall, snowfall and air temperature is discussed, followed by description of two hydrological models selected to explore the impact of spatial precipitation data from the new method and existing methods on catchment hydrology.

3.2 Marmot Creek Research Basin

Marmot Creek Research Basin (MCRB) is a 9.4 km^2 catchment located in the Front Ranges of the Canadian Rocky Mountains (50.95^{o}N, 115.15^{o}W) which discharges into the Kananaskis River, forming part of the Saskatchewan River Basin (Figure 3.1). MCRB has a long study history dating back to 1961, when it was established by Alberta provincial and federal Canadian government agencies as the Marmot Creek Experimental Watershed (Rothwell et al., 2016). From 1988, research activities in the basin ceased, until in 2004, the Universities of Saskatchewan and Calgary, along with Environment Canada, recommenced research activities (Pomeroy, 2013). Research since 2004 has covered a range of topics including: impact of forest canopy and forest clearings on snow accumulation and snowmelt energetics; slope and aspect controls on snow accumulation and melt; blowing snow and sublimation in the alpine treeline environment with respect to local wind and topography; alpine snowmelt runoff generation; hillslope hydrology of the forest organic layer; and precipitation phase partitioning (Fang et al., 2018). MCRB has three sub-basins: these are Cabin Creek (2.35km^2), Middle Creek (2.94 km^2) and Twin Creek (2.79km^2). These creeks converge above the main Marmot Creek stream gauging station. Elevations across the basin range from 1600 m above sea level (m a.s.l.) at the

primary gauging station to 2825 m a.s.l. at the peak of Mount Allan. A summary of dominant land cover is presented in Table 3.1 (Fang et al., 2012).

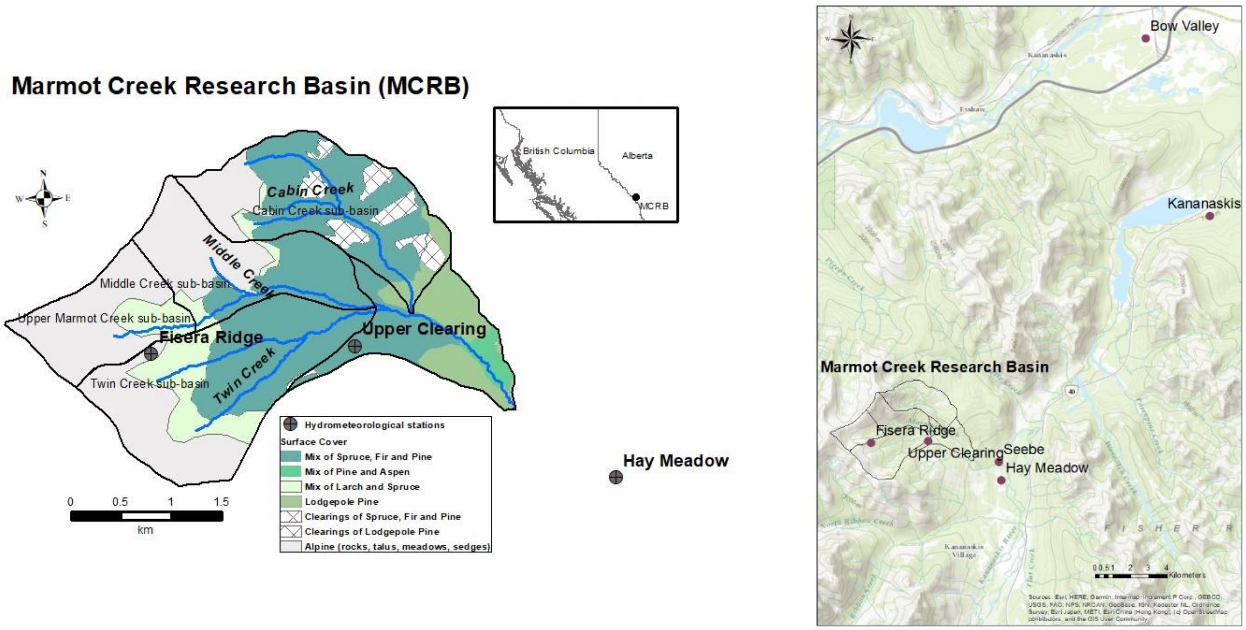

Figure 3.1. Location map of Marmot Creek Research Basin (MCRB), Alberta, Canada, showing hydrometeorological stations at Fisera Ridge, Upper Clearing, Hay Meadow, Kananaskis and Bow Valley and a flow gauging station at Seebe

Table 3.1. Marmot Creek Research Basin land cover

Elevation range	Dominant land cover
1590 – 2015 m a.s.l.	Engelmann spruce and lodge-pole pine
1710 – 2277 m a.s.l.	Engelmann spruce and subalpine fir
2016 – 2397 m a.s.l.	Alpine larch and short shrubs
1956 – 2819 m a.s.l.	Exposed rock, grass and talus

An 8m resolution Digital Elevation Map (DEM) for the basin was obtained, based on LiDAR data from 2008. A hypsometric curve for the Marmot Creek basin, downstream of the confluence of Upper Marmot Creek, Twin Creek, Middle Creek and Cabin Creek, was created for the basin, as presented in Figure 3.2.

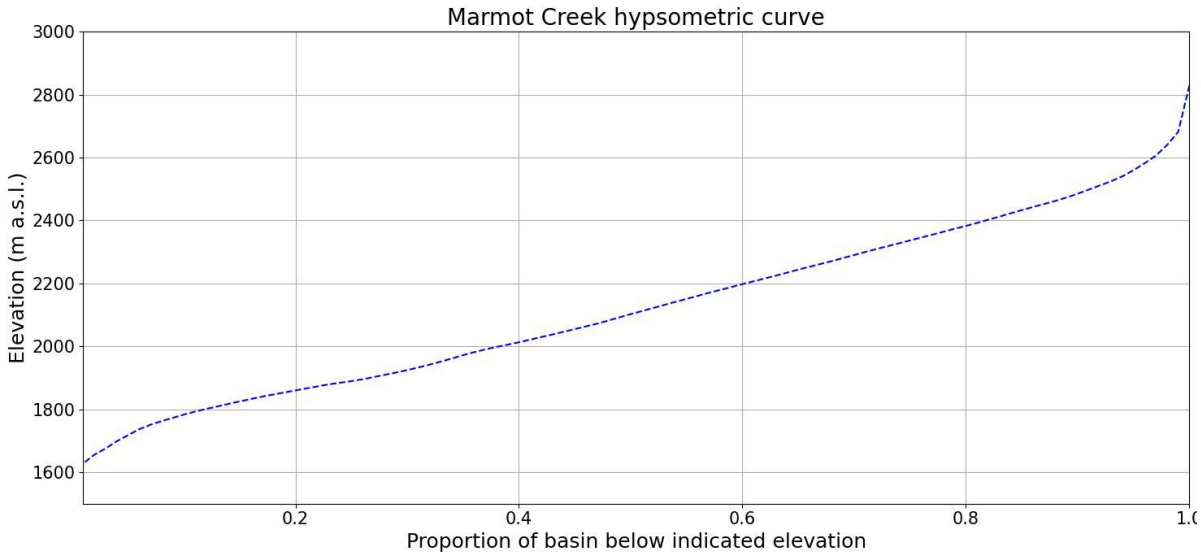

Figure 3.2. Hypsometric curve for MCRB showing the relationship between elevation and proportion below the indicated elevation

3.3 Collation of hydrometeorological data

Quality controlled hydrometeorological data (Fang et al., 2019) was obtained initially from five Automatic Weather Stations (AWS) across the catchment, the locations of which are shown in the basin map (Figure 3.1). The data, in water years, spanning from 1 October 2005 to 30 September 2016, was downloaded from the Federated Research Data Repository (FRDR, 2021). As water years contain months from two calendar years, three months (October to December) of one calendar year, followed by nine months (January to September) of the subsequent calendar year, the convention used here is to refer to a water year by only its second calendar year, i.e. 2006-2007 is referred to as 2007, and so on.

These hourly data are: air temperature (^{o}C), relative humidity (%), soil temperature (^{o}C), wind speed (m/s), precipitation (mm) and incoming solar radiation (W/m^2). Attention is focused on data obtained from the three stations at which all precipitation (rainfall and snowfall) is measured, namely Fisera Ridge (2325 m a.s.l.), Upper Clearing (1845 m a.s.l.) and Hay Meadow (1436 m a.s.l.). Fisera Ridge station is above the treeline where vegetation cover is short grasses and dwarfed conifers (larch and fir). The station at Upper Clearing is on a 100 m wide level clearing covered in short grasses, while Hay Meadow station is situated near the Kananaskis River, on a large grass-covered valley bottom terrace (Pomeroy et al., 2011). Details and images of the stations at Fisera Ridge, Upper Clearing and Hay Meadow (Fang et al., 2019) are below (Table 3.2, Figure 3.3).

a. b. c.

Figure 3.3. Photos of MCRB stations: a. Fisera Ridge (2325 m), b. Upper Clearing (1845 m), c. Hay Meadow (1436 m)

Table 3.2. Key hydrometeorological variables and instrumentation at Fisera Ridge, Upper Clearing and Hay Meadow stations

Station	Fisera Ridge	Upper Clearing	Hay Meadow
Coordinates and elevation	50.9560°N; 115.2041°W 2325 m a.s.l.	50.9565°N; 115.1754°W 1845 m a.s.l.	50.9441°N; 115.1389°W 1436 m a.s.l.
Record	13 Oct 2006 – 30 Sep 2016	7 Jun 2005 – 30 Sep 2016	1 Oct 2005 – 30 Sep 2016
Rainfall (mm)	Hydrological Services TB4 tipping-bucket rain gauge 4.2 m above ground	Hydrological Services TB4 tipping-bucket rain gauge 2.36m above ground	Texas TE525M rain gauge 2.56 m above ground
All precipitation (mm)	Geonor T200B gauge with alter shield 4.1 m above ground	Geonor T200B gauge with alter shield 1.85 m above ground	Geonor T200B gauge with alter shield 1.8 m above ground
Air temperature (°C) and relative humidity (%)	Vaisala HMP45C212 1.93 m above ground	Vaisala HC2-S3 2.15 m above ground	Vaisala HMP45C212 1.86 m above ground
Wind speed (ms^{-1}) and wind direction (°)	RM Young 05305-10 wind monitor	RM Young 05305-10 wind monitor 2.85 m above ground	RM Young 05305-10 wind monitor 7 m above ground
Snow depth (m)	SR50 1.19 m above ground	SR50 1.76 m above ground	SR50 1.65 m above ground

The sensitivity of the Geonor T200B precipitation gauges is 0.05 mm to 0.1 mm. Hourly streamflow data was also obtained from the same repository, for the main Marmot Creek gauging station, and also for the sub-basin stations on Cabin Creek, Marmot Creek, Middle Creek and Twin Creek, date ranges for which are presented below (Table 3.3). There is a degree of commonality between the date record for the sub-basins, i.e. 9 June 2007 to 1 November 2012, a period of 5 years and 5 months. However, the flow record at the main Marmot Creek gauge lies outside this period. To overcome this, daily mean flow values from 1 October 2005 to 30 September 2012 were obtained from the Environment Canada website (Government of Canada, 2021), for Marmot Creek main stem near Seebe (station number 05BF016).

Seebe station details:

- Latitude = 50° 57’ 01’’ = 50.95028°
- Longitude = -115° 09’ 10’’ = -115.15278°

Station 05BF016 is a V-notch gauging station, which was in use from 1962 until 2016. Flow observations were recorded between May and August of each year, during which periods there was no recorded ice blockages at the gauge site. Also, streamflow recordings between May and August, when daily mean air temperatures are above zero, are considered unlikely to be affected by snow blockage, hence uncertainty of flow measurements is low. There is very little sediment movement in the river channel and no bank erosion was observed between October 2005 and September 2012 (Fang, 2025), the period for which observed streamflow data was used in this study.

For modelling purposes, all hourly data was aggregated to daily values, which is consistent with the aim of this research project to produce daily precipitation datasets.

Table 3.3. Marmot Creek Research Basin gauging station records

Gauging station	**Record**
Upper Marmot Creek	9 Jun 2007 – 28 Jun 2016
Cabin Creek	7 May 2007 – 1 Nov 2012
Middle Creek	8 May 2007 – 1 Nov 2012
Twin Creek	9 Jun 2007 – 1 Nov 2012
Marmot Creek	26 Jun 2013 – 1 Nov 2016

3.4 Meteorological data

All meteorological data obtained is hourly quality-controlled (QC) data, from the 15-minute raw data gathered from the weather stations. Hourly air temperature (T, ^{o}C), relative humidity (rh, %), wind speed (ws, ms^{-1}), incoming solar radiation (sr, W m^{-2}) and soil temperature (ST, ^{o}C) were derived by averaging the 15-minute raw data. The sum of 15-min observations was used to arrive at hourly precipitation (P) values (mm). Where T, rh, ws, sr and ST data was missing at a given station, values were calculated in two ways: for missing data periods of less than three consecutive hours, values were calculated by temporal averaging using observations at the same station, before and after the gap; if the period of missing data was more than three hours, linear regression relationships were derived between stations using the available raw data. Those regression relationships with the highest r^2 values were used to generate data to fill the gaps. Where there was missing P data, observations from the closest station were adjusted using precipitation-elevation relationships to complete the datasets (Fang et al., 2018). The data used in this project are labelled as 'hourly modelling data', providing 11 water years of data, from 1 October 2005 – 30 September 2016. However, Fisera Ridge station was not operational until 13 October 2006, hence values between 1 October 2005 and 13 October 2006 were estimated, via linear interpolation for T, rh, ws, sr and ST; and by adjusting precipitation observations at Upper Clearing for elevation.

Total annual precipitation, both rain and snow, and the annual mean air temperature for water years 2006 to 2016 at Fisera Ridge, Upper Clearing and Hay Meadow stations are summarised below (Table 3.4 and Figure 3.4). The mean annual total precipitation range is between 1072 mm at Fisera Ridge, the highest of the three stations, and 544 mm at the station with the lowest elevation, Hay Meadow. The expected pattern of precipitation amounts decreasing with falling elevation is observed in all years between 2006-2016. Also as expected, more snow falls at higher elevations than at lower elevations: at Fisera Ridge, 70% of annual mean precipitation is snowfall; at Upper Clearing the corresponding value is 52%; and at Hay Meadow only 37% of precipitation falls as snow. The highest recorded annual precipitation amounts between 2006-2016 were in 2013: 1329 mm at Fisera Ridge, 868 mm at Upper Clearing and 762 mm at Hay Meadow; the lowest annual precipitation years were 2015 at Fisera Ridge (857 mm) and 2016 at Upper Clearing (591 mm) and Hay Meadow (426 mm). The mean annual temperatures at the three stations clearly demonstrates a pattern of warmer temperatures

at lower elevations, consistent with the lower snowfall totals at Upper Clearing and Hay Meadow, compared to Fisera Ridge.

Table 3.4. Water year total precipitation and mean air temperature data at Fisera Ridge, Upper Clearing and Hay Meadow stations

Water year	**Precipitation (mm)**									**Mean air temperature (°C)**		
	Fisera Ridge (2325 m a.s.l.)			**Upper Clearing (1845 m a.s.l.)**			**Hay Meadow (1436 m a.s.l.)**			**Fisera Ridge**	**Upper Clearing**	**Hay Meadow**
	rf	**sf**	**total**	**rf**	**sf**	**total**	**rf**	**sf**	**total**			
2006	351	551	902	340	306	646	337	155	492	0.1	2.3	4.0
2007	400	815	1215	376	421	797	435	196	631	-0.5	1.5	3.3
2008	292	926	1218	383	421	804	462	231	693	-1.7	0.6	2.3
2009	306	638	943	278	332	610	240	210	450	-0.7	1.0	2.8
2010	236	904	1140	260	410	670	271	205	476	-1.0	0.6	2.6
2011	263	865	1128	275	396	671	251	271	522	-1.2	0.4	1.9
2012	325	922	1247	375	419	794	385	201	586	-0.2	1.6	3.6
2013	535	794	1329	548	320	868	555	207	762	-0.2	1.4	3.1
2014	219	658	877	231	419	650	243	267	510	-0.8	0.5	2.2
2015	314	543	857	321	272	593	277	163	440	0.9	2.5	4.2
2016	325	614	939	323	268	591	308	118	426	1.0	2.7	4.4
11 water-year mean	324	748	1072	337	362	699	342	202	544	-0.4	1.4	3.1

Total monthly precipitation and monthly mean air temperature values were calculated by grouping months together for each year, from 2006-2016 (Table 3.5). Values for total monthly precipitation, and monthly mean air temperature, were generated by grouping separate months together (from 2006-2016), to identify the monthly patterns of rainfall and snowfall at the differing elevations (Table 3.5 and Figure 3.5). Box plots, indicating median, upper quartile (75%) and lower quartile (25%) values for monthly rainfall and snowfall for the three stations were also generated to further illustrate observed monthly precipitation patterns (Figure 3.6).

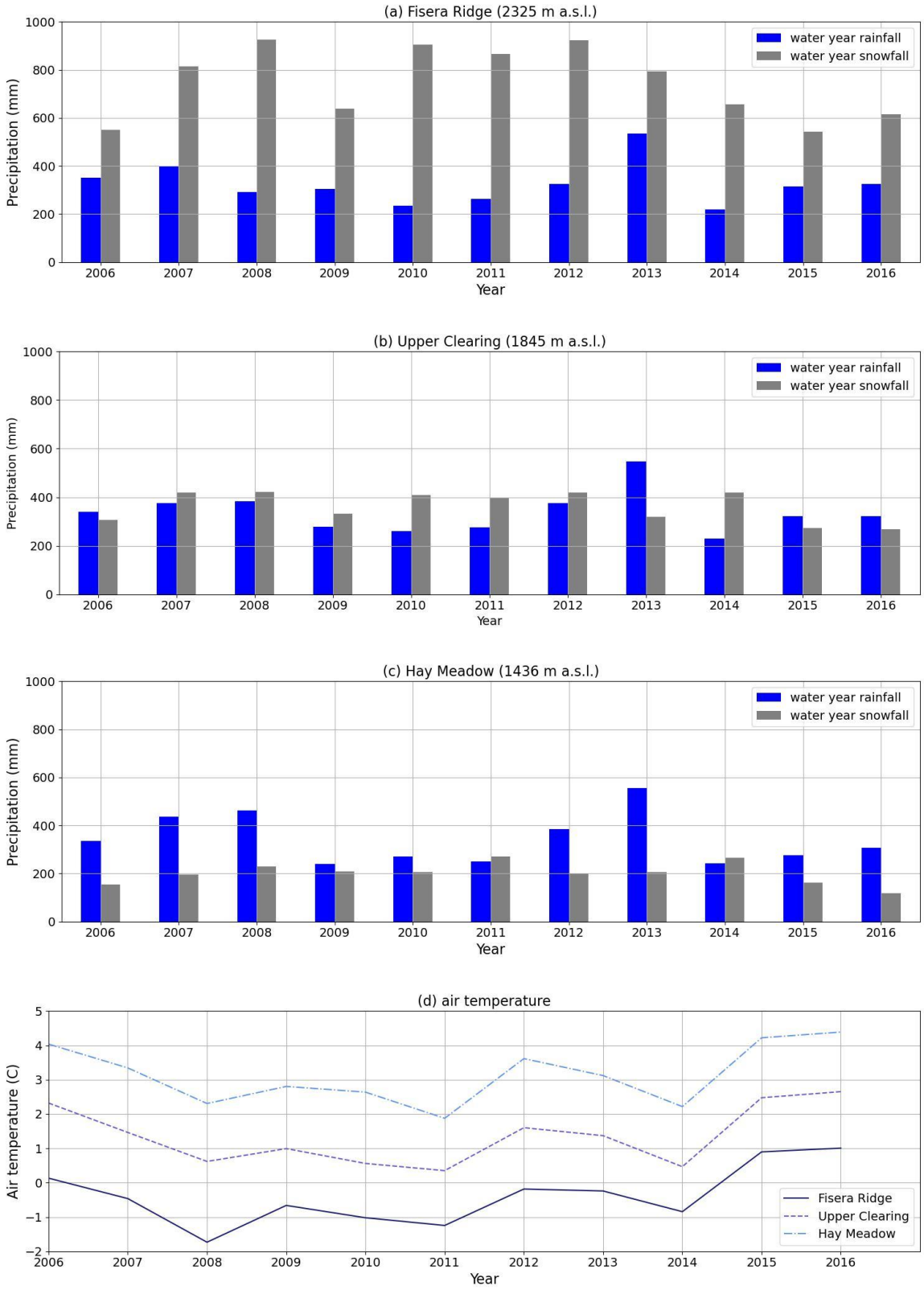

Figure 3.4. Annual precipitation for 11 water years at: (a) Fisera Ridge, (b) Upper Clearing, (c) Hay Meadow; (d) mean annual air temperature at all 3 stations

Table 3.5. Monthly total precipitation and mean air temperature data at Fisera Ridge, Upper Clearing and Hay Meadow stations

Month	Precipitation (mm)									Mean air temperature (°C)		
	Fisera Ridge (2325 m a.s.l.)			Upper Clearing (1845 m a.s.l.)			Hay Meadow (1436 m a.s.l.)			Fisera Ridge	Upper Clearing	Hay Meadow
	rf	sf	total	rf	sf	total	rf	sf	total			
Jan	0	626	626	3	331	334	17	236	253	-7.5	-7.2	-5.5
Feb	0	552	552	4	288	292	17	215	232	-8.3	-7.2	-5.3
Mar	22	1074	1096	42	503	545	74	291	365	-6.3	-3.8	-1.7
Apr	40	1176	1216	63	630	693	135	360	495	-2.9	-0.1	2.0
May	346	1309	1655	499	537	1036	687	181	868	2.3	4.7	6.7
Jun	1117	474	1591	1112	159	1271	1080	45	1125	6.4	9.0	10.9
Jul	730	47	777	619	7	626	422	1	423	10.9	13.3	14.6
Aug	746	134	880	662	36	698	491	7	498	9.9	11.9	13.0
Sep	417	582	999	463	257	720	490	104	594	6.1	7.7	9.0
Oct	98	636	734	163	312	475	197	180	377	-0.1	1.7	3.8
Nov	48	1038	1086	75	612	687	137	395	532	-6.5	-5.2	-3.0
Dec	2	581	583	5	312	317	18	208	226	-9.4	-9.0	-7.4

The lowest rainfall observations are recorded in December, January and February, when the mean monthly temperatures are lowest at all three stations. At Fisera Ridge, only snowfall (no rainfall) is recorded in January and February. Rainfall amounts at Upper Clearing and Hay Meadow are also very small, with most precipitation between December and February falling as snow. However, the largest recorded snowfall totals occur at slightly warmer temperatures, in November, and from March to May. This phenomenon is more pronounced at higher elevations, as highlighted by the bar plots in Figure 3.5a to Figure 3.5c. The snowfall box plots in Figure 3.6b, Figure 3.6d and Figure 3.6f also indicate the reduction in snowfall amounts in all months as we progress downhill from Fisera Ridge to Hay Meadow via Upper Clearing.

3.5 Precipitation phase partitioning

Precipitation phase was estimated using a psychometric energy balance method (PEBM), taking into account humidity as well as temperature (Harder & Pomeroy, 2013), rather than traditional empirical methods often used in hydrological applications which tend to use a daily time step and consider temperature only (known as *Ta* index methods). The effect of humidity is important as falling hydrometeors (water or ice particles) are subject to transfer of heat and water vapour with the atmosphere through which they are falling, hence the psychometric energy balance method, using an approximation of the temperature at the surface of the falling hydrometeor (*Ti*) provides a physical basis for phase estimation that empirical *Ta* index methods do not have. Precipitation phase has high spatiotemporal variability in the Rockies.

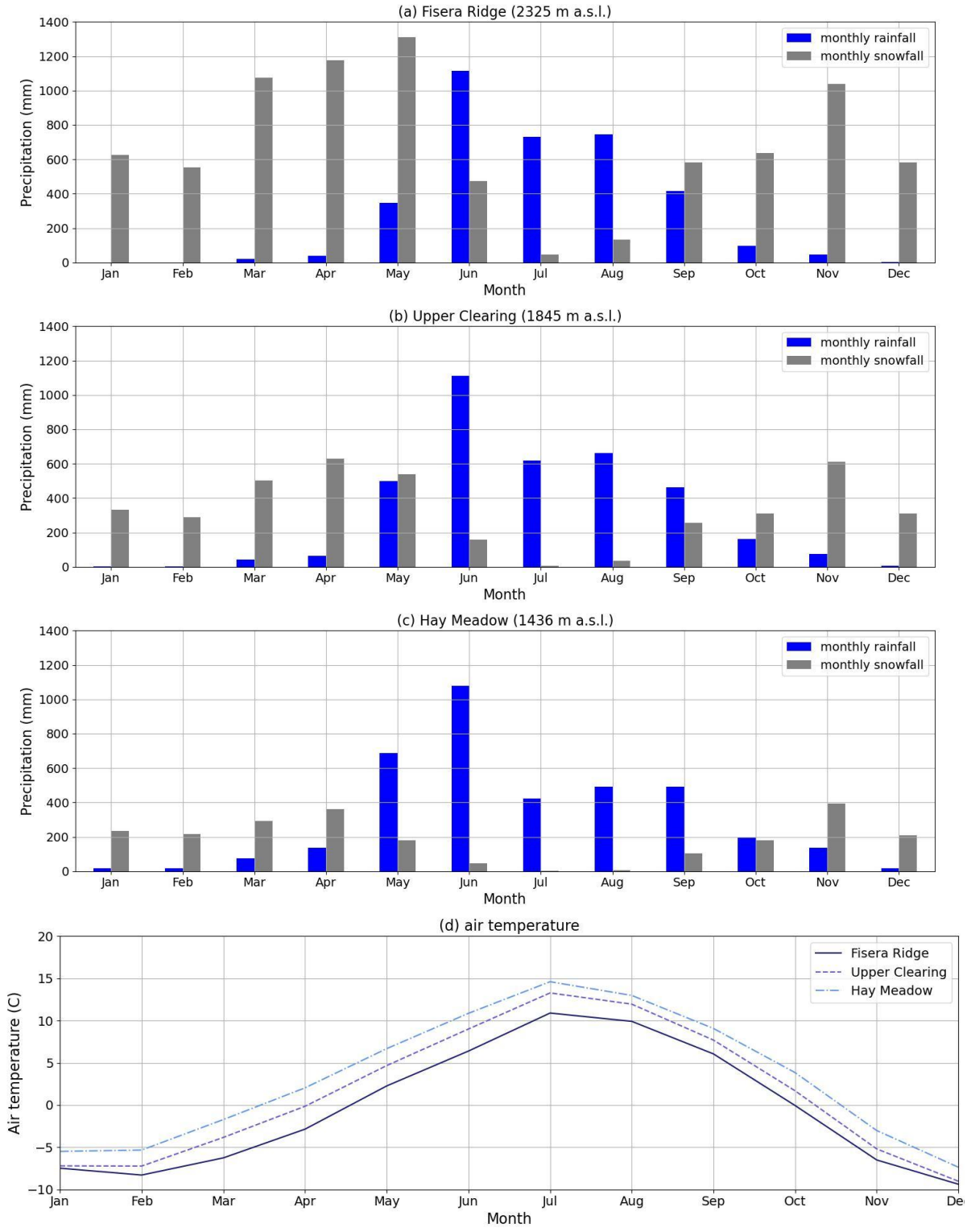

Figure 3.5. Monthly precipitation for 11 water years at: (a) Fisera Ridge, (b) Upper Clearing, (c) Hay Meadow; (d) mean monthly air temperature at all 3 stations

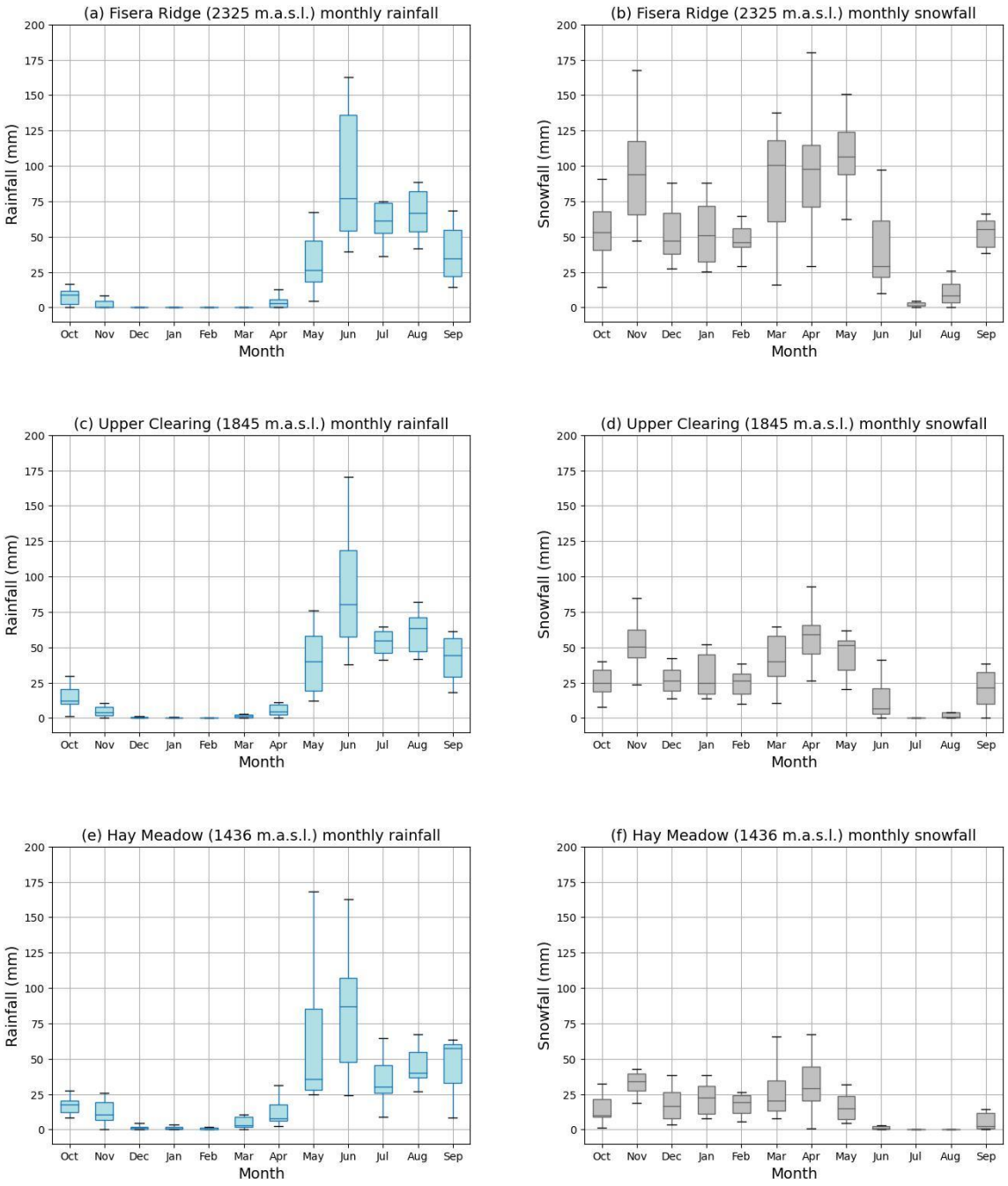

Figure 3.6. Monthly rainfall and snowfall box plots for Fisera Ridge (a-b), Upper Clearing (c-d) and Hay Meadow (e-f)

Elevation has a big influence on temperature and water vapour, and precipitation can fall as snow and rain in most months of the year, as highlighted in Figure 3.5. Many traditional methods used in hydrological applications to estimate phase are calibrated to a particular region; due to the temporal variability of precipitation, their use of a daily time step in phase calculations increases uncertainty. Harder & Pomeroy used meteorological data measured at MCRB stations at 15-minute intervals to develop and test their method, finding that it provides

better results than *Ta* index methods and that the accuracy of the method increases as the time step gets smaller, i.e. the temperature range over which mixed precipitation occurs is smaller with a 15-minute time step than a one hour time step. However, it was concluded that the optimal time step, giving the best balance between length of time step and mixed precipitation phase temperature range is one hour. Cumulative plots of rainfall and snowfall, produced using the hourly observed data from Fisera Ridge, Upper Clearing and Hay Meadow for water years 2006 to 2016 are shown in Figure 3.7.

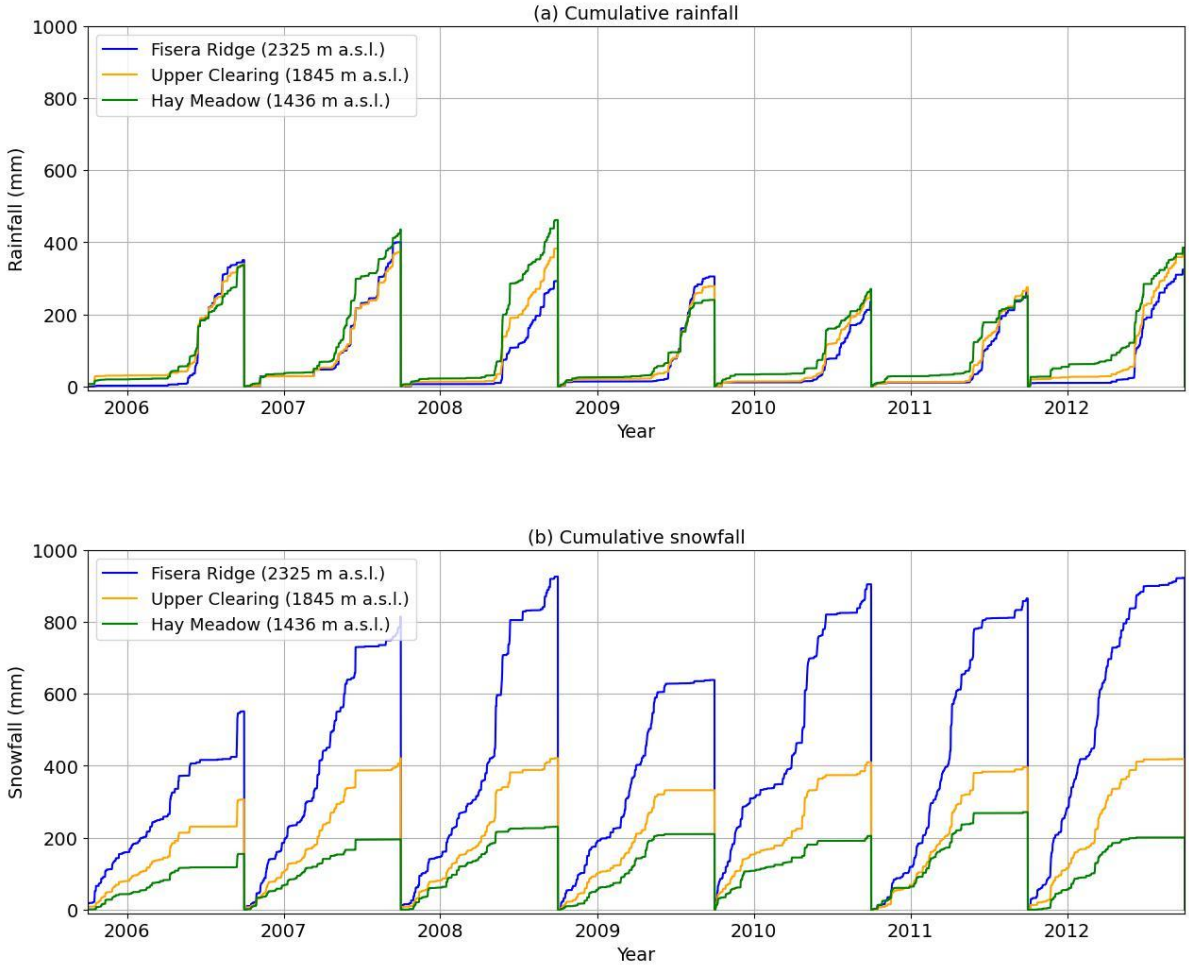

Figure 3.7. Cumulative precipitation for 11 water years at Fisera Ridge, Upper Clearing and Hay Meadow stations: (a) cumulative rainfall, (b) cumulative snowfall

3.6 Hydrological models

3.6.1 Introduction

A wide range of hydrological models is used extensively across a range of applications including flood and drought forecasting and water resources management. Hydrological models adopt different approaches in attempting to represent real-world processes and they can be classified according to the following main categories. Firstly, models are either deterministic, i.e., they always generate the same outputs from a given set of inputs; or stochastic, meaning that they contain an element of randomness which leads to different outputs for every simulation of an event with the same input data. Secondly, models can be differentiated by the way they represent space: they can be either lumped, semi- or fully spatially distributed. The third main method of classifying hydrological models is how hydrological processes are represented, with models typically being categorised as those that are physically based, i.e., they include methods of solving differential equations to represent physical processes; other models, referred to as conceptual hydrological models, typically parameterise physical processes using single values or arrays of values. To explore how spatial precipitation fields generated using the RM-mountain method would impact on the catchment hydrology, two very different hydrological models were used. The first, a fully spatially distributed version of the conceptual Hydrologiska Byråns Vattenbalansavdelning (HBV) hydrological model (Bergström, 1992, 1976; Lindström et al., 1997; Saelthun, 1996) and the partially distributed physically based Cold Regions Hydrological Model, or CRHM (J.W. Pomeroy et al., 2022; Pomeroy et al., 2007a). These two models are discussed in the following sections.

3.6.2 HBV hydrological model

The hydrological model used is a Python version of HBV adapted for this study, on a 50 m x 50 m resolution spatial grid, from wflow hbv (Deltares, 2021). HBV has been tested and developed over several decades (Bergström, 1976, 1992; Saelthun, 1996; Lindström et al., 1997). As initial RM-mountain test run times to simulate spatial precipitation fields were lengthy, its relatively simple structure made HBV a suitable hydrological model to use for testing development of RM-mountain. GIS input files for the HBV model were derived from FRDR data (FRDR, 2021) using ArcMap and QGIS. Modifications made for this study include the method used for simulation of runoff routing and the inclusion of functions to represent snowpack accumulation, melt and refreezing and gravitational snow redistribution through

avalanching (Bernhardt & Schulz, 2010). The model incorporates temporary stores for interception, solid and liquid snowpack, soil moisture, upper and lower zones and snow water equivalent (SWE). Conceptual upper zone outflow is calculated using the HBV-96 approach (Lindström et al., 1997). The runoff routing method is based on calculating a time lag for runoff to reach the catchment outlet depending on the distance of a cell from the outlet (Buitink et al., 2020). The HBV model code was updated to receive climate input data from more than one station and to apply a variation of the MicroMet approach (Liston & Elder, 2006) incorporating Inverse Distance Weighting (IDW) for initial spatial interpolation of precipitation across the catchment for baseline model calibration. Objective functions used for model calibration and validation were Nash-Sutcliffe Efficiency (NSE) (Nash & Sutcliffe, 1970), Root Mean Square Error (RMSE) and bias. The formulae for these metrics are presented in Table 3.7. A Python scipy.optimize.minimize routine (Virtanen et al., 2020) was applied, using the Sequential Least Squares Programming method to optimise HBV model parameters to satisfy objective function criteria, i.e., to maximise NSE and minimise bias when comparing observed and simulated streamflow at the catchment outlet (see Table *3.6* for parameters and optimised values). The precipitation and flow time series were split for calibration (October 2005 – September 2009) and validation (October 2009 – September 2012).

Table 3.6. HBV model parameters and optimised values

Parameter name	**Optimised parameter value**
Maximum interception storage (icf)	2.0 mm
Fractional soil moisture limit for aet=pet (lpf)	0.9
Field capacity (fc)	250.0 mm
Melt threshold temperature (ttm)	273.15 K
Snow temperature index melt factor (cfmax)	3.0 mm/K-timestep
Snow refreezing factor (cfr)	0.1
Fractional snow water holding capacity (whc)	0.16523
Soil seepage exponent (beta)	2.0
Maximum percolation rate through soil (perc)	3.0 mm/timestep
Maximum capillary flux (cflux)	2.0 mm/timestep
Coefficient for upper zone outflow (k)	0.01
Exponent for upper zone outflow (alpha)	0.7
Coefficient for lower zone outflow (k1)	0.04335
Travel speed (tau)	1.0/86400.0 timestep/m
Minimum slope angle for snow redistribution (ssm)	25.0º
Coefficient for exponent in snow holding depth function (ssc)	20000.0
Coefficient for slope in snow holding depth function (ssa)	-0.05468
Minimum holding depth (sshdm)	5.0

A NSE value = 1 indicates a perfect fit between observed and modelled flows, whereas NSE = 0 signifies the model performance is only as good as the mean of the observed time series of flows. NSE is particularly useful for evaluating model performance at higher flows. RMSE is the square root of the mean squared errors, a measure of the differences between observed and modelled discharge values, with a value of zero representing ideal model performance. Finally bias, which calculates overall volume error, is used as a water balance indicator, comparing the system water balance from observations with that from the model. Perfect model performance would result in a bias value of zero. Optimised values of 0.76 for NSE and -20.94 for bias were obtained, the purpose of which is to provide a baseline for evaluation of RM-mountain ensemble simulations in Section 5.2. The negative bias of -20.94 indicates a negative water balance in the model, likely due to underestimation of spatial precipitation in the mountainous MCRB catchment, with precipitation data from only three gauges (Goovaerts, 2000; Mair & Fares, 2011; Borges et al., 2016). Reducing this negative bias is the primary issue to address in developing the RM-mountain method.

Table 3.7. Objective functions used to optimise HBV model parameters

Objective Function	**Formula**
Nash-Sutcliffe Efficiency (NSE)	$NSE = 1 - \frac{\sum_{t=1}^{T}(Qo,t - Qm,t)^2}{\sum_{t=1}^{T}(Qo,t - \overline{Qo})^2}$
Bias	$Bias = 100 \times \frac{\sum_{t=1}^{T} Qo,t - \sum_{t=1}^{T} Qm,t}{\sum_{t=1}^{T} Qo,t}$

where Qo,t = observed flow at time t
Qm,t = modelled flow at time t
$\overline{Qo}$ = mean observed flow
T = no. of timesteps

HBV uses a daily timestep as determined by daily precipitation inputs. It was enhanced for this project with functions to represent snowpack accumulation, melt and refreezing and gravitational snow redistribution, i.e., avalanching, the latter based on the SnowSlide method (Bernhardt & Schulz, 2010). Storage and flux parameters were optimised via model calibration and validation. Climate inputs are precipitation (rainfall and snowfall), near-surface air temperature (2 m above ground level) and potential evapotranspiration (PET). Elevation gradients for precipitation are taken from a Cold Regions Hydrological Model (CRHM) study of MCRB (Pomeroy et al., 2007a; University of Saskatchewan, 2022; Shook, 2021) and used in calculating the initial spatial interpolation of daily precipitation from the observed station records for calibration and validation of the MCRB catchment model.

It is important to adopt a suitable spin-up period to allow hydrological model to adjust from estimated initial conditions to a state that represents catchment behaviour, during which period the model's internal variables stabilise. The required length of the spin-up period can vary depending on factors that include catchment characteristics and hydrological model complexity. The relatively simple structure of the conceptual HBV hydrological model allows for a relatively short spin-up period, as the model will settle fairly quickly to an equilibrium state. For this study, a one-year spin-up period was adopted for all simulations, with final storage values at the end of the spin-up period used as initial conditions for model simulations. Monthly mean near-surface air temperature (tas) vs elevation linear regression coefficients were calculated and used in the model; r^2 values between 0.806 (January) and 0.981 (June) show that the linear regression model gives a good level of fit.

3.6.3 Cold Regions Hydrological Model (CRHM)

The study of cold regions can involve hydrological processes that are not always effectively addressed in hydrological models, for example many cold region catchments are snow-covered for parts of the year or even all year round (Pomeroy et al., 2012; Fang & Pomeroy, 2020) and snowmelt is often a key driver of streamflow. Cold region catchments are often sparsely gauged or ungauged which presents additional challenges to hydrologists who need to deal with processes such as blowing snow redistribution, precipitation phase changes and the effects of seasonal variability. Lack of adequate streamflow observations can pose challenges for hydrological model calibration (Pomeroy et al., 2022). To enable better representation of cold regions processes, the Cold Regions Hydrological Model (CRHM) was devised as a modular, object-oriented system, designed to incorporate and connect a set of algorithms to model small and medium-sized river catchments (Pomeroy et al., 2007b). The hydrological processes represented by these algorithms, all of which are subject to significant uncertainty, are: snow redistribution by wind and snow interception; sublimation (the process of ice or snow changing state directly to water vapour without first melting into water); snowmelt; infiltration into frozen soils; hillslope water movement over permafrost; actual evaporation; and radiation exchange to complex surfaces. The model represents landscape elements that affect hydrological processes such as: blowing snow transport; overland flow; organic layer subsurface flow; mineral interflow; groundwater flow; and streamflow. CRHM has been tested primarily in Canadian river catchments dominated by semi-arid prairie, boreal forest, mountain and wetland

conditions, where it has previously been difficult for traditional hydrological models to adequately represent catchment hydrology (Pomeroy et al., 2007b).

In CRHM, the user can build a bespoke catchment model by selecting from a range of modules to represent physical processes and by specifying an appropriate spatial resolution. Hydrological response units (HRUs) are used to spatially discretise a catchment, with the number and characteristics of HRUs specified by the user based on their understanding of the catchment, for example geology, land cover, elevation or topography. Surface runoff, groundwater flow and blowing snow processes can flow between HRUs. Runoff and groundwater are routed as streamflow to the basin outlet, whereas blowing snow can be directed to and from a catchment. Where applicable, HRUs can be clustered into a 'representative basin' which can be duplicated and amended to enable rapid parameterisation of larger catchments that combine a collection of sub-catchments. Modules are executed within HRUs with models being lumped with one HRU per sub-catchment, fully distributed with lots of HRUs on a high-resolution grid, or semi-distributed where HRUs are defined by landscape, with each having a single parameter set based on shared physical and hydrological properties (J. W. Pomeroy et al., 2022). It is recommended that length scales of HRUs should be between 100 m and 3 km; time steps depend on input observations, typically assumed to be hourly. Observations are of meteorological variables: air temperature, relative humidity, ground temperature, wind speed, precipitation and solar radiation. Input data is available to all modules via observation (.obs) files which also specify simulation start and end dates/times and the time step. Model output values, or variables, can be plotted and saved to file for analysis.

A graphical user interface (GUI) version of CRHM (CRHM_GUI) has been used in this project to model the Marmot Creek Research Basin (MCRB) previously described in Section 3.2. CRHM incorporates the following modules for modelling cold regions processes: snow transport, interception and sublimation, albedo, radiation, evapotranspiration, snowmelt, glacier, infiltration, soil moisture balance, skin surface temperature, routing and Quinton modules. The MCRB model is semi-distributed and comprises four sub-basins, each with a different number of HRUs, as follows: Middle (7 HRUs), Twin (9 HRUs), Cabin (12 HRUS) and confluence (8 HRUs); 36 HRUs in total, details of which are summarised in Table 3.8. The HRUs here are assigned according to shared land surface and topographical characteristics. In general, the highest elevation HRUs are exposed alpine rock, while at lower elevations much

of the basin is covered in Alpine larch, spruce, fir or pine trees, with some forest clearings also identified.

The modules used in the MCRB catchment model in this project are described in Table 3.9. A useful feature of CRHM when constructing a catchment model is the facility to group modules together for each sub-basin under a single name, that can be handled by the model as one group. CRHM enables the user to establish such groups, known as Representative Basins (RBs) using the Macro Group feature 'declgroup', specifying the number of HRUs in each group/sub-basin. The RBs are combined into a group, 'REW_Grp' for routing of surface runoff, subsurface runoff and groundwater flow (see the description of the 'REW_route' module in Table 3.9).

Table 3.8. MCRB sub-basin HRU areas and elevations

HRU no	Sub-basin							
	Middle		Twin		Cabin		Confluence	
	Area (km^2)	Elevation (m a.s.l.)	Area (km^2)	Elevation (m a.s.l.)	Area (km^2)	Elevation (m a.s.l.)	Area (km^2)	Elevation (m a.s.l.)
1	0.52	2462	0.79	2386	0.23	2387	0.01	1903
2	1.37	2422	0.16	2380	0.17	2379	0.38	1786
3	0.26	2246	0.28	2228	0.02	2222	0.24	1724
4	0.08	2211	0.28	2182	0.02	2194	0.05	1688
5	0.16	1995	0.38	1966	0.35	2046	0.44	1752
6	0.52	1953	0.36	2014	0.93	1972	0.03	1724
7	0.3	2057	0.26	1966	0.05	1931	0.15	1687
8			0.24	2014	0.4	1927	0.02	1664
9			0.04	1988	0.06	1882		
10					0.07	1798		
11					0.01	1780		
12					0.04	1951		

Colour key:

- Alpine rock (north-facing)
- Alpine rock (south-facing)
- Alpine larch/spruce mix (south-facing)
- Alpine larch/spruce mix (north-facing)
- Spruce/fir/lodgepole pine mix (north-facing)
- Spruce/fir/lodgepole pine mix (south-facing)
- Valley bottom
- Circular clearings (north-facing)
- Circular clearings (south-facing)
- Spruce/fir/lodgepole pine mix (level)
- Forest clearings
- Lodgepole fir (level)
- Lodgepole fir (south-facing)
- Lodgepole fir (north-facing)

Table 3.9. CRHM module descriptions

Module	Description
basin	General module for declaring general parameters for the model such as basin area, HRU area, latitude, elevation, ground slope (GSL) and aspect angle (ASL).
global	Radiation module which calculates the theoretical interval short-wave direct and diffuse solar radiation, handling ground slope and aspect.
obs	General module that reads climate data from the observation data file(s) into the model. The time step is determined by the observation file interval. The module copies the observations to the HRUs, with the facility to specify corrections for redirection, elevation height and climate change.
calcsun	Radiation module to estimate sunshine hours from observed Qsi and the values QdroD, QdfoD and SunMax (maximum sunshine hours) calculated by the 'global' module using the HRU's latitude.
Slope_Qsi#1	Radiation module that estimates incoming solar radiation (Qsi) for a slope from the measured incoming short-wave Qsi on the level. The ratio of measured Qsi and the calculated clear sky direct (QdroD) and diffuse (QdfoD) radiation on a horizontal plane is used to adjust the calculated clear sky value on the slope.
albedo_Richard	Albedo module that uses the CLASS (Canadian Land Surface Scheme) algorithm to estimate snow albedo and is used for the energy-balance snowmelt module SnobalCRHM.
walmsley_wind	Snow transport module which is a parametric version of a windflow model for estimating wind speed variation induced by small-scale topographic features including: 2D hills (ridges), 3D hills, 2D escarpments, 2D rolling terrain, 3D rolling terrain, and flat terrain.
longVt	Radiation module that calculates long-wave radiation using measured or estimated shortwave irradiance.
netall	Radiation module that models net all-wave radiation from the calculated short-wave and long-wave radiation. It requires temperature, vapour pressure and actual sunshine hours data.
evap_Resist	Evapotranspiration module which calculates evapotranspiration using interval values for snow cover-free periods via one of three methods: Penman-Monteith, Dalton-type bulk transfer and Priestley-Taylor.
CanopyClearingGap#3 (variation 3)	Interception module that models net all-wave radiation, short-wave and long-wave radiation at the snow surface under a needleleaf forest canopy from observed incoming short-wave radiation.
pbsmSnobal	Snow transport module that calculates snow transport and sublimation for each interval using observed wind speed, air temperature and relative humidity. The model can simulate transport of snow between HRUs.
SnobalCRHM#1 (variation 1)	Snowmelt module which uses energy balance to calculate snowmelt, and to predict runoff, from input data on snow

Module	Description
	properties, measurement heights & depths, and energy exchanges. The model approximates the snow cover as comprising a top active layer and a lower layer. Melt is calculated in either layer when accumulated energy > cold content or when cold content > 0 (cold content is the energy needed to bring the snow cover temperature up to 0ºC. Runoff is estimated when the accumulated melt and liquid H_2O content exceed a specified threshold.
frozenAyers	Infiltration module that simulates rainfall infiltration into unfrozen soil and snowmelt infiltration into frozen soil.
Soil	Soil moisture balance module which handles soil moisture accounting throughout the year and calculates the soil moisture balance, groundwater storage, subsurface and groundwater discharge, depressional storage, and runoff for control volumes of two soil layers, a groundwater layer, and surface depressions.
K_Estimate#1	Soil moisture balance module used to estimate drainage factor parameters in modules such as Soil (based on Darcy's law for unsaturated flow), for lateral flow in soil layers and groundwater layer (i.e. subsurface and groundwater discharges) and vertical flow of excess soil water to groundwater (i.e. groundwater recharge). Variation #1 estimates drainage factors in detention layer.
Netroute_M_D	Route module that handles the routing of surface runoff, subsurface runoff and HRU routing using the Muskingum method. Outflow from an HRU is calculated by lagging its inflow by the travel time through the HRU, then routing it through a calculated volume of storage. The outflow from an HRU can be routed as inflow to other HRUs and to the basin outlet. The parameter 'distrib_Route' controls the outflow of an HRU to other HRUs. The parameter 'distrib_Basin' determines the outflow of an HRU to the basin outflow.
REW_route	This module handles the routing of surface runoff, subsurface runoff, and groundwater flow from representative basins (RBs). Total outflow (the sum of surface and subsurface runoff) and groundwater (GW) flow from an RB is calculated by lagging the inflow and GW inflow by the travel time through the RB, then routing it through an amount of storage defined by a storage constant, K. The outflow and GW outflow from an RB can be diverted to the inflow and GW inflow of another RB or directed to the catchment outlet.

Each CRHM module in Table *3.9* has several parameters which are listed in Appendix C. Values for these parameters must be set for each of the 36 HRUs in the catchment model. Manual sensitivity testing was undertaken to explore the sensitivity of the MCRB model to changes in parameters values in terms of their impact on streamflow outputs. It was identified that changes in parameter values in the snow melt (SnobalCRHM) module had the greatest impact on streamflows, primarily because flows in May and June of each year are driven by

snow melt. As the performance of the RM-mountain generated spatial precipitation fields is evaluated using bias and NSE metrics (by comparing observed and simulated streamflows), and CRHM-simulated streamflows are sensitive to changes in some SnobalCRHM parameters, evaluation of precipitation field performance is contingent on selecting optimal parameter values for CRHM.

The MCRB catchment model for each simulation is saved as a project (.prj) file which contains modules, observation (.obs) files with hydrometeorological variables (air temperature, relative humidity, ground temperature, wind speed, precipitation and incoming solar radiation), parameters and output variables required for analysing and evaluating simulation results. A .prj file can be run using the CRHM_GUI or from the command line, the latter enabling many .prj files to be run as a batch. CRHM can handle point precipitation data from precipitation gauge locations and gridded precipitation data from a range of potential sources. Where point precipitation data is used, all meteorological variables are incorporated in a single .obs file for the length of time series to be used, typically on an hourly basis. Depending on the available data, a separate value can be input for each hour or, where daily data is being used, the daily value can be input for the first hour of each day and CRHM distributes this across the 24 hours of each day in the time series. An initial 'baseline' CRHM MCRB simulation was run using a single .obs file, with point observations of hourly precipitation data from weather stations at Fisera Ridge, Upper Clearing and Hay Meadow. When gridded precipitation inputs are to be input, two .obs files are needed. Point precipitation data is removed from the initial .obs file and a second .obs file is created with precipitation amounts for each HRU for each hour in the time series. This approach was taken when using gridded precipitation inputs derived from RM-mountain and other methods of spatial interpolation, Nearest Neighbour, Inverse Distance Weighting, Ordinary Kriging and Kriging with External Drift. As was done for HBV, a CRHM baseline simulation was run, yielding metric values of 0.64 for NSE and 0.24 for bias. These metric values form part of the discussion of model performance using RM-mountain generated spatial precipitation fields in Chapter 6.

3.7 Modifying the random mixing approach for a sparsely gauged mountain region

The following chapters aim to show how a stochastic method of spatial precipitation field generation, random mixing, can be modified to enhance its suitability for use in a mountain catchment and to use precipitation fields obtained with the modified random mixing technique as inputs to two different hydrological models. Three modifications made to the RMWSPy technique (Hörning & Haese, 2021) will be introduced to enhance spatial precipitation fields generated for Marmot Creek Research Basin and explore how these spatial fields perform when used as inputs in conceptual (HBV) and physically-based (CRHM) hydrological models.

Chapter 4. Random mixing for mountain precipitation

4.1 Introduction

The aim of this chapter is to present the development of the random mixing technique for spatial interpolation of precipitation for the small mountainous Marmot Creek Research Basin. This involves three modifications to the Random Mixing Whittaker Shannon Python (RMWSPy) technique mentioned previously in Section 1.2, an outline of which is presented below in Section 4.3. In summary, the modifications involve changing the way in which the algorithm randomly samples from observed precipitation for spatial copula fitting to improve the representation of spatial variability for a sparsely gauged catchment; introducing elevation dependence into the computation of precipitation values for each grid cell in the model domain; and the ability to include seasonal precipitation marginal distributions and seasonal spatial covariance relationships in the method. This chapter explores and analyses observed precipitation patterns required for successful implementation of the random mixing algorithm. Firstly, dry days and wet days must be represented separately in the model, hence precipitation observations are analysed to identify dry day probability values and wet day probability density functions (pdfs). The method uses repeated random sampling from the probability distributions to fit spatial covariance functions: to check the validity of this approach, autocorrelation calculations were necessary to evaluate the temporal independence of daily precipitation values relative to preceding days' observations. Spatial correlation of precipitation observations for each pair of stations included in the study was an important factor in determining an appropriate spatial covariance function for the modified random mixing model; this was done by computing Pearson correlation coefficients and plotting them to identify spatial correlation patterns between different station locations across a range of separation distances. Conditional wet/dry day probabilities are evaluated as they are another important consideration in understanding temporal precipitation patterns. An outline of the RMWSPy method (Hörning & Haese, 2021) is presented along with the outcomes of its initial application to MCRB. The three subsequent modifications to the method are then discussed before an evaluation of the performance of the method with each of these modifications.

4.2 Statistical Characterisation of MCRB Precipitation

It was important to characterise the statistics of observed precipitation in MCRB in order to make decisions about how to represent wet days and dry days in the random mixing algorithm, and to select appropriate marginal distributions, or probability density functions (pdfs) from which to randomly sample precipitation data in fitting a suitable spatial covariance relationship. Other key characteristics of precipitation to consider are autocorrelation in time and, to a lesser extent, conditional wet day/dry day probabilities. The importance of these characteristics, and how they have been evaluated, are discussed in the following sections.

A Python script was developed to read and analyse total daily precipitation data, i.e., rainfall and snowfall, initially from the three weather stations at Fisera Ridge (2325 m a.s.l.), Upper Clearing (1845 m a.s.l.) and Hay Meadow (1436 m a.s.l.). Snowfall amounts were based on snow water equivalent (SWE) values. In an attempt to improve the representation of the spatial variability of precipitation fields generated using the random mixing method, the availability of precipitation data from other gauges in the vicinity was explored. An initial 23 additional stations within an initial 50km radius of MCRB were identified (Environment and Climate Change Canada, 2011). Once gauge records had been obtained, 21 were rejected, either due to only short records of one or two years being available, or because of large quantities (i.e., several years' worth) of missing data. This left two additional gauges, at Kananaskis (1391 m a.s.l.) and Bow Valley (1298 m a.s.l.) with continuous precipitation records covering the 11-year period from October 2005 to September 2016 (Table 4.1, Figure 3.1).

Table 4.1. Additional stations with sufficient precipitation data, within a 20 km radius of MCRB

Station	**Kananaskis**	**Bow Valley**
Coordinates	51.0275^{o}N; 115.0347 ^{o}W	51.0833 ^{o}N; 115.0667 ^{o}W
Elevation (m a.s.l.)	1391	1298

The following sections describe how wet and dry days are defined.

4.2.1 Probability of zero precipitation

In the random mixing method, dry and wet days are modelled separately. The number of observed dry days in the gauge records is used to calculate the probability of experiencing a dry day, here referred to as $p0$. To do this, it is essential to first decide on a threshold to define dry days and wet days. Four different dry day threshold values were tested: 0 mm, < 0.1 mm, ≤ 0.1 mm and < 1.0 mm, resulting in a set of dry day probability values (Table 4.2). Only Fisera Ridge, Upper Clearing and Hay Meadow are shown as these are the stations whose records are used to constrain the spatial precipitation fields generated for the MCRB catchment by RM-mountain; Kananaskis and Bow Valley are additionally used for spatial covariance function fitting, to enhance the representation of spatial variability. Analysis of basic statistics of the threshold values (Table 4.3) shows that the mean, minimum and maximum values for thresholds of 0 mm, < 0.1 mm and ≤ to 0.1 mm are very similar. Only when considering a dry day threshold of 1.0 mm is there a noticeable difference in values, for example mean probability values range from 0.49 - 0.52 for the three lower thresholds, to 0.71 with a 1.0 mm threshold. The chance of a dry day is identical for the < 0.1 mm and ≤ 0.1 mm thresholds. Of these two thresholds, only the < 0.1 mm limit was retained. As the sensitivity of the precipitation gauges at Fisera Ridge, Upper Clearing and Hay Meadow is in the range 0.05 to 0.1 mm, it would not be good practice to adopt a dry day threshold of exactly 0 mm, hence this was also removed from consideration. To summarise, only two threshold values have been considered from this point: < 0.1 mm and < 1.0 mm.

Table 4.2: Probability of zero precipitation

Station	**Elevation (m a.s.l.)**	**Probability of zero precipitation**			
		Threshold = 0.0 mm	**Threshold < 0.1 mm**	**Threshold ≤ 0.1 mm**	**Threshold < 1.0 mm**
Fisera Ridge	2325	0.42	0.44	0.44	0.63
Upper Clearing	1845	0.47	0.52	0.52	0.72
Hay Meadow	1436	0.58	0.61	0.61	0.77

Table 4.3: Summary statistics of dry day threshold values

Statistic	**Threshold = 0.0 mm**	**Threshold < 0.1 mm**	**Threshold ≤ 0.1 mm**	**Threshold < 1.0 mm**
Mean	0.49	0.52	0.52	0.71
Minimum	0.42	0.44	0.44	0.63
Median	0.47	0.52	0.52	0.72
Maximum	0.57	0.61	0.61	0.77

4.2.2 Wet day probability distributions

The next stage in characterising precipitation patterns at MCRB was to fit probability distributions to wet day daily precipitation records, initially on an annual basis, at each of the five stations that will be used for spatial copula fitting, i.e., Fisera Ridge, Upper Clearing, Hay Meadow, Kananaskis and Bow Valley, for the 11 years between October 2005 and September 2016. Each of the five complete 11-year time series consists of a total of 4019 daily precipitation values. The number of wet days in each series varies according to the selected dry day threshold (Table 4.4) with a noticeable difference between the number of wet days depending on the threshold value adopted. The higher elevation stations in the mountains, Fisera Ridge (2325 m a.s.l.) and Upper Clearing (1845 m a.s.l.) experience more wet days than those at lower elevations towards the plain. At these stations, the effect of changing the dry day threshold on wet day numbers is greatest. Clearly a greater number of wet days is defined by the lower threshold.

Table 4.4: Number of wet days for two different thresholds

Station	No. of wet days Threshold < 0.1 mm	No. of wet days Threshold < 1.0 mm	Difference (days)	Percentage difference
Fisera Ridge	2243	1482	761	-33.9
Upper Clearing	1925	1129	796	-41.4
Hay Meadow	1551	916	635	-40.9
Kananaskis	1298	1027	271	-20.9
Bow Valley	1543	947	596	-38.6

As a further check, the difference in total precipitation, over the 11-year period (2005-2016), comparing dry day thresholds of < 0.1 mm and < 1.0 mm, was investigated. Clearly the 11-year totals using the < 1.0 mm threshold are smaller than those for the < 0.1 mm threshold. In applying the < 0.1 mm cut-off, only daily precipitation amounts between 0.1 mm and 1.0 mm are removed, hence the percentage differences are small, ranging between 1.5% at Kananaskis to 4.6% at Hay Meadow. In summary, using the < 0.1 mm threshold is justifiable as it yields a larger number of wet days but a negligible increase in total 11-year precipitation.

As one of the aims of this project is to investigate variability in precipitation by using an ensemble modelling approach, reducing the number of wet days in the observed time series is likely to restrict variability, and hence the extreme precipitation values that will be simulated in the ensemble. For that reason, it was concluded that the reduction in the number of wet days associated with the < 1.0 mm limit was not acceptable. For that reason, a dry day threshold of

< 0.1 mm was retained for the remainder of the project. The probability of experiencing a dry day, $p0$, is calculated accordingly for each station whose precipitation data will be used for sampling to generate spatial fields, i.e. only Fisera Ridge, Upper Clearing and Hay Meadow. As both annual and seasonal precipitation patterns will be used for generating spatial precipitation fields in the modified random mixing method, $p0$ values have been calculated for both annual and seasonal scenarios (Table 4.5). The months assigned to each season are: autumn (SON - September, October, November), winter (DJF - December, January, February), spring (MAM - March, April, May) and summer (JJA - June, July, August). The $p0$ values for the three stations show the expected pattern; the probability of a dry day is lowest at the highest elevation and vice versa, i.e., there is a higher occurrence of wet days at high elevations, and fewer wet days at lower elevations. When considering seasonality, the season with fewest dry days (i.e., the lowest $p0$ values) at all three stations is spring. However, the season with most dry days (the highest $p0$) is summer at Fisera Ridge, autumn and summer at Upper Clearing and winter at Hay Meadow. For initial attempts to generate spatial precipitation fields using RMWSPy, an annual three-station average $p0$ value of 0.53 was adopted.

Table 4.5. Dry day probability values

Station	**Elevation (m a.s.l.)**	**Dry day probability ($p0$)**				
		Annual	**Autumn**	**Winter**	**Spring**	**Summer**
Fisera Ridge	2325	0.44	0.47	0.40	0.37	0.52
Upper Clearing	1845	0.52	0.55	0.51	0.48	0.55
Hay Meadow	1436	0.61	0.60	0.66	0.56	0.63

The importance of selecting a suitable marginal distribution (pdf) for modelling wet days has already been explained (Section 2.4). Unlike RMWSPy, in which a Kernel Density Estimation (KDE) approach is used, here a range of pdfs was evaluated manually to determine which would best represent the daily precipitation values observed at Fisera Ridge, Upper Clearing and Hay Meadow stations, on annual and seasonal bases. Using the selected dry day threshold of < 0.1 mm, histograms, using 50 bins, were generated for each station and, as expected for daily data, these demonstrated a pattern of exponential-style decay. Python scipy.stats modules (Virtanen et al., 2020) were used to optimise parameters to best fit exponential and gamma distributions to the daily data. The gamma distribution provides a better fit to the histograms plotted at each of the five stations. Although maximum daily precipitation values within the time series considered exceed 100 mm, the distribution plots have been truncated at 30 mm on the x-axis to make the figure easier to read.

The probability of occurrence of a random variable y, given parameters α and β is:

$$P(y|\alpha,\beta) = \frac{\beta^{\alpha}}{\Gamma(\alpha)} y^{\alpha-1} e^{-\beta y} \qquad (y \geq 0) \tag{1}$$

When α = 1, the $\frac{\beta^{\alpha}}{\Gamma(\alpha)}$ term can be omitted as it is not a function of the random variable y, and the $y^{\alpha-1}$ term equals one, hence $P(y|\alpha = 1,\beta) \sim e^{-\beta y}$, i.e., exponential decay at a rate of β. The gamma parameters, α and β are sometimes written as k and θ (Table 4.6).

Table 4.6: Gamma distribution parameters

Symbol	Name	Parameter condition
α or k	Shape parameter	> 0
β or θ	Scale or rate parameter	> 0

The shape parameter α determines the distribution's level of skewness (or asymmetry), while the spread of values, i.e., whether the distribution is stretched or squeezed, is described by the scale parameter β. With the exception of winter at Hay Meadow, there is little variation in the values of shape parameter α in the annual or seasonal pdfs across the three stations (Figure 4.1 and Table 4.7) meaning that the skewness of the distributions is very similar. Again with the exception of Hay Meadow in winter, where the value is essentially the same as at Upper Clearing, gamma scale values β decrease with falling elevation, e.g., annual values drop from 8.414 at Fisera Ridge to 5.993 at Hay Meadow, representing the fact that there are more wet days and a larger volume of precipitation at higher elevations and vice versa (Table 4.4). β values also vary noticeably between seasons at all three stations: autumn values are similar to annual values; winter values are considerably smaller, while the highest values are experienced in summer.

Table 4.7. Gamma shape and scale parameters for daily precipitation

Station	Gamma shape (α)					Gamma scale (β)				
	annual	autumn	winter	spring	summer	annual	autumn	winter	spring	summer
Fisera Ridge	0.625	0.647	0.686	0.629	0.649	8.414	8.184	4.334	9.891	10.376
Upper Clearing	0.615	0.622	0.684	0.660	0.665	6.482	6.664	2.790	6.525	8.592
Hay Meadow	0.643	0.638	0.763	0.678	0.636	5.993	5.919	2.791	5.744	8.498

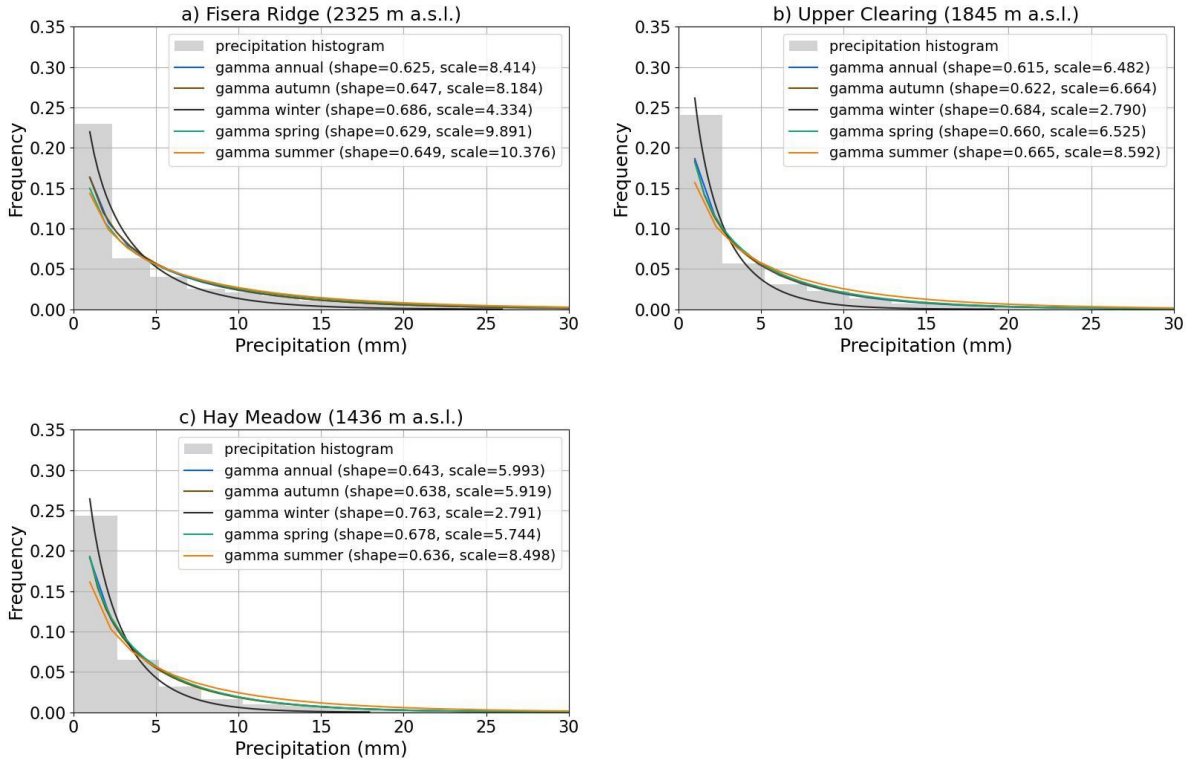

Figure 4.1. Fitted gamma distributions for daily precipitation (annual and seasonal), with frequency histograms for the annual case

4.2.3 Spatial correlation of precipitation for station pairs

A key step in characterising daily MCRB precipitation patterns was to calculate correlation coefficients and plot correlation of observed precipitation values for pairs of stations. In this project the Pearson correlation method was used, for which the formula for a data sample is:

$$r_{xy} = \frac{\sum_{i=1}^{n}(x_i - \bar{x})(y_i - \bar{y})}{\sqrt{\sum_{i=1}^{n}(x_i - \bar{x})^2 \sum_{i=1}^{n}(y_i - \bar{y})^2}} \quad (1)$$

where:

n is the sample size of precipitation values

x_i, y_i are individual precipitation values for a pair of stations x, y

$\bar{x}$ and $\bar{y}$ are the sample mean values for stations x, y

The higher the correlation coefficient, the stronger the relationship between the observed precipitation values at a given pair of stations, with a perfect correlation being indicated by a coefficient value of 1. To calculate the Pearson correlation coefficients for each station pair, it is important that each precipitation value is unique. If this is not the case, and there are instances

where $x_i = y_i$, referred to as 'tied values', the differences $(x_i - \bar{x})$ and $(y_i - \bar{y})$ are zero, which will result in instability and potentially inaccurate correlation coefficients. In the observed precipitation records for the five stations considered here, tied pairs of values do exist. To overcome the tied pairs problem, each observed value has been 'jittered', which involves adding a very small number randomly sampled from a standard normal distribution in the range 0 to 0.0001. This yields a set of unique daily values which can then be used for correlation calculations. To explore correlation relationships on both annual and seasonal bases, correlation coefficients were calculated (Table 4.8) and correlation scatter plots were generated for annual (Figure 4.2) and seasonal (autumn: Figure 4.3, winter: Figure 4.4, spring: Figure 4.5, summer: Figure 4.6) scenarios for the five stations listed in Table 4.13. The station pairs, ordered by shortest to longest separation distance, are: Fisera Ridge and Upper Clearing (FR-UC), Upper Clearing and Hay Meadow (UC-HM), Fisera Ridge and Hay Meadow (FR-HM), Kananaskis and Bow Valley (K-BV), Upper Clearing and Kananaskis (UC-K), Fisera Ridge and Kananaskis (FR-K), Upper Clearing and Bow Valley (UC-BV), Hay Meadow and Bow Valley (HM-BV), Fisera Ridge and Bow Valley (FR-BV), Hay Meadow and Kananaskis (HM-K) – see Table 4.8. Annual correlation plots (Figure 4.2) for the closest station pairs with the strongest positive correlation, FR-UC (0.937) and UC-HM (0.946), demonstrate a relatively linear pattern, especially at lower daily precipitation values, while scatter increases as precipitation amounts increase. For station pairs with greater separation distances and weaker positive correlation (i.e., lower coefficient values), annual plots show quite dense clusters of correlation points at lower precipitation amounts, typically < 20 mm/day. At higher values, there is an increasing degree of scatter. The autumn correlation plots (Figure 4.3) demonstrate the same patterns as those observed for the annual scenario, although with a reduced spread of daily precipitation amounts as the highest precipitation is not experienced during the autumn months. During the winter months, precipitation is almost entirely snowfall (see data for Fisera Ridge, Upper Clearing and Hay Meadow in Table 3.5 and Figure 3.5). Consequently, winter precipitation totals are lower than for the other three seasons, as seen in the winter correlation plots in Figure 4.4. Summer experiences the wettest rainfall months (see Table 3.5 and Figure 3.5), coinciding with the highest positive correlation values for most station pairs, irrespective of separation distance (Table 4.8), with the exception of the UC-K pair where the Pearson coefficient is slightly higher in spring than in summer. The same linear and cluster patterns, and the decay in correlation coefficients with increasing separation distance, already identified for annual and autumn data, can also be seen in winter, spring and summer.

Table 4.8. Summary of annual and seasonal Pearson correlation coefficients for MCRB station pairs

Station pair	Separation distance (km)	Elevation difference (m)	Pearson correlation coefficients				
			Annual	Seasonal			
				Autumn (SON)	Winter (DJF)	Spring (MAM)	Summer (JJA)
FR-UC	2020	480	0.937	0.941	0.929	0.915	0.973
UC-HM	2910	409	0.946	0.937	0.918	0.926	0.962
FR-HM	4770	889	0.871	0.859	0.842	0.838	0.927
K-BV	6600	93	0.682	0.593	0.549	0.715	0.725
HM-K	11820	45	0.651	0.594	0.586	0.727	0.594
UC-K	12650	454	0.637	0.606	0.591	0.672	0.631
FR-K	14310	934	0.599	0.584	0.524	0.609	0.617
UC-BV	16040	547	0.761	0.617	0.608	0.691	0.873
HM-BV	16300	138	0.764	0.616	0.586	0.728	0.859
FR-BV	17140	1027	0.679	0.576	0.512	0.590	0.842

Station elevations (m a.s.l.): Fisera Ridge (2325), Upper Clearing (1845), Hay Meadow (1436), Kananaskis (1391), Bow Valley (1298)

Pearson correlation significance testing was undertaken on the annual and seasonal Pearson correlation coefficients, using $\alpha = 0.01$, i.e., testing at a 1% significance level, meaning that there is a less than 1% likelihood that the observed correlations occurred due to random chance. For each station pair for the annual case as well as for all four seasonal cases, a p-value of 0.0 was calculated, hence all correlations are said to be statistically significant.

To represent the spatial variability between station locations, we must plot the gauge pair Pearson correlation values against separation distance between each gauge pair. A best fit spatial covariance function can then be fitted to these points. A range of spatial covariance functions exist that can be used to represent spatial variability, including: Hole-effect, Matern, Exponential, Spherical, Gaussian, Linear, Nugget, Power-Law and Cauchy. A best fit covariance curve must pass through the point (0, 1) as, at a separation distance of zero, there must be a perfect correlation value of 1.0, i.e., at each station location, the observed values at that point correlate perfectly with themselves.

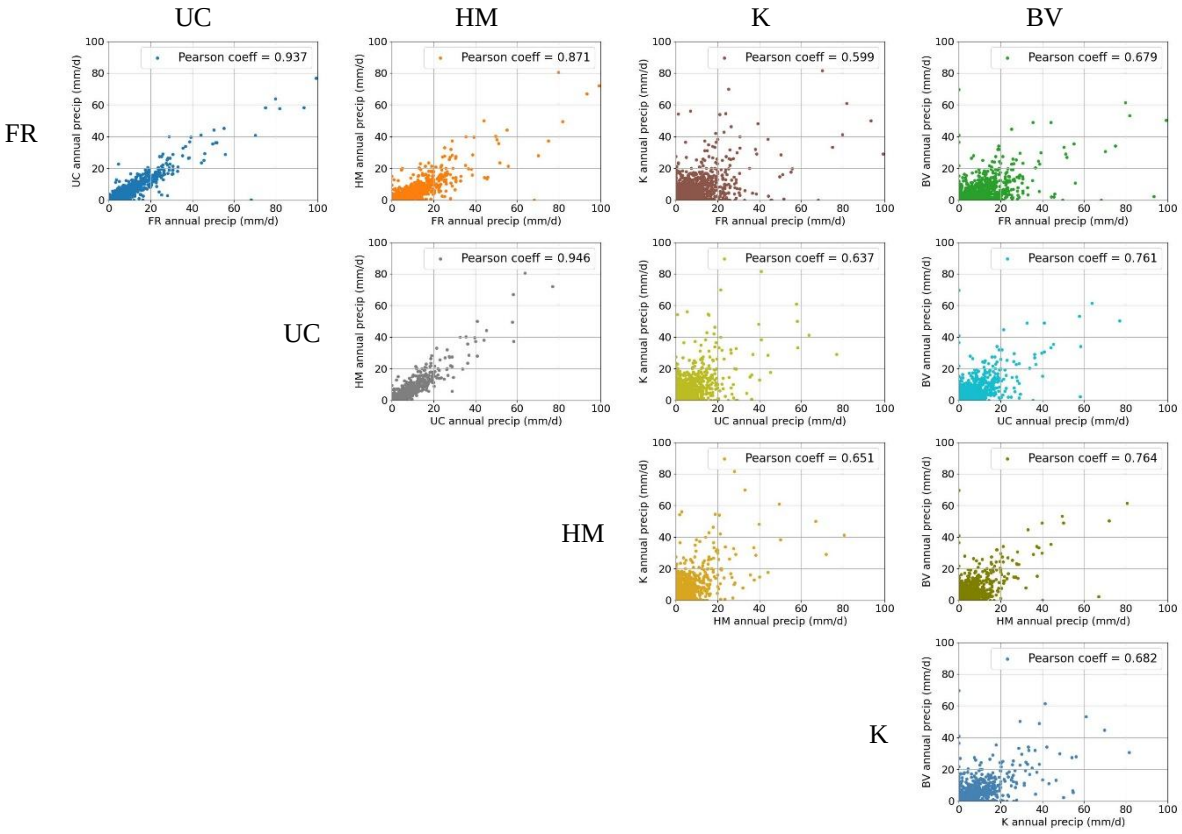

Figure 4.2. Correlation of observed annual daily precipitation values for station pairs

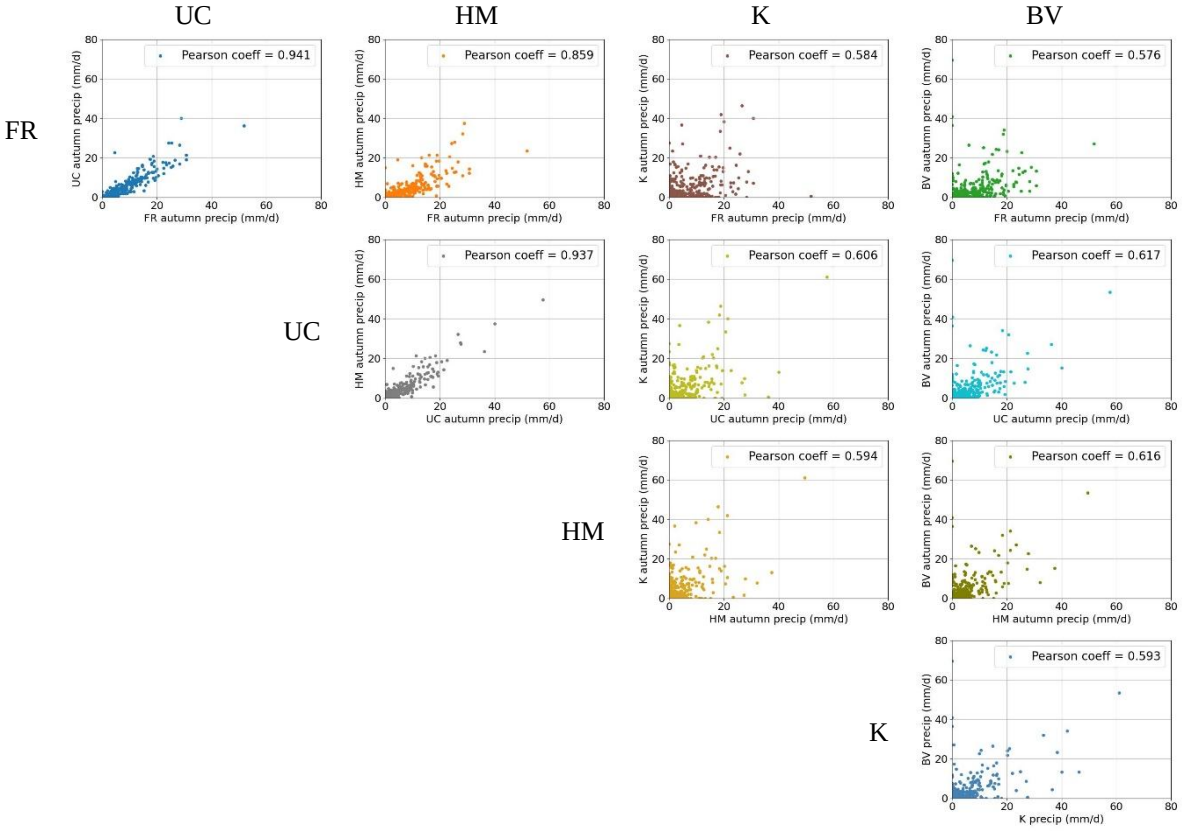

Figure 4.3 Correlation of observed autumn daily precipitation values for station pairs

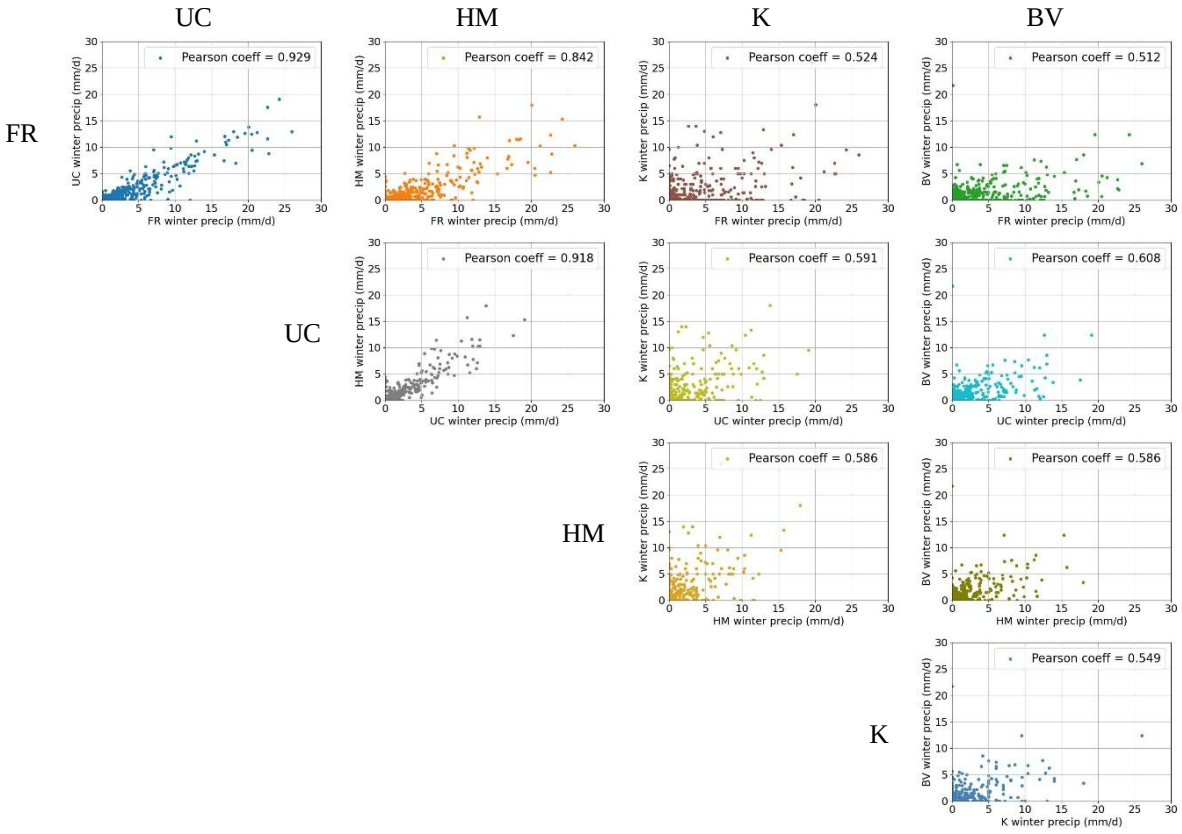

Figure 4.4. Correlation of observed winter daily precipitation values for station pairs

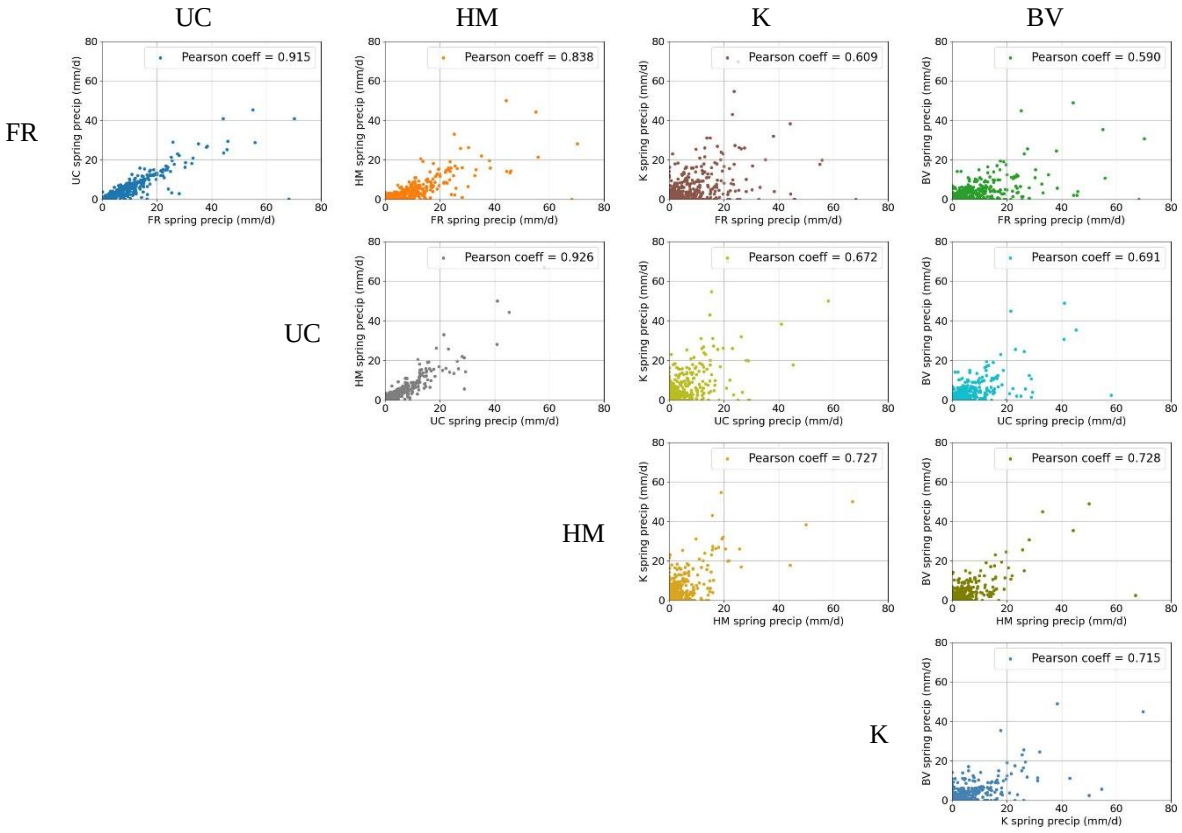

Figure 4.5. Correlation of observed spring daily precipitation values for station pairs

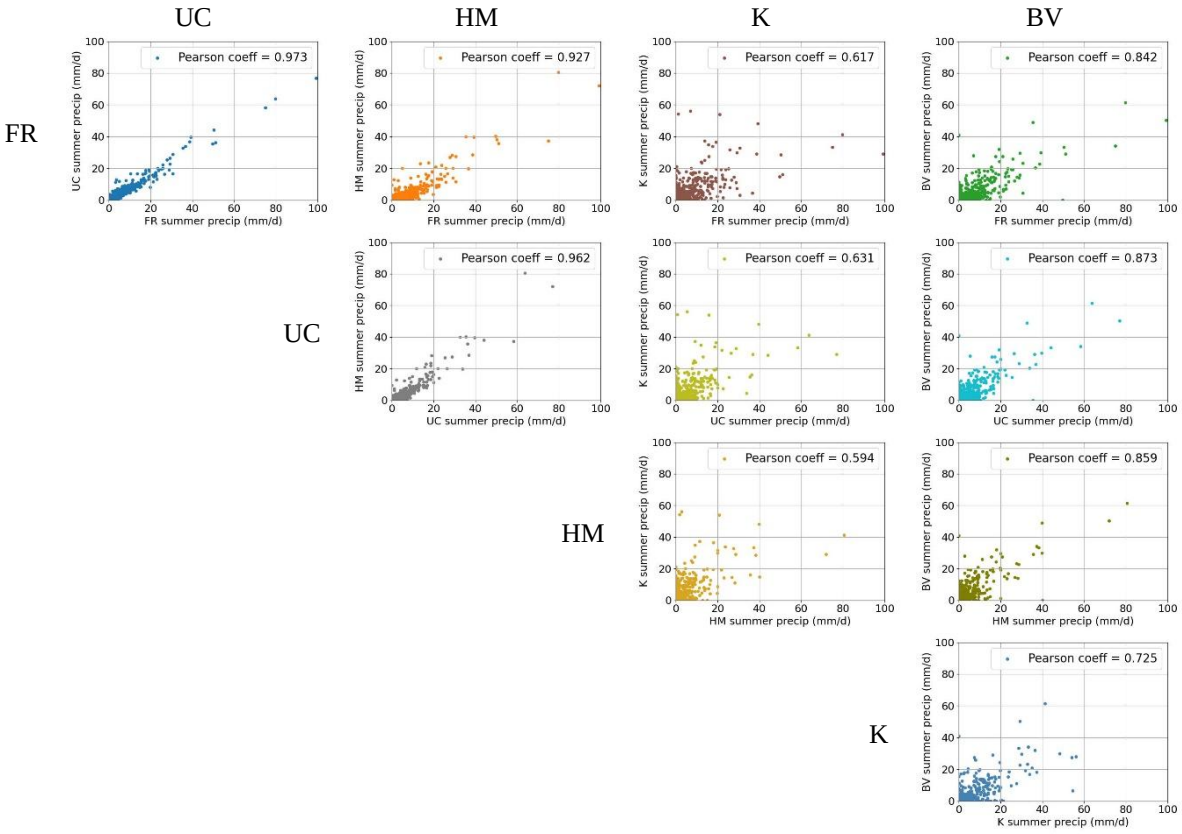

Figure 4.6.Correlation of observed summer daily precipitation values for station pairs

In fitting a covariance function model, it is necessary to identify the point on the covariance curve beyond which increasing separation distance between station locations has negligible impact on correlation values, i.e., the distance at which the covariance curve 'flattens'. The difference between a perfect correlation of 1.0 and the lowest correlation value on the covariance curve is termed the 'sill'. Due to uncertainty in 'real-world' observations, it is possible to have a situation where the fitted covariance curve does not pass perfectly through the point (0,1). To overcome the problems associated with this kind of measurement 'error', the sill requires two components: the partial sill and the nugget, where the nugget value compensates for the uncertainty/error. The distance at which the curve flattens is the 'range' value, and this is the key variable, as it determines the rate of decay of the covariance curve. An example covariance curve highlighting the sill, nugget and range is shown in Figure 4.7. Spatial covariance curve fitting is discussed further in Section 4.3.

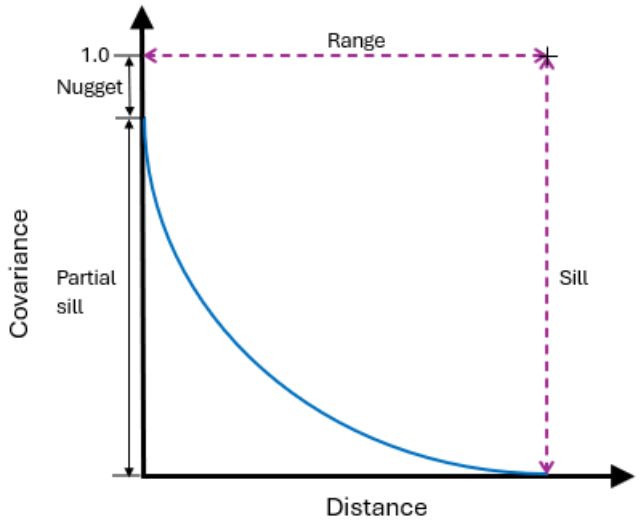

Figure 4.7. Example spatial covariance curve illustrating range, sill and nugget

4.2.4 Conditional wet/dry probabilities for pairs of stations

When characterising spatial correlation patterns between stations it is important to calculate conditional wet/dry probabilities, based on a dry day threshold of <0.1 mm, for each station pair across the five stations considered in the study. This produces, for each station pair, a 2x2 array of values based on the four possibilities, i.e.:

- station 1 dry: station 2 dry
- station 1 dry: station 2 wet
- station 1 wet: station 2 dry
- station 1 wet: station 2 wet.

As described in Section 4.2.3, there are 10 possible station pair combinations. The conditional probability values were calculated for each pair (Table 4.9), along with minimum, lower quartile, median, upper quartile and maximum values for each combination of probabilities (Table 4.10).

Table 4.9. Conditional wet/dry probabilities for pairs of stations

Station pair	Separation distance (m)	Conditional probabilities			
		dry-dry	dry-wet	wet-dry	wet-wet
FR-UC	2020	0.229	0.213	0.289	0.269
UC-HM	2910	0.317	0.201	0.295	0.187
FR-HM	4770	0.270	0.172	0.341	0.217
K-BV	6600	0.417	0.260	0.199	0.124
HM-K	11820	0.414	0.197	0.263	0.126
UC-K	12650	0.351	0.167	0.326	0.156
FR-K	14310	0.299	0.143	0.378	0.180
UC-BV	16040	0.319	0.199	0.297	0.185
HM-BV	16300	0.376	0.235	0.240	0.149
FR-BV	17140	0.272	0.170	0.344	0.214

Table 4.10. Summary relating to conditional dry/wet day probabilities

Statistic	Probability of dry-dry	Probability of dry-wet	Probability of wet-dry	Probability of wet-wet
Minimum	0.229	0.143	0.199	0.124
Lower quartile	0.279	0.170	0.270	0.151
Median	0.318	0.198	0.296	0.182
Upper quartile	0.370	0.210	0.337	0.207
Maximum	0.417	0.260	0.378	0.269

The highest median probability, of 0.318 (Table 4.10), relates to both stations in a pair being dry. The next highest median probability is wet-dry (0.296) followed by dry-wet (0.198), with the lowest median probability of 0.182 for wet-wet. So, on average it is 1.75 times more likely that, during the 11-year period under review, both gauges in any given pair experienced a dry day than a wet day, based on a dry day threshold of < 0.1 mm. To give some additional context to these conditional probabilities, the total number of wet and dry days for the full 11-year time series is presented (Table 4.11). The five stations are shown in descending order of elevation, from Fisera Ridge to Bow Valley. With the exception of Bow Valley, which experiences different weather patterns due to its lower elevation location to the east of the mountain range towards the plain, there is an overall upwards trend in the number of dry days with reducing elevation. Conversely, the higher the elevation, the greater the number of wet days experienced. Although important to evaluate conditional probabilities as presented above, it was found that they have no bearing on modifications made to the random mixing method for sparsely gauged mountain catchments, therefore only the annual case has been discussed; it is not necessary to also analyse seasonal conditional probabilities.

Table 4.11. Total number of wet and dry days at each station

Station	Elevation (m a.s.l.)	Total no. of dry days	Total no. of wet days
Fisera Ridge	2325	1776	2243
Upper Clearing	1845	2094	1925
Hay Meadow	1436	2468	1551
Kananaskis	1391	2721	1298
Bow Valley	1298	2476	1543

4.3 The Random Mixing Whittaker Shannon Python (RMWSPy) method

In Hörning & Haese (2021), the authors set out to develop an inverse modelling technique to generate conditional random fields, either using linear constraints alone, i.e., precipitation gauge observations, or a combination of linear and non-linear constraints, which in their instance was integral rain rates derived from Commercial Microwave Link (CML) data. The goal is to generate random spatial fields that honour the observations at the measurement locations, e.g., the gauge sites. As there is a different set of observed values for each interval, e.g., daily, hourly or sub-hourly, a new spatial field is generated for each individual time step. First, a spatial grid with suitable resolution is established for the study area which is then transformed to a standard xy grid, with lower left coordinates of (0, 0). Coordinates for gauge locations also need to be converted to fit the standard grid. The first steps in this method are to fit a suitable univariate marginal distribution to the observed gauge data and select a spatial covariance function to represent the spatial variability of the observations. A marginal distribution is the probability distribution used to describe a subset (observed precipitation values from a single gauge site) of a larger set of multivariate random variables (observed precipitation values from all gauge sites). Generating the random spatial fields is a mathematically complex and computationally demanding process. Therefore, to simplify the problem the data are transformed to standard normal values and a range of unconditional spatial fields is generated using the fitted spatial covariance function. Kernel Density Estimation (KDE) is used to fit a marginal distribution to the observed wet values; zero precipitation values are not included in the distribution, instead they are treated as inequality constraints using values for dry day probability calculated at each measurement location. Then, a cumulative distribution function (cdf) and inverse cdf are built from the marginal distribution. The cdf is used to transform wet observations from actual data space to standard normal space before fitting a spatial covariance function. This involves using a Gaussian copula, which is a multivariate cdf where the marginal distribution of each variable, for example each set of gauge

observations, is uniform on the interval [0, 1], and the dependence between random variables is independent of their marginal distributions. Parameter values for the fitted copula are optimised via a Maximum Likelihood approach, i.e., maximising a likelihood function to fit the observed data points. Multiple unconditional spatial fields, i.e., produced without constraining to any observations, are generated using the random mixing algorithm, with the fitted spatial covariance function. To generate a conditional field that fulfils the observations, the number of unconditional fields generated must be greater than the number of observation locations. It should be noted that the random mixing algorithm has additional steps to fulfil non-linear constraints, for example CML or radar precipitation estimates. In this study, only point observations of precipitation from gauges have been used as conditioning constraints, therefore the non-linear elements of the method are not presented here.

A linear combination of these fields is formed, with weights assigned to each. Conditional field W_0 can be expressed as:

$$W_0 = \sum_{l=1}^{L} \alpha_l V_l \tag{2}$$

where $W_0 =$ conditional field

$V =$ unconditional field

$l =$ number of fields

$\alpha =$ weights

To fulfil the observations, solve:

$$\omega_j = \sum_{l=1}^{L} \alpha_l V_l(x_j) \tag{3}$$

where ω_j = standard normal values within the random field at locations x_j.

Singular value decomposition (SVD) is used to find a solution where the L^2 norm of the weight vector $(\alpha_1, \ldots, \alpha_l)$ is minimised:

$$A = \sum \alpha_l^2 \rightarrow min \tag{4}$$

If the minimum $A \ll 1$, the field is termed W^*. If not, an additional unconditional field is added, and equation (2) is solved again; this process is repeated until a solution is achieved for which $A \ll 1$. From the standard normal values generated, field W^* is constructed thus:

$$W^* = \sum_{l=1}^{L} \alpha_l V_l \tag{5}$$

This results in a random field that will satisfy the observations, but it is a low variance field that does not honour the spatial covariance required. Additional fields U_s and U_t are therefore generated to repair the covariance:

$$U_t = \sum_{s=1}^{S} \beta_{s,t} V_{s,t} \text{ with } S \geq J + 1 \tag{6}$$

$$\text{with weights } \beta_{s,t} = 1 - \sum_{l=1}^{L} \alpha_l^2 = 1 - A \tag{7}$$

$V_{s,t}$ are standard normal unconditional fields. To preserve the observed values at locations x_j, the condition $U_t(x_j) = 0$ must be imposed. A conditional standard normal field W is obtained that fulfils the observations and has the correct covariance:

$$W = W^* + U_t \tag{8}$$

Finally, the fields are backtransformed from standard normal space to original data space, i.e., precipitation values in mm.

Three example applications are provided for the RMWPSy code (Hörning & Haese, 2021): a basic use case to simulate random fields based on linear observations only; 'cml_example' which combines linear observations with CML data; and 'modflow_example' for groundwater applications. At the outset of this study, it was decided to adapt the version of the code that would allow the potential for both linear and non-linear precipitation data to be introduced as model constraints, hence the 'cml_example' case was used. The code consists of several modules for linear problems (Table 4.12).

Table 4.12. Original RMWSPy code modules (Hörning & Haese, 2021)

Module	Purpose
cml.py	Creates a non-linear problem template for CML data.
covariancefunction.py	Enables selection of the most suitable of eight possible covariance models for representing spatial covariance.
gaussian_copula.py	Establishes theoretical Gaussian copula model
gcopula_sparaest.py	Fits a spatial copula using maximum likelihood
random_mixing_whittaker_shannon.py	Approximates objective function for problem optimisation using Whittaker-Shannon interpolation on a unit circle.
run_inv.py	Script that runs all elements of the code.
spectralsim.py	Simulates standard normal random fields.

4.3.1 RM-mountain Modification 1: improving spatial covariance (rm_mountain.py)

To improve spatial variability in the generation of spatial precipitation fields using the random mixing method with a small number of precipitation gauges from which to sample data, a plausible technique available is to randomly sample from the full time series of precipitation data for each available gauge. In this study, there are 11 years of data (October 2005 to September 2016), equivalent to 4019 daily precipitation values. The modifications made to the RMWSPy method to enable this functionality are explained in the following sections.

In this project, random sampling of time series observed precipitation data will be employed for spatial copula fitting to determine spatial covariance. It is important to ensure that subsets of data used are independent of each other, i.e., not affected by positive autocorrelation of precipitation values from one time step to the next. To achieve this fitting, the dataset is divided into randomly selected subsets (Hörning & Haese, 2021) which maximises the likelihood of independence of the data samples used in the process. To determine the dependence of daily precipitation values on events in preceding days, a series of autocorrelation analyses has been performed on the complete precipitation time series at each station. This involves correlating each gauge's time series with itself, but with a time lag, here ranging from one day to five days. To generate the lag 1 values, the correlation between a complete time series and its equivalent, but with a time lag of one day, is calculated. Additional lag values are calculated in the same way but for time lags of two days, three days, etc. Autocorrelation values range between -1 and 1: an autocorrelation value of 1 would mean that there is a perfect positive

correlation between the time series and itself for a given lag time. Similarly, an autocorrelation value of -1 represents a perfect negative correlation between the time series and the lagged version of itself. The outputs from these analyses are presented below, with lag values for 1 day to 5 days (Table 4.13) and 7 days (Figure 4.8); by 5 days, the autocorrelation values have effectively fallen to zero.

Table 4.13: Autocorrelation values for lags of 1 day to 5 days

Station	Lag 1	Lag 2	Lag 3	Lag 4	Lag 5
Fisera Ridge	0.298	0.079	0.033	0.005	0.001
Upper Clearing	0.303	0.056	0.016	-0.003	-0.002
Hay Meadow	0.347	0.074	0.025	-0.003	-0.008
Kananaskis	0.318	0.098	0.033	0.027	-0.006
Bow Valley	0.332	0.064	0.013	0.010	0.024

The lag 1 correlations range between 0.298 at Fisera Ridge (2325 m a.s.l.) and 0.347 at Hay Meadow (1436 m a.s.l.). These values imply a small positive autocorrelation at a lag of one day. Beyond the one-day lag period, the correlation values quickly drop away towards zero, signifying no strong correlation beyond lag 1 (Figure 4.8). If all values selected for copula fitting were ordered sequentially, the lag 1 autocorrelation pattern would appear throughout the dataset, skewing the shape of the fitted copula. Randomly selecting from a large enough sample overcomes this potential problem.

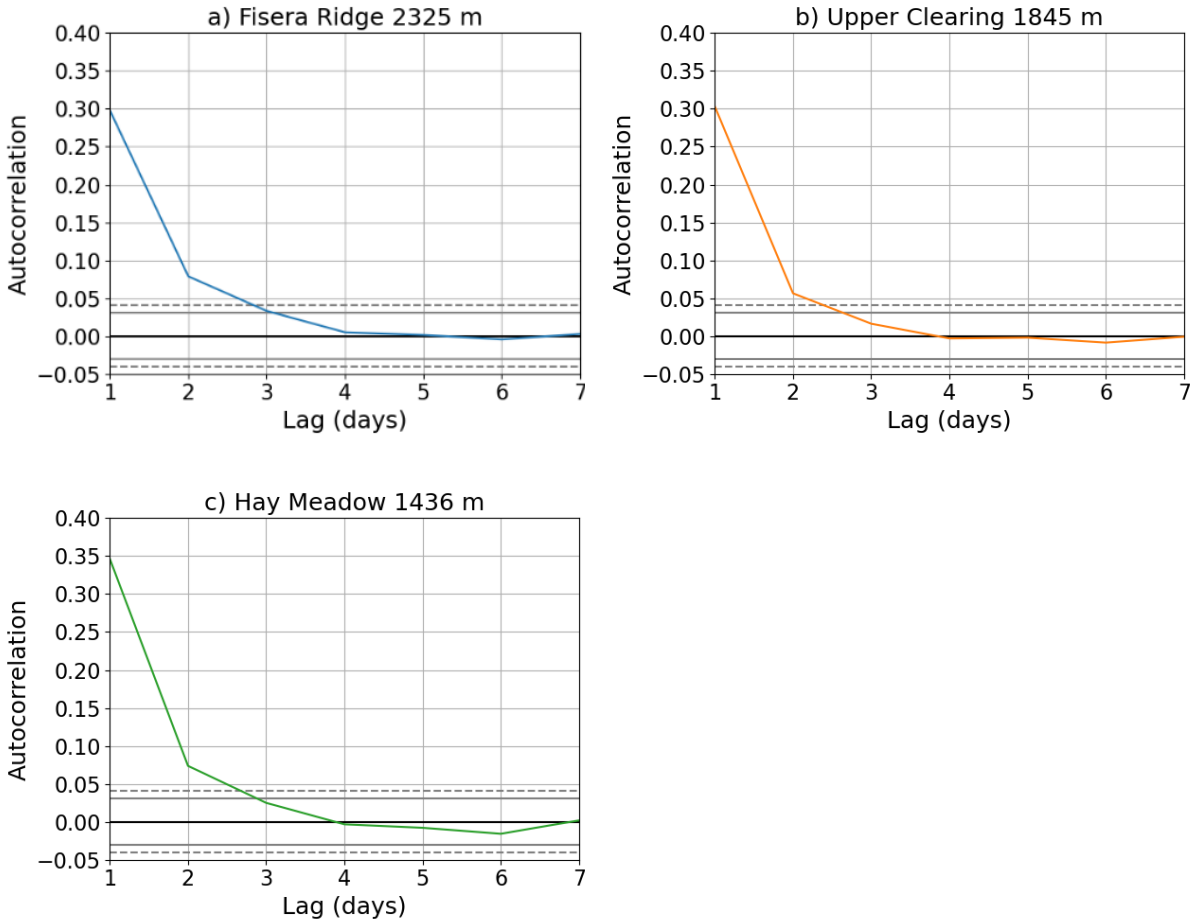

Figure 4.8: Autocorrelation plots for lags of 1 day to 7 days

The sill and range values generated by the random mixing model are sensitive to the sampling process used to select the number of timesteps. The RMWSPy code features a variable 'n_subsets' which determines the size of the sample of data points used to fit the spatial copula. Different values of 'n_subsets' were tested, varying between 100 and 4000 to evaluate its effect on the range and sill values generated in the covariancefunction.py module. It was determined that, for n_subsets ≥ 1000, there was negligible impact on range and sill values, hence n_subsets = 1000 was used for copula fitting in subsequent modifications to the random mixing algorithm for application in the mountainous MCRB catchment. Avoiding the use of very large values of 'n_subsets' has the added benefit of reducing simulation times, as sampling from a larger number of subsets requires more computing power. As introduced in Section 4.2.3, a spatial covariance model must be fitted to the gauge pair Pearson correlation values when plotted against gauge pair separation distance. In the original RMWSPy model, the covariancefunction.py script contains a function 'Nested_Cov' enabling it to represent the following range of covariance functions: Hole-effect, Matern, Exponential, Spherical,

Gaussian, Linear, Nugget, Power-Law and Cauchy. The 10 station pair points in Figure 4.9 show the change in gauge pair correlation with separation distance. As expected, correlation decreases with increasing distance between the gauge locations. The first four plotted points, FR-UC, UC-HM, FR-HM and K-BV, with separation distances less than 10 km, demonstrate an exponential decay pattern. At separation distances between 10 km and 12.5 km, exponential decay is still evident, although the correlation of observed values at the HM-K pair is a little high to fit the pattern precisely. Beyond 12.5 km, the relationship between correlation and separation distance is less reliable, with the correlation values being higher than might have been expected between the stations at higher elevations (Fisera Ridge, Upper Clearing and Hay Meadow) with the most remote, lowest elevation station at Bow Valley. Overall, the covariance function that best fits these points is exponential. However, this is not entirely straightforward: firstly, the best fit curve must pass through the point (0, 1) as, at a separation distance of zero, there has to be a perfect correlation of 1.0; secondly, the correlation values at separation distances greater than 12.5 km are comparatively high. These two features combined present a challenge when copula fitting with the random mixing algorithm. It is necessary to identify the point beyond which increasing distance has negligible impact on correlation, i.e., where the covariance curve 'flattens'. As explained in Section 4.2.3, the sill has two components, the partial sill and the nugget, the latter compensating for measurement uncertainty. A range of fixed sill values was tested in a bid to correct the problem, but this approach yielded unsatisfactory results with spatial covariance curves poorly fitted to the observed correlation/separation distance points. To improve copula fitting, the gcopula-sparaest.py script was updated to allow the model to fit a 'dynamic' sill value rather than imposing a fixed sill, as highlighted by the green line in Figure 4.9. The dynamic sill curve is not yet useful for generating spatial precipitation fields as the curve does not flatten within the 20 km (equivalent to 400 x 50 m model grid cells) radius from MCRB of the stations, i.e., there is no useable range value. To enable better representation of decay in spatial covariance over the relatively short distances in a small catchment, an offset term (equivalent to 1 – sill) was introduced to the exponential formula in the covariancefunction.py script. The inclusion of the offset term allows convergence to non-zero (positive) correlation values for pairs of gauges that are furthest apart in the study area, generating the exponential covariance curve represented by the blue line in Figure 4.9. To enable evaluation of seasonal effects, seasonal spatial covariance relationships were also established by randomly sampling from seasonal precipitation marginal distributions derived for each of the five stations, incorporating the dynamic sill and offset terms explained above (Figure 4.10). The facility to select either annual or seasonal precipitation distributions

has been included in the RM-mountain Python code. Unlike RMWSPy, spatial covariance function parameters were determined using a method of least squares approach, as it was identified that, at greater separation distances, the least squares method resulted in higher correlation values than those obtained using maximum likelihood estimation, i.e., a slower exponential decay.

RM-mountain also enables the user to specify different sizes of model grid for copula fitting and for spatial field generation, which is useful in very small catchments where distances between gauges are small, for example from 2-5 km for MCRB. A smaller spatial domain, which also has the benefit of reducing computing time, can be the basis for generating spatial precipitation fields with precipitation data from only the gauges within/nearest the catchment. To generate a robust spatial relationship that accounts for greater gauge separation distances, a larger grid incorporating other gauges further from the catchment can be used. Allowance for separate grids is made in this study; precipitation data from five stations were used in copula fitting, and the daily spatial precipitation fields were generated using data from only the three stations within/near MCRB.

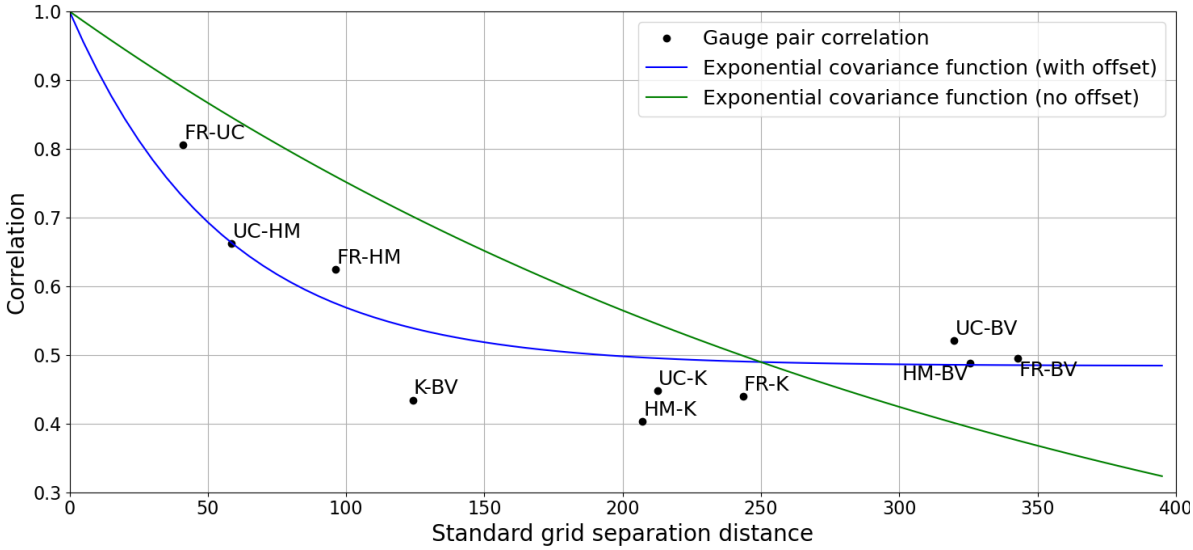

Figure 4.9. Annual spatial covariance curve fitting: a) gauge pair Pearson correlation against gauge pair separation distance; b) with fitted exponential covariance curves, original without offset term (green) and improved with offset term (blue)

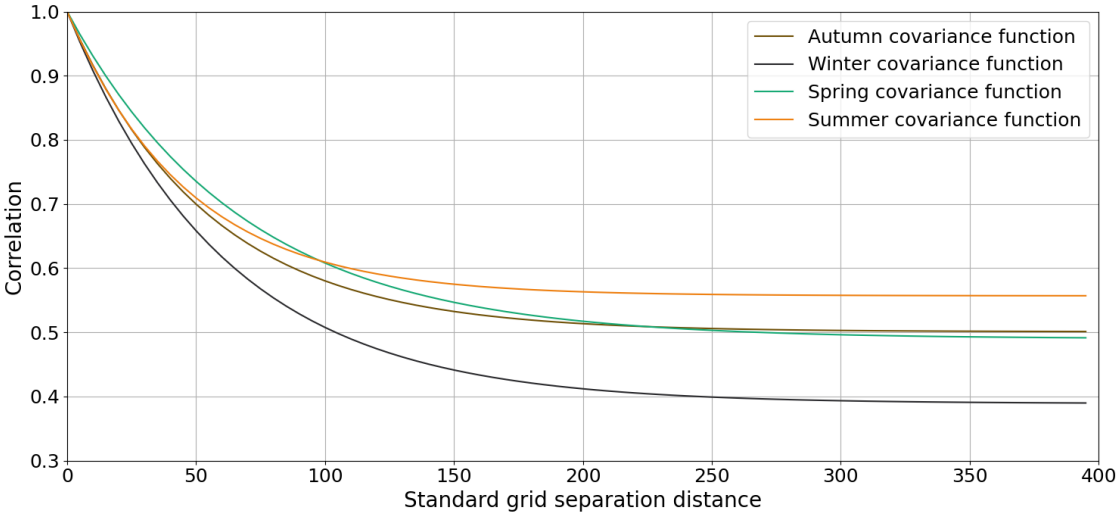

Figure 4.10. Seasonal spatial covariance curve fitting

4.4 Modifying RMWSPy for the mountainous Marmot Creek Research Basin (MCRB)

Before developing any modifications to the RMWSPy code, it was important to test the original code and evaluate its performance in simulating daily precipitation fields conditioned using precipitation observations from three MCRB stations over the 11-year duration of the data record (1 October 2005 to 30 September 2016). The study areas and number of gauges differ noticeably between MCRB and the region chosen in the Hörning & Haese (2021) paper. While the latter is a 57,850 km^2 region of southern Germany with 71 rain gauges, MCRB is a 9.4 km^2 catchment in the Canadian Rockies with only three gauges located at Fisera Ridge (2325 m a.s.l.), Upper Clearing (1845 m a.s.l.) and Hay Meadow (1436 m a.s.l.) stations. The original RMWSPy method fits a spatial copula by randomly sampling from the precipitation values for each separate timestep. When there is a sufficiently large number of gauges, e.g., 71 (Hörning & Haese, 2021), this is a justifiable approach, as an appropriate covariance function can be fitted using that subset of data points. However, with only three gauges to sample from, there are only three observed values at each timestep, hence only a very weak spatial relationship can be generated from such a small sample of precipitation values, leading to low variance spatial fields, like the randomly selected single realisation in Figure 4.11, using the three-station mean $p0$ value of 0.53. Note that the lower left corner of all spatial precipitation fields generated in this research are: latitude -115.24º W, longitude 50.925º N. Although the observed precipitation values are honoured at the gauge locations, marked with crosses on Figure 4.11, much of what is generated by the random mixing algorithm is background statistical ‘noise’ rather than plausible precipitation values. (Note: the standard grid distances

on Figure 4.11 represent the number of 50 m grid squares in the x and y-directions). The colour bar range of 0-30 mm is governed by the range of observed precipitation values on that given day (randomly selected from the time series); there are lighter areas to the south west and north of the study area, indicating some higher precipitation values in accordance with the higher observed precipitation value at the highest station (Fisera Ridge). However, much of the model domain shows lower precipitation values with very little variation between grid cells. To improve spatial precipitation fields for the MCRB catchment, a modification to the method is needed to overcome the limitation of only three gauges from which to sample; this, and other modifications, are discussed in the following sections.

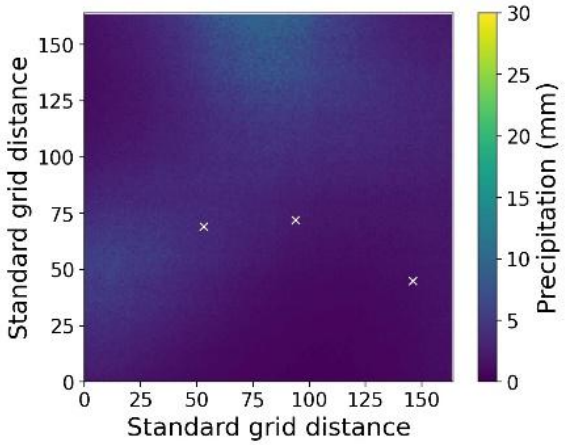

Figure 4.11. Randomly selected single realisation of a low variance daily precipitation field generated using RMWSPy with no modifications

4.4.1 RM-mountain Modification 2: introducing elevation dependence (run_rm_mountain.py)

The next modification introduced to the RMWSPy method to improve the quality of random spatial precipitation fields generated for MCRB was to account for elevation differences across the study area. To achieve this, elevation gradients, i.e., relationships to describe the change in precipitation with rising or falling elevation, were required for both dry and wet days. Using the elevations and annual dry day probability values (Table 4.5) for the stations at Fisera Ridge (2325 m a.s.l., $p0$ = 0.44), Upper Clearing (1845 m a.s.l., $p0$ = 0.52) and Hay Meadow (1436 m a.s.l., $p0$ = 0.61), linear regression analyses were performed to derive dry day elevation gradients for annual and seasonal scenarios. These gradients have negative values because $p0$ decreases with increasing elevation. Wet day elevation gradients

were calculated in a similar manner although there are two gamma distribution parameters to consider, unlike the dry day situation where only $p0$ is required. As demonstrated earlier in Table 4.7, the gamma marginal distributions were primarily determined by scale parameter values which differ noticeably between stations at different elevations. In contrast, the shape parameter varies very little across the range of annual and seasonal scenarios being considered. Therefore, elevation gradients have been calculated only for gamma scale values. These gradients have positive values (Table 4.14) as gamma scale increases with elevation.

Table 4.14. Dry day p0 and wet day gamma scale elevation gradients for annual and seasonal scenarios

Scenario		**Dry day $p0$ elevation gradient**	**Wet day gamma scale (β) parameter elevation gradient**
Annual		-1.93×10^{-4}	2.76×10^{-3}
Seasonal	autumn	-1.47×10^{-4}	2.57×10^{-3}
	winter	-2.91×10^{-4}	1.78×10^{-3}
	spring	-2.14×10^{-4}	4.73×10^{-3}
	summer	-1.22×10^{-4}	2.16×10^{-3}

The approach used to apply elevation gradients across the model domain is similar to the Micromet method (Liston & Elder, 2006). Calculated daily precipitation values for each grid cell are adjusted to a reference elevation using the appropriate elevation gradient, depending on whether it is a dry ($p0$) or wet (β) day. The reference elevation is taken as the catchment mean elevation which is calculated from the elevations for each 50 m x 50 m grid cell across the model domain. For dry days, the $p0$ gradient is used to adjust $p0$ values for each gauge to a reference elevation (the catchment mean elevation); IDW is used to interpolate $p0$ to all grid cells; then the elevation signal is reintroduced at each grid cell using the $p0$ gradient. For wet days, the same procedure is followed, using β values.

4.4.2 Modification 3: evaluating seasonal effects (run_rm_mountain.py)

Seasonality was evaluated using the seasonal marginal distributions (Table 4.7, Figure 4.1) and spatial covariance relationships (Figure 4.10), and seasonal $p0$ values (Table 4.5) for autumn, winter, spring and summer, incorporating the elevation dependence described in modification 2.

4.4.3 RM-mountain workflow

The steps required to modify or create the Python script, 'run_rm_mountain.py', which produces ensemble simulations of RM-mountain are described here and summarised in the blue boxes in Figure 4.12:

1. Set user input values: wet day threshold (mm), number of timesteps for RM-mountain simulations.
2. Set marginal distribution and copula fitting parameters. The run_rm_mountain.py script enables the user to specify separate time groupings for precipitation marginal distributions (marginal_time_grouping) and spatial copula fitting (copula_time_grouping). These can be set to 'annual', 'seasonal' or 'custom', the latter enabling the user to investigate the impacts of, for example, grouping by precipitation intensity. Elevation gradients can be incorporated by setting 'include_elevation=True').
3. Specify the grid for spatial copula fitting. Set the spatial covariance function, if copula fitting has previously been done (see step 9).
4. Set simulation details for RM-mountain: time step, start and end dates, grid map input files.
5. If generating RM-mountain precipitation fields as inputs to the HBV hydrological model, specify HBV-specific climate inputs for initial spatial interpolation of station precipitation observations: elevation gradients for precipitation and air temperature.
6. Specify general simulation details: simulation random seed value, ensemble size, multi-processing option for running ensemble simulations in parallel, observed flow data path and RM-mountain output files' destination folder.
7. If generating RM-mountain precipitation fields as inputs to the HBV hydrological model, set optimised HBV model parameters (refer to the run_rm_mountain.py script for a full list).
8. Read and format climate input data for RM-mountain (precipitation, temperature, PET).
9. Fit the spatial copula if not specified at step 4 (see step I in rm_mountain.py).
10. If generating RM-mountain precipitation fields as inputs to the HBV hydrological model, prepare HBV initialisation and read observed flow data for calculating performance metrics (NSE, RMSE, bias).

11. Interpolate, and account for elevation dependence, in marginal distributions.
12. Set multi-processing options, depending on processing capacity and number of ensemble simulations to be run.

The run_rm_mountain.py script calls functions in rm_mountain.py to generate spatial fields and run RM-mountain ensemble simulations, as follows (see the yellow boxes in Figure 4.12):

I. Set up spatial copula fitting parameters to represent spatial covariance between station locations. Spatial copula fitting (for MCRB, an exponential function is fitted) can be selected in run_rm_mountain.py (fit_copula=True) or it can be determined by running rm_mountain.py and specifying the cmod string output, in which case set fit_copula=False in run_rm_mountain.py.
II. Generate spatial precipitation field per time step (in a loop):
    a. Transform precipitation values to standard normal using the fitted cdf.
    b. Initialise and run RMWS to simulate spatial fields.
    c. Back-transform spatial fields from standard normal to original data space.
    d. Plot generated fields if desired.
III. Run RM-mountain:
    a. Simulate ensemble members for each time step.
    b. If required, run HBV simulations.
    c. Write HBV simulation outputs to csv files.
IV. Calculate performance metrics for each ensemble member and output to csv file.

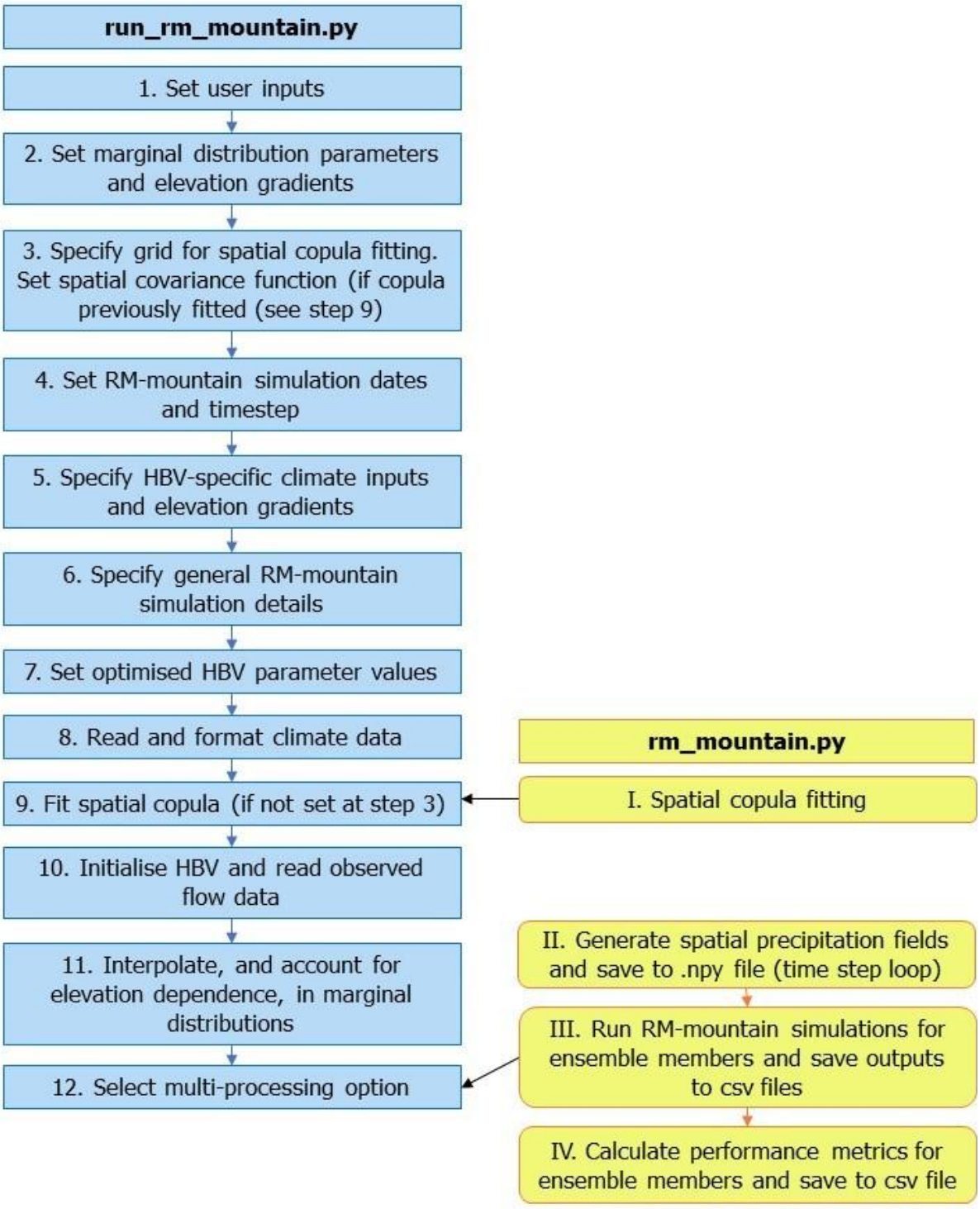

Figure 4.12. Flowchart summarising steps in the RM-mountain method. Steps 5, 7 and 10 in run_rm_mountain.py, and steps III and IV in rm_mountain.py, apply only when HBV hydrological model simulations are to be run. When using an alternative hydrological model, use the .npy files saved in step II of rm_mountain.py as precipitation field inputs.

4.5 Results: variance in RM-mountain spatial precipitation fields

Four randomly selected single realisations, representing RMWSPy with no modifications, and RM-mountain with modification 1, modifications 1 & 2 and modifications 1-3, of spatial precipitation fields generated using RM-mountain for MCRB, for the same day in November 2005, are presented in Figure 4.13, along with one-dimensional variograms to represent the variability in precipitation values for each spatial field. The spatial precipitation field generated using RMWSPy with no modifications (Figure 4.13a) has precipitation amounts within the range of observed values, but is a low variance field (Figure 4.13b) that does not adequately represent the spatial covariance due to sampling from only three observed precipitation values each day, resulting in a smoothing effect on simulated precipitation values across the study area (see Figure 4.11 in Section 4.4). The RM-mountain modification 1 spatial field (Figure 4.13c) shows an enhanced distribution of spatial precipitation resulting from the improved variance (Figure 4.13d) with time series sampling. The introduction of elevation dependence in RM-mountain modification 2 (Figure 4.13e) further improves the field variance (Figure 4.13f), as does modification 3 for seasonal effects (Figure 4.13g and Figure 4.13h). Spatial precipitation fields generated for other days, evaluated across a wide range of observed daily precipitation totals, all demonstrate increased variability of simulated precipitation amounts resulting from the introduction of RM-mountain modifications 1, 2 and 3. A time series animation showing the best performing daily spatial precipitation field for each day between 1 October 2005 and 30 September 2012 is available at https://doi.org/10.25405/data.ncl.28832420. Note that the lower left corner of all spatial precipitation fields generated in this research are: latitude 115.24º W, longitude 50.925º N.

4.6 Comparison of RM-mountain with other spatial interpolation techniques

The performance of the RM-mountain method in simulating daily precipitation values is evaluated by comparing its outputs with those from other commonly used techniques for spatial interpolation of precipitation. The alternative techniques used for this comparison are Nearest Neighbour (NN), Inverse Distance Weighting (IDW), Ordinary Kriging (OK) and Kriging with External Drift (KED). All of these techniques are discussed in Sections 2.3 and 2.4. RM-mountain was set up to generate spatial precipitation fields on a 50 m x 50 m regular grid; the other four comparative methods have also been used to calculate daily precipitation values for each 50 m grid square. The precipitation time series resulting from these four methods have

been used as inputs to the HBV and CRHM hydrological models of MCRB, as discussed in Chapter 5 and Chapter 6.

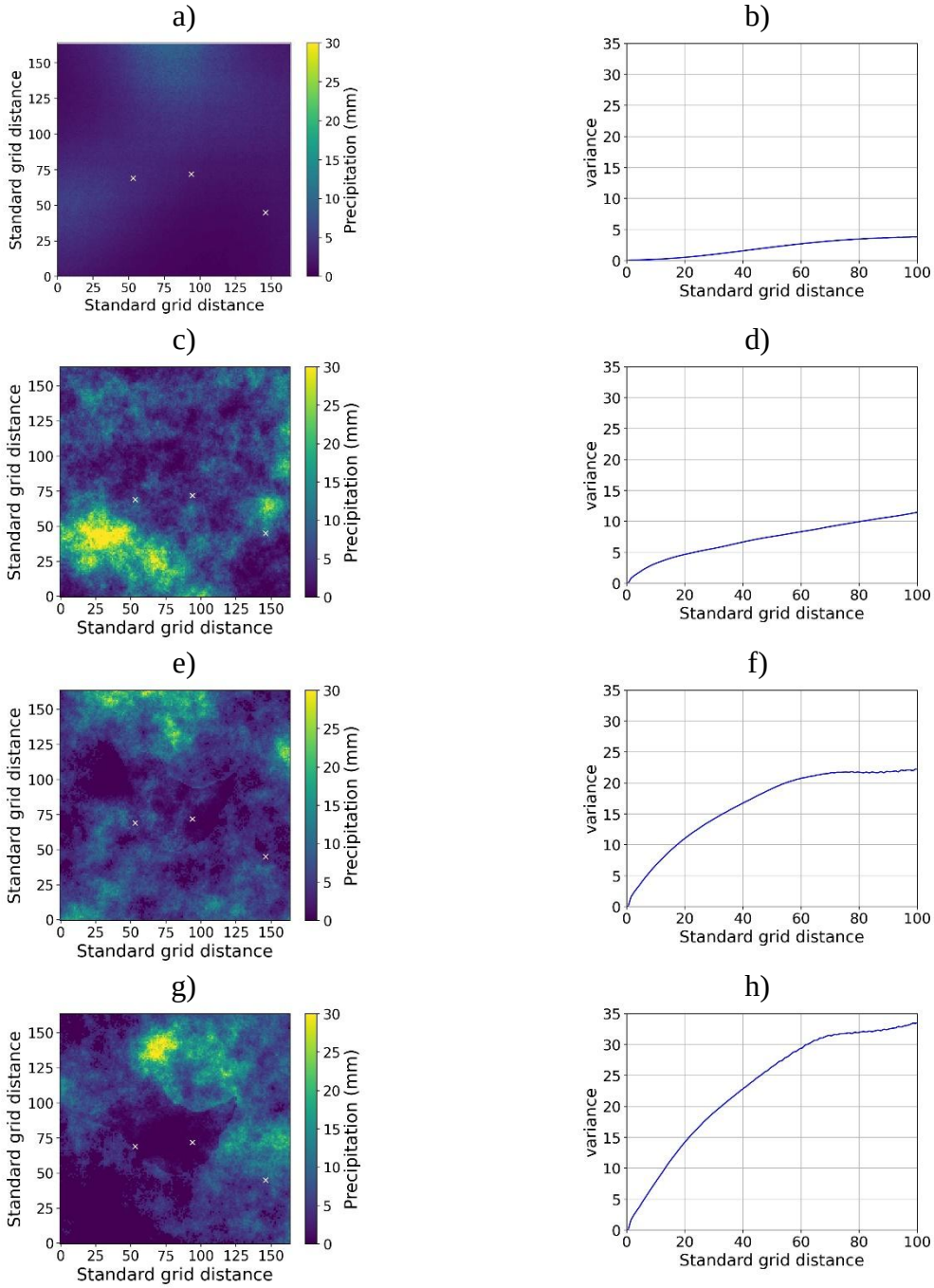

Figure 4.13. Single realisations of daily conditional precipitation random spatial fields for MCRB: a) RMWSPy with no modifications; c) RM-mountain with modification 1; e) RM-mountain with modifications 1 & 2; g) RM-mountain with modifications 1-3. One-dimensional variograms for: b) no modifications; d) modification 1; f) modifications 1 & 2; h) modifications 1-3.

4.6.1 Leave-one-out cross-validation for deterministic methods

The leave-one-out cross-validation technique is used here to evaluate the performance of RM-mountain, NN, IDW, OK and KED spatial interpolation methods by checking simulated precipitation values at gauge locations. This is done by applying each method while leaving out one of the gauges at a time. For example, to assess the accuracy of precipitation values generated at Fisera Ridge, apply the method using only observed precipitation inputs from Upper Clearing and Hay Meadow stations. Comparing the simulated precipitation values with observations at Fisera Ridge, and similarly for the other stations when each is left out in turn, enables evaluation of each method. The deterministic methods, i.e., NN, IDW, OK and KED, each yield a single spatial precipitation time series; for visual comparison of the four deterministic methods, the precipitation time series generated for 2011, focusing on the period between May and August, are presented in Figure 4.14. The May to August period was selected for these figures as they focus on what is typically the part of the year that experiences the highest precipitation, as well as to coincide with streamflow hydrograph figures from hydrological modelling (see further discussion on this in Chapter 5). The precipitation time series generated using the leave-one-out cross-validation approach for the four deterministic methods are very similar to one another, as well as to the observed precipitation, at each station when seen plotted for Fisera Ridge (Figure 4.14a), Upper Clearing (Figure 4.14b) and Hay Meadow (Figure 4.14c) stations. The only notable exceptions to this pattern in 2011 are on a number of peak precipitation days at Fisera Ridge, the highest of the three stations, where the simulated precipitation values are less than the observed amounts. The fact that the deterministic methods yield precipitation values close to observed values at the three left out locations tells us that these techniques work well for a single target location where distances between gauge sites are small (see Table 4.8).

Another consequence of the deterministic methods simulating only one time series for each station is that a single performance metric value can be calculated from the application of each of these techniques. For this project, Root Mean Square Error (RMSE), Mean Absolute Error (MAE) and Affinity Index (AI) have been used as performance metrics. MAE uses the absolute value of the difference between observed and simulated precipitation values at each timestep, hence it considers only the magnitude of error, not the direction, unlike RMSE (see formulae for RMSE and MAE in Table 4.15). The closer the values of RMSE and MAE are to zero, the smaller the error. AI is a matching statistic used to compare the numbers of observed and

simulated dry days (Lewis et al., 2021), using the adopted dry day threshold of < 0.1 mm. AI values range between 0 and 1, with values closer to 1 indicating a better match between observed and simulated wet days and dry days.

Calculated values of RMSE, MAE and AI for the deterministic spatial interpolation techniques considered are shown in Table 4.16. Note the unique feature of the simplistic NN technique, where metric values at Fisera Ridge and Upper Clearing gauges are the same, because each is the nearest station to the other (Figure 3.1). When calculating metrics for either of these two gauges, the differences between the observed value at one with the simulated value at the other are used, and vice versa. RMSE uses the sum of the square of the differences, and MAE uses the sum of the absolute value of the differences; as the number of timesteps is the same, the values of RMSE, MAE and AI are identical. Hay Meadow RMSE and MAE values using NN are lower than those for the other two stations as, across the 11-year time series duration, the difference in precipitation amounts between Hay Meadow and its nearest neighbour at Upper Clearing is less than the difference in precipitation amounts between Fisera Ridge and Upper Clearing, as highlighted by the water year precipitation totals, and the 11-year mean values (see Table 3.4). Metric values in Table 4.16 obtained using the kriging methods (OK and KED) are very similar to those from NN and IDW, indicating that for MCRB, there is no obvious improvement gained from the more complex kriging techniques. The one notable exception is the higher AI value for Hay Meadow obtained with KED, implying that KED performs more consistently in simulating dry days than the other deterministic spatial interpolation methods tested here for the MCRB catchment. The AI values computed for all methods of spatial precipitation interpolation in Table 4.16 are higher at Fisera Ridge and Upper Clearing than at Hay Meadow, mainly due to the influence of elevation and topography on the numbers of wet and dry days experienced. Fisera Ridge (2325 m a.s.l.) and Upper Clearing (1845 m a.s.l.) are at higher elevations and experience a smaller difference in the number of wet days (see Table 4.4 for the wet day threshold < 0.1 mm), between them compared with the differences between Fisera Ridge and Hay Meadow or between Upper Clearing and Hay Meadow (1436 m a.s.l.), which is at a lower elevation towards the plains.

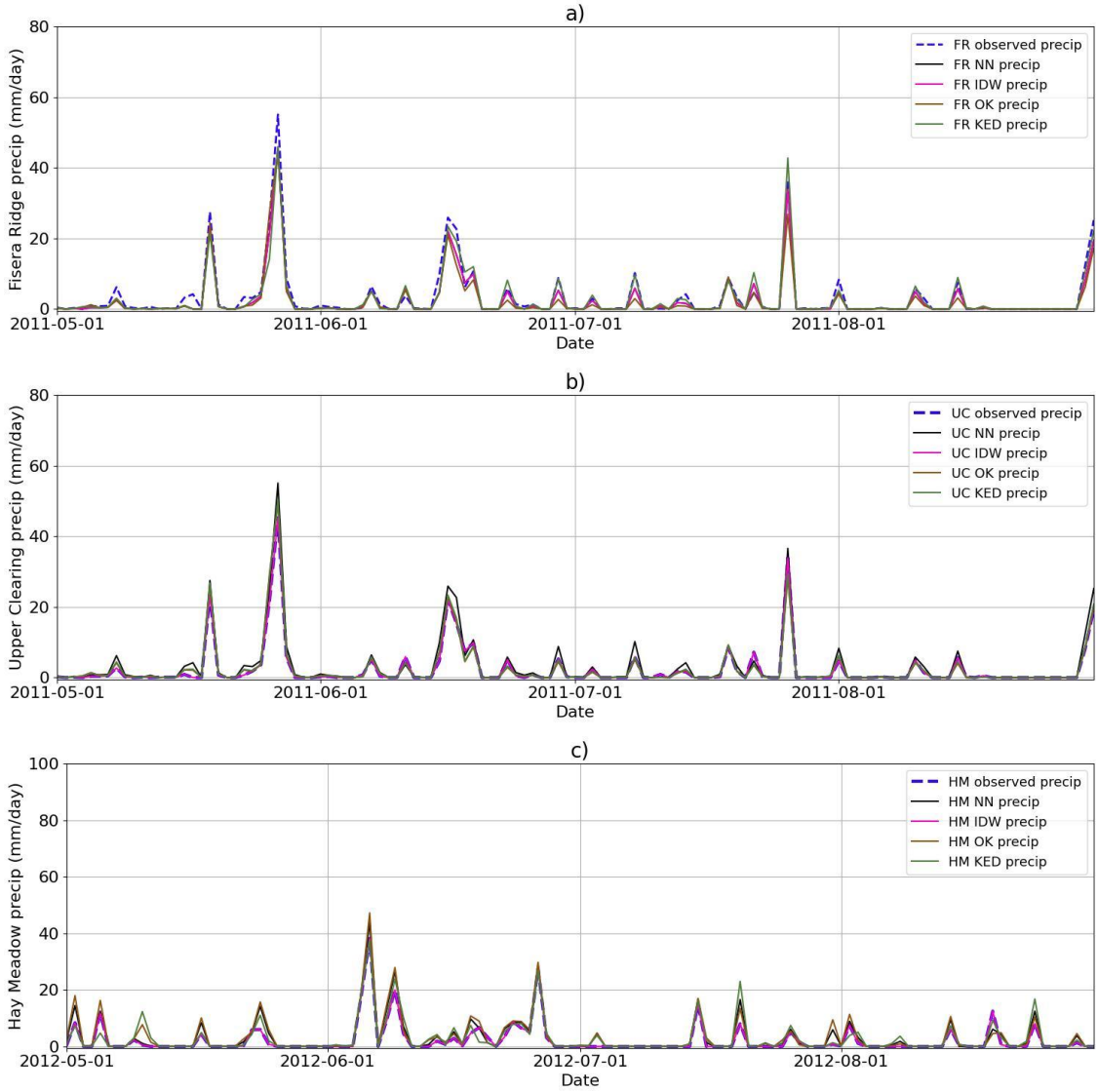

Figure 4.14. Observed daily precipitation time series and simulated daily precipitation time series, using leave-one-out cross-validation for Nearest Neighbour (NN), Inverse Distance Weighting (IDW), Ordinary Kriging (OK) and Kriging with External Drift (KED) techniques at Fisera Ridge, for May-August 2011: a) Fisera Ridge, b) Upper Clearing, c) Hay Meadow

Table 4.15. Formula for Mean Absolute Error (MAE)

Metric	Formula
Root Mean Square Error (RMSE)	$RMSE = \sqrt{\frac{\sum_{t=1}^{T}\left(Po_g, t_g - Pm_n, t_n\right)^2}{T}}$
Mean Absolute Error (MAE)	$MAE = \frac{\sum_{t=1}^{T}\lvert Po_g, t_g - Pm_n, t_n\rvert}{T}$

where Po_g, t_g = observed precipitation at the gauge of interest, at time t
Pm_n, t_n = modelled precipitation at the nearest neighbour gauge, at time t
T = no. of timesteps

Table 4.16. Performance metric values for NN, IDW, OK and KED resulting from leave-one-out cross-validation using observed daily precipitation values at Fisera Ridge, Upper Clearing and Hay Meadow stations

Spatial interpolation method	Station	RMSE	MAE	AI
NN	Fisera Ridge	3.09	1.17	0.95
	Upper Clearing	3.09	1.17	0.95
	Hay Meadow	1.81	0.75	0.89
IDW	Fisera Ridge	3.16	1.21	0.92
	Upper Clearing	2.51	0.90	0.95
	Hay Meadow	3.34	1.35	0.85
OK	Fisera Ridge	3.55	1.43	0.92
	Upper Clearing	1.45	0.52	0.95
	Hay Meadow	2.80	1.20	0.85
KED	Fisera Ridge	2.85	1.01	0.92
	Upper Clearing	1.61	0.57	0.96
	Hay Meadow	2.95	1.05	0.92

4.6.2 Leave-one-out cross-validation for RM-mountain method

In contrast to deterministic spatial interpolation techniques, the stochastic RM-mountain method yields multiple realisations of precipitation time series; while it would be possible to calculate metric values for each ensemble member, such an approach would not be consistent with the purpose of stochastic modelling, i.e., to explore possible realisations but not taking any single one of them as 'truth'. Leave-one-out cross-validation for the RM-mountain method was applied with an ensemble size of 100, i.e., the algorithm was run 100 times with Fisera Ridge left out, and likewise for Upper Clearing and Hay Meadow. As was done for observed precipitation data at the three stations in Section 4.2.2, gamma probability density functions (pdfs) were generated using the wet day (≥ 0.1 mm/day) RM-mountain modifications 1-3 simulated precipitation values from the cross-validation exercise. For cross-validation, it was not considered necessary to produce seasonal pdfs, hence only annual pdfs are shown (Figure 4.15). The spread of the ensemble is very small, and the ensemble pdfs closely match the pdfs fitted to observed data at the three stations. There are differences in fitted gamma shape (α) parameter values though: values for the RM-mountain cross-validation ensemble are higher than observed fitted gamma parameters (Table 4.17), implying that the simulated pdfs have a more skewed shape than the observed pdf, a pattern which is illustrated in Figure 4.15. Conversely, ensemble mean gamma scale (β) parameter values (which quantify how stretched or squeezed the distribution is) are lower than the observed β values, most noticeably at Fisera Ridge where there is a greater difference between the frequency of observed and simulated

precipitation values: below 7 mm/day, the frequency of simulated precipitation is higher, whereas above 7 mm/day the frequency of simulated values is lower across the ensemble. The gaps between β values for Upper Clearing and Hay Meadow, where there is a closer fit between observed and ensemble pdfs, are smaller, particularly at lower precipitation amounts.

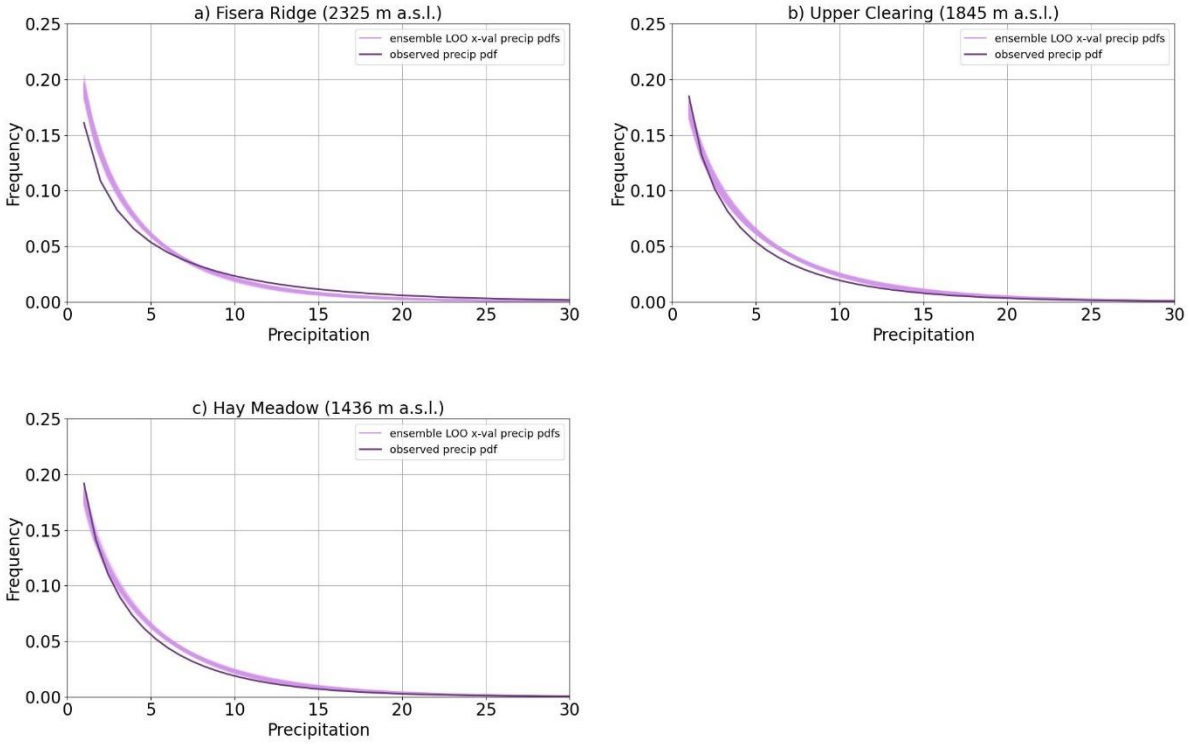

Figure 4.15. Fitted gamma distributions for daily precipitation: observed and RM-mountain simulated from leave-one-out cross-validation (annual only)

Table 4.17. Fitted gamma shape and scale parameter values for observed daily precipitation and ensemble mean RM-mountain simulated daily precipitation from leave-one-out cross-validation

Station	**Annual gamma shape (α)**		**Annual gamma scale (β)**	
	observed	ensemble mean	observed	ensemble mean
Fisera Ridge	0.625	0.735	8.414	5.487
Upper Clearing	0.615	0.768	6.482	6.300
Hay Meadow	0.643	0.800	5.993	5.666

Time series plots were generated for each station to summarise the distribution of spread of precipitation values across the 100-member ensemble at each daily time step. Also, by evaluating daily which of the ensemble time series yields the precipitation value closest to the observed value at a given station, a ‘best match’ line is plotted along with the observed

precipitation. Plots showing ensemble, best match and observed daily precipitation were produced for each water year from 2007-2012. Those for 2011, focusing on the period between May and August, are presented in Figure 4.16 (Fisera Ridge), Figure 4.17 (Upper Clearing) and Figure 4.18 (Hay Meadow). Similar figures for 2007-2010 and 2012 are included in Appendix A. From the 2011 time series plots there is an increased spread at Fisera Ridge in the ensemble as we proceed from modification 1 (a), through modifications 1 & 2 (b) to modifications 1-3 (c). This pattern of increasing spread is consistent with the increase in variance demonstrated in the spatial precipitation fields as well as the 1D variance figures in Section 4.5. The observed precipitation line typically falls within the extent of the ensemble at Fisera Ridge, Upper Clearing and Hay Meadow, particularly when RM-mountain is applied with modifications 1 to 3 (Figure 4.16c, Figure 4.17c and Figure 4.18c); this confirms that the RM-mountain technique is generating realistic values. On peak precipitation days on 19.05.2011, 27.05.2011, 16-17.06.2011 and 26.07.2011, higher precipitation amounts are simulated within the modifications 1-3 ensemble than for modification 1 or modifications 1 and 2 scenarios, signifying that the inclusion of all modifications in the RM-mountain algorithm typically returns an ensemble with a greater likelihood of matching the observed values on peak precipitation days. Even more encouragingly, the best match lines for all modification combinations typically overlay the observed precipitation line. However, on 27.05.2011, even the best performing ensemble member generates a precipitation value less than the observed value at Fisera Ridge, the highest elevation station. A similar phenomenon, not only at Fisera Ridge but also at Upper Clearing and Hay Meadow stations, is observed on a number of peak precipitation days in other years: 17.06.2007, 08.05.2008, 24.05.2008 and 06.06.2012 (see Appendix A). On all of these dates, the recorded precipitation value is much greater than the days immediately before and after. The observed daily precipitation values for the three-day period around each of the dates in question, and the percentage differences between each peak precipitation day and the days immediately preceding/succeeding them, are presented in Table 4.18.

Table 4.18. Observed daily precipitation amounts for days where RM-mountain best fit ensemble members underestimate precipitation values, and percentage differentials compared with day before and day after amounts

Station		Observed total precipitation: mm/day (% differential)			
		17.06.07	**08.05.08**	**24.05.08**	**06.06.12**
Fisera Ridge	Day before	7.1 (+93%)	3.1 (+93%)	23.8 (+74%)	19.3 (+62%)
	Peak pr date	**99.2**	**70.2**	**93.3**	**50.4**
	Day after	0.8 (-99%)	45.9 (-35%)	19 (-80%)	0 (-100%)
Upper Clearing	Day before	5.5 (+93%)	2.1 (+95%)	15.4 (+73%)	19.2 (+56%)
	Peak pr date	**76.9**	**40.8**	**58.1**	**44.1**
	Day after	0.6 (-99%)	29.4 (-28%)	12.6 (-78%)	0 (-100%)
Hay Meadow	Day before	2.9 (+96%)		18.9 (+72%)	
	Peak pr date	**72.0**		**66.9**	
	Day after	0.5 (-99%)		13.0 (-81%)	

With the exceptions of 08.05.2008 and 06.06.2012 at Hay Meadow, on which days RM-mountain does not underestimate daily precipitation, there is a high percentage difference between either the day before or the day after the peak precipitation dates, ranging from -78% (between 24.05.2008-25.05.2008 at Upper Clearing) to -100% when the peak precipitation day is immediately followed by a dry day (between 06.06.2012-07.06.2012 at both Fisera Ridge and Hay Meadow). These large percentage changes between consecutive days have a noticeable impact on the ability of the RM-mountain algorithm to accurately estimate precipitation amounts when Fisera Ridge and Upper Clearing, the stations at higher elevations, are the left-out locations. A potential reason for this underestimation on days where there is a large precipitation difference between the preceding and/or succeeding days may be related to the way in which the RM-mountain algorithm, when fitting a spatial copula to represent spatial variability for each day in the time series, randomly samples from the full daily precipitation time series instead of randomly sampling from each separate day's precipitation values, i.e. modification 1. As previously explained, modification 1 is fundamental to the application of the random mixing method to sparsely gauged catchments, to generate a robust spatial covariance model for each day. However, it seems that, for heavy precipitation days that are immediately preceded and/or succeeded by dry or very light precipitation days, the RM-mountain method requires further development to overcome the problem of underestimation. This is a potential area of further work, explored in more detail in Chapter 7.

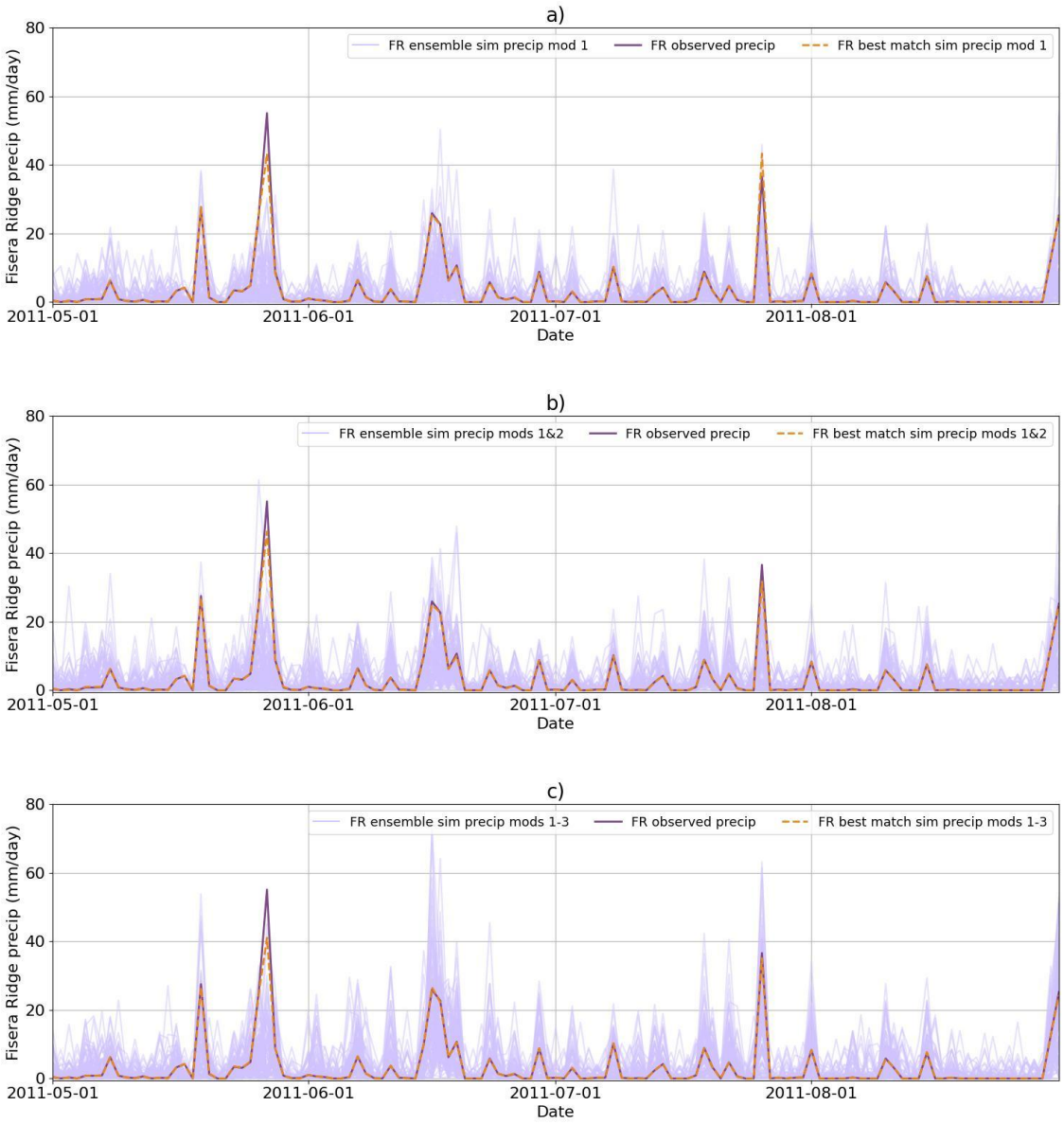

Figure 4.16. Observed daily precipitation time series and RM-mountain simulated daily precipitation time series, using leave-one-out cross-validation at Fisera Ridge, for May-August 2011, showing 100-member ensemble and best match to observed precipitation for: a) modification 1; b) modifications 1 & 2; c) modifications 1-3

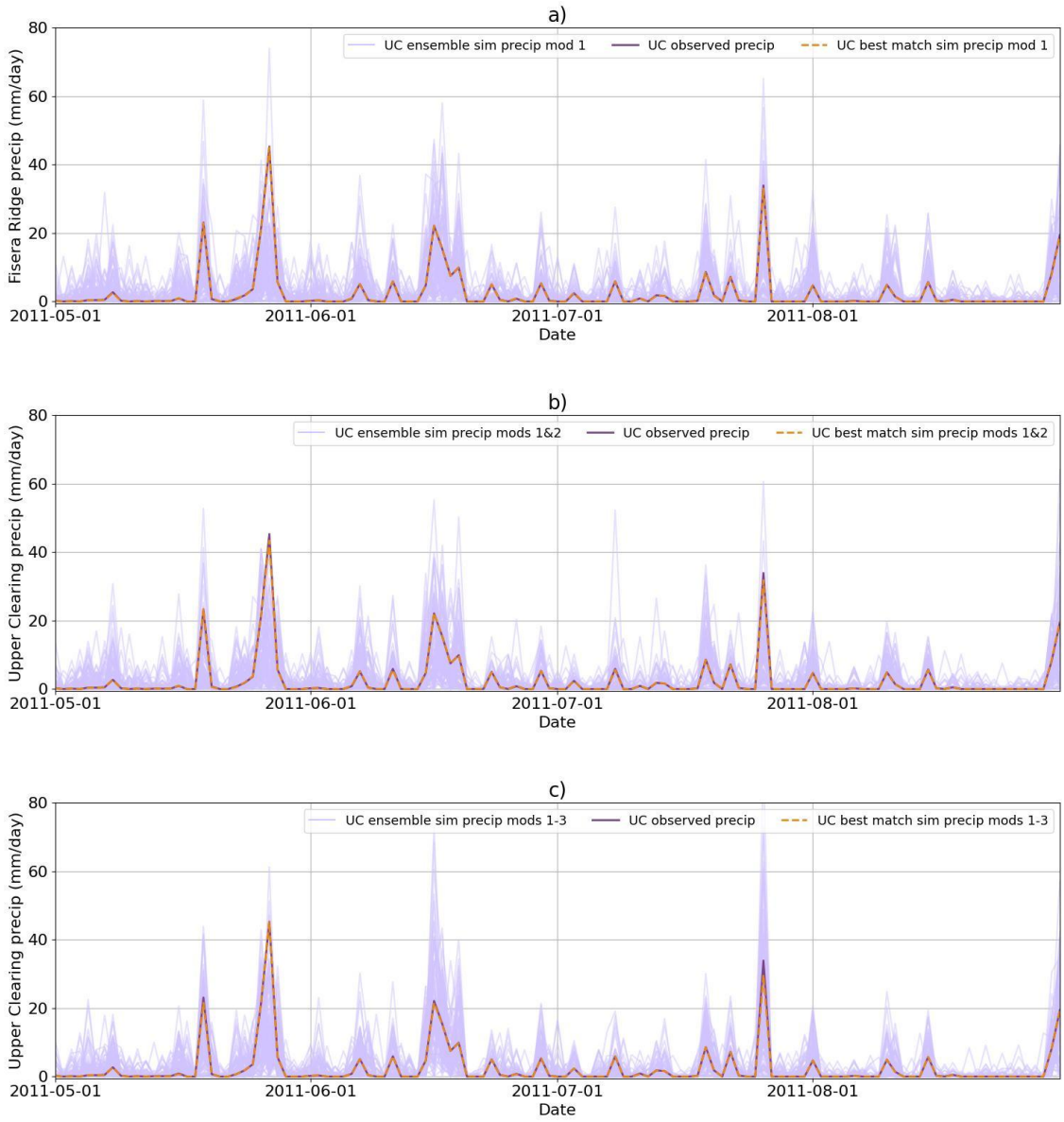

Figure 4.17. Observed daily precipitation time series and RM-mountain simulated daily precipitation time series, using leave-one-out cross-validation at Upper Clearing, for May-August 2011, showing 100-member ensemble and best match to observed precipitation for: a) modification 1; b) modifications 1 & 2; c) modifications 1-3

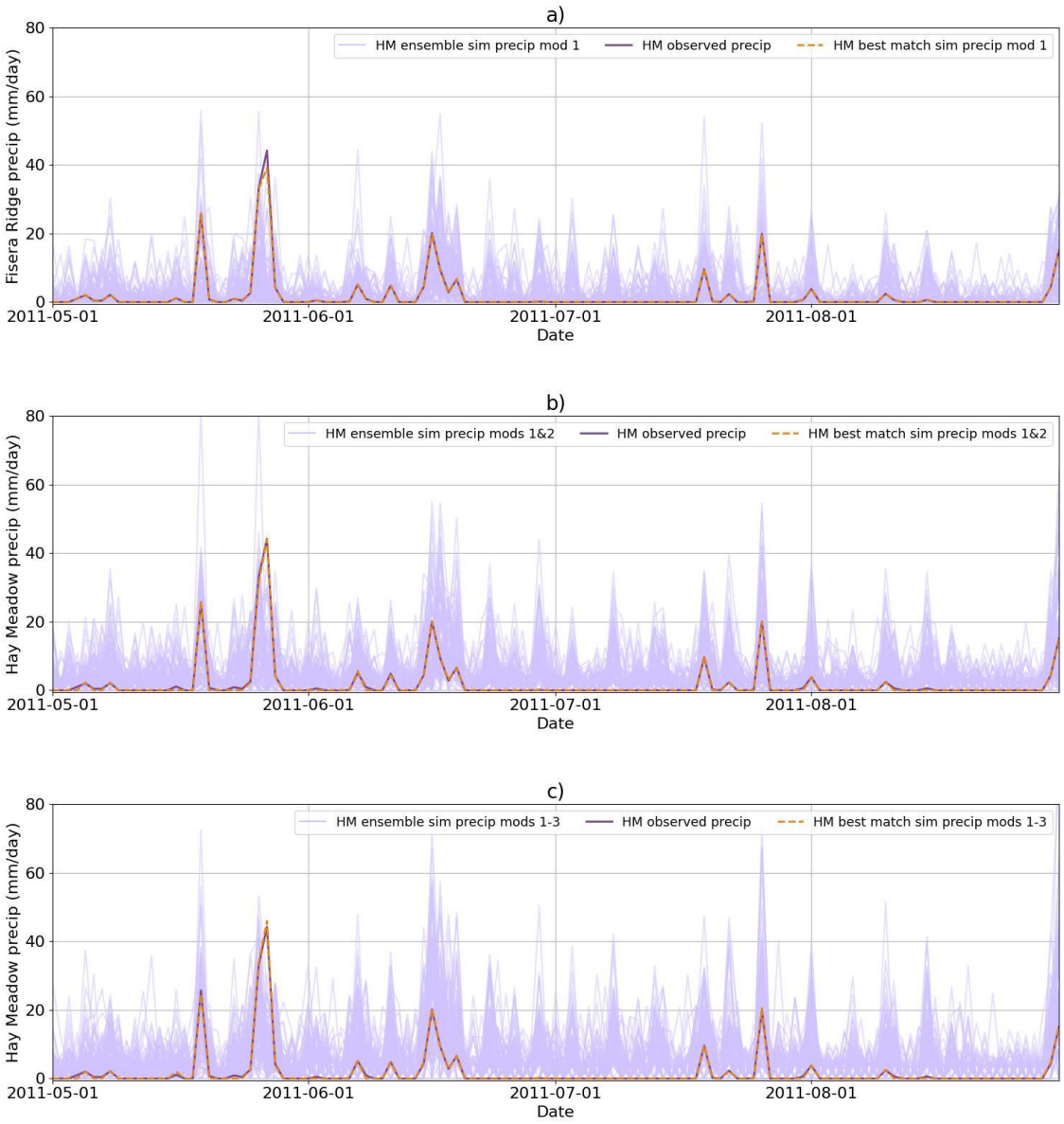

Figure 4.18. Observed daily precipitation time series and RM-mountain simulated daily precipitation time series, using leave-one-out cross-validation at Hay Meadow, for May-August 2011, showing 100-member ensemble and best match to observed precipitation for: a) modification 1; b) modifications 1 & 2; c) modifications 1-3

4.7 Conclusions

As highlighted in Figure 4.11, for the small, mountainous MCRB catchment, the unmodified RMWSPy technique generated low variance spatial precipitation fields. The RMWSPy algorithm randomly samples from observed precipitation values for a given time step in spatial copula fitting, which establishes the spatial covariance relationship used to simulate precipitation fields for that individual time step. This works well with a suitably large number of observation locations. For application in more sparsely gauged catchments such as MCRB, a modification to the original RMWSPy approach is required. Increasing the number of observation locations is unlikely to be a realistic solution in most mountain catchments with few gauges, hence an alternative method devised in this chapter, referred to as modification 1, was to randomly sample from the full time series of precipitation observations: this increases the set of precipitation values that can be used for spatial copula fitting, resulting in a much more robust spatial covariance relationship for each time step. In this thesis, a daily time step has been adopted but the technique can be applied to any time step duration. The introduction of modification 1 increases variance which results in more plausible precipitation fields (see Figure 4.13). Modification 1 is fundamental to the operation of the RM-mountain method. However, as discussed in Section 4.6.1, the time series sampling approach may need further refinement to overcome the issue of underestimating precipitation values on a heavy precipitation days that are immediately preceded and/or succeeded by dry or very low precipitation days, with a percentage difference in precipitation between days of approximately 80% or greater. The addition of modification 2 for elevation dependence and modification 3 for seasonality further increase the variance of simulated spatial precipitation fields (Figure 4.13). In addition, the outcomes of the cross-validation process further confirm the validity of including modifications 1-3 to maximise the likelihood of simulating more realistic fields within the generated ensemble.

In the next two chapters, the RM-mountain simulated daily time series ensemble spatial precipitation fields will be used as inputs to HBV (Chapter 5) and CRHM (Chapter 6) to evaluate and compare the performance of the method with conceptual and physically-based hydrological models.

Chapter 5. Hydrological modelling: HBV

5.1 Introduction

The previous chapter presented the modifications made to the random mixing technique to develop the RM-mountain method, which can be used to simulate ensemble spatial precipitation fields for mountainous catchments. A 200-member ensemble of spatial precipitation fields was generated for Marmot Creek Research Basin (MCRB) incorporating all three modifications discussed in Section 4.4: modification 1 in which the spatial covariance parameters for each time step are derived by randomly sampling from the full time series of observed precipitation from the Fisera Ridge, Upper Clearing and Hay Meadow stations; modification 2 which incorporates grid cell elevations across the model domain into the algorithm to account for precipitation/elevation gradients; and modification 3 which enables the user to account for seasonal effects by using seasonal precipitation probability density functions (pdfs) and fitted seasonal spatial covariance functions when simulating precipitation fields. The inclusion of all three modifications was identified in Chapter 4 as yielding the most plausible precipitation fields, hence the combined 3-modification configuration was used for ensemble modelling in this chapter and in Chapter 6. The aim of this chapter, and Chapter 6, is to use an ensemble modelling approach to evaluate the performance of RM-mountain generated daily spatial precipitation fields when used as time series inputs for two different hydrological models.

This chapter explores the outcomes from representing MCRB using the relatively simple spatially distributed conceptual Hydrologiska Byråns Vattenbalansavdelning (HBV) hydrological model described in Section 3.6.2. To explore the performance of the RM-mountain method when coupled with two very different hydrological models, differences in model outputs between HBV and the more complex physically-based CRHM (discussed in Section 3.6.3) are presented in Chapter 6. For each of the three modifications introduced in the RM-mountain method described in Sections 4.3.1 to 4.4.2, a 200-member ensemble of spatial daily precipitation fields was generated as an 11-year daily time series, a total of 600 fields. Although observed precipitation data between 2005 and 2016 were available, streamflow observations could be accessed only between October 2005 and September 2012. Each of the 600 spatial precipitation fields was used as an input dataset for a separate hydrological model simulation of MCRB, run for the period 01.10.2005 to 30.09.2012. As discussed in Section 4.6, a leave-one-out cross-validation approach was used to compare the performance of the RM-mountain method of generating daily spatial precipitation fields for MCRB with the performance of four

other spatial interpolation techniques: Nearest Neighbour (NN), Inverse Distance Weighting (IDW), Ordinary Kriging (OK) and Kriging with External Drift (KED). In addition to running hydrological model simulations using precipitation inputs from the new RM-mountain method, the time series spatial precipitation fields produced using NN, IDW, OK and KED were also used as hydrological model inputs. Unlike the ensemble approach taken with the stochastic RM-mountain method, only one hydrological model simulation was required for each of the NN, IDW, OK and KED techniques, as these deterministic methods generate only a single spatial precipitation field. Using precipitation fields from all five techniques in this way enables comparison of hydrological model outputs generated from each spatial interpolation technique, indicating the relative usefulness of each method. HBV simulations in this chapter, and CRHM simulations in Chapter 6 were driven by exactly the same sets of precipitation inputs. Results from HBV simulations are discussed in the following sections.

5.2 Modelling MCRB with HBV

The Python-coded version of the HBV hydrological model used here is full spatially distributed, on a 50 m x 50 m regular grid, adapted from wflow hbv (Deltares, 2021). Adaptations included functions to represent snowpack accumulation, melt and refreezing and gravitational snow redistribution through avalanching. Runoff routing is based on calculating a time lag for runoff to reach the catchment outlet depending on the distance of a cell from the outlet. A detailed HBV specification is described in Section 3.6.2. Saved outputs from each HBV simulation are: catchment average precipitation (pr), which is the average of the precipitation values across all grid cells in the model domain; actual evapotranspiration (aet), snowmelt (melt), runoff (roff), snow water equivalent (swe), soil moisture (sm), upper and lower zone storage (uz, lz), canopy interception (incps), snow covered area (sca), change in storage (ds) and mass balance (mb). Outputs from HBV (and CRHM in Section 6.1) model simulations enable comparison of streamflow hydrographs, generated from each set of precipitation inputs, with observed streamflow. HBV-simulated snowmelt and catchment average precipitation were also generated to explore catchment responses, to identify how hydrological model structure, i.e., how physical processes are represented in two very different models, impact on streamflow. HBV output figures in this chapter and in Chapter 6 present the period between May and August for each full water year simulated, from 2006-2007 to 2011-2012 (2005-2006 is treated as a ‘spin-up’ period and is not included in any presentation or analysis of hydrological model outputs). The periods from September to April each water year

are not shown because there is no flow in Marmot Creek at these times; the absence of flow is a consequence of low, often sub-zero temperatures, precipitation falling as snow rather than rain, and snowpack accumulation. It is only in spring as temperatures increase that rainfall is experienced, the snowpack begins to melt and flow is again observed in the river. During the late spring and summer months, from mid-May onwards, observed daily mean air temperatures increase. Taking 2011 as an example, mean monthly temperature values are 1.5°C in May to 10.7°C in August at Fisera Ridge (2325 m a.s.l.); 3.8°C in May to 12.7°C in August at Upper Clearing (1845 m a.s.l.); and 5.7°C in May to 13.7°C in August at Hay Meadow (1436 m a.s.l.). During the late spring/summer period, there is more frequent and more intense rainfall, hence precipitation replaces snowmelt as the main driver of streamflow. In each streamflow hydrograph figure, the blue dashed line indicates the observed flow at the streamflow gauge at Seebe, which is described in Section 3.3. The yellow dashed line in all streamflow figures in this chapter represents the baseline flow obtained from the calibrated HBV catchment model (explained in Section 3.6.2). The collection of pale blue lines in each streamflow figure represents the 200-member ensemble of flows generated using time series spatial precipitation field inputs generated by combining modifications 1, 2 and 3 in RM-mountain.

5.2.1 Precipitation inputs from deterministic spatial interpolation methods

In all years from 2007 to 2012, flows resulting from NN and IDW generated precipitation fields are essentially the same (see Figure 5.1) the IDW (pink dash-dot) line overlies the NN (black) line. Figure 5.1 also reveals that, in every year from 2007 to 2012, for at least the first two weeks in May, OK and KED precipitation inputs result in the highest flows, typically exceeding observed flows. During May, discharge is primarily driven by snowmelt but precipitation also contributes to river flows, and the KED technique, which uses elevation gradients calculated from grid cell elevations, results in higher flows in May than the OK method. From late June onwards, another common feature detected across 2007 to 2012 is that, during periods of flow recession, an opposite trend is seen to that observed in May and early June, i.e., flows from OK and KED precipitation inputs are lower than those from NN and IDW inputs. The HBV-simulated baseline flow was generated using spatial precipitation inputs obtained from a variation of the MicroMet approach (Liston & Elder, 2006) incorporating Inverse Distance Weighting (IDW), as described in Section 3.6.2. This HBV-simulated baseline flow typically falls between the flows resulting from OK and KED inputs, and those from the NN/IDW inputs, i.e., the baseline flow is lower than the OK/KED flows and higher than the

NN/IDW flows in May, yet exceeds the OK/KED flows and is less than the NN/IDW flows from mid-June to August. In 2007 (Figure 5.1a), on the rising limb of the hydrograph during the first two weeks of May, flows resulting from NN, IDW and OK are initially lower than observed flows. By week 3 of May 2007, where there is a decreasing flow trend, all methods underestimate flows. The timing of the peak flow in early June coincides with the observed peak, at which time only NN and IDW flows exceed the observed flow while OK and KED underestimate peak flow. The HBV-simulated flow peak in mid-June is earlier and of greater magnitude than the observed flow peak, then in periods of receding flow from late June onwards, all methods yield flows lower than observed flow. In 2008 (Figure 5.1b), there is a very sharp flow peak in the last week of May, mainly due to rapid simulated snowmelt caused by warming temperatures. Flows resulting from all deterministic interpolation techniques exceed observed flows until the end of May; throughout June, when flow is primarily driven by precipitation rather than snowmelt, flows from all four methods closely track observed flow, with NN and IDW flows slightly higher than observed, OK and KED flows. In contrast to 2007 and 2008, much lower flows are experienced in 2009 (Figure 5.1c) when the snowmelt process is much more gradual in May and June. From mid-June 2009 onwards, flows from all methods are considerably lower than observed flow. In 2010 (Figure 5.1d) there is a similar pattern to 2009, with relatively low flows throughout May to August. In 2011 and 2012 (Figure 5.1e and Figure 5.1f), more rapid snowmelt than in 2009-2010 is experienced in May: flows from all four spatial interpolation method inputs are higher than the observed flow for most of this period, particularly in 2011. To summarise, in May when flow is primarily driven by snowmelt, the OK and KED methods generate higher flows than NN and IDW; from late June onwards, when precipitation is the streamflow driver, NN and IDW yield higher flows than OK and KED. However, all four techniques result in underestimation of flow throughout most of July and August across all years from 2007 to 2012.

Bias and NSE metrics (see formulae in Table 3.7), calculated using the full time series of HBV-simulated flows (from 01.10.2006 to 30.09.2012), for the NN, IDW, OK and KED methods are presented in Table 5.1. Compared with the HBV baseline scenario, higher NSE values from NN and IDW inputs represent a slight improvement in simulated flows, while lower NSE values are recorded for OK and KED inputs. Although OK and KED inputs yield higher HBV-simulated flows in May than inputs from NN and IDW, overall there are more days between mid-June and August where OK and KED inputs generate lower flows than NN and IDW inputs. Also, with the exception of 2008 (Figure 5.1b) simulated flows from all spatial

interpolation methods tend to be lower than observed flows, hence large negative bias values are recorded. In summary, there is a contrast in NSE values from HBV-simulated flows depending on the spatial interpolation method adopted: inputs from NN and IDW result in NSE values slightly higher than the HBV baseline scenario. In contrast, flows from OK and KED return NSE values noticeably lower than the HBV baseline. NN, IDW, OK and KED techniques all yield more negative bias values than the initial baseline simulation, especially the bias values resulting from OK and KED. Taken together, these results suggest that, for HBV-simulated flows in the MCRB catchment, NN and IDW techniques perform better than OK and KED.

Table 5.1. Bias and NSE metric values calculated from observed and HBV-simulated streamflows from HBV baseline and deterministic spatial interpolation method precipitation inputs

Spatial interpolation method	**Bias**	**NSE**
HBV baseline	-20.94	0.76
NN	-27.56	0.80
IDW	-27.56	0.80
OK	-39.43	0.60
KED	-35.22	0.53

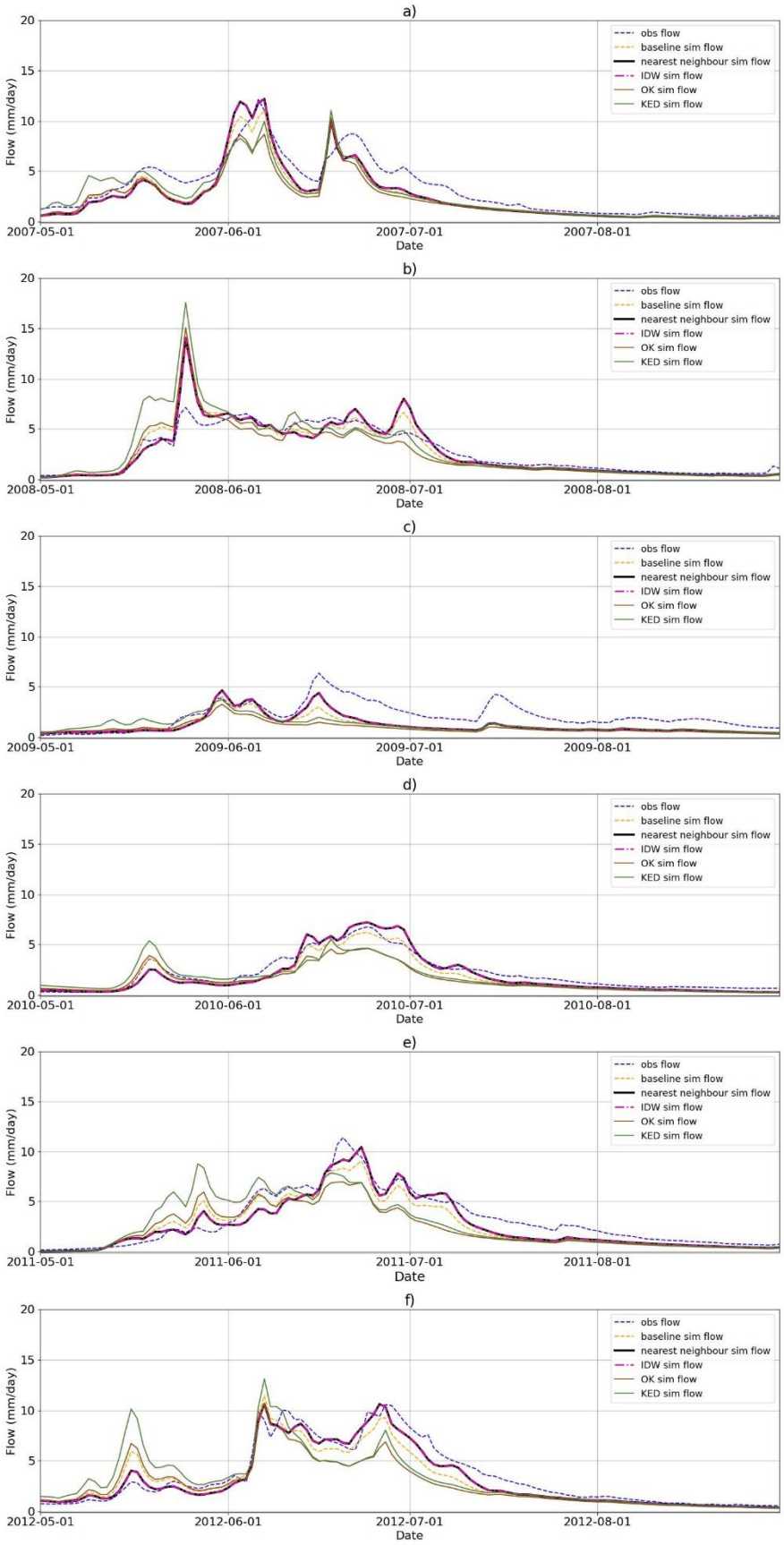

Figure 5.1. HBV hydrographs 2007-2012: observed, baseline, nearest neighbour, IDW, OK and KED flows

5.2.2 Precipitation inputs from stochastic RM-mountain method

Figure 5.2 shows streamflow outputs for 2007 to 2012, from the calibrated HBV model, using optimised parameter values, featuring flows generated from the 200-member ensemble of RM-mountain precipitation inputs (for modifications 1, 2 and 3 combined), observed flow, HBV baseline flow and best performing deterministic spatial interpolation method, which for HBV is Inverse Distance Weighting (IDW). Modifications 1-3 are used in combination because, as explained in Section 4.6.2, the inclusion of all modifications in the RM-mountain algorithm typically returns an ensemble with a greater likelihood of matching the observed values on peak precipitation days. This is a key consideration in developing the RM-mountain method, as it is important to capture extremes of precipitation as accurately as possible. As outlined in Section 3.6.2, HBV baseline outputs yielded bias and NSE values of -20.94 and 0.76, respectively. To explore the potential for improving these metric values using RM-mountain spatial precipitation inputs, a best constructed time series has been identified, selecting the ensemble member that yields the closest match to the observed flow for each daily timestep (evaluated using NSE and bias metric values), for each stage in the development of the RM-mountain method, i.e., modification 1 only, modifications 1 and 2 combined, and modifications 1 to 3 combined. It was relevant to generate best constructed time series for each modification stage, to demonstrate the relative benefit of each modification and to highlight the effectiveness of combining all three modifications. One of the advantages of an ensemble modelling approach is that a range of potential realisations of spatial precipitation fields is generated, none of which is intended or expected to represent actual reality. An advantage of the ensemble is that an inverse approach can be used, to work backwards from the observed time series flows to identify the optimum precipitation inputs to match the observations. This is a valid approach as, although it involves taking different spatial precipitation fields for successive days, each day's spatial fields are random and conditioned using the observed precipitation values for that specific day, so daily fields are interchangeable in this way. Such an approach is not possible with deterministic methods which generate only one spatial precipitation field realisation which then have to be treated as 'reality' although it is unlikely to be so. The best constructed time series from within the ensemble yields the bias and NSE values shown in Table 5.2: the optimum scenario combining modifications 1-3 gives bias and NSE values of 0.14 and 0.96, respectively. Comparing the metric values from the best constructed time series with the metric values from the HBV baseline, a noticeable improvement is evident in both bias and NSE. Bias and NSE are also provided for the best performing individual ensemble members (Table 5.2). Note that

bias and NSE values for each ensemble member are calculated by comparing the full simulated and observed time series flows, i.e., from 01.10.2006 to 30.09.2012.

Table 5.2. Bias and NSE values from baseline and RM-mountain best constructed time series flows

Spatial interpolation method	Bias	NSE
HBV baseline	-20.94	0.76
RM-mountain best constructed time series mod 1	12.41	0.93
RM-mountain best constructed time series mods 1&2	2.63	0.96
RM-mountain best constructed time series mods 1-3	0.14	0.96
Best performing ensemble members mod 1	-13.32	0.84
Best performing ensemble members mods 1&2	-0.05	0.88
Best performing ensemble members mods 1-3	-0.55	0.88

Some general observations on Figure 5.2 are that, between May and August for all years from 2007 to 2012, the observed flow is matched more closely within the 200-member ensemble than by the HBV baseline flow or the IDW-generated flow. Ensemble flows typically exceed baseline and IDW flows most of the time, unlike baseline and IDW flows which frequently underestimate flows. The best constructed time series flows generally match or exceed observed flows in May and early June of each year. Conversely, in July and August, simulated flows tend to be lower than observed flows.

To explore simulated time series streamflow patterns further, they have been plotted for 2007 and 2008 (Figure 5.3 and Figure 5.4) along with the following variables (corresponding figures for 2009 to 2012 are included in Appendix B):

panel b) simulated snowmelt time series (note that, due to the absence of any recordings of snowmelt rates, observed snowmelt could not be plotted);

panel c) observed catchment average air temperature time series (*1);

panel d) 200-member ensemble catchment average precipitation time series (*2) and observed catchment average precipitation time series (*1);

panel e) 200-member ensemble catchment average cumulative precipitation time series (*2) and observed catchment average cumulative precipitation time series (*1).

(*1): calculated as the average of the observations at Fisera Ridge, Upper Clearing and Hay Meadow stations

(*2): calculated as the average of RM-mountain generated precipitation values for each grid cell in the 164 x 164 square 50 m grid

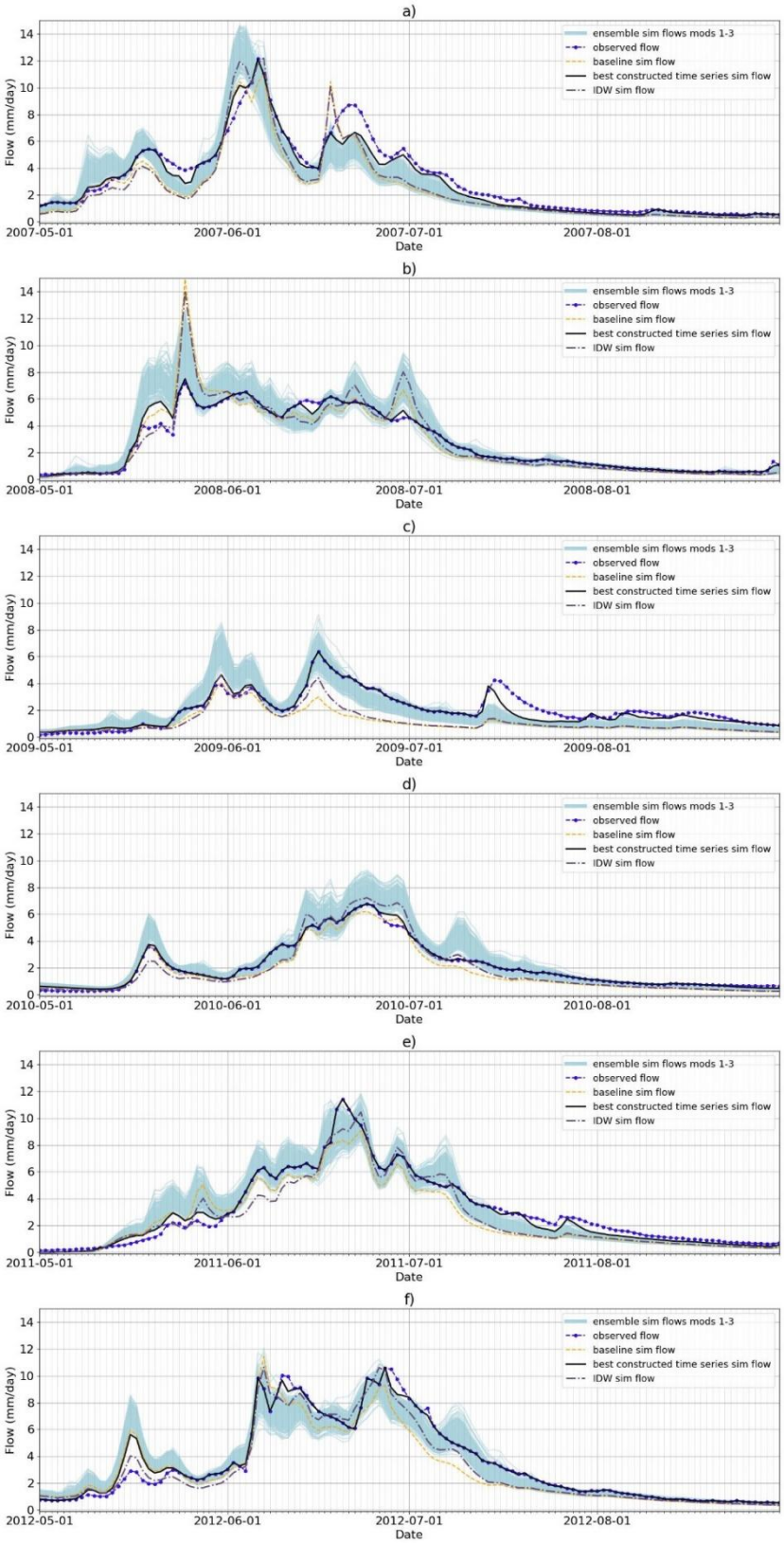

Figure 5.2. HBV hydrographs for May-August 2007-2012 (a-f): 200-member ensemble streamflows generated using RM-mountain precipitation fields (modifications 1-3); observed, baseline, best constructed time series and IDW streamflows

Also, to explore the performance of individual ensemble members, the best performing single ensemble members that yield the bias value closest to zero and the highest NSE value (Table 5.2) have also been identified and are shown on the streamflow plots for 2007 (Figure 5.3a) and 2008 (Figure 5.4a). Some common annual flow patterns can be detected from Figure 5.3a and Figure 5.4a. Firstly, as temperatures warm in May (Figure 5.3c and Figure 5.4c), increased runoff is experienced, with annual peak flows within the ensemble varying between around 12 mm/day in 2008 to 14.5 mm/day in 2007. While there is intermittent precipitation throughout each May, as a combination of both rainfall and snowfall, the proportions of which depend on elevation (see Table 3.5), May runoff is driven both by snowmelt and precipitation, and the 200-member ensemble RM-mountain simulated flows are typically greater than the observed flow. Peak snowmelt is typically in mid- to late May, with more melt evident on warmer days, as seen when comparing the snowmelt and air temperature plot pairs for any year. In June of all years, as the upward temperature trend continues, snowmelt rates fall as the much of the snowpack has already melted; by the first week in July, melt rates have fallen to zero and, from that point on, flow is driven solely by precipitation. The best constructed time series and the best performing ensemble members adhere to this pattern of generally exceeding observed flow on the rising limb of the hydrographs throughout May and even into June. It is likely that this difference is due to the relatively simple method used to model rainfall/snowfall phase partitioning in HBV, with a single threshold temperature of 273.15K (0°C). On the receding limb of the hydrographs, after the flow peaks between May and early July, the ensemble flows fall below the observed flow values. During July and August, streamflow is driven primarily by precipitation in the form of rainfall (Table 3.5 and Figure 3.5). The discussion of Figure 5.2 has already highlighted that HBV-simulated flows in July and August are lower than observed flows. This is in spite of the fact that, as demonstrated in panels d) and e) of Figure 5.3 and Figure 5.4, daily catchment average precipitation values within the ensemble are greater than the daily observed catchment average values. The daily time series plots in panels d) show that, on observed dry days and when observed precipitation is low, RM-mountain simulated ensemble precipitation values are higher than observed. This difference between observed and simulated precipitation amounts is discussed in Chapter 6 on modelling MCRB with the physically-based CRHM, where the variations between observed and simulated flows is much greater than those seen in HBV model outputs.

Although there are periods of exception, from mid-June onwards, the observed flow line is typically within the extent of the RM-mountain generated flows ensemble. In contrast, baseline flows sometimes lie well outside ensemble bounds, for example baseline flow lies beneath the ensemble lower bound for periods from late June through July and August of 2009 to 2012. These observations indicate better performance of RM-mountain generated flows in periods of low/zero snowmelt, when flow is driven solely by precipitation, i.e., in July and August. The pink lines in Figure 5.3c and Figure 5.4c represent the observed catchment average precipitation obtained by calculating the daily mean of the recorded total precipitation (rainfall and snowfall) values at Fisera Ridge, Upper Clearing and Hay Meadow stations.

For the majority of precipitation events, the observed catchment average precipitation values lie within the upper and lower bounds of the HBV-simulated catchment average precipitation amounts in the 200-member ensemble; in fact, on many days, the best performing ensemble members demonstrate precipitation values that exceed the observed amounts (a feature which, as stated above, will be discussed in detail in Chapter 6). However, at the highest peak precipitation event on 17.06.2007, the observed catchment average precipitation value is higher than any of the HBV-simulated 200-member ensemble catchment average precipitation amounts. The same phenomenon occurs for peak precipitation days on 24.05.2008, 27.05.2011 and 06.06.2012. It should also be noted that, on these four dates, the simulated baseline flow exceeds the RM-mountain flows, i.e., the peak baseline flow is above the ensemble flows. These four peak precipitation days are all preceded and/or succeeded by dry or very light precipitation days; the fact that the average catchment precipitation value for each of the 200 simulated ensemble member spatial fields is lower than the observed average on these four dates may be related to RM-mountain modification 1, where random sampling for spatial copula fitting at each time step makes use of the full time series of observed precipitation at each station, rather than only the values for a given time step. This possible cause, which is a potential area for further investigation, was discussed in detail in Section 4.6.2 on cross-validation.

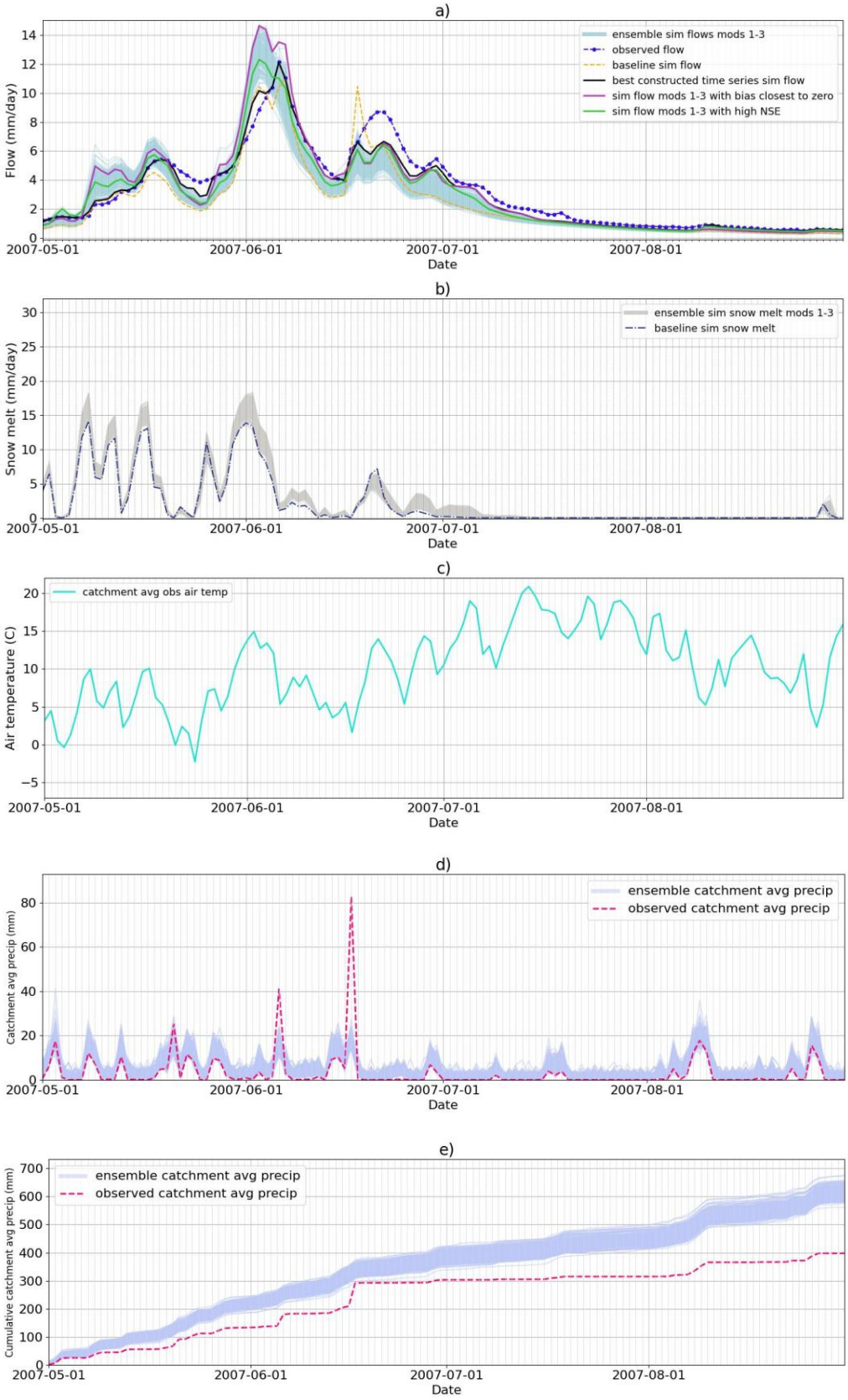

Figure 5.3. HBV outputs for water year 2007: a) 200-member ensemble streamflows with best constructed time series and best performing ensemble members for bias closest to zero and high NSE, HBV baseline and observed flows; b) 200-member ensemble and HBV baseline snowmelt; c) observed air temperature; d) time series observed and RM-mountain catchment average precipitation; e) cumulative observed and RM-mountain catchment average precipitation.

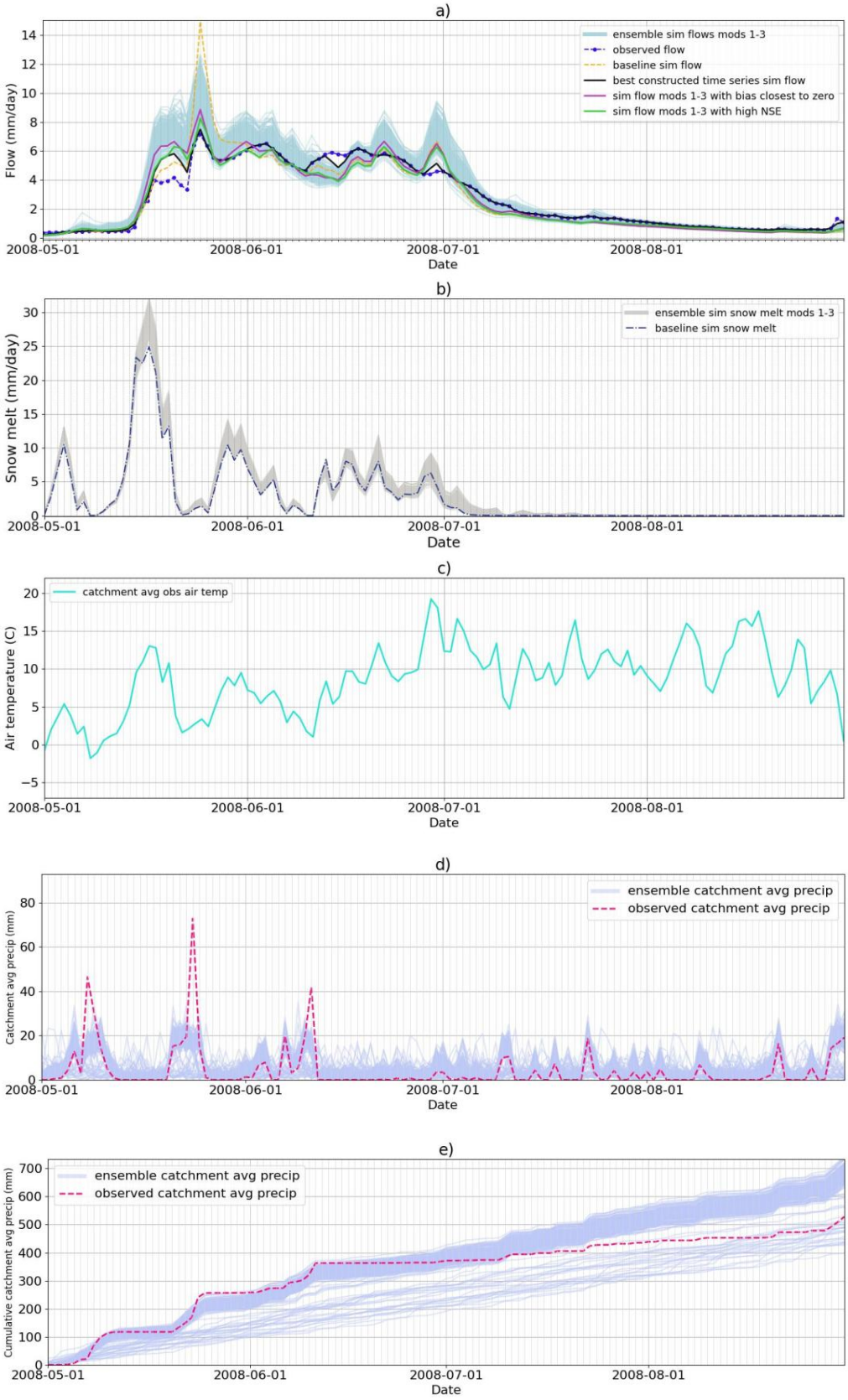

Figure 5.4. As in Figure 5.3 but for 2008.

Other features of model response to RM-mountain precipitation inputs are worth exploring. In 2007, the ensemble flows and best performing ensemble member flows (Figure 5.3a) exceed the baseline flow and more closely match the observed flow most of the time, indicating improved model performance with RM-mountain precipitation inputs. The exception is the peak discharge in mid-June, where the baseline flow is greater than the RM-mountain simulated flows. Simulated flows from RM-mountain precipitation inputs exceed observed and HBV baseline flows until the 3rd week in May, the period with greatest snowmelt (Figure 5.3b) after which time they briefly dip below the observed flow line. In late May there is a sequence of days with increased precipitation (Figure 5.3c) which drives the model's quick response, with rapidly increasing flow in the last week of May, causing the simulated flow in early June to peak several days before the observed flow. The timing of the maximum flow in the baseline simulation also coincides with the RM-mountain generated simulations. The later arrival of the observed discharge peak is associated with increased snowmelt in late May/early June. Simulated discharge peaks also precede, by several days, the observed maximum flow in the second half of June, following very heavy precipitation on 17.06.2007. This pattern of earlier simulated flow peaks indicates that the model has a flashier response to periods of heavy precipitation than that seen in the observed streamflow data. On the receding limb of the 2007 hydrograph from late June to mid-August, simulated flows are lower than the observed flow. During this period there is essentially no snowmelt and a long period of dry/low precipitation days. The relatively flashy behaviour of the catchment in the HBV model has seen more water pass through Marmot Creek in May-June than observed at the Seebe streamflow gauge; water that has been held back for longer in the catchment in reality causes higher observed discharge later on in July, although the difference between observed and simulated flows narrows throughout late summer, until zero discharge is experienced by the end of August in both the observed and simulated discharge. In contrast to 2007, both observed and simulated maximum flow peaks in other years typically coincide in time. In 2007, increasing flows were initially driven by heavy precipitation followed by a period of snowmelt, resulting in the early arrival of the simulated peak discharge. In 2008 for example, the opposite sequence is observed, where rising discharge is already occurring due to a period of increased snowmelt in mid-May (Figure 5.4b) followed immediately by a spell of heavy precipitation days (Figure 5.4c), resulting in simulated and observed peaks arriving at the same time.

Bias and NSE performance metric values, for best constructed time series and best performing low bias ensemble members were calculated for HBV-simulated flows resulting from RM-mountain precipitation field inputs, generated across the full time series from 01.10.2006 to 30.09.2012 (Table 5.3). The introduction of RM-mountain modification 1, where we randomly sample from the full time series of precipitation data, results in a noticeable improvement in bias values (from -20.94 to 12.41) and NSE (from 0.76 to 0.93) when comparing the HBV baseline simulation (the spatial interpolation method for which was described in Section 3.6.2) with the best constructed time series. Next, adding modification 2 (elevation dependence) and modification 3 (seasonal effects) ultimately result in a bias of 0.14 as well as further increasing NSE to 0.96. To explore the improvement in bias across the full 200-member ensemble with modifications 1-3, Figure 5.5 shows a frequency histogram of all 200 ensemble member bias values, revealing that the values are normally distributed, with a mean bias of 1.28. Minimum and maximum bias values from the ensemble are -5.2 and 8.7, respectively. These improvements are very encouraging, particularly in closing the negative gap in water balance (bias of -20.94) experienced in the HBV baseline run. They also represent a noticeable improvement on the simulated flows generated using the deterministic NN, IDW, OK and KED spatial interpolation techniques (see Table 5.3).

Table 5.3. Bias and NSE values for: RM-mountain best constructed time series and best performing ensemble members for low bias and high NSE; HBV baseline setup, NN, IDW, OK and KED

RM-mountain 200-member ensemble	**Bias**	**NSE**
Best constructed time series mod 1	12.41	0.93
Best constructed time series mods 1&2	2.63	0.96
Best constructed time series mods 1-3	0.14	0.96
Best performing ensemble members mod 1	-13.32	0.84
Best performing ensemble members mods 1&2	-0.05	0.88
Best performing ensemble members mods 1-3	-0.55	0.88
Deterministic spatial interpolation method		
HBV baseline	-20.94	0.76
NN	-27.56	0.80
IDW	-27.56	0.80
OK	-39.43	0.60
KED	-35.22	0.53

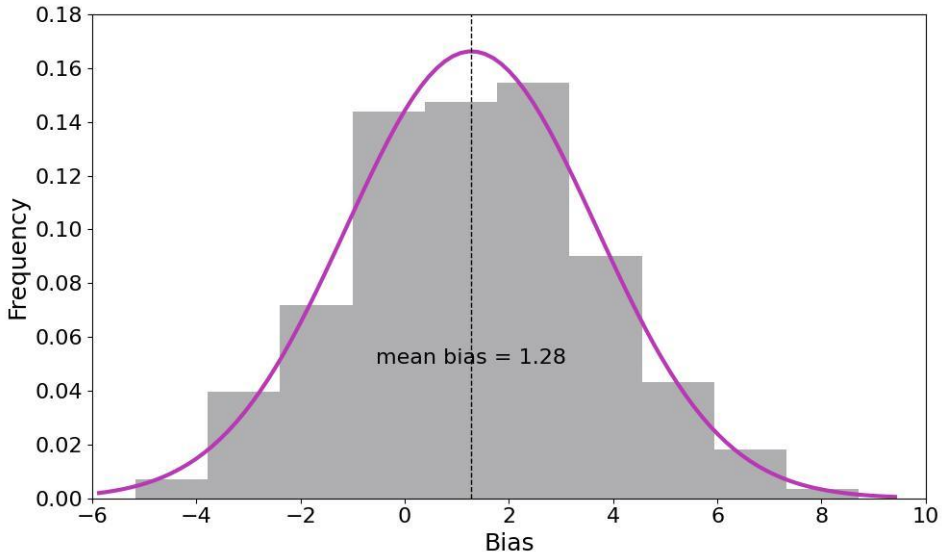

Figure 5.5. Histogram and fitted normal distribution curve for bias values across the full 200-member ensemble of HBV simulations

Figure 5.6 provides a visual demonstration of the improvement in bias between the best performing deterministic spatial interpolation method (NN and IDW yield the same bias value so only one of them needs to be shown, in this case IDW was chosen) and the best constructed time series/best performing RM-mountain ensemble member, for May to August 2009 (Figure 5.6a) and May to August 2011 (Figure 5.6b). The best constructed time series hydrograph matches observed flows more precisely than the IDW flow at almost all times. The best constructed time series, low bias ensemble member and IDW flows all exceed observed flow for most of May, when snowmelt predominantly drives streamflow. In the latter half of June, at times of higher discharge rates, the IDW flow closely matches observed flow better than at any other time. However, for the July-August period, the best constructed and best performing hydrographs from the RM-mountain generated ensemble perform better than IDW. Taken together with the improved bias and NSE values in Table 5.3, it can be seen that, when modelling the MCRB catchment with the HBV hydrological model, the best performing RM-mountain generated input precipitation fields yield flows closer to observed flows than the best performing deterministic spatial interpolation method (IDW) used in this study.

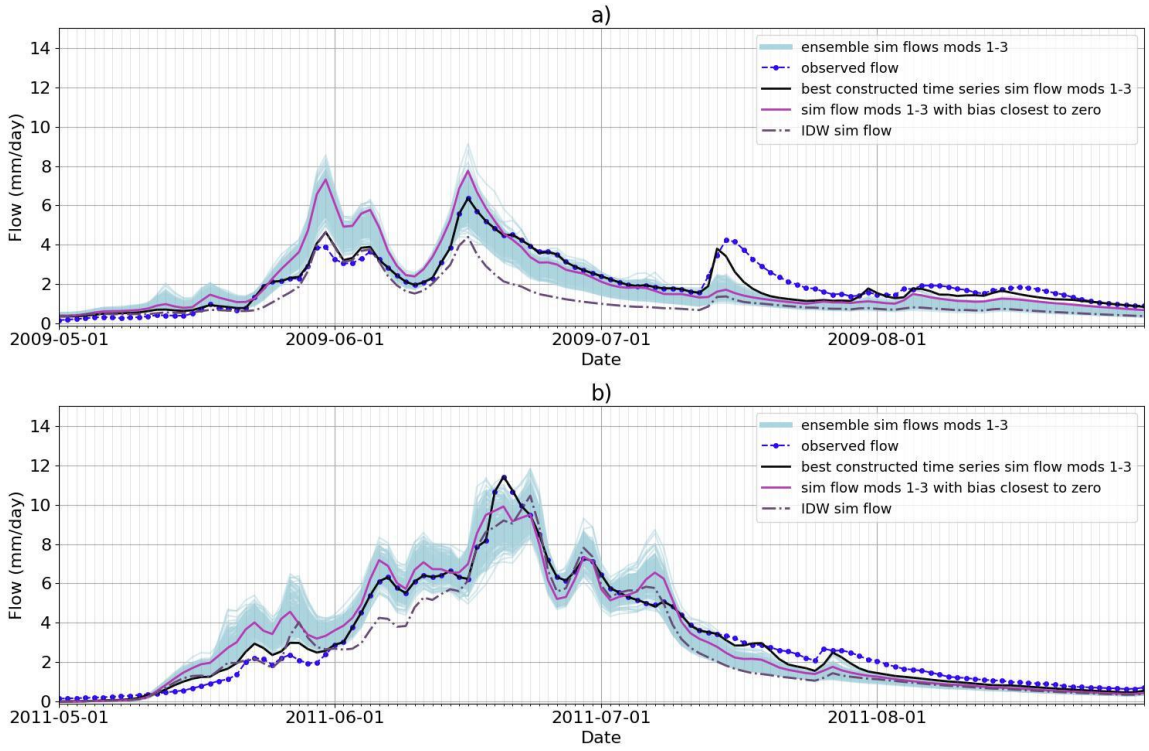

Figure 5.6. HBV streamflow outputs for May-August 2011: RM-mountain 200-member ensemble; observed; best constructed time series; best performing RM-mountain ensemble member for bias closest to zero; and best performing deterministic spatial interpolation method (IDW)

The results presented so far in this section rely on bias and NSE calculations based on the full time series of non-zero daily observed flows and HBV-simulated flows, i.e., from 01.05.2006 to 31.08.2006, 01.05.2006 to 31.08.2006, and so on up to 01.05.2012 to 31.08.2012. When combined, the May to August period covers 123 days for each year, resulting in a total of 738 days across the six water year period from 2007 to 2012. The periods between 01.09 and 30.04 for each water year, when observed flows are zero, are excluded from the bias and NSE calculations. Metric values have therefore been calculated using a total of 738 days of observed and simulated flow data for each ensemble member. As a consequence of these no-flow 'breaks' between water years, the non-zero flow periods of each water year have to be analysed separately. It is therefore worth identifying the best performing ensemble members using bias and NSE values calculated separately using observed and simulated flows for the May to August part of each water year. This is briefly explored next in Section 5.2.3.

5.2.3 Calculating performance metric values by water year

The set of HBV-simulated and observed streamflow, HBV-simulated snowmelt and HBV-simulated and observed catchment average precipitation figures in Section 5.2.2 were reproduced, except this time best performing ensemble members have been identified from bias and NSE values calculated separately for each water year. To enable comparison of the two different approaches, bias and NSE values for separate water years are shown in Table 5.4, where only a small variation in bias values from year to year is apparent. Similarly, there is little difference between annual NSE values, except for 2009 which has a noticeably low NSE value of 0.68. The simulated flow ensemble underestimates flows in the second half of July (see Figure 5.6a) and, since the metric values are calculated using only the observed and simulated flows for the short period between May and August 2009, this reduces the NSE value for 2009. As the computation of metrics for each separate year has little impact on the bias and NSE values and on the overall interpretation of HBV model performance, it is therefore concluded that there is negligible benefit in exploring bias values for all ensemble members using separate water year flow data.

Table 5.4. Best performing ensemble member bias and NSE metric values calculated for separate water years' observed and HBV-simulated streamflows using RM-mountain generated spatial precipitation inputs

200-member ensembles	**Bias closest to zero**					
	2007	**2008**	**2009**	**2010**	**2011**	**2012**
Modifications 1, 2 and 3	-1.05	-0.23	-0.12	0.19	0.00	0.00
	High NSE					
	2007	**2008**	**2009**	**2010**	**2011**	**2012**
Modifications 1, 2 and 3	0.86	0.91	0.68	0.95	0.93	0.92

5.3 Conclusions

The best constructed time series and best performing RM-mountain ensemble members yield improved bias values and higher NSE values than the deterministic techniques and the HBV baseline scenario (Table 5.3). Bias values from the full 200-member ensemble of HBV simulations are normally distributed with a mean ensemble bias of 1.28 (ensemble minimum and maximum bias values are -5.2 and 8.7, respectively), indicating a noticeable improvement as a result of using RM-mountain precipitation inputs. Bias and NSE values were calculated for both the full time series of observed flows (2006-2012), and also for each individual water year. It was concluded that the full time series approach is more suitable, as the individual year calculation method did not yield any worthwhile improvement in metric values.

In addition to improved metric values, plots of simulated and observed flow demonstrate that flows from the best constructed time series and best performing RM-mountain ensemble members more closely match observed flows than those resulting from the best performing deterministic interpolation method (i.e., the method whose precipitation inputs yield HBV-simulated flows closest to observed flows, which in this study was IDW). Encouragingly, in July and August of each water year, when runoff is driven mainly by precipitation rather than by snowmelt, ensemble streamflows from RM-mountain generated precipitation inputs more closely match observed streamflow than the flows generated by precipitation inputs from NN, IDW, OK and KED spatial interpolation techniques.

In MCRB, where cold region processes are so important, early season (May) streamflow is primarily driven by snowmelt, as snow is released from accumulated snowpack as air and ground temperatures increase. The single threshold temperature method (0ºC) used in HBV is the likely cause of simulated snowmelt being more rapid than observed snowmelt. Timings of HBV-simulated flow peaks can also be affected by the way in which snowmelt is simulated by HBV. Although simulated flow peaks typically coincide with observed maxima, there is an exception in 2007 when rapid snowmelt and a period of particularly heavy rainfall generates earlier simulated flow peaks than the observed maxima in June 2007.

Increased precipitation from RM-mountain, when compared with other spatial interpolation techniques, is discussed in Chapter 6, on modelling MCRB with the physically-based CRHM. Underestimated precipitation values on days with heavy precipitation that are preceded and/or succeeded by dry/very light precipitation days, are likely due to the random sampling techniques introduced in RM-mountain modification 1, where values are sampled from the full observed time series rather than each time step. This is discussed further in Chapter 7.

Chapter 6. Hydrological modelling: CRHM

6.1 Introduction

To evaluate the performance of RM-mountain generated time series spatial precipitation fields when used as hydrological model inputs, this chapter explores the outcomes from representing Marmot Creek Research Basin (MCRB) using the physically-based Cold Regions Hydrological Model (CRHM, introduced in Section 3.6.3) and compares them with outputs from the Hydrologiska Byråns Vattenbalansavdelning (HBV) hydrological model presented in Chapter 5. The motivation for representing the MCRB catchment using a physically-based model is to evaluate the potential benefits gained by improving estimation of spatial precipitation where physical processes, particularly those such as snow accumulation and snowmelt that are so pertinent in cold regions, are more explicitly represented than in the relatively simple HBV model. As discussed in Section 5.1, exactly the same time series (water years 2006 to 2012) 200-member ensemble of spatial daily precipitation fields from RM-mountain were used as inputs to both the HBV and CRHM models, for RM-mountain modifications 1 to 3. As in Chapter 5, the performance of the RM-mountain method is also assessed by comparing hydrological model outputs with those resulting from spatial precipitation inputs from the four deterministic spatial interpolation techniques, Nearest Neighbour (NN), Inverse Distance Weighting (IDW), Ordinary Kriging (OK) and Kriging with External Drift (KED). Again, in contrast to the ensemble hydrological model simulations run with stochastic RM-mountain inputs, only one hydrological model simulation was run for each of the deterministic methods, as each of these techniques generates only a single spatial precipitation field. Results from the CRHM simulations are discussed in the following sections.

6.2 Modelling MCRB with CRHM

As described in Section 3.6.3, the CRHM hydrological model for MCRB was designed using a combination of modules that represent the relevant physical processes within the catchment (see Table 3.9). Unlike the version of HBV developed for this project, which is fully spatially distributed on the same 50 m x 50 m regular grid structure adopted for spatial precipitation generation in RM-mountain, CRHM uses hydrological response units (HRUs) to spatially discretise the catchment. MCRB is divided into four sub-basins: Cabin Creek, Middle Creek (which incorporates Upper Marmot Creek), Twin Creek and the downstream confluence of Cabin, Middle and Twin creeks. The sub-basins are represented as a combination of 36 HRUs

(Figure 6.1), as outlined in Table 3.8. It is important to note that CRHM simulations were run using exactly the same RM-mountain generated daily spatial precipitation fields as were used with HBV. With HBV, the model read the separate daily precipitation amount for each individual grid square. In CRHM, a different approach was required. The precipitation field grid was mapped onto the 36 HRUs, assigning each grid square to an HRU. For each time step, the average precipitation value for each HRU was calculated from the corresponding grid values and these average HRU values were then used as CRHM inputs. Assigning average precipitation values across HRUs is a coarser method than the individual grid square approach used in modelling MCRB with HBV; although the HRUs are small in area (see Table 3.8), they are considerably larger than the 50 m x 50 m grid cells in the RM-mountain precipitation fields. The area of the smallest MCRB HRU is 0.01 km^2 (10,000 m^2), which equates to 4 precipitation field grid cells. The largest HRU is 1.37 km^2 (1,370,000 m^2) in area, or 548 grid cells. By sub-basin, the mean HRU areas and the number of grid cells the areas equate to are:

- Middle: 0.46 km^2 = 460,000 m^2 184 grid cells
- Twin: 0.31 km^2 = 310,000 m^2 124 grid cells
- Cabin: 0.20 km^2 = 200,000 m^2 80 grid cells
- Confluence: 0.17 km^2 = 170,000 m^2 68 grid cells

These mean HRU areas and the corresponding number of grid cells gives an indication of the typical averaging of precipitation values needed to convert the spatial field inputs to a resolution that can be handled by CRHM. One of the advantages of the random mixing method is that it enables, depending on catchment size and available computing power, spatial precipitation to be represented on a high resolution regular grid. Clearly, adjusting the data to a lower spatial resolution for CRHM introduces a compromise that was not needed for modelling with HBV. However, that has to be set against the enhanced representation of cold regions physical processes in CRHM compared with HBV.

CRHM enables the user to select from a wide array of model outputs; for direct comparison with the HBV outputs presented in Chapter 5, figures showing daily streamflow, snowmelt, observed air temperature, catchment average time series precipitation and catchment average cumulative precipitation are presented in the following sections. As explained in Section 5.2, figures generated from hydrological model outputs show only the period between May and August for each full water year simulated; for consistency with HBV hydrological modelling, water year 2005-2006 was omitted as a ‘spin-up’ period, hence figures provided show the

period from 01.10.2006 to 30.09.2012, as no surface runoff is experienced in MCRB during the September to April periods. The yellow dashed line in all streamflow figures in this chapter represents the baseline flow obtained using point precipitation inputs from the Fisera Ridge, Upper Clearing and Hay Meadow stations interpolated by CRHM. In CRHM, point precipitation data is spatially distributed by assigning the nearest station to each HRU. Station precipitation observations can then be adjusted for the difference between the HRU elevation and the assigned station elevation. Precipitation adjustments for elevation are calculated as follows:

$$adjusted\ precip = obs\ precip \times \left(1.0 + \frac{elev\ adjustment \times elev\ difference}{100}\right) \quad (9)$$

where precip = precipitation, obs = observed, elev = elevation.

In the CRHM baseline configuration, which was used for baseline simulations in this project, the elevation adjustment factor is set to zero for all 36 HRUs in the MCRB model. Hence, in baseline simulations, the assigned station precipitation values are used with no adjustment made for the difference in elevation between a given HRU and its assigned station.

6.2.1 Precipitation inputs from stochastic RM-mountain method

As in Chapter 5 on modelling with HBV, modifications 1-3 are again used in combination because the inclusion of all three modifications in the RM-mountain algorithm gives the highest likelihood of matching the observed values on peak precipitation days. Streamflow outputs are presented (Figure 6.2) for 2007 to 2012, from the CRHM model of the MCRB catchment, featuring flows from RM-mountain inputs, observed flow, CRHM baseline flow, best constructed time series (the rationale for which was presented in Section 5.2.2) and best performing deterministic spatial interpolation method (see bias and NSE values in Table 6.4), which for CRHM is Ordinary Kriging (OK). As for HBV in Section 5.2.2, although the streamflow periods of each water year are presented separately, bias and NSE values for a single time series constructed from daily fields, where the best performing daily field is selected, are calculated by comparing the full simulated and observed time series flows, i.e., from 01.10.2006 to 30.09.2012. As will be discussed throughout this chapter, CRHM simulation outputs are highly sensitive to changes in meteorological input data. As well as precipitation data, CRHM also uses air temperature (t), relative humidity (rh), ground temperature (T_g), wind speed (u) and incoming solar radiation (Qsi) observations to simulate catchment behaviour. In addition

to meteorological observations from Fisera Ridge, Upper Clearing and Hay Meadow stations, additional observations of t, rh, T_g, u and Qsi were made available from automatic weather stations at four other locations: Centennial Ridge, Vista View, Upper Forest and Level Forest (Figure 6.1). Wind speed measurements recorded at a height of 18 m above ground surface level at Upper Clearing Tower were also obtained (Fang et al., 2019).

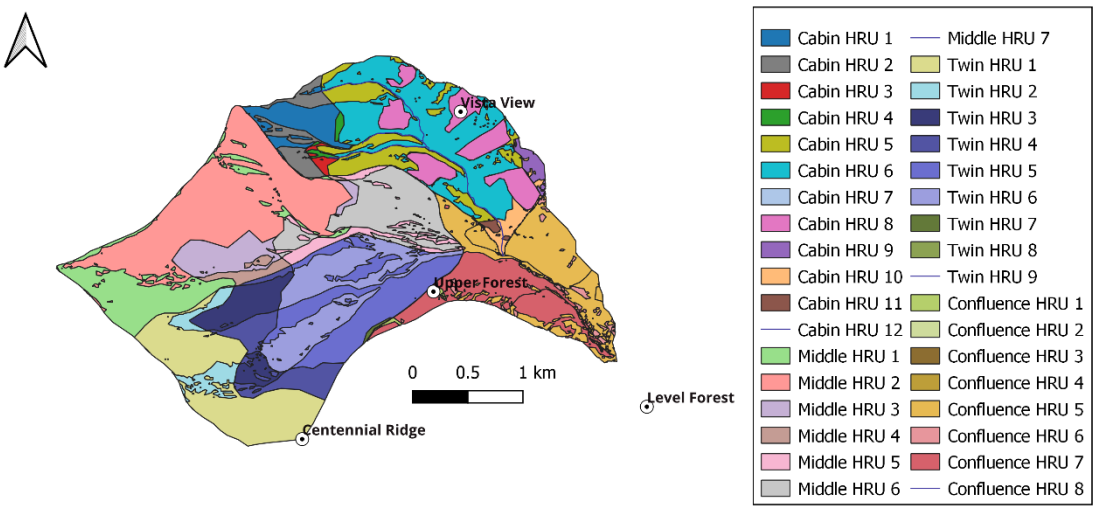

Figure 6.1. Map of Marmot Creek Research Basin (MCRB), Alberta, Canada, showing layout of the 36 HRUs used in CRHM for Cabin, Middle, Twin and Confluence sub-basins and locations of Centennial Ridge, Vista View, Upper Forest and Level Forest stations

A clear feature of the RM-mountain generated ensemble flow plots, when compared with the observed flow, in Figure 6.2 is the exceedingly high discharge rates in all years, and the later peak flows in July and August, when the simulated ensemble flows are much higher than observed and baseline flows. To evaluate the nature of the differences between observed and simulated precipitation totals, observed and RM-mountain simulated catchment average precipitation patterns for winter and summer were compared, as was variation between the percentage of observed and simulated wet days (Figure 6.3). The observed catchment average precipitation values, shown as dashed vertical lines in Figure 6.3a and Figure 6.3b were calculated using the observed time series data (October 2006 to September 2012) at Fisera Ridge, Upper Clearing and Hay Meadow stations. The histograms in Figure 6.3a and Figure 6.3b show the simulated catchment average precipitation for each of the 200-member ensemble spatial precipitation fields, also for the duration of the observed time series.

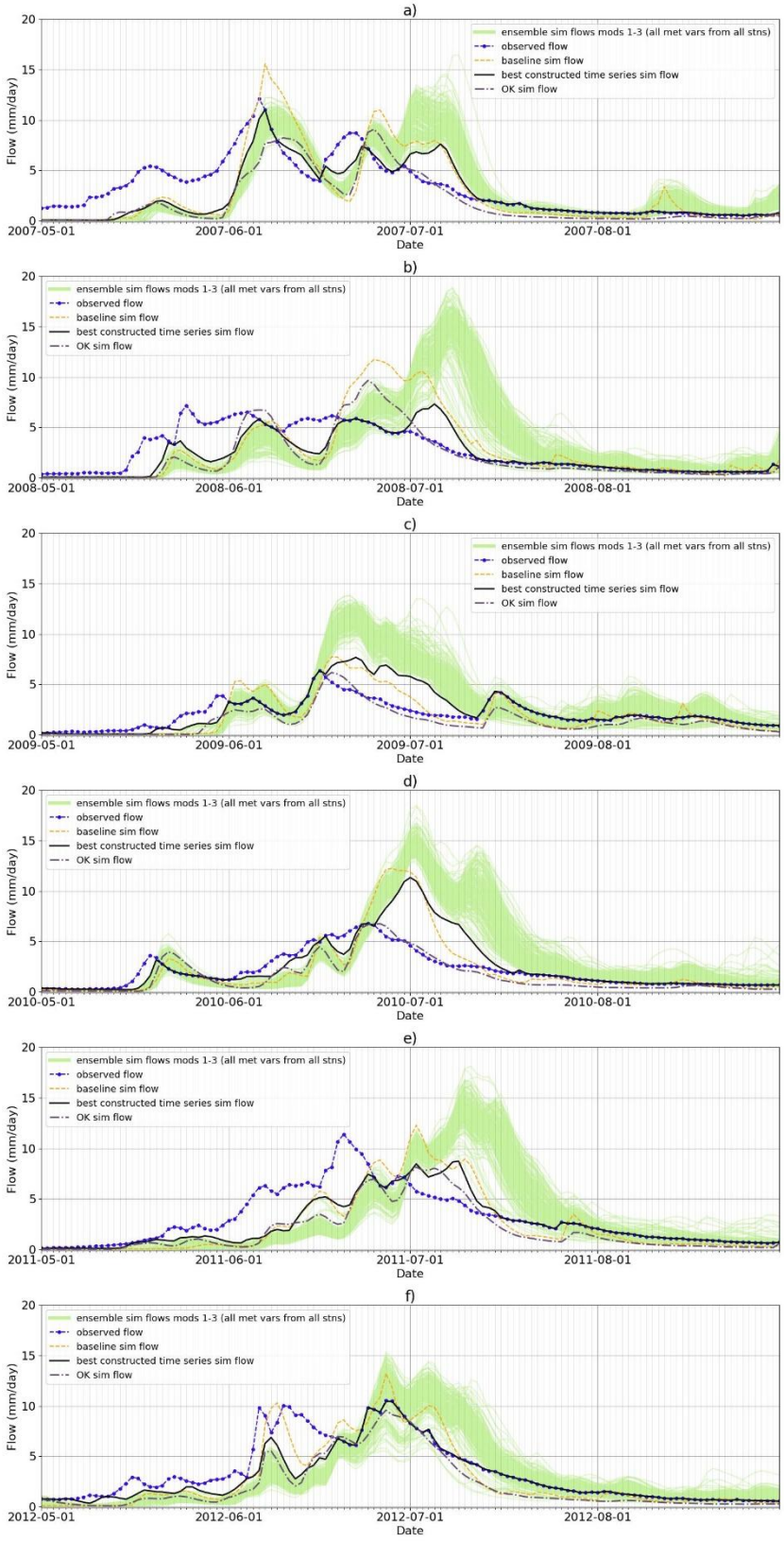

Figure 6.2. CRHM hydrographs for May-August 2007-2012 (a-f): 200-member ensemble streamflows generated using RM-mountain precipitation fields (modifications 1-3), observed, baseline, best constructed time series and OK streamflows

The mean observed catchment average winter precipitation value across water years 2006 to 2012 is 2577 mm (Figure 6.3a); the corresponding value for the simulated 200-member ensemble is 4275 mm (Table 6.1), a 66% increase on the observed value. The minimum catchment average winter precipitation amount from the ensemble is 3912 mm, which is itself 52% higher than the observed winter average. Across the seven summers between water years 2006 to 2012, the mean observed catchment average precipitation is 839 mm. The ensemble mean of 1211 mm (Table 6.1) is a 44% increase on the observed catchment average, while even the minimum summer mean of 972 mm is 16% greater than the corresponding observed amount. So, for winter and summer, RM-mountain simulated precipitation values are noticeably higher than those calculated using the observed values at Fisera Ridge, Upper Clearing and Hay Meadow stations.

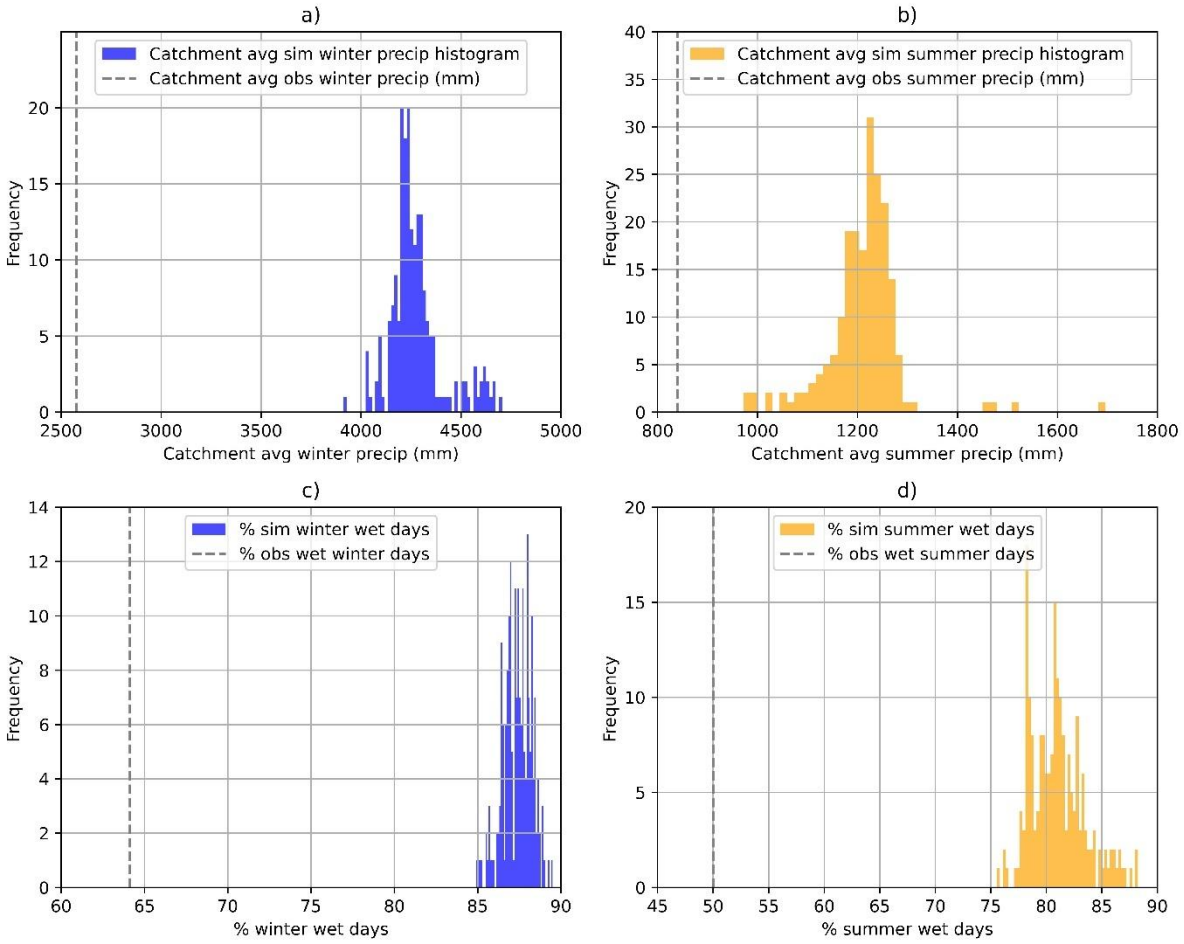

Figure 6.3. Observed and RM-mountain 200-member ensemble simulated catchment average precipitation and percentage wet days for winter and summer, calculated using full time series 2005-2012: a) winter precipitation amounts; b) summer precipitation amounts; c) percentage winter wet days; d) percentage summer wet days

Table 6.1. Ensemble catchment average precipitation statistics for winter and summer

Ensemble catchment average precipitation statistics	Season	
	Winter	**Summer**
Mean (mm)	4275	1211
Minimum (mm)	3912	972
Maximum (mm)	4706	1697
Range (mm)	794	725
Observed catchment average precipitation (mm)	2577	839

In line with higher RM-mountain precipitation totals exceeding observed amounts, the percentage of wet days (days when precipitation is ≥ 0.1 mm) within the ensemble is also larger than the observed wet day percentages (see Figure 6.3c and Figure 6.3d). From the observed data, a day is categorised as wet if the average of the observations is ≥ 0.1 mm, and dry if the average of the observations is < 0.1 mm. For the simulated precipitation fields, a wet day is identified when the average precipitation across the entire field is ≥ 0.1 mm, and dry when the average precipitation across the entire field is < 0.1 mm. In winter, the observed percentage of wet days is 64%, whereas in the 200-member ensemble the mean winter percentage is 87% (Table 6.2). The range of wet day percentage values for winter is small (5%), indicating that a similar number of wet winter days is generated across the entire ensemble. In summer, the observed wet day percentage is 50%, much lower than the winter value of 64%. However, the simulated summer wet day percentages are much greater than the observed summer value (50%), with an ensemble mean of 81%. Compared to the winter values, there is a wider range of simulated summer wet day percentages (13% compared with 5%).

Table 6.2. Ensemble percentage wet day statistics for winter and summer

Ensemble % wet day statistics	Season	
	Winter	**Summer**
Mean (%)	87	81
Minimum (%)	85	76
Maximum (%)	90	88
Range (%)	5	13
Observed % wet day statistics	64	50

A potential advantage of using the random mixing method to generate ensemble spatial precipitation fields is that, on days when the gauge locations are dry, precipitation can still be generated at other locations in the catchment. This is in contrast to the deterministic methods which, when the gauges are dry, spatial interpolation yields zero precipitation values

everywhere in the catchment. The RM-mountain technique allows for the more realistic possibility of small bands of convective summer rainfall in MCRB (Fang & Pomeroy, 2016) that pass between and around the gauge locations, which the deterministic methods are unable to do. The fact that the RM-mountain method enables precipitation on days when the gauges are dry is a viable explanation of the increased simulation of wet days in the ensemble, and hence the higher winter and summer precipitation totals in the simulated ensemble, compared to the observations. These increases in the number of simulated wet days and precipitation totals potentially explain the high CRHM streamflow outputs presented for 2007 to 2012 in Figure 6.2. It is important to note that RM-mountain modification 1, in which the random sampling method in RMWSPy was updated to enable sampling from the full time series to enable robust spatial copula fitting (Section 4.3.1), also increases the likelihood of more wet days being simulated. This is especially true in winter when the percentage of observed wet days is highest, and at lower elevations where observed dry day probabilities are greater than 0.5 (Table 4.5). Without considerable further work, it is not feasible to evaluate the extent to which the addition of modification 1 to the method increases the number of wet days and precipitation totals. The prospects for this are discussed in Chapter 7.

To explore the excess streamflow issue in more detail, CRHM simulation outputs are presented individually for all water years from 2007 to 2012, in Figure 6.4 to Figure 6.9, respectively. As in the HBV simulation results presented in Section 5.2.2, streamflows (Figure 6.4a to Figure 6.9a), simulated snowmelt (Figure 6.4b to Figure 6.9b), observed air temperature (Figure 6.4c to Figure 6.9c), catchment average time series precipitation (Figure 6.4d to Figure 6.9d) and catchment average cumulative precipitation (Figure 6.4e to Figure 6.9e) are also shown to give a clearer picture of model outputs. The observed, baseline and ensemble hydrographs in Figure 6.4a to Figure 6.9a are similar to those in Figure 6.2; Figure 6.4a to Figure 6.9a and Figure 6.2 differ in that the OK line has been removed, and, to evaluate the performance of individual ensemble members, best performing ensemble members have also been added.

Snowmelt, snow transport and sublimation in CRHM are calculated by the pbsmSnobal module (Table 3.9) which uses an energy balance approach where snowmelt is calculated when accumulated energy > cold content or when cold content > 0 (cold content is the energy needed to bring the snow cover temperature up to 0ºC. As a consequence, the onset of snowmelt in the CRHM simulations (Figure 6.4b to Figure 6.9b) is later and more gradual than in the HBV simulations, in which a simple single threshold temperature of 0ºC is used. This is part of the reason why CRHM flows in May are typically lower than observed flows, in contrast to HBV where more rapid snowmelt resulted in simulated flows exceeding observed flows through much of May. Another factor here is that CRHM enables sublimation of snow, a process not represented in HBV. This loss of water due to sublimation contributes to lower than expected flows in May.

Table 6.3. Best constructed time series and performing individual ensemble member bias and NSE metric values calculated from observed and CRHM-simulated streamflows using spatial precipitation inputs from RM-mountain and deterministic methods

RM-mountain 200-member ensemble	**Bias**	**NSE**
Best constructed time series mod 1	16.27	0.82
Best constructed time series mods 1&2	-1.50	0.61
Best constructed time series mods 1-3	1.88	0.74
Best performing ensemble members mod 1	-10.36	0.60
Best performing ensemble members mods 1&2	14.40	0.18
Best performing ensemble members mods 1-3	7.54	0.35
Deterministic spatial interpolation method		
CRHM baseline	2.04	0.54
NN	-49.11	-1.35
IDW	-46.79	-1.15
OK	-46.15	-1.10
KED	-54.01	-2.34

Bias and NSE performance metric values, for best constructed time series and best performing low bias ensemble members, were calculated for CRHM-simulated flows resulting from RM-mountain precipitation field inputs, generated across the full time series from 01.10.2006 to 30.09.2012 (Table 6.3). Metric values are presented separately in Table 6.3 for modification 1 only, modifications 1 and 2, as well as modifications 1 to 3 to highlight the improvements in bias values (from comparing simulated flows with observed flows) as we progress through the combinations of modifications. However, for clarity, CRHM-simulated streamflows in Figure 6.2 are for modifications 1 to 3 only. With HBV (Section 5.2.2), the introduction of RM-mountain modification 1, where random sampling is from the full time series of precipitation data, resulted in improved bias and NSE metric values compared to the

HBV baseline simulation. This is not repeated with the results so far obtained from CRHM simulations: the metric values in Table 6.3 reveal that it is only with the inclusion of all three RM-mountain modifications that the best constructed time series achieves improved bias and NSE values compared to the CRHM baseline run. It is likely that this is for similar reasons to those presented in Chapter 5 on modelling MCRB with HBV, i.e., that the inclusion of modification 3 with its separate seasonal precipitation distributions for autumn, winter, spring and summer, simulates the most realistic spatial fields. Due to ensemble flows being much higher than observed flows, the best performing individual ensemble member (bias = 7.54, NSE = 0.35) perform less well than the baseline (bias = 2.04, NSE = 0.54). The simulated flows in Figure 6.4a to Figure 6.9a were achieved by the simultaneous introduction of air temperature, relative humidity, ground temperature, wind speed and incoming solar radiation values for additional stations.

To determine which of these meteorological variables has the greatest impact in generating simulated flows that more realistically represent observed flows, five sets of extra ensemble simulations were run, introducing the additional meteorological variable data sets one at a time, to evaluate the impact of introducing each variable individually. For consistency, in each ensemble, observed values of air temperature, relative humidity, ground temperature, wind speed and incoming solar radiation recorded at Fisera Ridge, Upper Clearing and Hay Meadow are included, as they have been in all simulations up to this point. Figure 6.10 is designed to enable the impact of introducing each set of meteorological variables to be evaluated by showing 200-member ensemble streamflows, observed and baseline streamflows for water year 2011. Best performing ensemble members are not included in Figure 6.10 as we are interested mainly in the impact on flows across the entire ensemble here, more than in individual ensemble members. Streamflows from CRHM simulations using all five of air temperature, relative humidity, ground temperature, wind speed and incoming solar radiation (as previously shown in Figure 6.8a), are presented in Figure 6.10a. Flows resulting from the introduction of air temperature only, relative humidity only, ground temperature only, wind speed only and incoming solar radiation only, are shown in Figure 6.10b to Figure 6.10f, respectively.

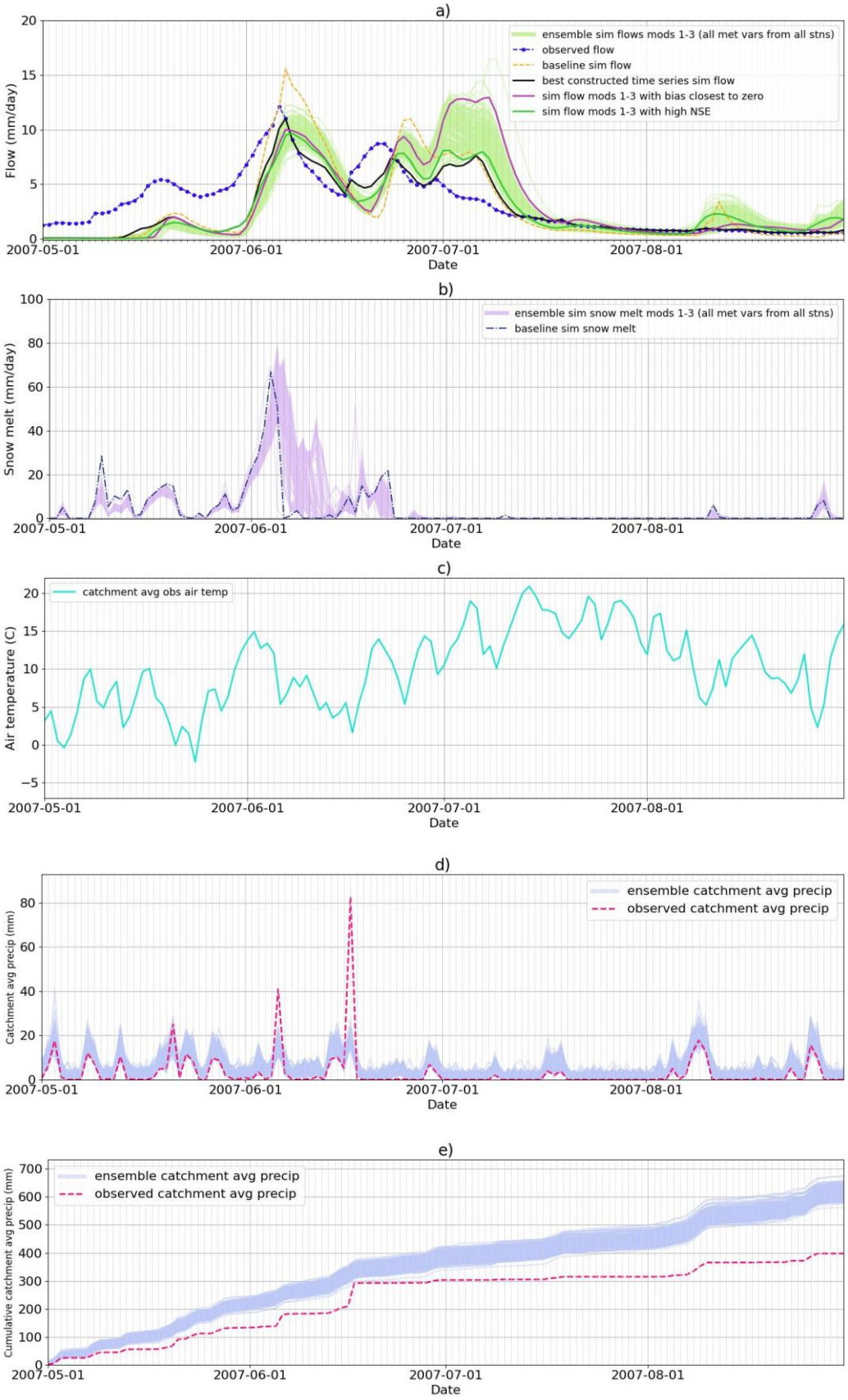

Figure 6.4. CRHM outputs for May-August 2007: a) streamflows: 200-member ensemble RM-mountain modifications 1-3, observed, baseline, best constructed time series; b) snowmelt; c) air temperature; d) time series RM-mountain catchment average precipitation; e) cumulative RM-mountain catchment average precipitation.

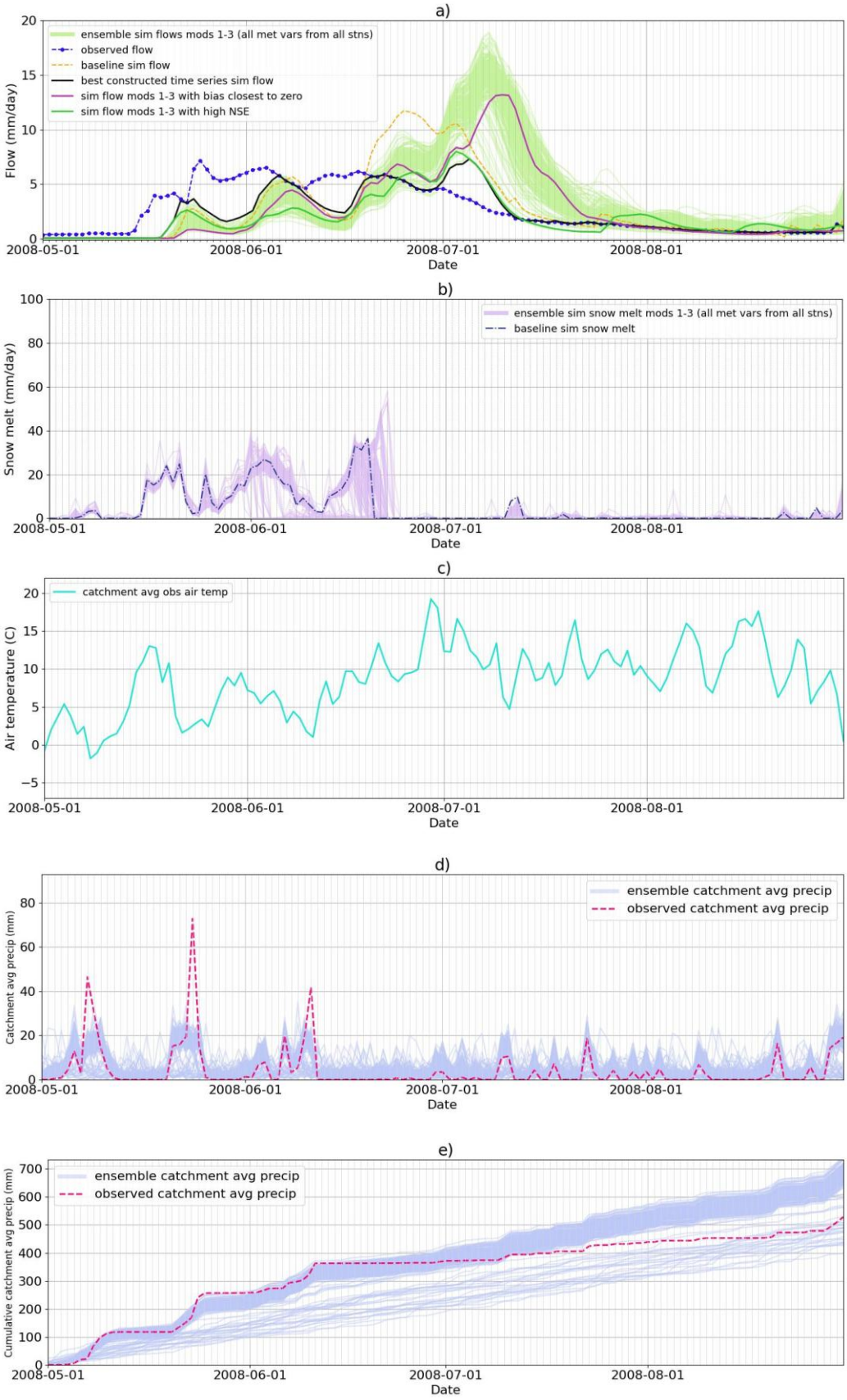

Figure 6.5. As in Figure 6.4 but for 2008.

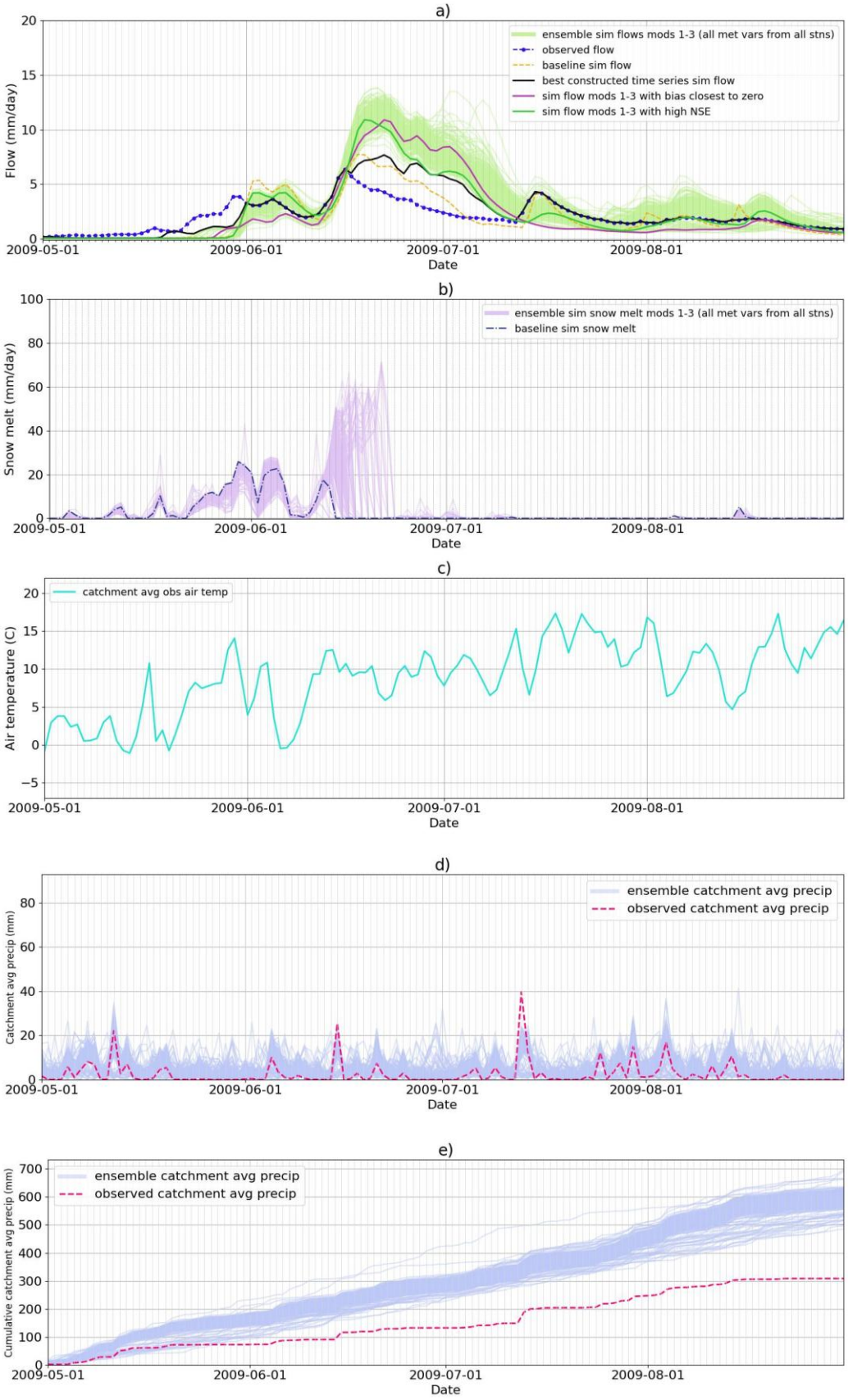

Figure 6.6. As in Figure 6.4 but for 2009.

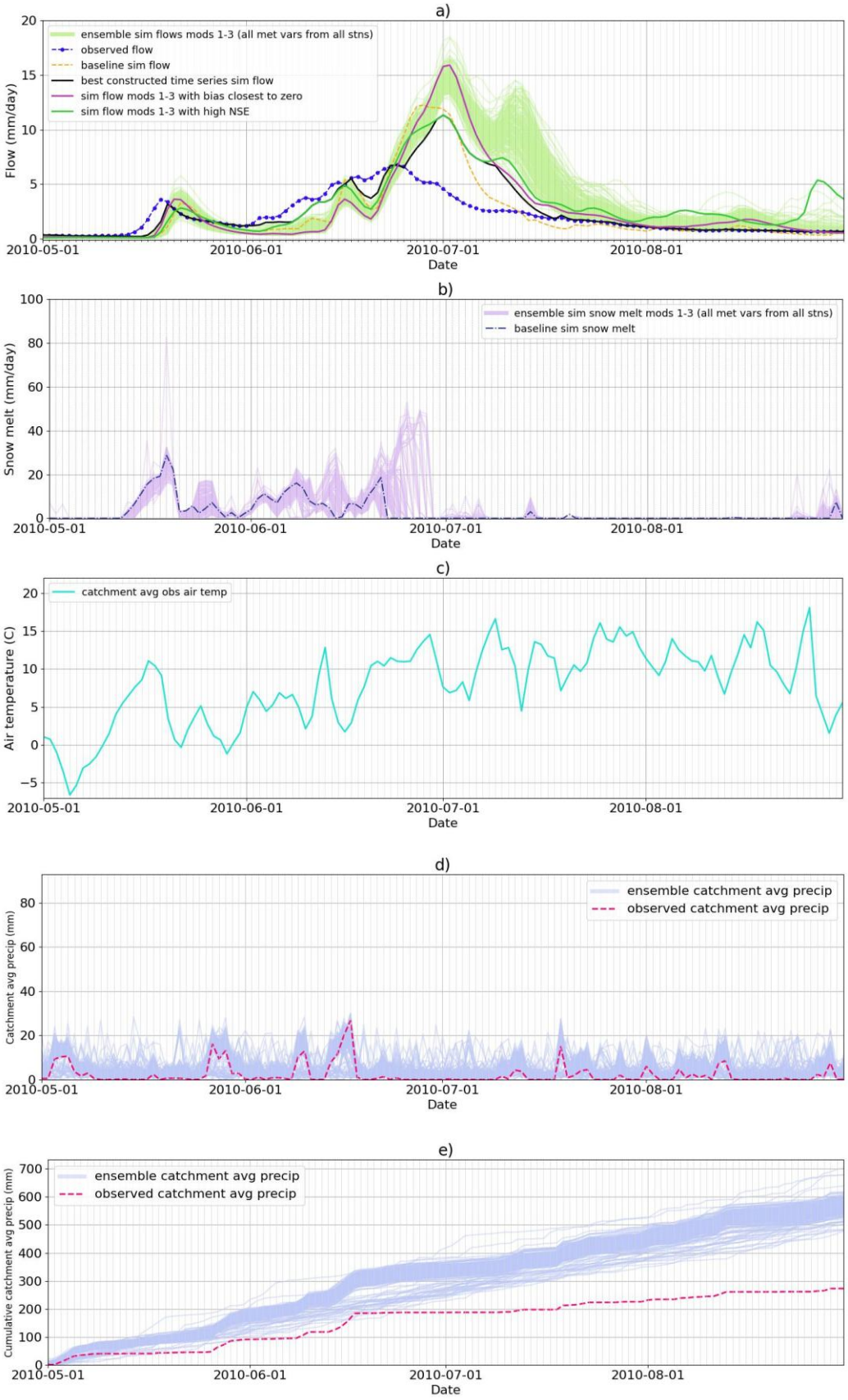

Figure 6.7. As in Figure 6.4 but for 2010.

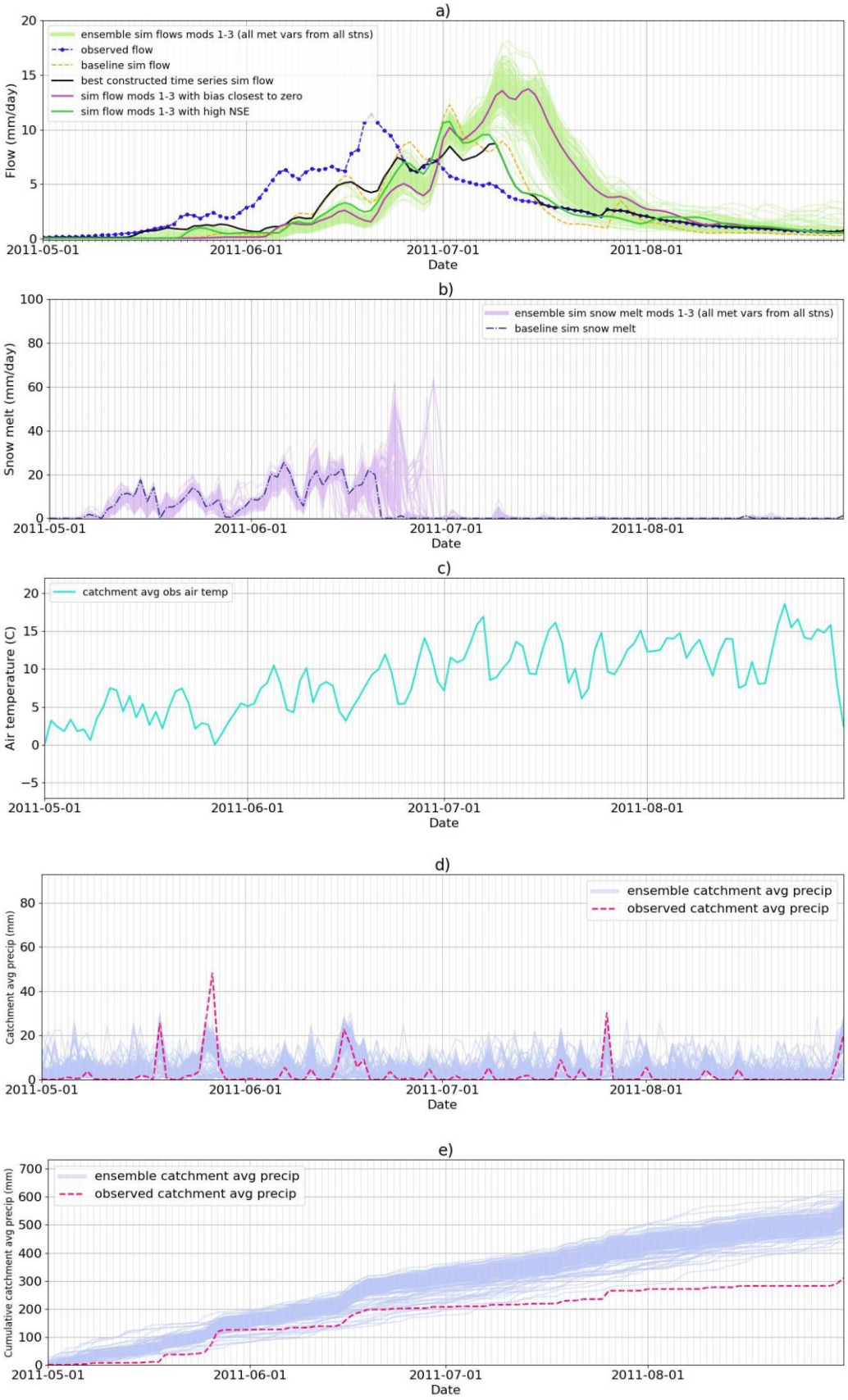

Figure 6.8. As in Figure 6.4 but for 2011.

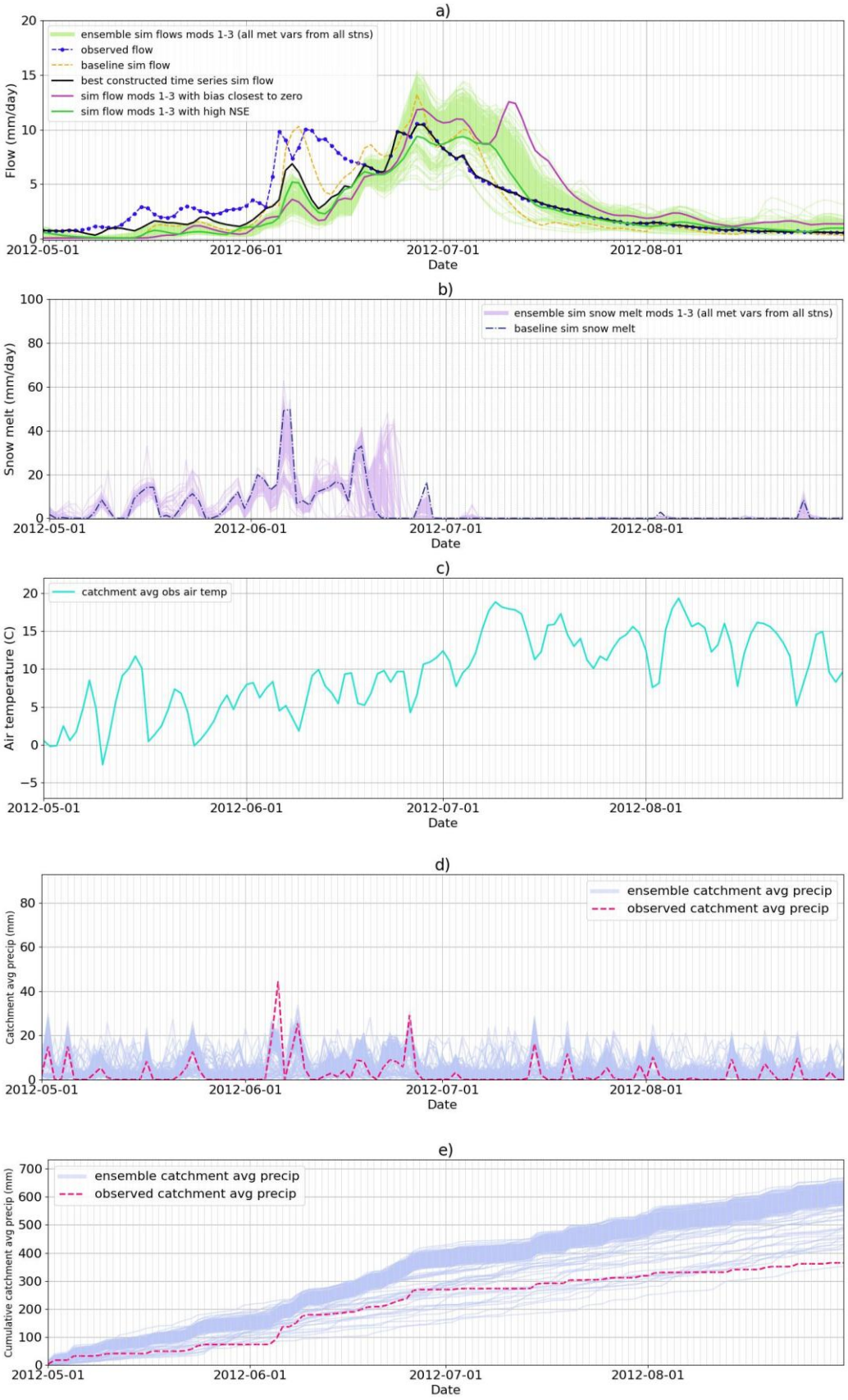

Figure 6.9. As in Figure 6.4 but for 2012.

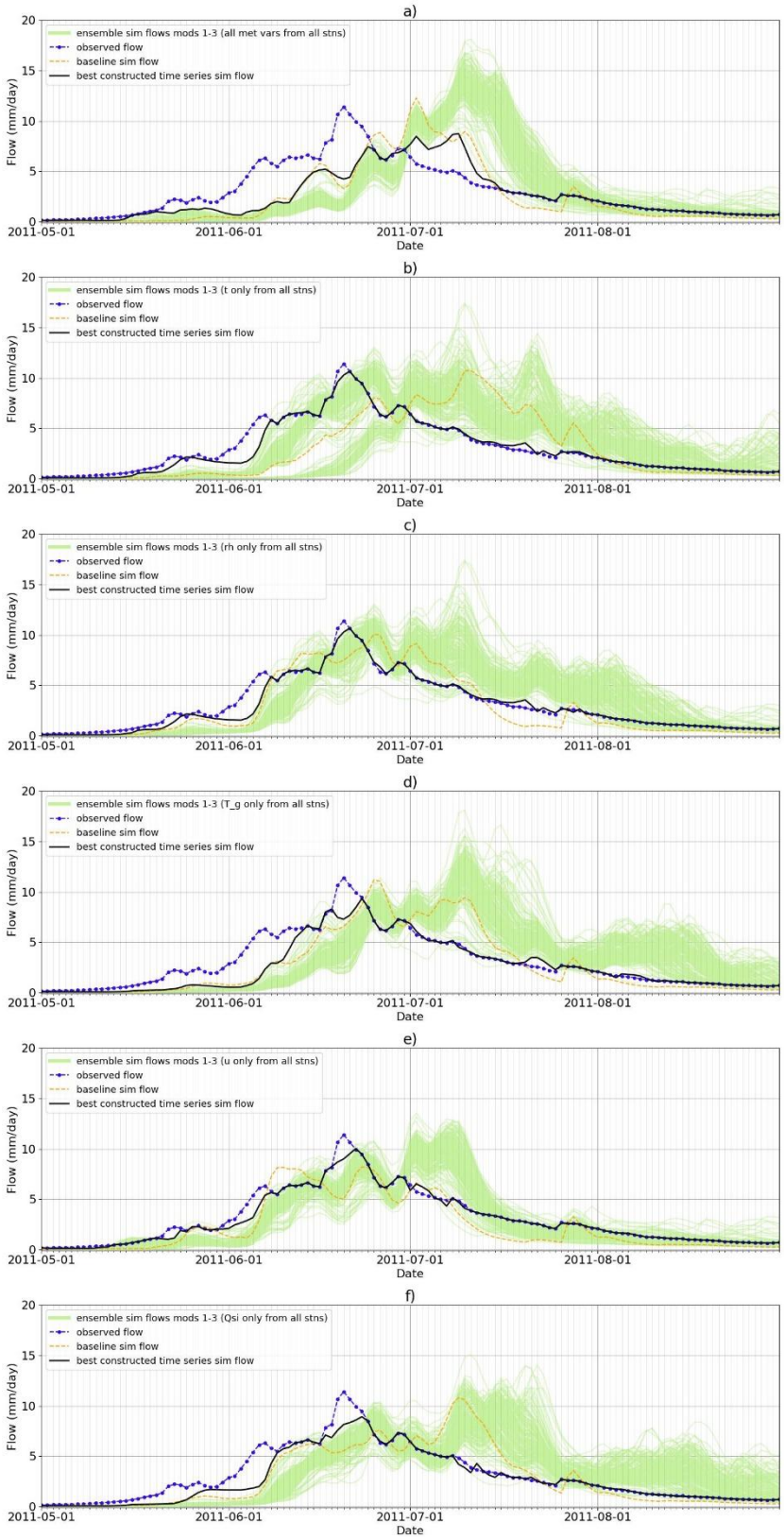

Figure 6.10. CRHM hydrographs for water year 2011 showing: 200-member ensemble simulated flows from RM-mountain generated spatial precipitation fields (modifications 1-3), observed flow, CRHM baseline flow and best constructed time series from ensemble simulated flows. Each plot shows simulation outputs using input meteorological variables for all stations as follows: a) t, rh, T_g, u, Qsi; b) t only; c) rh only; d) T_g only; e) u only; f) Qsi only.

The variability in streamflow outputs demonstrated in Figure 6.10a to Figure 6.10f indicates the sensitivity of the CRHM hydrological model to differences in meteorological variable inputs. Inspection of the streamflow hydrographs in each panel of Figure 6.10 shows a varying spread in the streamflow ensembles, and a very obvious increase in flows in some ensemble members in July and August. To compare the spread in the streamflow ensembles for each scenario represented in Figure 6.10, the range of the streamflow values for each day between June 2011 and August 2011 was calculated (May 2011 was excluded as the range of daily ensemble flows in May is typically much smaller than in June, July and August). The mean of these daily range values was then computed: the mean range is greatest (7.2) when air temperature (t) only is included (Figure 6.10b). The mean range is smallest (4.2) for two scenarios: when all variables are used (Figure 6.10a) and when wind speed (u) only is used (Figure 6.10e). Therefore, it can be seen that the inclusion of wind speed has the biggest impact on reducing the spread in the streamflow ensembles and yields a more 'realistic' rapid recession of flow through July, and much lower flows in August. Since MCRB is a snowmelt dominated catchment largely influenced by snow accumulation and melt in the alpine zone (Fang et al., 2019; Pomeroy et al., 2012), wind speed, particularly at higher elevations, is likely to be influential in simulated catchment responses. To investigate potential reasons why observed wind speed inputs seem to have such an impact on simulated July and August streamflows, observed daily time series of wind speed for May-August 2011 were plotted in Figure 6.11. At Centennial Ridge, the highest elevation station, there are higher wind speed recordings throughout the May-August 2011 period than at any other station. Even the difference between Centennial Ridge (2470 m a.s.l.) and Fisera Ridge (145 m lower at 2325 m a.s.l.) is large; the mean 2011 observed wind speeds at Centennial Ridge and Fisera Ridge are 6.8 m/s and 2.7 m/s, respectively.

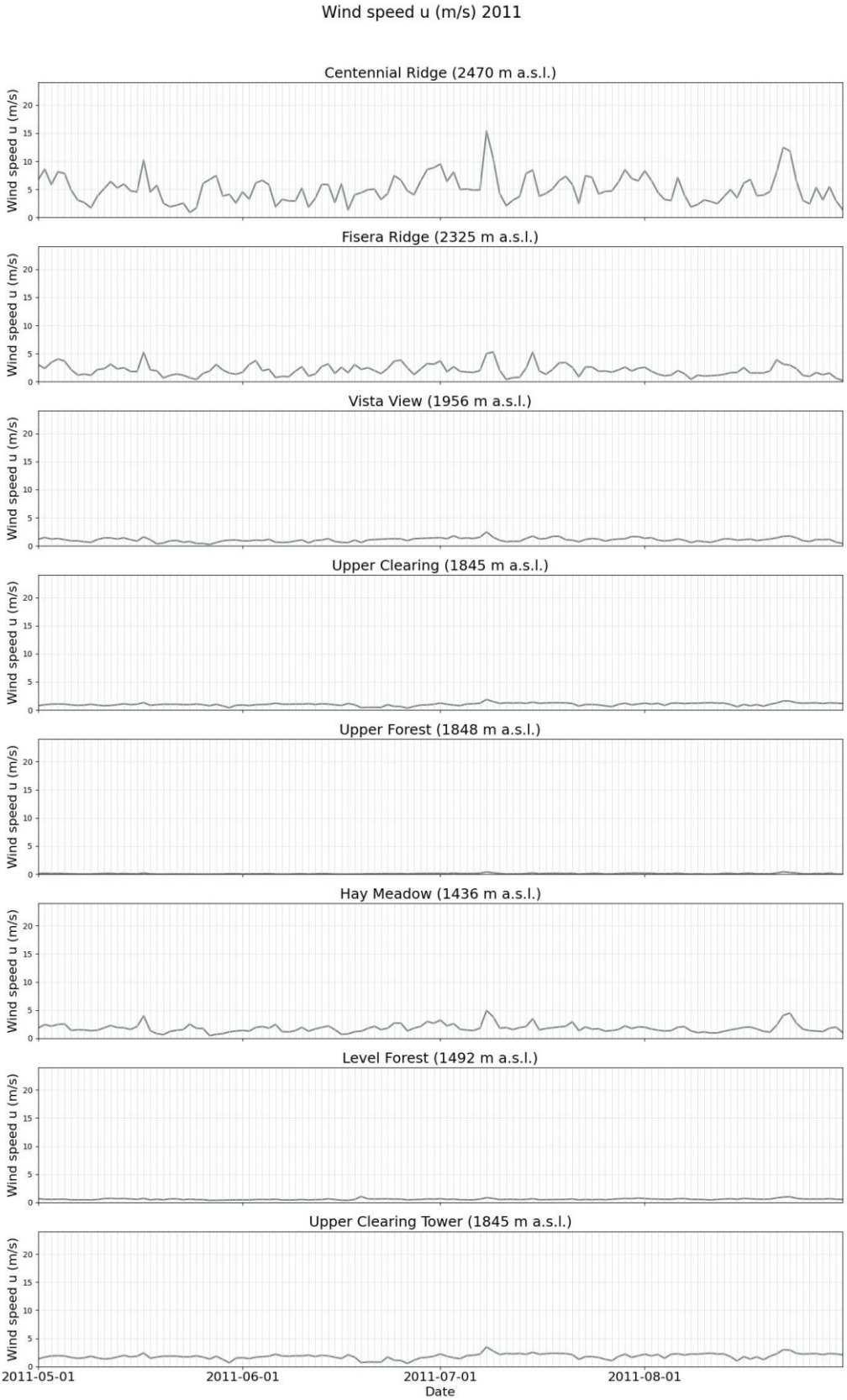

Figure 6.11. Observed daily wind speed for the period May to August 2011, at all stations where records were available

Having evaluated the effects of introducing the observed meteorological variables (air temperature, relative humidity, ground temperature, wind speed and incoming solar radiation) from all stations in turn, and determined that wind speed has the most noticeable impact on streamflow generation in CRHM, it was considered worthwhile to then explore the impact of introducing all of the meteorological variable input data for each additional station in turn in another set of CHRM simulations (data from the main three stations at Fisera Ridge, Upper Clearing and Hay Meadow have been used in all hydrological model simulations). Streamflows from these additional CRHM simulations are presented in Figure 6.12. The first scenario (Figure 6.12a) involves using air temperature, relative humidity, ground temperature, wind speed and incoming solar radiation from all stations (as previously shown in Figure 6.8a). Flows resulting from the introduction of data from Centennial Ridge only, Vista View only, Upper Forest only and Level Forest only, are shown in Figure 6.12b to Figure 6.12e, respectively. As was done for the scenarios presented in Figure 6.10 when introducing the meteorological variable inputs one at a time, to compare the spread in the streamflow ensembles for each scenario in Figure 6.12, the mean of the ensemble daily streamflow ranges (for June 2011 to August 2011) was computed. The means of the daily streamflow ranges when using observed data at Vista View only, Upper Forest only and Level Forest only are the same (6.1). The streamflow ensemble generated using Centennial Ridge observed data (Figure 6.12b) has the same (lower) mean ensemble streamflow range (4.2) as the ensemble using all observed variables from all stations (Figure 6.10a and Figure 6.12a), indicating that observed wind speed data at Centennial Ridge is the most influential in reducing simulated flows in August. In CRHM, wind speed observations are used in the pbsmSnobal module (Table 3.9) which calculates snow transport and sublimation. The sublimation and transport of blowing snow, which can be transported between HRUs, are calculated at every time step using the wind speed, air temperature and relative humidity. As MCRB's hydrology is largely controlled by snow accumulation and melt in the alpine zone at higher elevations (Fang et al., 2019; Pomeroy et al., 2012), the inclusion of wind speed data from the highest elevation station improves CRHM's representation of catchment hydrology in a way that seems evident in the simulation of streamflows. It would appear, from the results of the analysis of CRHM streamflow outputs using different combinations of meteorological observations from additional weather stations, that wind speed recordings at higher elevations have greater influence than other meteorological variables in determining simulated streamflow. The importance of high elevation wind speed data is likely to be a feature worthy of consideration when modelling other mountainous catchments with CRHM.

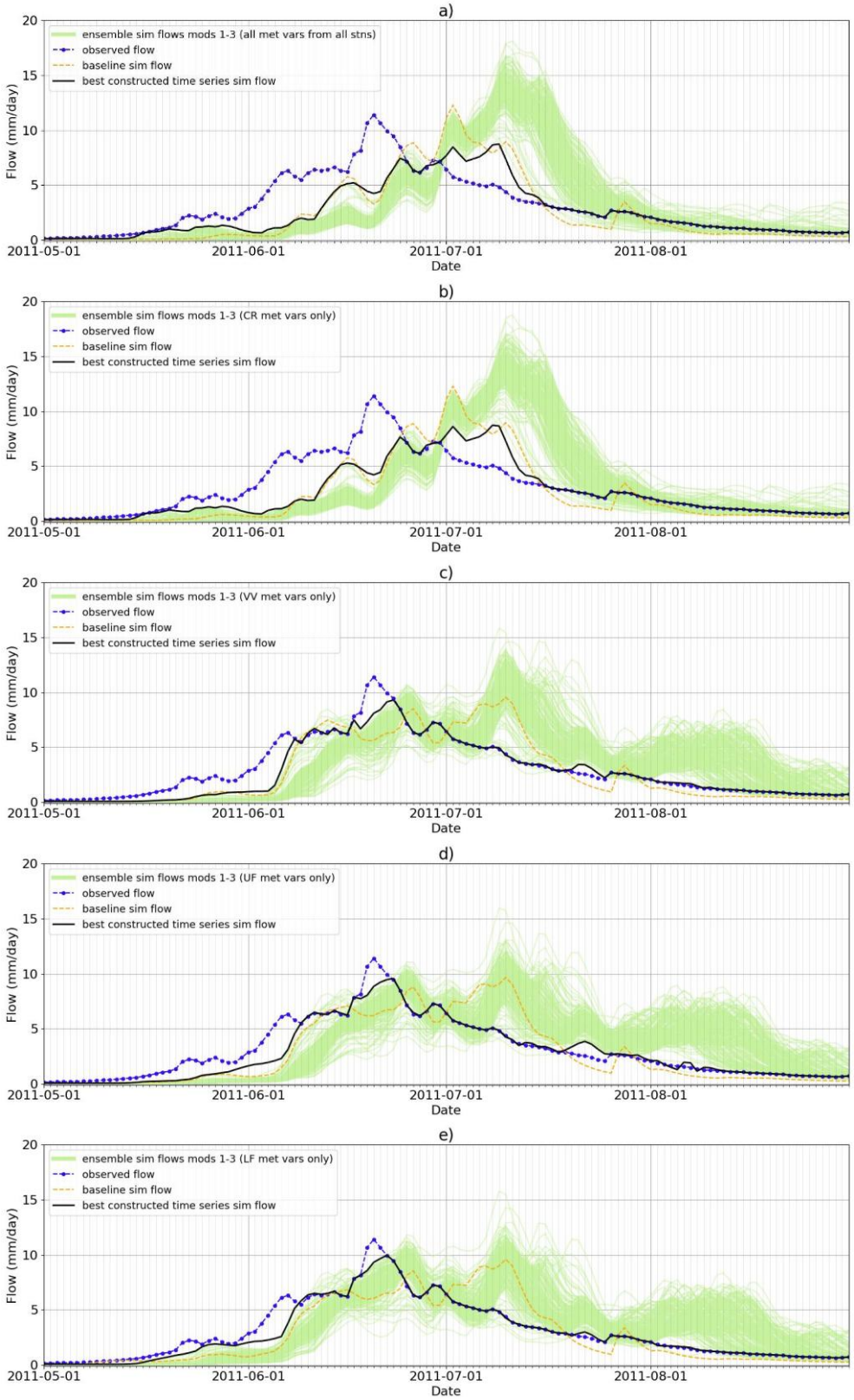

Figure 6.12. CRHM hydrographs for water year 2011 showing: 200-member ensemble simulated flows from RM-mountain generated spatial precipitation fields (modifications 1-3), observed flow, CRHM baseline flow and best constructed time series from ensemble simulated flows. Each plot shows simulation outputs using all input meteorological variables (t, rh, T_g, u, Qsi) as follows: a) all stations; b) Centennial Ridge only; c) Vista View only; d) Upper Forest only; e) Level Forest only

6.2.2 Precipitation inputs from deterministic spatial interpolation methods

CRHM streamflow outputs were also generated using the single daily precipitation time series from each of the deterministic methods (NN, IDW, OK and KED) as precipitation inputs. The CRHM simulations using these four separate precipitation time series used all observed meteorological input data from all available stations. Streamflow bias and NSE values from RM-mountain inputs and the four deterministic methods (Table 6.4) indicate that flows from NN, IDW, OK and KED inputs are typically lower than both observed flows and RM-mountain generated flows. As highlighted earlier in Section 6.2.1, based on streamflow bias values, the best performing of the deterministic techniques is OK, which was plotted with the RM-mountain ensemble, CRHM baseline and observed flows in Figure 6.2. Taking the metric values in Table 6.4 and the OK hydrographs in Figure 6.2 together, it is apparent that CRHM-simulated flows from deterministic method precipitation inputs are typically lower than observed flows and RM-mountain generated flows. As discussed in Section 6.2.1, the NN, IDW, OK and KED techniques simulate zero precipitation across the entire model domain on days when gauges are dry; in contrast, RM-mountain can simulate precipitation on dry gauge days, contributing to much higher catchment average precipitation amounts and hence higher streamflows. The bias and NSE metric values in Table 6.4 indicate the extent to which the deterministic methods underestimate spatial precipitation, with large negative streamflow bias values between -54.01 (KED) and -46.15 (OK), compared with a small positive bias of 1.88 from the best constructed timeseries from the RM-mountain driven streamflow ensemble.

Table 6.4. Bias and NSE metric values calculated from observed and CRHM-simulated streamflows from CRHM baseline and deterministic spatial interpolation method precipitation inputs

RM-mountain 200-member ensemble	**Bias**	**NSE**
Best constructed time series mod 1	16.27	0.82
Best constructed time series mods 1&2	-1.50	0.61
Best constructed time series mods 1-3	1.88	0.74
Best performing ensemble members mod 1	-10.36	0.60
Best performing ensemble members mods 1&2	14.40	0.18
Best performing ensemble members mods 1-3	7.54	0.35
Deterministic spatial interpolation method		
CRHM baseline	2.04	0.54
NN	-49.11	0.25
IDW	-46.79	0.25
OK	-46.15	0.25
KED	-54.01	0.34

6.3 Conclusions

The aim of this chapter was to explore the performance of RM-mountain generated spatial precipitation fields when used as time series inputs to CRHM, comparing CRHM outputs, particularly streamflow and snowmelt, with the HBV model outputs discussed in Chapter 5. The best constructed time series and best performing RM-mountain ensemble members yield improved bias values and higher NSE values than the deterministic techniques and the CRHM baseline scenario (Table 6.4), in which observed point precipitation data is spatially distributed by assigning the nearest station to each of the 36 HRUs. Using a best constructed time series approach yields a best bias value of 1.88. The bias values resulting from RM-mountain precipitation inputs show a noticeable improvement compared with bias values from CRHM baseline (2.04), NN (-49.11), IDW (-46.79), OK (-46.15) and KED (-54.01). In both winter and summer, RM-mountain simulates more precipitation across the catchment than is derived from the average of the observed amounts. Comparison, for water years 2006 to 2012, of mean observed winter catchment average precipitation at Fisera Ridge, Upper Clearing and Hay Meadow stations (2577 mm) and RM-mountain simulated ensemble catchment average precipitation (4275 mm), showed simulated amounts exceeded observations by 66%. When comparing observed (839 mm) and simulated (1211 mm) catchment average summer precipitation, there is a 44% increase. The percentage of wet days in the RM-mountain ensemble is also more than the observed percentage of wet days. In winter, the percentage of observed wet days (days with recorded precipitation, either rainfall or snowfall) is 64% and the ensemble mean percentage is 87%. In summer, the observed wet day percentage is 50%, while the simulated summer wet day percentages are much greater, with an ensemble mean of 81%. In contrast to deterministic spatial interpolation techniques, the random mixing method can generate spatial fields with precipitation in parts of the catchment on days when the gauge locations are dry. The RM-mountain technique allows for the more realistic possibility of small bands of precipitation, as experienced during convective summer storms, that pass between and around the gauge locations, which is a likely explanation of the increase in the percentage of wet days in the ensemble, and hence the higher winter and summer precipitation totals in the simulated ensemble, compared to the observations. RM-mountain modification 1, where random sampling from the full time series of observed precipitation data was introduced to enable robust spatial copula fitting, also increases the likelihood of a higher number of simulated wet days than observed wet days. This is likely to be most evident in winter when there are more wet days (i.e., days with precipitation), and at lower elevations where observed

dry day probabilities are greater than 0.5. Wind speed observations play an important role in CRHM's physically-based snowmelt module and, as MCRB is a snowmelt dominated catchment, the impact of the largest magnitude wind speed observations at the highest elevation station is apparent in improving simulation of streamflows.

This chapter has demonstrated that a best constructed time series from the CRHM-simulated streamflow ensemble, driven by RM-mountain generated spatial precipitation inputs, shows better performance than the CRHM baseline setup and four deterministic spatial interpolation methods (NN, IDW, OK, KED) when measured using streamflow bias and NSE metrics. It has also been shown that, due to the physical basis of CRHM and the way cold regions processes such as snowmelt are represented, streamflow simulation in CRHM is much more sensitive to observed meteorological input data that the simpler setup in HBV.

Chapter 7. Discussion and further work

7.1 Discussion of results

This thesis set out to develop RM-mountain, a new version of the random mixing method, based on RMWSPy (Hörning & Haese, 2021), to improve its suitability for generating spatial precipitation fields in a sparsely gauged mountain catchment, Marmot Creek Research Basin (MCRB) in the Canadian Rockies (research objectives O1 to O3, Section 1.3). The time series datasets generated using RM-mountain were then used as precipitation inputs for two very different hydrological models: the conceptual Hydrologiska Byråns Vattenbalansavdelning (HBV) and the physically-based Cold Regions Hydrological Model (CRHM), to explore the performance of the precipitation fields by evaluating hydrological model outputs, particularly streamflow and snowmelt (research objective O4 to O7, Section 1.3).

The initial spatial precipitation fields produced using the existing RMWSPy technique were low variance fields that were of a lower quality than spatial fields generated using more traditional deterministic spatial interpolations methods, Nearest Neighbour (NN), Inverse Distance Weighting (IDW), Ordinary Kriging (OK) and Kriging with External Drift (KED), which have been demonstrated in this thesis as inadequate for use in the sparsely gauged mountainous MCRB. As a consequence, modifications to the RMWSPy technique were required to improve its suitability for a small, mountain catchment. Modification 1, time series sampling, which is fundamental to the method, was introduced as a feasible way of increasing the number of precipitation gauge observations that could be used for random sampling in a sparsely gauged catchment, to generate a robust spatial relationship between gauge locations and hence across the study area (research objective O3). Modification 2, for elevation dependence, and modification 3, for seasonality, further improved the spatial precipitation fields generated, increasing field variance. Leave-one-out cross-validation reinforced the conclusion that combining modifications 1-3 maximised the likelihood of simulating realistic spatial precipitation fields (research objective O4). Also, leave-one-out cross-validation precipitation amounts calculated for Fisera Ridge, Upper Clearing and Hay Meadow station locations using RM-mountain with modifications 1-3 were closer to observed precipitation values than those computed using the NN, IDW, OK and KED techniques. This is a clear indication that the RM-mountain method yields improved estimates of time series precipitation data in a mountain catchment compared to the other techniques used in this research.

In this thesis, it has been demonstrated that, compared to four other spatial interpolation techniques, the RM-mountain method generates improved quality, high resolution time series spatial precipitation fields using observations from only three gauge locations. The relatively simple approaches used in deterministic methods of spatial interpolation, mean they are more reliable when the distances between gauge locations is relatively small. However, in mountainous regions, where gauge density is typically much less than at lower elevations (Frei & Schär, 1998), distances between gauges can be many kilometres. In addition, traditional interpolation methods do not take account of the rapidly changing topography of mountain regions (Mair & Fares, 2011). In contrast, RM-mountain has been developed to specifically account for greater distances between gauges in its spatial covariance curve fitting approach, and has the functionality to incorporate data from more distant gauges for establishing spatial dependence. Also, RM-mountain accounts much more effectively for mountain topography in its application of elevation gradients (modification 2) when calculating precipitation amounts for each model grid cell, based on Digital Elevation Model (DEM) data. In summary, RM-mountain is better able to estimate spatial precipitation data than other techniques due to its representation of spatial dependence and elevation changes within a study area. While access to observations from a larger number of gauges is beneficial (Hörning, 2016), the results presented in this thesis show that RM-mountain can be used successfully with precipitation data from only three locations.

While randomly sampling from the full time series of observations (modification 1) successfully achieved the aim of increasing the variance of spatial precipitation fields, it did mean that, instead of sampling from observations at each separate time step only, the RM-mountain method samples from a range of randomly selected time steps across the full time series. A potential consequence of this is that, on the days of heaviest precipitation, the RM-mountain algorithm samples not only from observations on those high precipitation days, but also uses observations from days with lower observed precipitation. The observations at the gauge locations are reproduced by the random mixing method at every time step. However, calculating simulated catchment average precipitation across the entire 50 m x 50 m resolution model grid revealed that simulated values were lower than averages calculated from observations on the four wettest days in the 2005-2012 time series: 17.06.2007, 24.05.2008, 27.05.2011 and 06.06.2012. On each of these four dates, not only were very high precipitation amounts observed, but they were immediately preceded and/or followed by low or zero

precipitation days where the percentage difference between days was 80% or greater. These heavy precipitation days drive rapid increases in runoff, especially in June 2007 and May 2008.

Simulated HBV baseline flows were generated using spatial precipitation inputs obtained from a variation of the MicroMet approach (Liston & Elder, 2006) incorporating IDW using gauge observations at Fisera Ridge, Upper Clearing and Hay Meadow stations. CRHM baseline flows were obtained using the same observations, interpolated by CRHM by assigning the nearest station to each hydrological response unit (HRU). These baseline flows, which follow the same pattern of timings in HBV and CRHM simulations, in terms of when they either exceed or fall below the ensemble flows, are typically above the modified streamflow ensemble on the high precipitation days immediately preceded and/or succeeded by very low/zero precipitation days. The way in which the algorithm computes precipitation for such days requires further investigation, and development of the RM-mountain technique to resolve this issue.

Unlike deterministic spatial interpolation techniques, the RM-mountain method has the potential advantage of being able to simulate precipitation across the model domain on days when there is no observed precipitation at the gauge locations, allowing for the possibility of representing bands of precipitation that pass between and around the gauge locations. In MCRB, this is especially relevant in summer, when smaller scale convective rain storms are most likely (Fang & Pomeroy, 2016). The presence of simulated precipitation on observed dry days, which in this study is days on which recorded precipitation is less than 0.1 mm, means that the RM-mountain simulated daily catchment average precipitation amounts are noticeably higher than those derived solely from the gauge observations. Clearly, the number of simulated wet days is also higher than the number of observed wet days. In comparison, RM-mountain generated catchment average precipitation amounts are noticeably higher than those resulting from the baseline methods employed by the hydrological models, and from the four deterministic techniques. Again, the impacts of RM-mountain modification 1 must be considered: sampling from the full observed precipitation time series at the gauge locations also increases the likelihood of more wet days being simulated. This is especially true in winter when the percentage of observed wet days (rainfall and snowfall) is highest, and at lower elevations where there are more days of observed rainfall than at the higher elevation stations.

The HBV simulation outputs exhibited little variation in the streamflow ensemble, as HBV demonstrated comparatively little sensitivity to changes in precipitation inputs, which is consistent with the relatively simple structure of the conceptual HBV model. In contrast, the hydrograph patterns produced by CRHM reveal distinct streamflow variations. In May, when snowmelt is the primary contributor to runoff, CRHM underestimates flows as snow is released from snowpack more gradually than in HBV simulations, where streamflows in May are higher than observed flows. The difference in snowmelt patterns is mainly due to the ways snowmelt is represented in the two hydrological models. The SnobalCRHM snowmelt module in CRHM uses an energy balance approach in which snowmelt is calculated when accumulated energy > cold content or when cold content > 0 (cold content is the energy needed to bring the snow cover temperature up to 0ºC). Runoff is estimated when the accumulated melt and liquid H_2O content exceed a specified threshold. This is a much more sophisticated technique than the single threshold temperature method used in HBV, which resulted in the early release of snow from the accumulated winter snowpack, with the onset of snowmelt initiated as soon as the observed air temperature exceeded 0ºC. A consequence of the sophisticated physically-based modular structure of CRHM with its many parameters is that, particularly in the SnobalCRHM snow melt module, simulated streamflows are more sensitive to changes in parameter values than in the simpler conceptual HBV model.

To identify 'best' model performance, a best constructed time series approach was conceived, which identified the ensemble member with the lowest bias at each time step, combining them to create a single final time series. The validity of this approach lies in the fact that each day's spatial fields are random and the observed precipitation values for a given specific day are used as conditioning constraints in generating the spatial field, hence fields for each time step are interchangeable. The best performing individual ensemble members for low bias and high NSE were also identified, but these were outperformed by the best constructed time series. Combining modifications 1-3 resulted in the most important improvements in reducing streamflow bias and increasing NSE compared to observed flows, as the inclusion of elevation gradients (modification 2) and seasonal characteristics in observed precipitation and spatial dependence (modification 3) increased the likelihood of simulating realistic spatial precipitation fields within the generated 200-member ensemble. In this study, spatial precipitation fields were simulated for each time step using observed data from three precipitation gauges as constraints on the random fields generated. It is suggested that the RM-mountain technique should not be used with fewer than three gauges. However, where observed

precipitation values are available from more than three gauge locations within a catchment, this should increase the likelihood that, for each individual time step, the simulated precipitation values across the ensemble are more likely to represent 'reality'. This in turn increases the likelihood that the single best performing ensemble member, as identified using NSE and bias metrics, will yield simulated flows that more closely match observed flows. This may reduce the importance of the best constructed time series approach, and is a feature that could be explored in possible future work.

HBV streamflows generated using the RM-mountain method showed closer alignment with observed flows (streamflow bias = 0.14, NSE = 0.96) than those generated using the four deterministic spatial precipitation interpolation techniques, NN, IDW, OK and KED (for NN and IDW, streamflow bias = -27.56, NSE = 0.80). Notably, in July and August, when precipitation rather than snowmelt primarily drives runoff, the RM-mountain method provided streamflows that more closely matched observations compared to those produced by the NN, IDW, OK, and KED methods. CRHM streamflows resulting from RM-mountain precipitation inputs were also closer to observed flows (streamflow bias = 1.88, NSE = 0.74) than flows from NN, IDW, OK and KED precipitation inputs (for OK, streamflow bias = -46.15, NSE = 0.25). The traditional deterministic methods of spatial interpolation have the advantage of simplicity and they require less computing power than stochastic methods like RM-mountain. However, compared to NN, IDW, OK and KED, RM-mountain has the advantages of generating multiple realisations of precipitation fields in an ensemble (rather than just a single realisation) which enables uncertainty analysis, increased spatial resolution, improved spatial covariance (Mair & Fares, 2011), elevation gradients and the ability to incorporate seasonal differences in precipitation patterns and spatial relationships. From the application of RM-mountain to MCRB, it is concluded that RM-mountain is an improvement on these other spatial interpolation techniques.

The performance of the CRHM model, particularly its use of RM-mountain precipitation data, highlights certain factors influencing hydrological modelling in mountainous regions. It was anticipated that, compared with HBV, the physically-based CRHM would better utilise RM-mountain precipitation inputs, given its design to represent cold regions processes and meteorological interactions. CRHM simulation outputs suggest that antecedent conditions, not only of soil moisture and snowpack (Fang & Pomeroy, 2016), but also of the pattern and spatial distribution of precipitation, play a more critical role than initially expected. This finding points

to the importance of considering antecedent soil moisture, snowpack and precipitation conditions together, and how they influence runoff generation. A key assumption in the best constructed time series approach, by which the ensemble member that generates the flow closest to the observed flow for each time step is identified, is that the influence of only the spatial precipitation field on simulated flow is considered for any given time step. The influence of antecedent soil moisture or snowpack, which also impact on the hydrology, are not accounted for in the selection of the best performing ensemble member for that time step. The inclusion of hydrological model outputs for soil moisture and snow pack at each time step in the selection of the best performing ensemble member would be a more thorough approach to take. A more sophisticated modelling approach could involve 'hot-starting,' where daily precipitation fields and antecedent soil moisture and snowpack conditions are fixed before progressing to the next simulation day. However, implementing such an approach in CRHM was overly challenging for the scope of this thesis, hence it remains an area for potential future research and model development. Relative to HBV, CRHM is a more much complex, physically-based hydrological model which, from the findings of this study of Marmot Creek Research Basin (MCRB), is highly sensitive to changes in input meteorological variable data: precipitation (and the method by which it is spatially distributed across the catchment), air temperature, relative humidity, ground temperature, wind speed and incoming solar radiation. Wind speed is one of the most influential variables but it is not plausible to calibrate a hydrological model to a subset of input data. Calibrating a hydrological model using only selected input variables in order to achieve 'better' streamflow outputs, i.e. to generate more realistic hydrographs and to reduce the bias between simulated and observed flows, is likely to result in 'over-fitting', which can increase modelling uncertainty and generate unreliable outputs. Although sensitivity test simulations were run using each meteorological variable (air temperature, relative humidity, ground temperature, wind speed and incoming solar radiation) in turn, as well as adding data from each of the additional stations (Centennial Ridge, Vista View, Upper Forest and Lower Forest) one station at a time, ultimately results from hydrological model simulations where all meteorological inputs from all stations were used are the most relevant. Nevertheless, it is important to note CRHM's sensitivity to changes in input data, as identified by the sensitivity test runs. MCRB is a small mountainous catchment where hydrology is heavily dominated by snowmelt in the spring and early summer months. However, in July and August, precipitation as rainfall is the main driver of streamflow and, as was identified in Section 6.2.1, summer precipitation fields from RM-mountain, across a 200-member ensemble, have an average of 62% more wet days than observed. Also, the RM-mountain simulated summer catchment

average precipitation is 44% higher than observed summer precipitation. In a small catchment like MCRB, using the physically-based CRHM hydrological model with its high sensitivity to differences in meteorological input data, an increase in the number of wet days, compounded by higher catchment average precipitation, results in large differences in runoff between simulated ensemble streamflows and observed flows.

In hydrological modelling, a longstanding debate persists around the use of simpler conceptual models such as HBV versus more complex physically-based models like CRHM, particularly in terms of their ability to handle uncertainty. The issue of equifinality (Beven & Binley, 2014), where multiple models or parameter sets can produce equally acceptable results, suggests that no single "true" model can be produced for a given catchment. Simpler conceptual models like HBV are sometimes said to yield "the right answers for the wrong reasons" due to their reliance on optimisation of parameter values rather than more realistic representation of physical processes. HBV model outputs for MCRB in Chapter 5 showed simulated streamflows largely consistent with observed flows, even with increased input precipitation data from RM-mountain compared to other spatial interpolation techniques. This consistency between simulated and observed flows was supported by improved streamflow bias values (0.14) and increased Nash-Sutcliffe Efficiency (NSE) values up to 0.96. Conversely, physically-based models like CRHM, which attempt to simulate detailed processes, are sometimes thought to give "the wrong answers for the right reasons," as they are more sensitive to input data (Beven, 2006). CRHM simulated outputs for MCRB showed a greater spread of ensemble streamflows, the magnitudes of which were sensitive to increases in precipitation inputs from RM-mountain, as well as to changes in observed meteorological variable input data. The best improvement in streamflow bias achieved from CRHM outputs was less than from HBV (absolute bias of 1.88 for CRHM versus 0.14 for HBV) and the improvement in NSE was also less (0.74 from CRHM versus 0.96 from HBV). Both conceptual and physically-based models are subject to sources of uncertainty, including model structure, parameterisation, and data errors. Despite the more sophisticated physical basis of more advanced hydrological models, they remain susceptible to errors, which can reduce their predictive reliability compared to simpler models. While physically-based models aim for better representation of underlying processes, their outputs are not always superior to those of conceptual models, especially where there may be issues surrounding the quality and/or quantity of observed data inputs (Beven & Binley, 2014). The results presented in this thesis suggest that, for a sparsely gauged mountain catchment, even with the input of additional meteorological observations from other weather stations, there is

greater uncertainty and variability in CRHM simulated hydrographs than in HBV generated streamflows. Reducing uncertainty in streamflow calculation, as demonstrated in this thesis with HBV, implies that, depending on the modeller's understanding of the catchment and the quantity and quality of observed meteorological data, using a simpler hydrological model structure can yield reliable results for water resource planning. Nevertheless, using RM-mountain spatial precipitation field inputs improves simulated streamflows in both conceptual (HBV) and physically-based (CRHM) models, compared to streamflows driven by traditional methods of interpolation of precipitation between point observations.

The findings of this research suggest that the RM-mountain method, which improves the suitability of the existing RMWSPy technique for a sparsely gauged mountain catchment, does yield enhanced estimates of spatial precipitation, compared to deterministic spatial interpolation techniques. RM-mountain represents a positive advancement in the estimation of spatial precipitation in sparsely gauged mountain regions that has positive implications for hydrological modelling of mountain regions, including the potential to increase the accuracy of water resource planning and forecasting of floods and droughts (Beck et al., 2017). It is anticipated that, with further developments as summarised in Section 7.3, RM-mountain has the capability to produce even better results than those demonstrated in this thesis.

7.2 Conclusions

For the small, sparsely gauged, mountainous MCRB catchment, the unmodified RMWSPy technique generated low variance spatial precipitation fields that performed less well than traditional deterministic methods NN, IDW, OK and KED. To enhance the random mixing method for use in a sparsely gauged mountain region, RM-mountain was developed, via three key modifications. Modification 1 enables random sampling from the full time series of precipitation observations for spatial copula fitting, resulting in an improved spatial covariance relationship for each time step. The introduction of modification 1 increased variance, thereby resulting in more plausible precipitation fields. The addition of modification 2 for elevation dependence and modification 3 for seasonality further increased the variance of simulated spatial precipitation fields, as well as maximising the likelihood of simulating more realistic precipitation values, as demonstrated by the results of the leave-one-out cross-validation exercise. RM-mountain simulates more precipitation across the catchment than is derived from the average of the observed amounts, by a margin of 44% in summer and 66% in winter. These increases are due to the ability of RM-mountain to generate precipitation in parts of the

catchment on days when the gauge locations are dry, in contrast to the deterministic techniques which simulate zero precipitation across the entire model domain on days when the gauges are dry. The RM-mountain technique allows for the more realistic possibility of small bands of precipitation, as experienced during convective summer storms, that pass between and around the gauge locations. RM-mountain modification 1 also increases the likelihood of a higher number of simulated wet days than observed wet days as, on days when gauges are dry, it randomly samples from a mixture of dry days and wet days.

RM-mountain precipitation inputs resulted in improved streamflows, compared with observed flows, in both HBV and CRHM hydrological model simulations. With HBV, best constructed time series and best performing individual ensemble member streamflow hydrographs yielded improved bias values and higher NSE values than any of the HBV baseline, NN, IDW, OK or KED generated precipitation fields. Also, in July and August of each water year from 2007 to 2012, when runoff is driven mainly by precipitation rather than by snowmelt, ensemble streamflows from RM-mountain generated precipitation inputs more closely matched observed streamflow than the flows generated by precipitation inputs from NN, IDW, OK and KED. Similarly, using CRHM, the best constructed time series and best performing RM-mountain ensemble members yielded improved bias values and higher NSE values than the deterministic techniques and the CRHM baseline scenario.

The variation within the HBV-simulated streamflow ensemble is less than in the CRHM-generated ensemble, due to the differences in model complexity and CRHM's greater sensitivity to changes in meteorological input data, most notably precipitation and wind speed. Observations of the latter play an important role in CRHM's physically-based snowmelt module and, as MCRB is a snowmelt dominated catchment, the impact of the largest magnitude wind speed observations at the highest elevation station is apparent in improving simulation of streamflows.

To conclude, the modifications made to the RMWSPy technique in developing the RM-mountain method result in improved spatial precipitation fields compared with Nearest Neighbour, Inverse Distance Weighting, Ordinary Kriging and Kriging with External Drift techniques for the small, mountainous Marmot Creek Research Basin. As demonstrated by hydrograph plots, reduced streamflow bias and increased Nash-Sutcliffe Efficiency values from HBV and CRHM hydrological model simulations, the best constructed time series simulated

hydrographs from RM-mountain precipitation inputs more closely match observed streamflows than flows generated by any of the other spatial interpolation methods considered.

7.3 Future work

Results presented in this thesis have demonstrated a technique for improving estimation of spatial precipitation patterns in a mountain region. There are areas of improvement and development of the RM-mountain method, from random sampling of observed precipitation data to enhancing the algorithm to explore high precipitation extremes in more depth. A potential way of further exploring CRHM's sensitivity to changes in meteorological input data is also considered.

In the current RM-mountain algorithm, the user selects the size of the subset of observations used in spatial copula fitting, say 1000 days, and these subsets are then sampled randomly. An area of further work would be to explore how the modification 1 time series random sampling technique could be developed. For example, a feasible approach could be to check the observations for each day in the time series and, in selecting the subset of observations to sample from for that day, apply upper and lower bounds around that day's values so that the subset contains observations more similar to the day in question.

To more comprehensively represent antecedent soil moisture, snowpack and precipitation conditions and how they influence simulation of surface runoff in CRHM, it could be advantageous to introduce a 'hot-starting,' approach in which, for each time step, spatial precipitation fields and antecedent soil moisture and snowpack conditions are fixed before moving on to simulate the next time step in the series. It is anticipated that this process would involve modification of the core CRHM model code which would require collaboration with the Centre for Hydrology at the University of Saskatchewan.

So far, the new RM-mountain method has been tested on only one mountain catchment. To evaluate its potential to be used more widely, applying the technique to another sparsely gauged mountain catchment, in a different mountainous region, would also enable further development and refinement of the RM-mountain technique. Using the spatial precipitation fields generated for a second catchment as inputs to HBV and CRHM, and exploring the hydrological model outputs, could shed additional light on the performance of the RM-mountain generated fields, again compared with the performance of spatial fields from deterministic methods.

Another area of future work would be to stratify precipitation observations into intensity bands and generate probability density functions (pdfs) for those separate bands, similar to the approach taken in this study to represent seasonal precipitations patterns. It would then be possible to randomly sample from these intensity band distributions to generate new sets of spatial precipitation fields to be used for additional hydrological modelling to explore in more depth the impact of different precipitation intensities, particularly the highest precipitation extremes.

Also not achieved in this study, but a potentially useful approach to pursue, is the application of climate change factors to precipitation fields before using the fields as hydrological model inputs, to investigate potential future high and low flows in a mountain catchment. Such additional development of the RM-mountain method, which enables generation of higher spatial resolution datasets than precipitation fields from climate model projections, could further enhance its usefulness for enabling improved hydrological modelling of future water resource and flooding or drought events in MCRB and other sparsely gauged mountain catchments.

References

Adam, J.C., Clark, E.A., Lettenmaier, D.P. & Wood, E.F. (2006) 'Correction of Global Precipitation Products for Orographic Effects', *Journal of Climate*, 19(1), pp. 15–38.

Bárdossy, A., Anwar, F. & Seidel, J. (2020) 'Hydrological Modelling in Data Sparse Environment: Inverse Modelling of a Historical Flood Event', *Water (Switzerland)*, 12(11), .

Bárdossy, A. & Hörning, S. (2016) 'Random Mixing: An Approach to Inverse Modeling for Groundwater Flow and Transport Problems', *Transport in Porous Media*, 114(2), pp. 241–259.

Bárdossy, A., Kilsby, C., Birkinshaw, S., Wang, N. & Anwar, F. (2022) 'Is Precipitation Responsible for the Most Hydrological Model Uncertainty?', *Frontiers in Water*, 4p. 836554.

Bárdossy, A. & Pegram, G. (2013) 'Interpolation of precipitation under topographic influence at different time scales', *Water Resources Research*, 49(8), pp. 4545–4565.

Beck, H.E., van Dijk, A.I.J.M., Levizzani, V., Schellekens, J., Miralles, D.G., Martens, B. & de Roo, A. (2017) 'MSWEP: 3-hourly 0.25° global gridded precipitation (1979–2015) by merging gauge, satellite, and reanalysis data', *Hydrology and Earth System Sciences*, 21(1), pp. 589–615.

Beck, H.E., Wood, E.F., McVicar, T.R., Zambrano-Bigiarini, M., Alvarez-Garreton, C., Baez-Villanueva, O.M., Sheffield, J. & Karger, D.N. (2020) 'Bias Correction of Global High-Resolution Precipitation Climatologies Using Streamflow Observations from 9372 Catchments', *Journal of Climate*, 33(4), pp. 1299–1315.

Bergström, S. (1976) 'Development and Application of a Conceptual Runoff Model for Scandinavian Catchments', *SMHI Norrköping, Report RH07*, p. 154.

Bergström, S. (1992) *The HBV model – its structure and applications*. SMHI.

Bernhardt, M. & Schulz, K. (2010) 'SnowSlide: A simple routine for calculating gravitational snow transport', *Geophysical Research Letters*, 37(11), .

Beven, K. (2006) 'A manifesto for the equifinality thesis', *Journal of Hydrology*, 320(1), pp. 18–36.

Beven, K. & Binley, A. (2014) ‘GLUE: 20 years on’, *Hydrological Processes*, 28(24), pp. 5897–5918.

Borges, P. de A., Franke, J., da Anunciação, Y.M.T., Weiss, H. & Bernhofer, C. (2016) ‘Comparison of spatial interpolation methods for the estimation of precipitation distribution in Distrito Federal, Brazil’, *Theoretical and Applied Climatology*, 123(1), pp. 335–348.

Buitink, J., Melsen, L.A., Kirchner, J.W. & Teuling, A.J. (2020) ‘A distributed simple dynamical systems approach (dS2 v1.0) for computationally efficient hydrological modelling at high spatio-temporal resolution’, *Geoscientific Model Development*, 13(12), pp. 6093–6110.

Burton, A., Kilsby, C.G., Fowler, H.J., Cowpertwait, P.S.P. & O’Connell, P.E. (2008) ‘RainSim: A spatial–temporal stochastic rainfall modelling system’, *Environmental Modelling & Software*, 23(12), pp. 1356–1369.

Buytaert, W., Celleri, R., Willems, P., Bièvre, B.D. & Wyseure, G. (2006) ‘Spatial and temporal rainfall variability in mountainous areas: A case study from the south Ecuadorian Andes’, *Journal of Hydrology*, 329(3), pp. 413–421.

Calvin, K., Dasgupta, D., Krinner, G., Mukherji, A., Thorne, P.W., Trisos, C., Romero, J., Aldunce, P., Barrett, K., Blanco, G., Cheung, W.W.L., Connors, S., Denton, F., Diongue-Niang, A., Dodman, D., Garschagen, M., Geden, O., Hayward, B., Jones, C., et al. (2023) *IPCC, 2023: Climate Change 2023: Synthesis Report. Contribution of Working Groups I, II and III to the Sixth Assessment Report of the Intergovernmental Panel on Climate Change [Core Writing Team, H. Lee and J. Romero (eds.)]. IPCC, Geneva, Switzerland.*

Caruso, B.S., Rademaker, M., Balme, A. & Cochrane, T.A. (2013) ‘Flood modelling in a high country mountain catchment, New Zealand: comparing statistical and deterministic model estimates for ecological flows’, *Hydrological Sciences Journal*, 58(2), pp. 328–341.

Cowpertwait, P.S.P., O’Connell, P.E., Metcalfe, A.V. & Mawdsley, J.A. (1996) ‘Stochastic point process modelling of rainfall. II. Regionalisation and disaggregation’, *Journal of Hydrology*, 175(1), pp. 47–65.

Deltares (2021) *wflow*. Available from: https://www.deltares.nl/en/software/wflow-hydrology/ (Accessed 8 October 2021).

Environment and Climate Change Canada, E. and C.C. (2011) *Historical Data - Climate - Environment and Climate Change Canada*. Available from: https://climate.weather.gc.ca/historical_data/search_historic_data_e.html (Accessed 8 April 2022).

Fang, X. (2025) Personal communication. 31 March.

Fang, X., Pomeroy, J., DeBeer, C., Harder, P. & Siemens, E. (2018) *Hydrometeorological data from Marmot Creek Research Basin, Canadian Rockies*.

Fang, X. & Pomeroy, J.W. (2020) 'Diagnosis of future changes in hydrology for a Canadian Rockies headwater basin', *Hydrology and Earth System Sciences*, 24(5), pp. 2731–2754.

Fang, X. & Pomeroy, J.W. (2016) 'Impact of antecedent conditions on simulations of a flood in a mountain headwater basin', *Hydrological Processes*, 30(16), pp. 2754–2772.

Fang, X., Pomeroy, J.W., DeBeer, C.M., Harder, P. & Siemens, E. (2019) 'Hydrometeorological data from Marmot Creek Research Basin, Canadian Rockies', *Earth System Science Data*, 11(2), pp. 455–471.

Fang, X., Pomeroy, J.W., Ellis, C.R., MacDonald, M.K., DeBeer, C.M. & Brown, T. (2012) *Multi-variable evaluation of hydrological model predictions for a headwater basin in the Canadian Rocky Mountains*.

Finger, D., Vis, M., Huss, M. & Seibert, J. (2015) 'The value of multiple data set calibration versus model complexity for improving the performance of hydrological models in mountain catchments', *Water Resources Research*, 51(4), pp. 1939–1958.

FRDR (2021) *Federated Research Data Repository*. [Online] [online]. Available from: https://www.globus.org/tags/frdr (Accessed 29 March 2021).

Frei, C. & Schär, C. (1998) 'A precipitation climatology of the Alps from high-resolution rain-gauge observations', *International Journal of Climatology*, 18(8), pp. 873–900.

Goovaerts, P. (2000) 'Geostatistical approaches for incorporating elevation into the spatial interpolation of rainfall', *Journal of Hydrology*, 228(1–2), pp. 113–129.

Government of Canada (2021) *Water Level and Flow - Environment Canada*. [Online] [online]. Available from: https://wateroffice.ec.gc.ca/index_e.html (Accessed 25 March 2021).

Grundmann, J., Hörning, S. & Bárdossy, A. (2019) 'Stochastic reconstruction of spatio-temporal rainfall patterns by inverse hydrologic modelling', *Hydrology and Earth System Sciences*, 23(1), pp. 225–237.

Guillory, A. (2017) *ERA5*. Available from: https://www.ecmwf.int/en/forecasts/datasets/reanalysis-datasets/era5 (Accessed 15 October 2021).

Haan, C.T., Allen, D.M. & Street, J.O. (1976) 'A Markov Chain Model of daily rainfall', *Water Resources Research*, 12(3), pp. 443–449.

Haese, B., Hörning, S., Chwala, C., Bárdossy, A., Schalge, B. & Kunstmann, H. (2017) 'Stochastic Reconstruction and Interpolation of Precipitation Fields Using Combined Information of Commercial Microwave Links and Rain Gauges', *Water Resources Research*, 53(12), pp. 10740–10756.

Harder, P. & Pomeroy, J. (2013) 'Estimating precipitation phase using a psychrometric energy balance method', *Hydrological Processes*, 27(13), pp. 1901–1914.

Henn, B., Clark, M.P., Kavetski, D., Newman, A.J., Hughes, M., McGurk, B. & Lundquist, J.D. (2018) 'Spatiotemporal patterns of precipitation inferred from streamflow observations across the Sierra Nevada mountain range', *Journal of Hydrology*, 556pp. 993–1012.

Henn, B., Newman, A.J., Livneh, B., Daly, C. & Lundquist, J.D. (2018) 'An assessment of differences in gridded precipitation datasets in complex terrain', *Journal of Hydrology*, 556pp. 1205–1219.

Herold, N., Alexander, L.V., Donat, M.G., Contractor, S. & Becker, A. (2016) 'How much does it rain over land?', *Geophysical Research Letters*, 43(1), pp. 341–348.

Hörning, S. (2016) *Process-oriented modeling of spatial random fields using copulas*. [Online]. Eigenverlag des Instituts für Wasser- und Umweltsystemmodellierung der Universität Stuttgart.

Hörning, S. & Haese, B. (2021) ‘RMWSPy (v 1.1): A Python code for spatial simulation and inversion for environmental applications’, *Environmental Modelling & Software*, 138p. 104970.

Hu, L.Y. (2000) ‘Gradual Deformation and Iterative Calibration of Gaussian-Related Stochastic Models’, *Mathematical Geology*, 32(1), pp. 87–108.

Hu, Q., Li, Z., Wang, L., Huang, Y., Wang, Y. & Li, L. (2019) ‘Rainfall Spatial Estimations: A Review from Spatial Interpolation to Multi-Source Data Merging’, *Water*, 11(3), p. 579.

Immerzeel, W.W., Lutz, A.F., Andrade, M., Bahl, A., Biemans, H., Bolch, T., Hyde, S., Brumby, S., Davies, B.J., Elmore, A.C., Emmer, A., Feng, M., Fernández, A., Haritashya, U., Kargel, J.S., Koppes, M., Kraaijenbrink, P.D.A., Kulkarni, A.V., Mayewski, P.A., et al. (2020) ‘Importance and vulnerability of the world’s water towers’, *Nature*, 577(7790), pp. 364–369.

Immerzeel, W.W., Petersen, L., Ragettli, S. & Pellicciotti, F. (2014) ‘The importance of observed gradients of air temperature and precipitation for modeling runoff from a glacierized watershed in the Nepalese Himalayas’, *Water Resources Research*, 50(3), pp. 2212–2226.

Immerzeel, W.W., Wanders, N., Lutz, A.F., Shea, J.M. & Bierkens, M.F.P. (2015) ‘Reconciling high-altitude precipitation in the upper Indus basin with glacier mass balances and runoff’, *Hydrology and Earth System Sciences*, 19(11), pp. 4673–4687.

IPCC (2019) *Chapter 2: High Mountain Areas — Special Report on the Ocean and Cryosphere in a Changing Climate*. Available from: https://www.ipcc.ch/srocc/chapter/chapter-2/ (Accessed 16 September 2024).

Kidd, C., Bauer, P., Turk, J., Huffman, G.J., Joyce, R., Hsu, K.-L. & Braithwaite, D. (2012) ‘Intercomparison of High-Resolution Precipitation Products over Northwest Europe’, *Journal of Hydrometeorology*, 13(1), pp. 67–83.

Kidd, C., Becker, A., Huffman, G.J., Muller, C.L., Joe, P., Skofronick-Jackson, G. & Kirschbaum, D.B. (2017) ‘So, How Much of the Earth’s Surface Is Covered by Rain Gauges?’, *Bulletin of the American Meteorological Society*, 98(1), pp. 69–78.

Kobayashi, S., Ota, Y., Harada, Y., Ebita, A., Moriya, M., Onoda, H., Onogi, K., Kamahori, H., Kobayashi, C., Endo, H., Miyaoka, K. & Takahashi, K. (2015) ‘The JRA-55 Reanalysis:

General Specifications and Basic Characteristics', *Journal of the Meteorological Society of Japan. Ser. II*, 93(1), pp. 5–48.

Levizzani, V., Laviola, S. & Cattani, E. (2011) 'Detection and Measurement of Snowfall from Space', *Remote Sensing*, 3(1), pp. 145–166.

Lewis, E., Pritchard, D., Villalobos-Herrera, R., Blenkinsop, S., McClean, F., Guerreiro, S., Schneider, U., Becker, A., Finger, P., Meyer-Christoffer, A., Rustemeier, E. & Fowler, H.J. (2021) 'Quality control of a global hourly rainfall dataset', *Environmental Modelling & Software*, 144p. 105169.

Lindström, G., Johansson, B., Persson, M., Gardelin, M. & Bergström, S. (1997) 'Development and test of the distributed HBV-96 hydrological model', *Journal of Hydrology*, 201(1), pp. 272–288.

Liston, G.E. & Elder, K. (2006) 'A Meteorological Distribution System for High-Resolution Terrestrial Modeling (MicroMet)', *Journal of Hydrometeorology*, 7(2), pp. 217–234.

Liu, A.Q., Mooney, C., Szeto, K., Thériault, J.M., Kochtubajda, B., Stewart, R.E., Boodoo, S., Goodson, R., Li, Y. & Pomeroy, J. (2016) 'The June 2013 Alberta Catastrophic Flooding Event: Part 1—Climatological aspects and hydrometeorological features', *Hydrological Processes*, 30(26), pp. 4899–4916.

Lv, Z. & Pomeroy, J.W. (2019) 'Detecting intercepted snow on mountain needleleaf forest canopies using satellite remote sensing', *Remote Sensing of Environment*, 231p. 111222.

Ma, L., Zhao, L., Tian, L., Yuan, L., Xiao, Y., Zhang, L., Zou, D. & Qiao, Y. (2019) 'Evaluation of the integrated multi-satellite retrievals for global precipitation measurement over the Tibetan Plateau', *Journal of Mountain Science*, 16(7), pp. 1500–1514.

Mair, A. & Fares, A. (2011) 'Comparison of Rainfall Interpolation Methods in a Mountainous Region of a Tropical Island', *Journal of Hydrologic Engineering*, 16(4), pp. 371–383.

Mair, E., Leitinger, G., Chiesa, S.D., Niedrist, G., Tappeiner, U. & Bertoldi, G. (2016) 'A simple method to combine snow height and meteorological observations to estimate winter precipitation at sub-daily resolution', *Hydrological Sciences Journal*, 61(11), pp. 2050–2060.

Morán-Tejeda, E., Zabalza, J., Rahman, K., Gago-Silva, A., López-Moreno, J.I., Vicente-Serrano, S., Lehmann, A., Tague, C.L. & Beniston, M. (2015) 'Hydrological impacts of climate and land-use changes in a mountain watershed: uncertainty estimation based on model comparison', *Ecohydrology*, 8(8), pp. 1396–1416.

Nash, J.E. & Sutcliffe, J.V. (1970) 'River flow forecasting through conceptual models part I — A discussion of principles', *Journal of Hydrology*, 10(3), pp. 282–290.

Pollock, M.D., O'Donnell, G., Quinn, P., Dutton, M., Black, A., Wilkinson, M.E., Colli, M., Stagnaro, M., Lanza, L.G., Lewis, E., Kilsby, C.G. & O'Connell, P.E. (2018) 'Quantifying and Mitigating Wind-Induced Undercatch in Rainfall Measurements', *Water Resources Research*, 54(6), pp. 3863–3875.

Pomeroy, J., Fang, X. & Ellis, C. (2012) 'Sensitivity of snowmelt hydrology in Marmot Creek, Alberta, to forest cover disturbance', *Hydrological Processes*, 26(12), pp. 1891–1904.

Pomeroy, J., Fang, X., Ellis, C. & Guan, M. (2011) *Sensitivity of Snowmelt Hydrology on Mountain Slopes to Forest Cover Disturbance*.

Pomeroy, J.W. (2013) *Introduction to the Marmot Creek ~50th Anniversary Workshop*, p. 15.

Pomeroy, J.W., Brown, T., Fang, X., Shook, K.R., Pradhananga, D., Armstrong, R., Harder, P., Marsh, C., Costa, D., Krogh, S.A., Aubry-Wake, C., Annand, H., Lawford, P., He, Z., Kompanizare, M. & Lopez Moreno, J.I. (2022) 'The cold regions hydrological modelling platform for hydrological diagnosis and prediction based on process understanding', *Journal of Hydrology*, 615p. 128711.

Pomeroy, J. W., Brown, T., Fang, X., Shook, K.R., Pradhananga, D., Armstrong, R., Harder, P., Marsh, C., Costa, D., Krogh, S.A., Aubry-Wake, C., Annand, H., Lawford, P., He, Z., Kompanizare, M. & Lopez Moreno, J.I. (2022) 'The cold regions hydrological modelling platform for hydrological diagnosis and prediction based on process understanding', *Journal of Hydrology*, 615p. 128711.

Pomeroy, J.W., Gray, D.M., Brown, T., Hedstrom, N.R., Quinton, W.L., Granger, R.J. & Carey, S.K. (2007a) 'The cold regions hydrological model: a platform for basing process representation and model structure on physical evidence', *Hydrological Processes*, 21(19), pp. 2650–2667.

Pomeroy, J.W., Gray, D.M., Brown, T., Hedstrom, N.R., Quinton, W.L., Granger, R.J. & Carey, S.K. (2007b) 'The cold regions hydrological model: a platform for basing process representation and model structure on physical evidence', *Hydrological Processes*, 21(19), pp. 2650–2667.

Ragettli, S., Immerzeel, W.W. & Pellicciotti, F. (2016) 'Contrasting climate change impact on river flows from high-altitude catchments in the Himalayan and Andes Mountains', *Proceedings of the National Academy of Sciences of the United States of America*, 113(33), pp. 9222–9227.

Rasmussen, R., Baker, B., Kochendorfer, J., Meyers, T., Landolt, S., Fischer, A.P., Black, J., Thériault, J.M., Kucera, P., Gochis, D., Smith, C., Nitu, R., Hall, M., Ikeda, K. & Gutmann, E. (2012) 'How Well Are We Measuring Snow: The NOAA/FAA/NCAR Winter Precipitation Test Bed', *Bulletin of the American Meteorological Society*, 93(6), pp. 811–829.

Roe, G.H. (2005) 'Orographic Precipitation', *Annual Review of Earth and Planetary Sciences*, 33(1), pp. 645–671.

Rothwell, R., Hillman, G. & Pomeroy, J.W. (2016) 'Marmot Creek Experimental Watershed Study', *The Forestry Chronicle*,

Saelthun, N.R. (1996) *The ``Nordic`` HBV model. Description and documentation of the model version developed for the project Climate Change and Energy Production*, p. 29.

Schneider, U., Becker, A., Finger, P., Meyer-Christoffer, A., Ziese, M. & Rudolf, B. (2014) 'GPCC's new land surface precipitation climatology based on quality-controlled in situ data and its role in quantifying the global water cycle', *Theoretical and Applied Climatology*, 115(1), pp. 15–40.

Shepard, D. (1968) 'A two-dimensional interpolation function for irregularly-spaced data', in *Proceedings of the 1968 23rd ACM national conference*. ACM '68. [Online]. 1 January 1968 New York, NY, USA: Association for Computing Machinery. pp. 517–524.

Shook, K.R. (2021) *CRHM_models*.

Thiessen, A.H. (1911) 'PRECIPITATION AVERAGES FOR LARGE AREAS', *Monthly Weather Review*, 39(7), pp. 1082–1089.

University of Saskatchewan (2022) *Centre for Hydrology - University of Saskatchewan*. [Online] [online]. Available from: https://research-groups.usask.ca/hydrology/ (Accessed 1 July 2022).

Virtanen, P., Gommers, R., Oliphant, T.E., Haberland, M., Reddy, T., Cournapeau, D., Burovski, E., Peterson, P., Weckesser, W., Bright, J., van der Walt, S.J., Brett, M., Wilson, J., Millman, K.J., Mayorov, N., Nelson, A.R.J., Jones, E., Kern, R., Larson, E., et al. (2020) 'SciPy 1.0: fundamental algorithms for scientific computing in Python', *Nature Methods*, 17(3), pp. 261–272.

Viviroli, D., Kummu, M., Meybeck, M., Kallio, M. & Wada, Y. (2020) 'Increasing dependence of lowland populations on mountain water resources', *Nature Sustainability*, 3(11), pp. 917–928.

Wagner, P.D., Fiener, P., Wilken, F., Kumar, S. & Schneider, K. (2012) 'Comparison and evaluation of spatial interpolation schemes for daily rainfall in data scarce regions', *Journal of Hydrology*, 464–465pp. 388–400.

Wang, L., Zhang, F., Zhang, H., Scott, C.A., Zeng, C. & Shi, X. (2018) 'Intensive precipitation observation greatly improves hydrological modelling of the poorly gauged high mountain Mabengnong catchment in the Tibetan Plateau', *Journal of Hydrology*, 556pp. 500–509.

Wang, X., Yang, T., Xu, C.-Y., Yong, B. & Shi, P. (2019) 'Understanding the discharge regime of a glacierized alpine catchment in the Tianshan Mountains using an improved HBV-D hydrological model', *Global and Planetary Change*, 172pp. 211–222.

Wrzesien, M.L., Durand, M.T. & Pavelsky, T.M. (2019) 'A Reassessment of North American River Basin Cool-Season Precipitation: Developments From a New Mountain Climatology Data Set', *Water Resources Research*, 55(4), pp. 3502–3519.

Yan, J., Li, F., Bárdossy, A. & Tao, T. (2021a) 'Conditional simulation of spatial rainfall fields using random mixing: a study that implements full control over the stochastic process', *Hydrology and Earth System Sciences*, 25(7), pp. 3819–3835.

Yan, J., Li, F., Bárdossy, A. & Tao, T. (2021b) 'Simulation of rainfall fields conditioned on rain gauge observations and radar estimates using random mixing', *Hydrology and Earth System Sciences Discussions*, pp. 1–23.

Zhang, H., Wang, Yu-jie, Wang, Yun-qi, Li, D. & Wang, X. (2013) ‘Quantitative comparison of semi- and fully-distributed hydrologic models in simulating flood hydrographs on a mountain watershed in southwest China’, *Journal of Hydrodynamics*, 25(6), pp. 877–885.

Appendix A

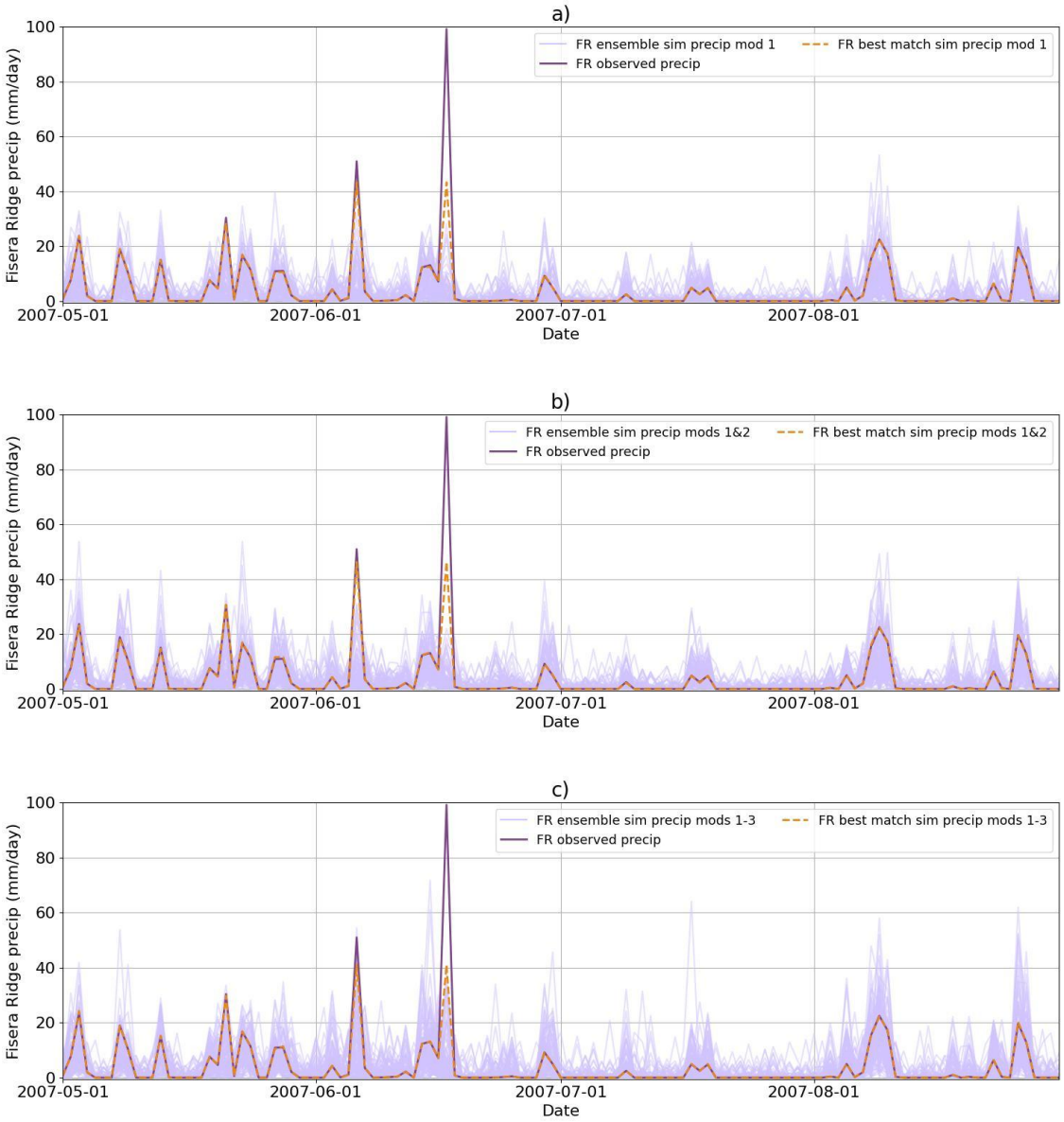

Figure A.1. Observed daily precipitation time series and RM-mountain simulated daily precipitation time series, using leave-one-out cross-validation at Fisera Ridge, for May-August 2007, showing 100-member ensemble and best match to observed precipitation for: a) modification 1; b) modifications 1 & 2; c) modifications 1-3

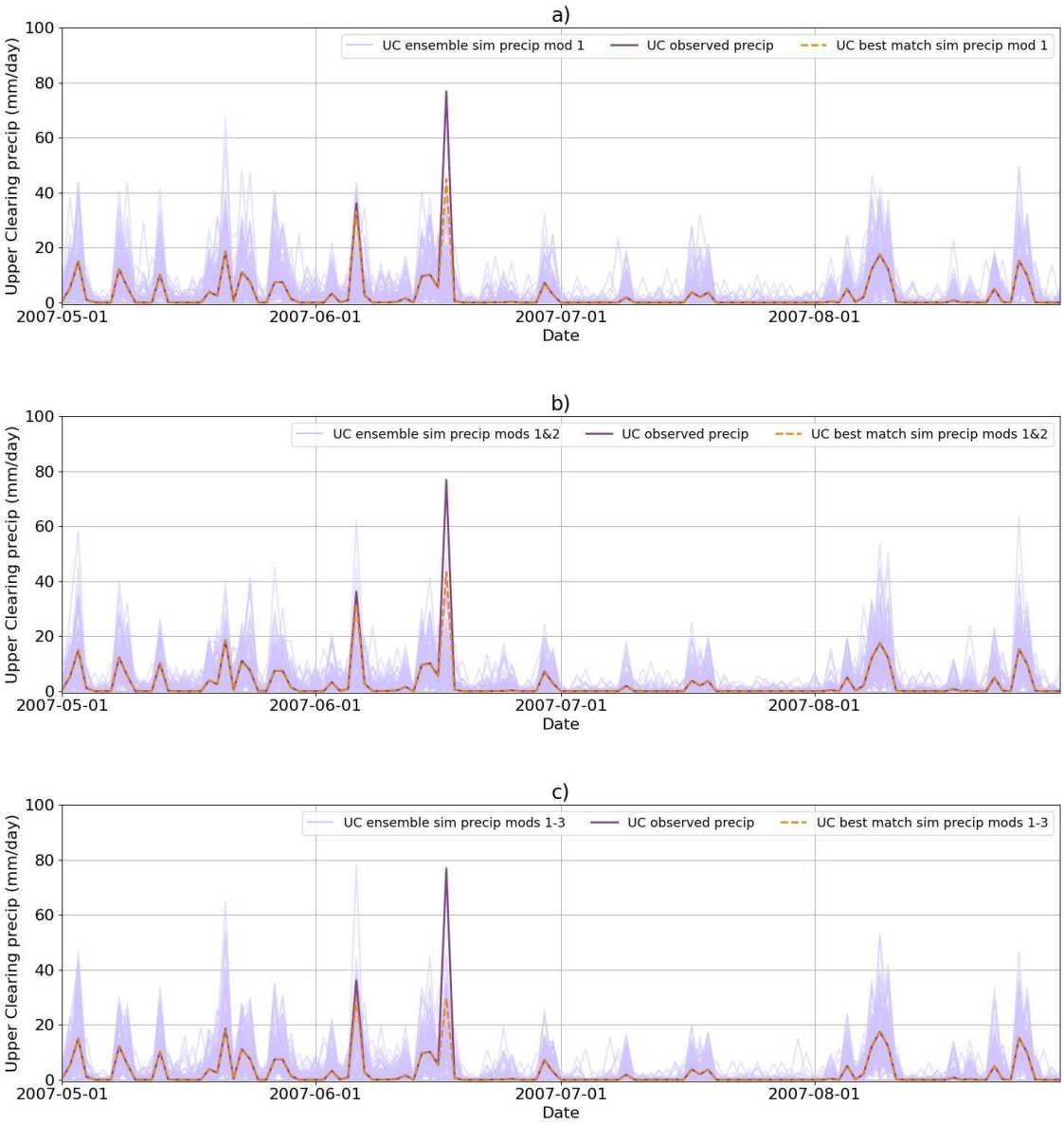

Figure A.2. As Figure A.1 but for Upper Clearing

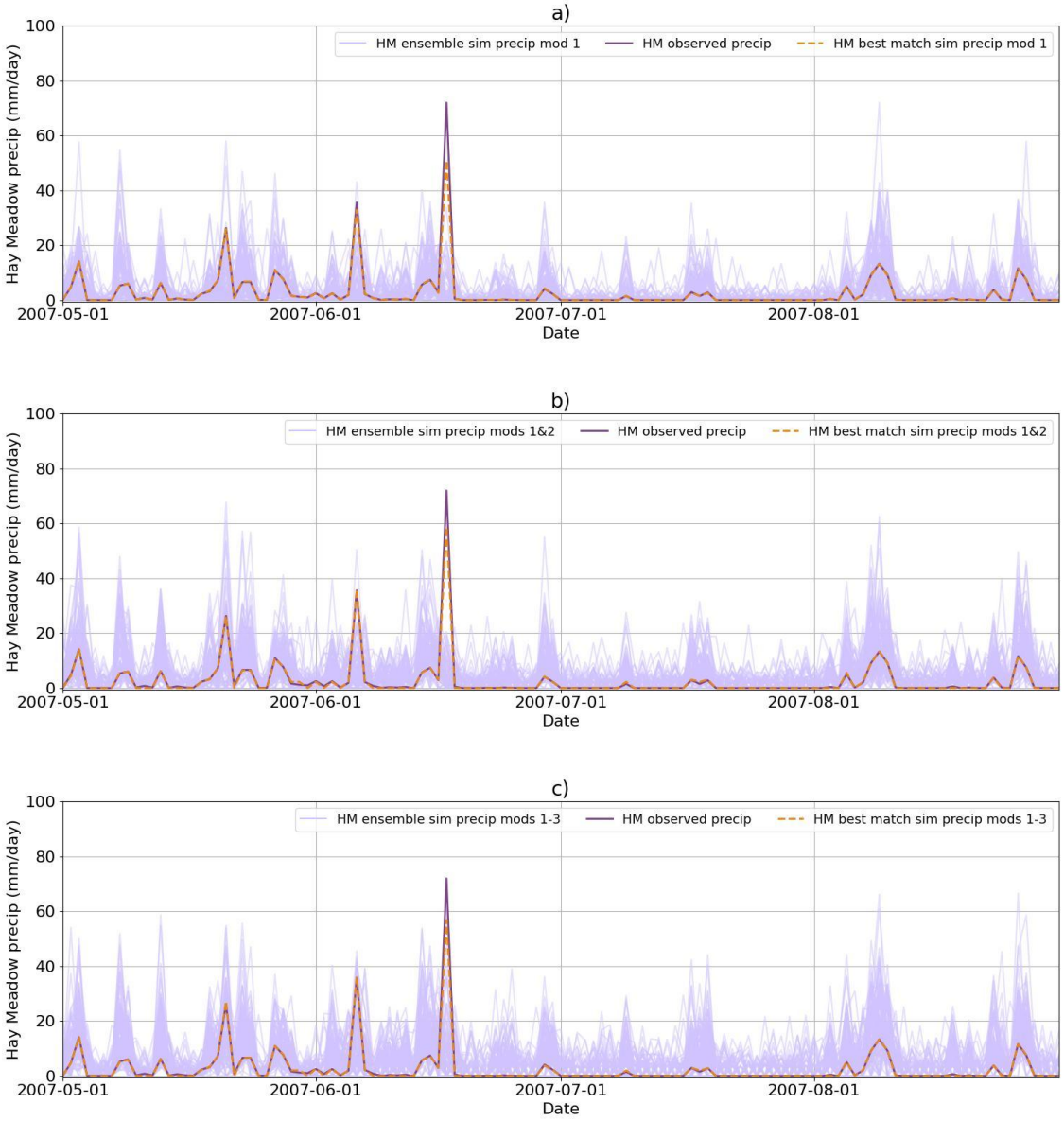

Figure A.3. As Figure A.1 but for Hay Meadow

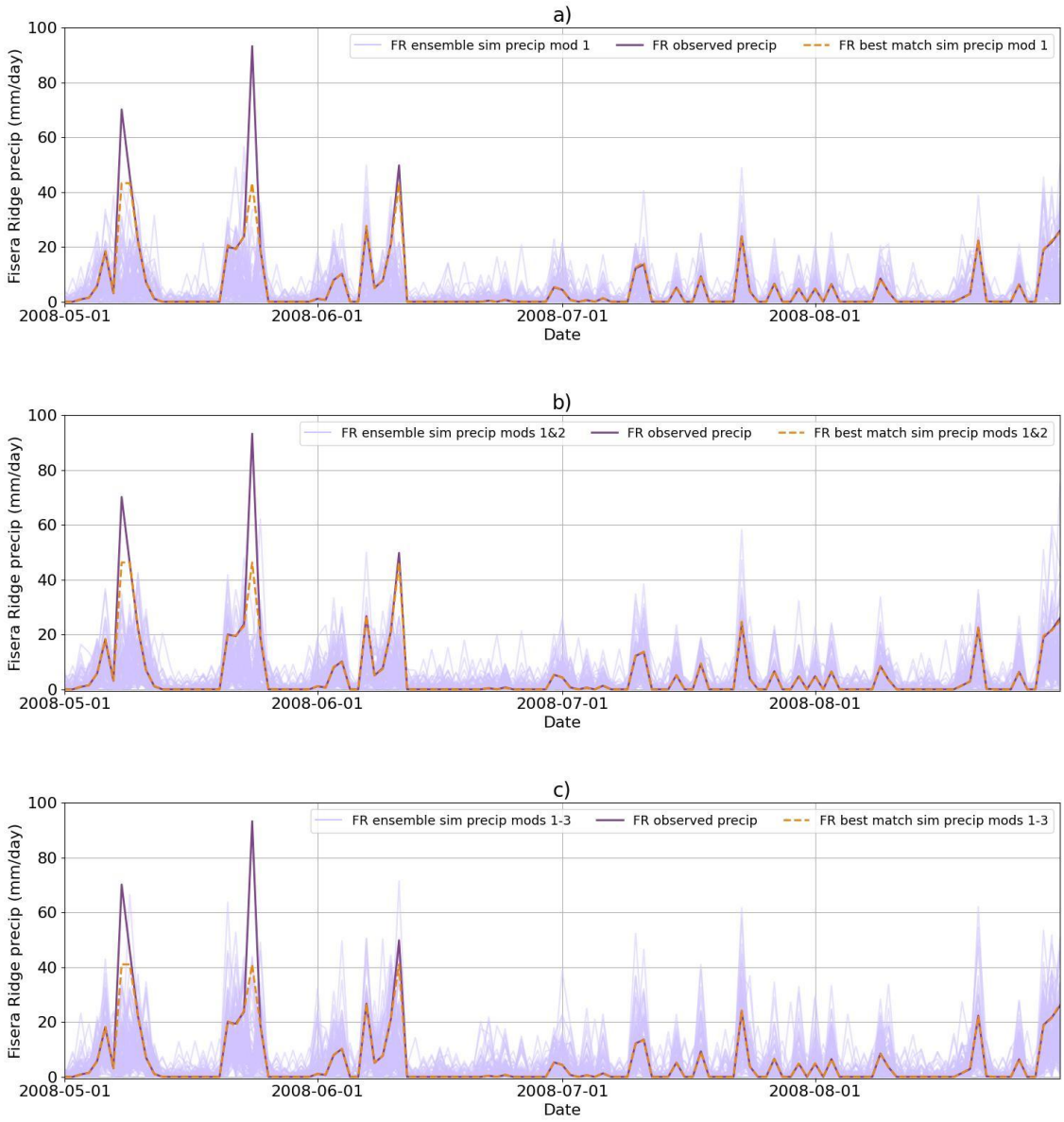

Figure A.4. As Figure A.1 but for 2008

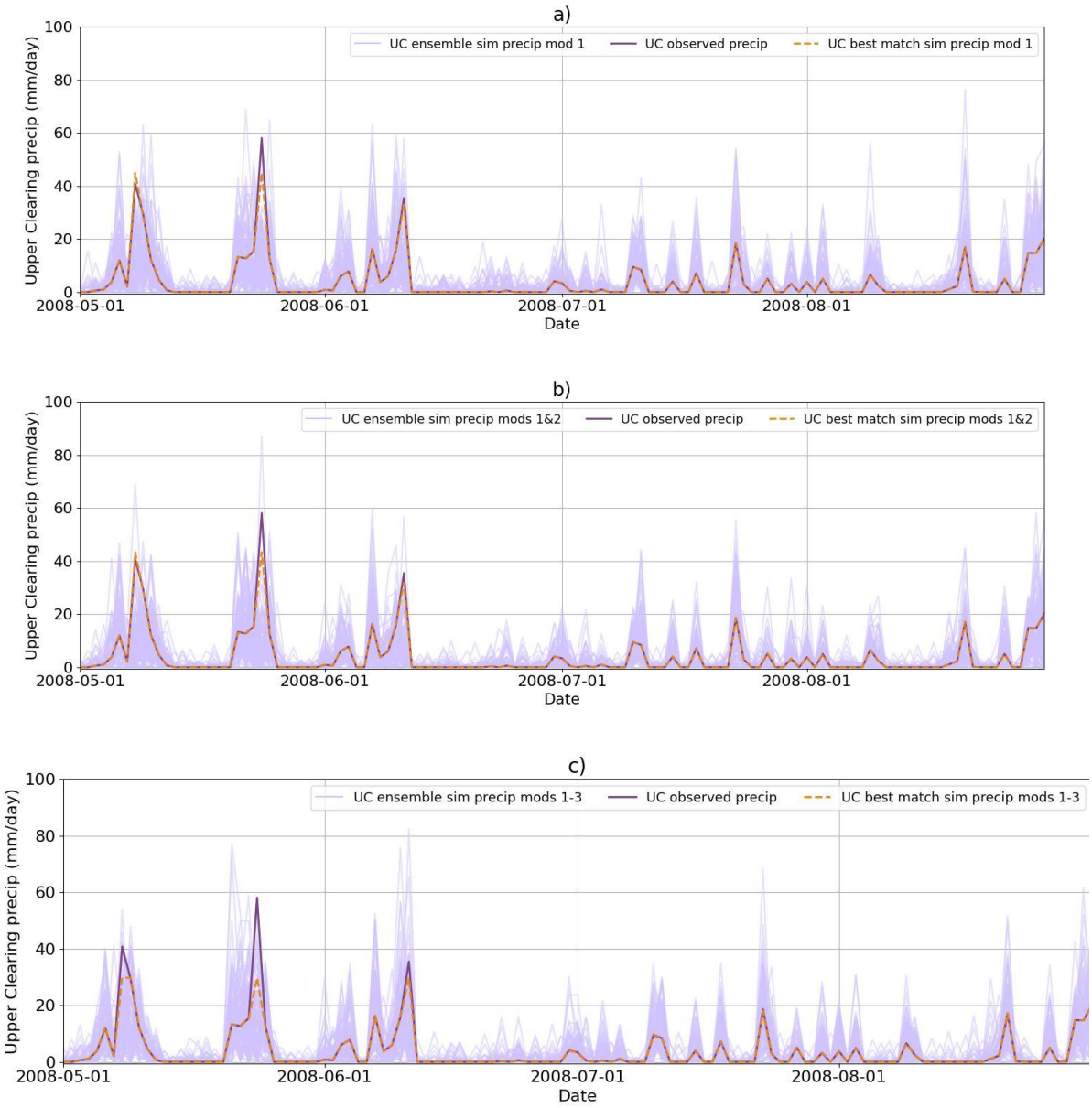

Figure A.5. As Figure A.2 but for 2008

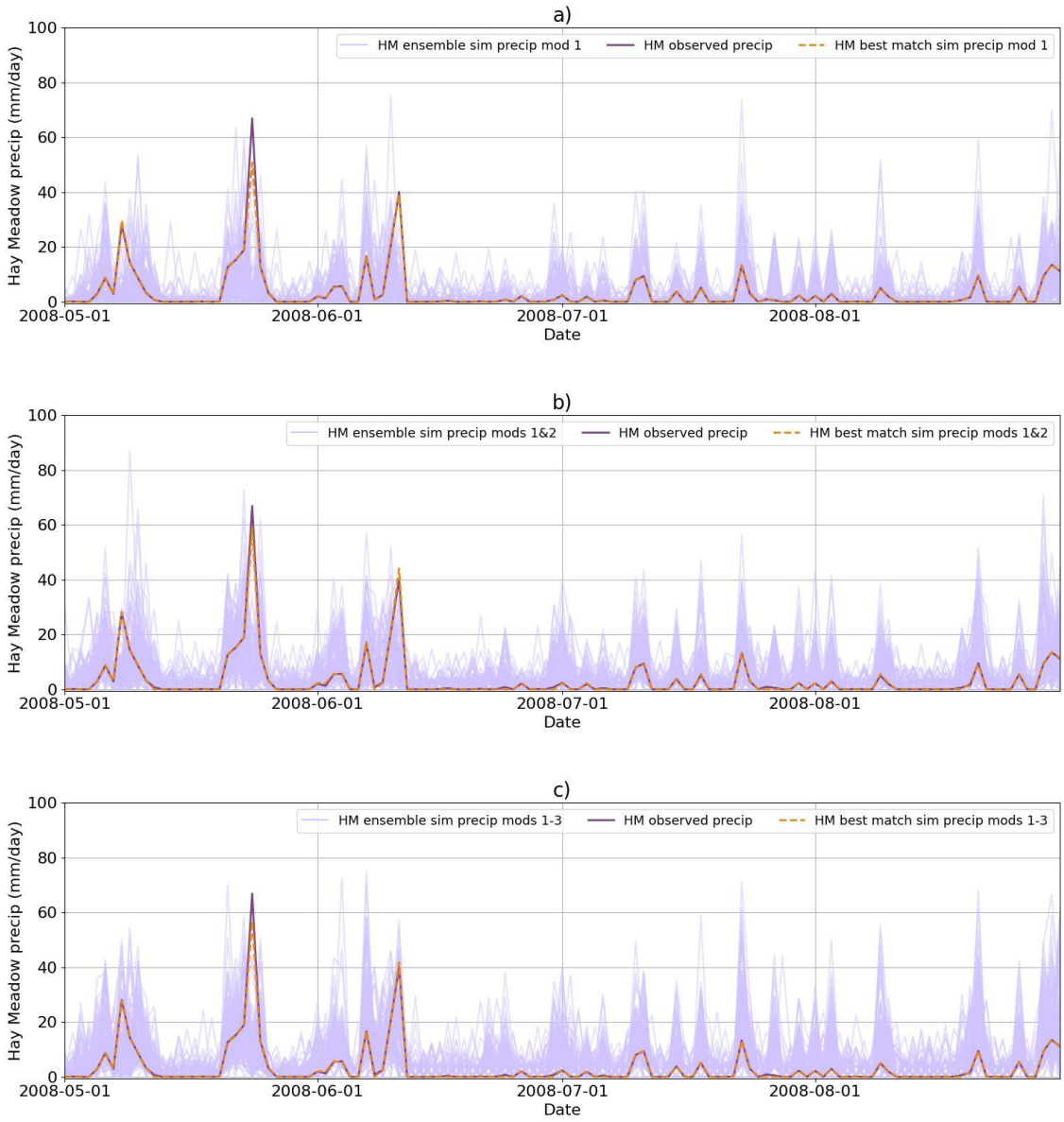

Figure A.6 As Figure A.3 but for 2008

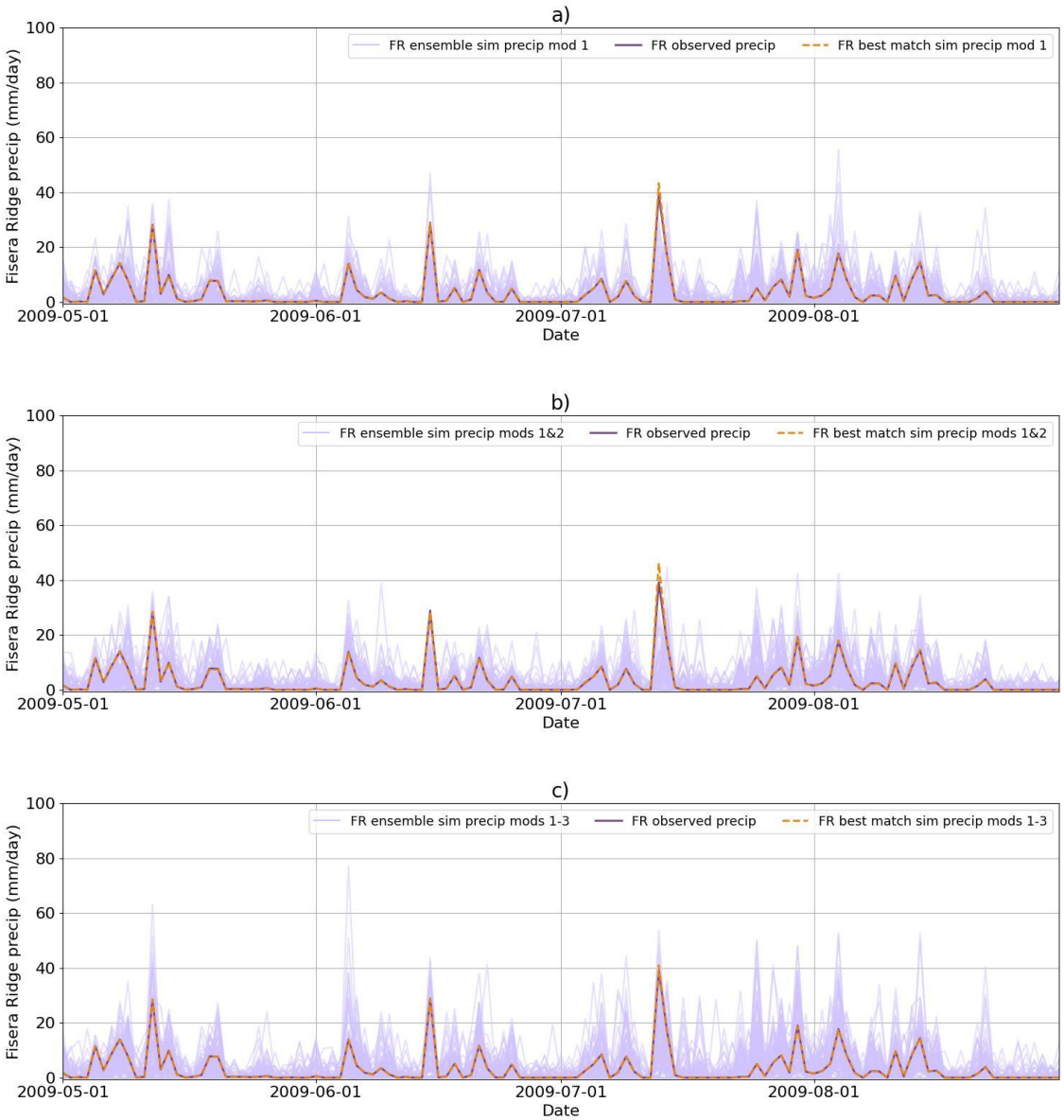

Figure A.7. As Figure A.1 but for 2009

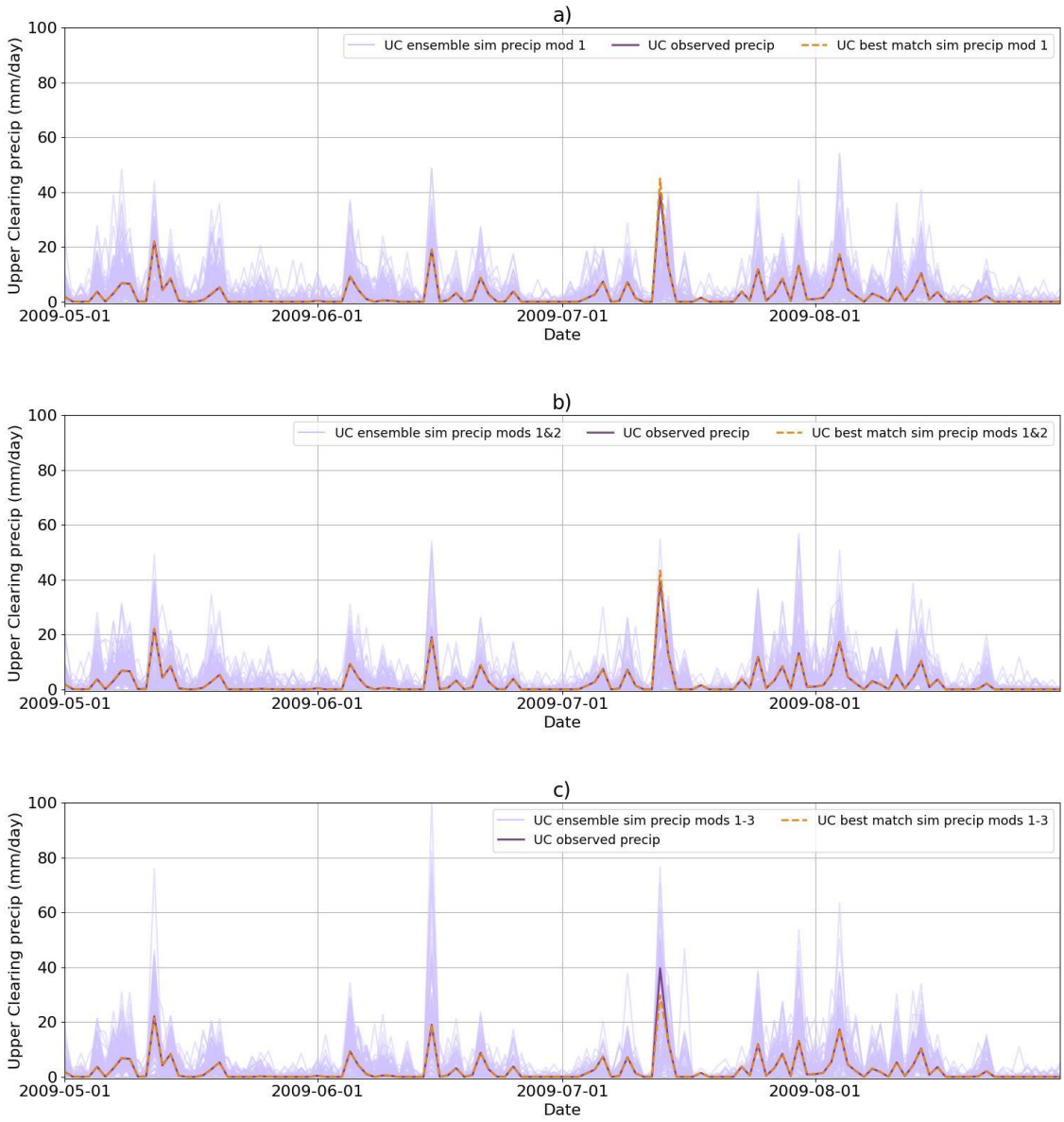

Figure A.8. As Figure A.2 but for 2009

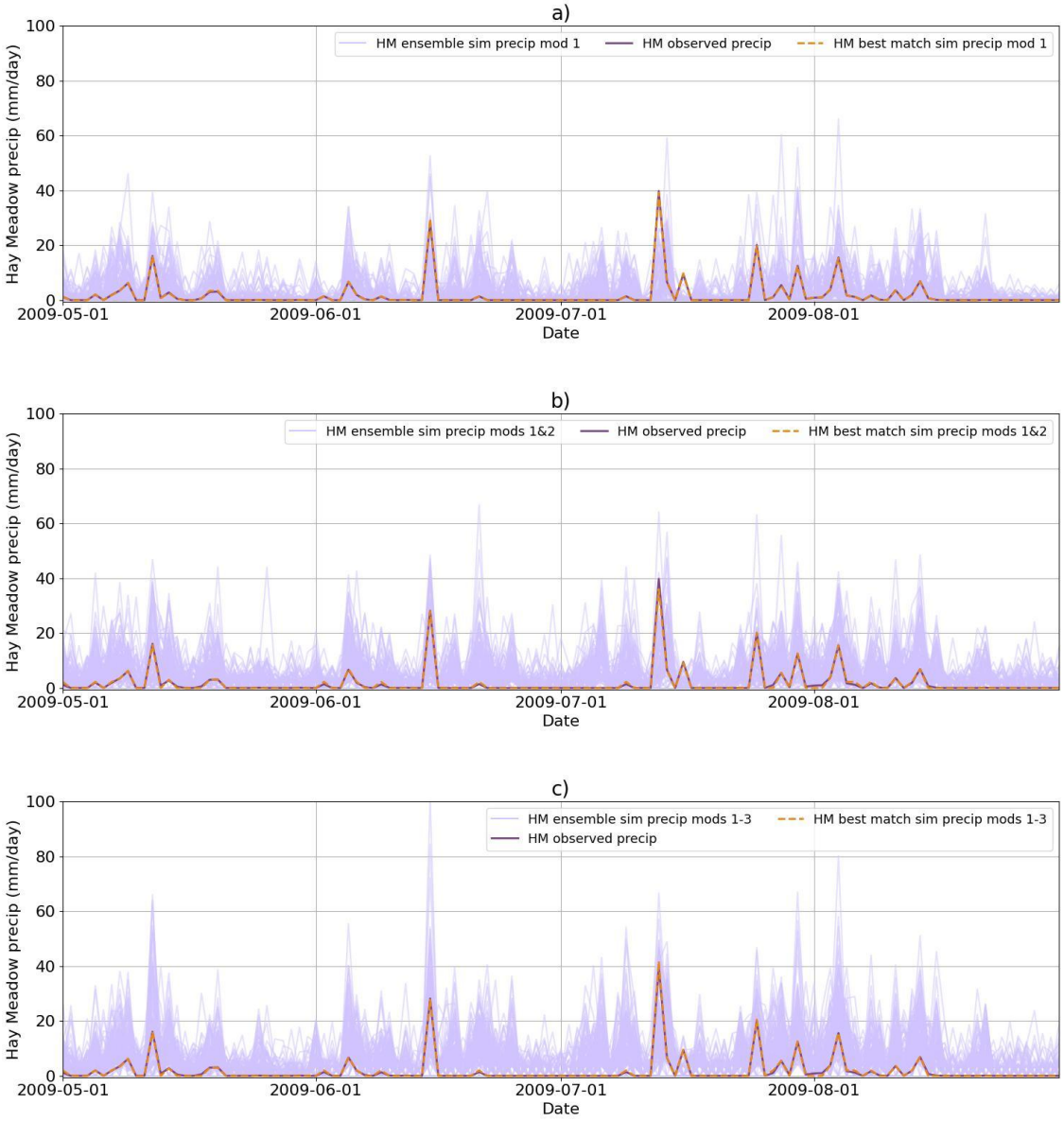

Figure A.9. As Figure A.3 but for 2009

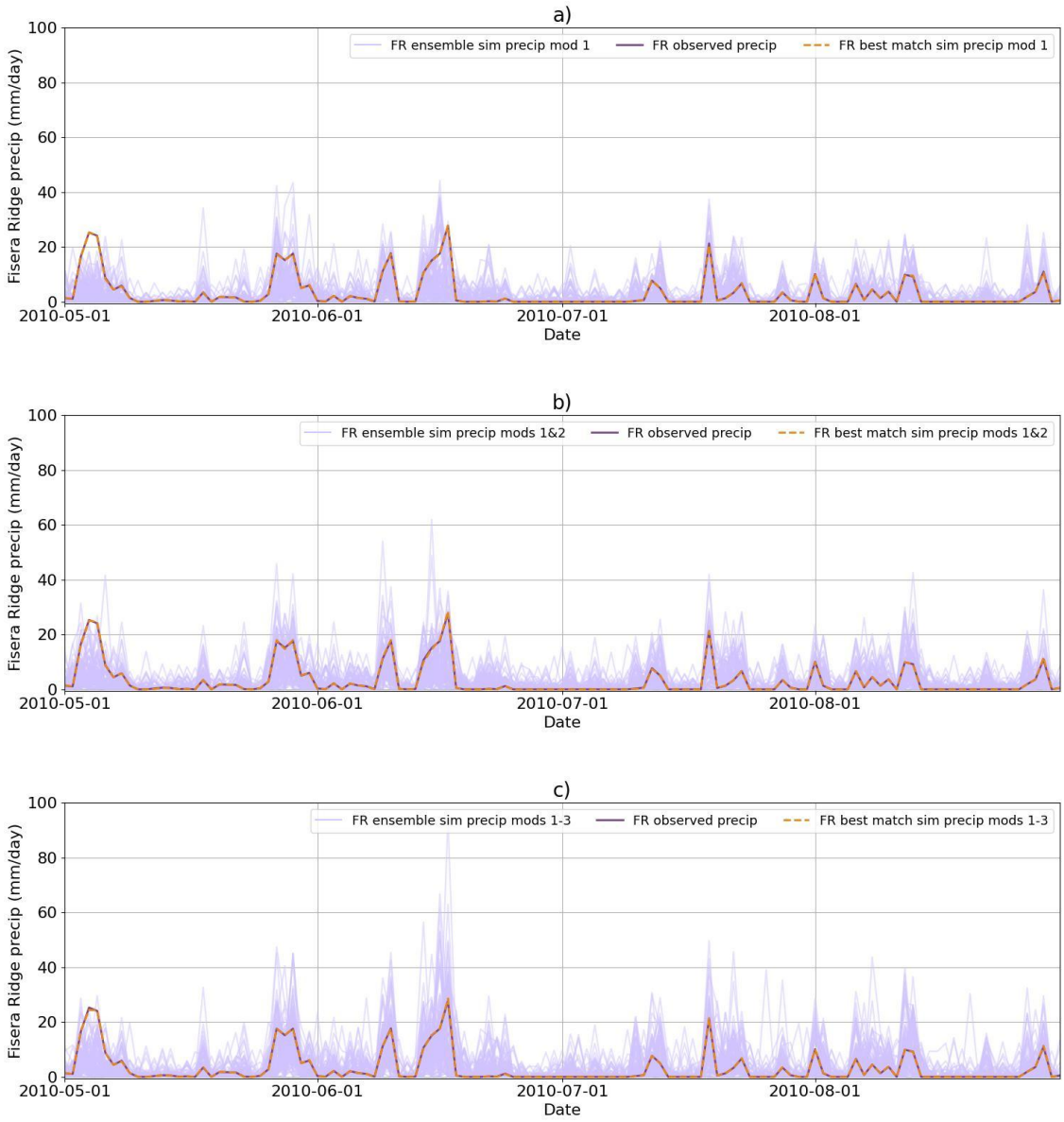

Figure A.10. As Figure A.1 but for 2010

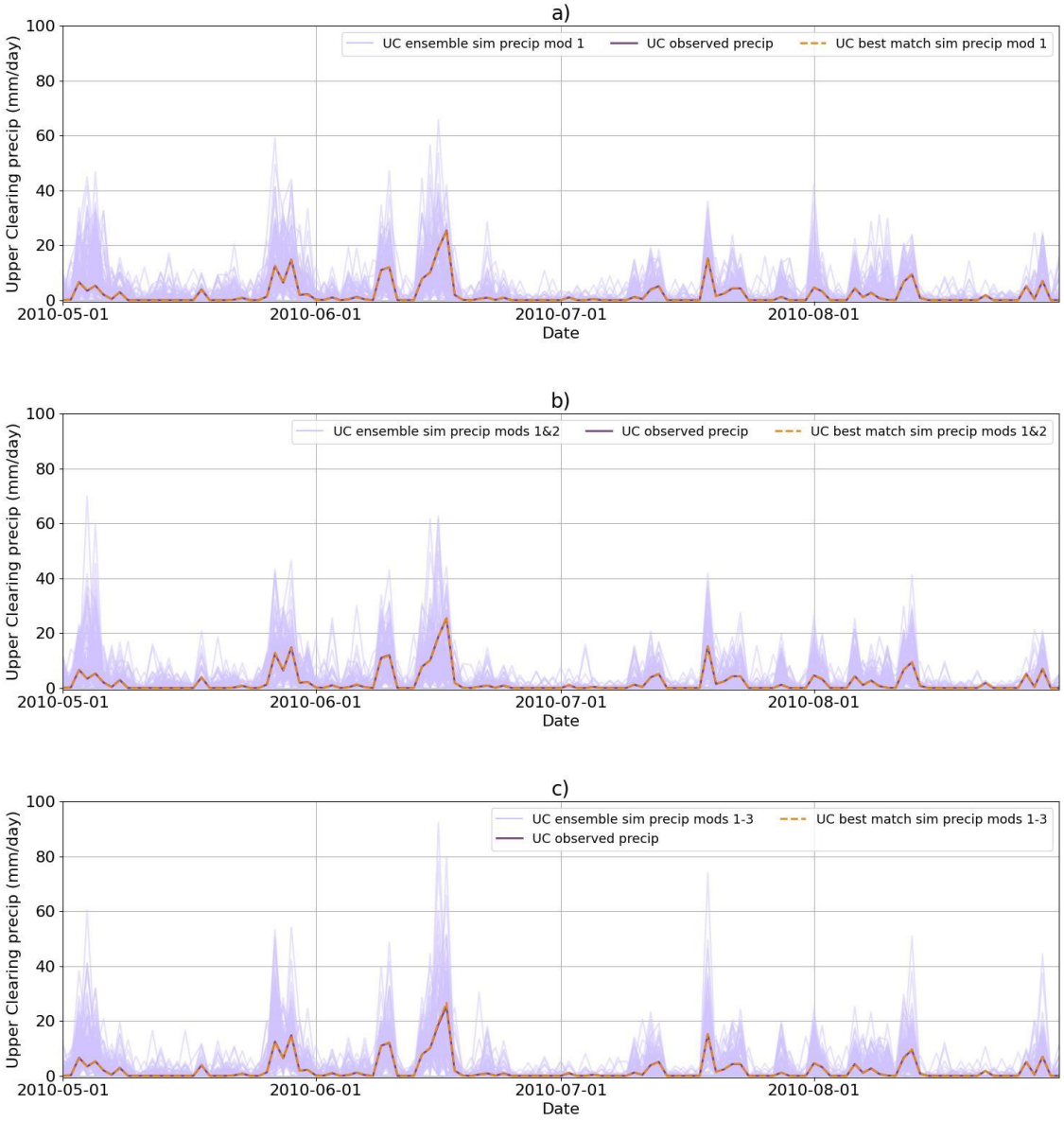

Figure A.11. As Figure A.2 but for 2010

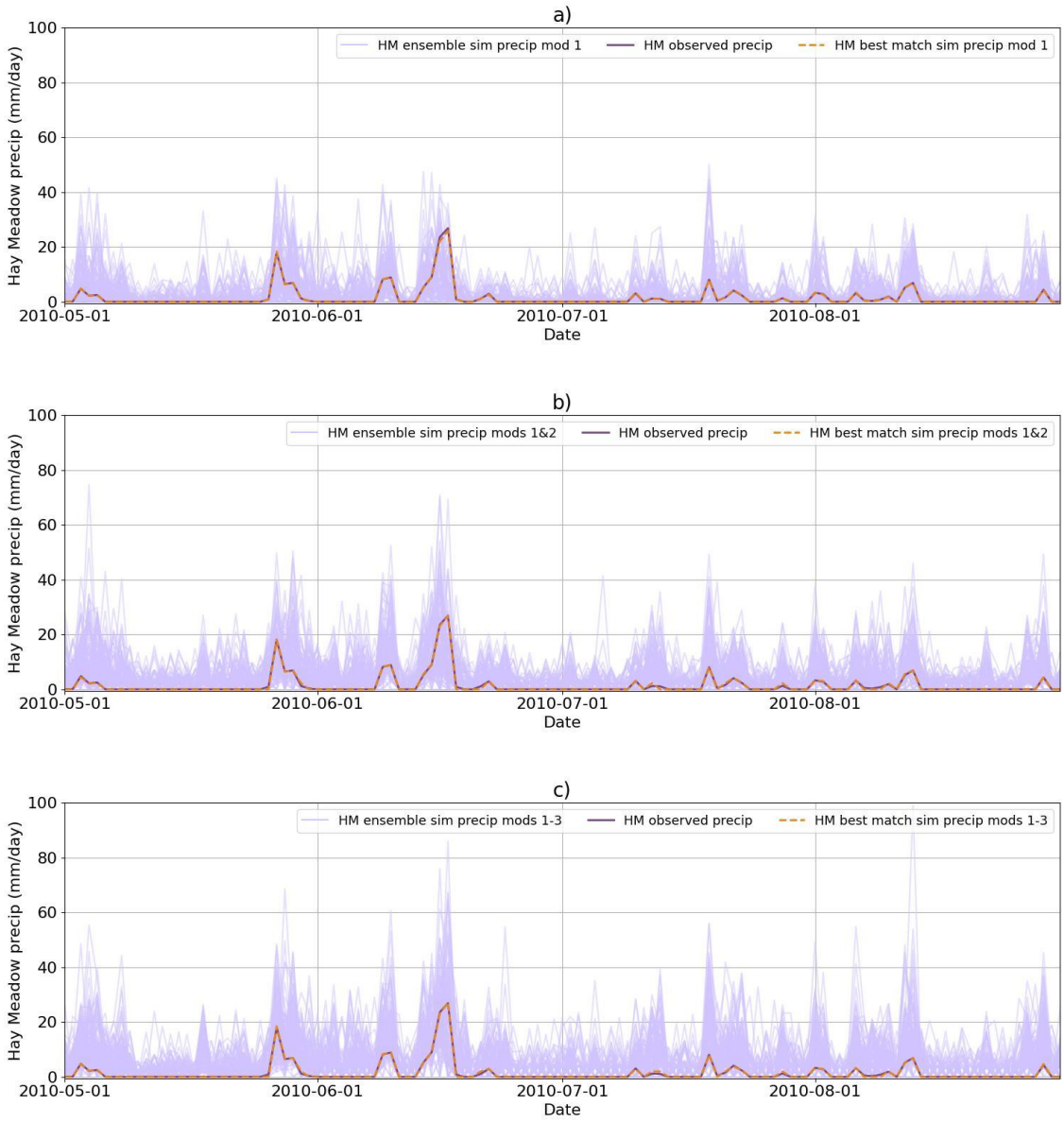

Figure A.12. As Figure A.3 but for 2010

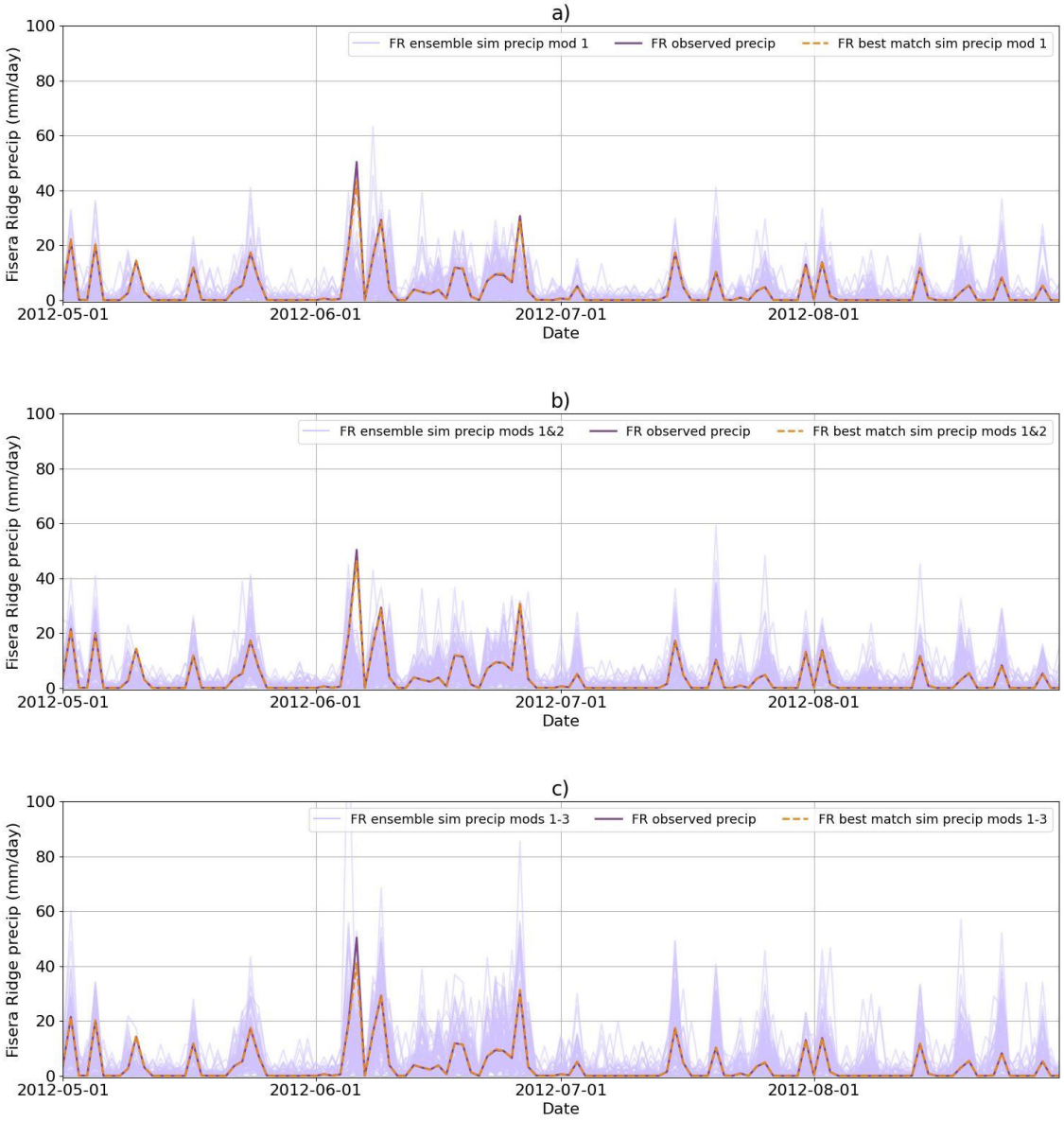

Figure A.13. As Figure A.1 but for 2012

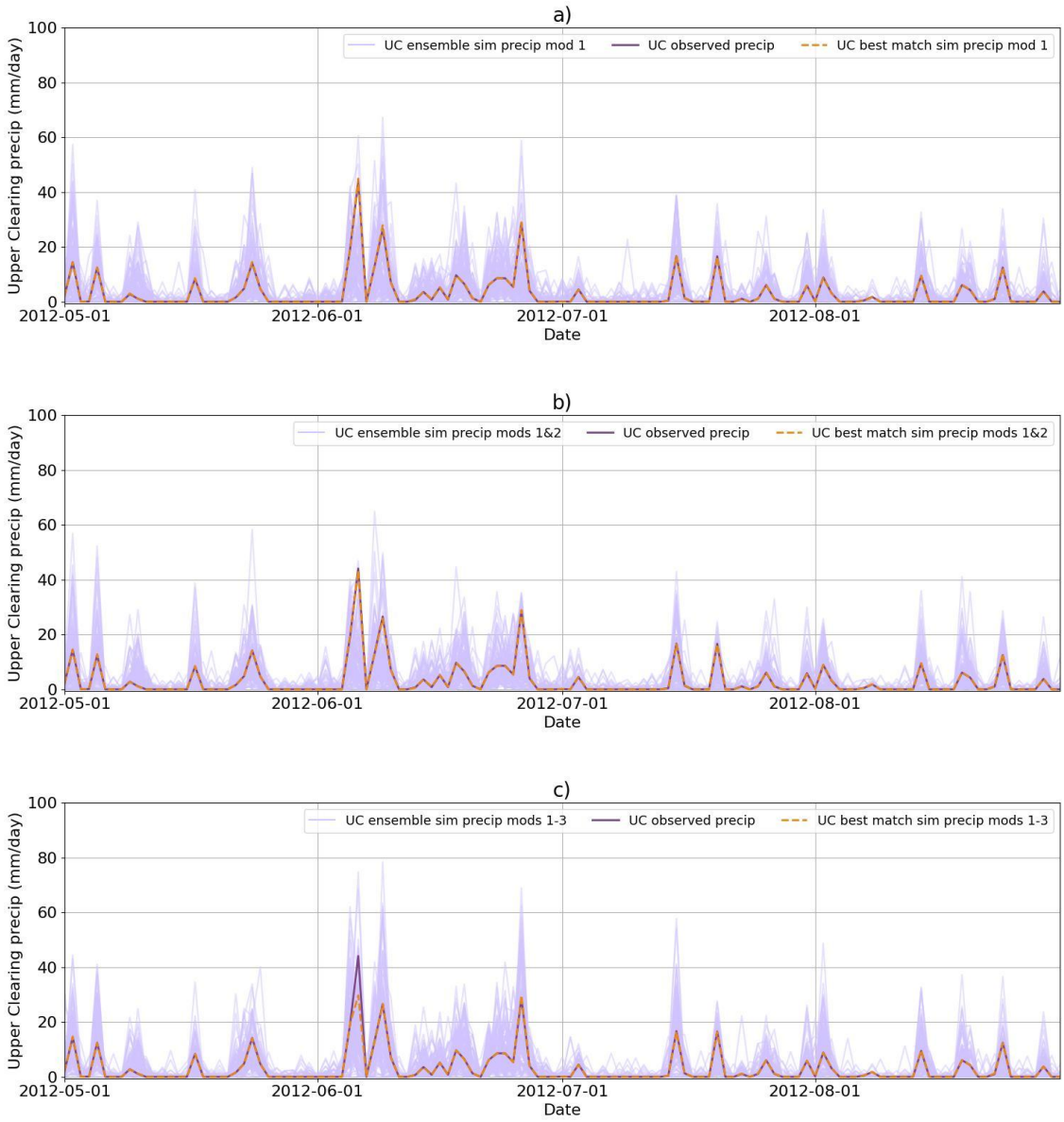

Figure A.14. As Figure A.2 but for 2012

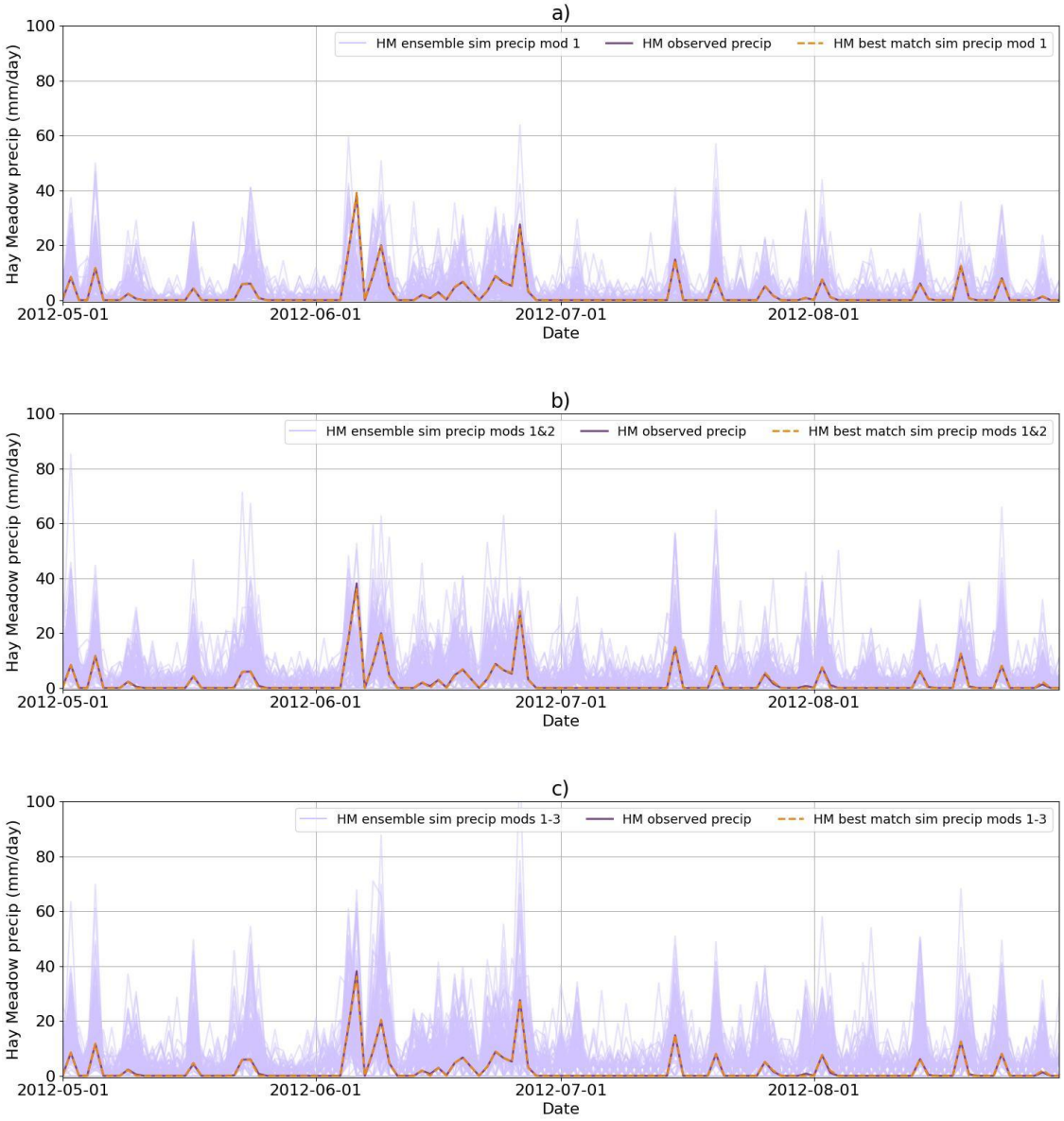

Figure A.15. As Figure A.3 but for 2012

Appendix B

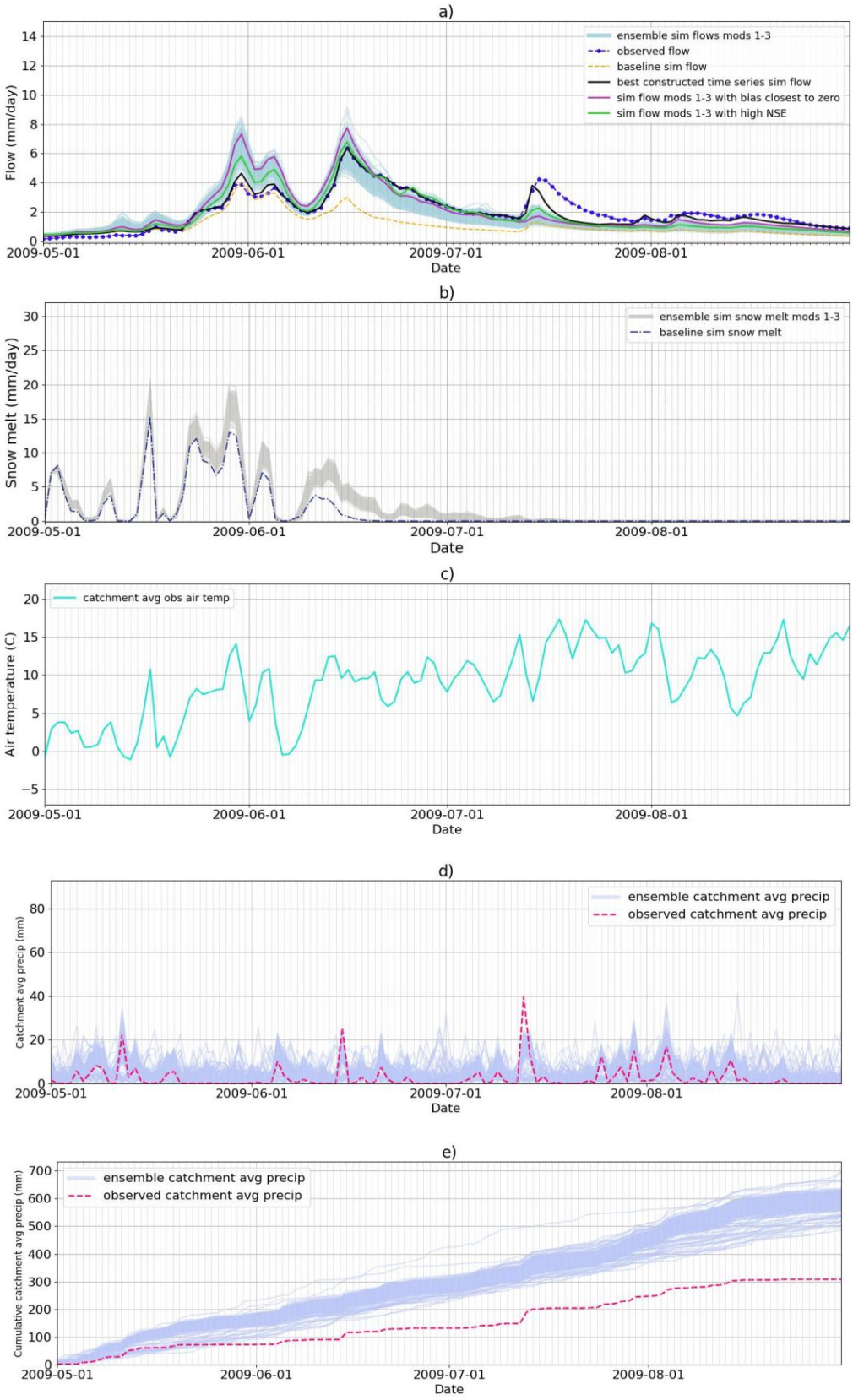

Figure B.1. HBV outputs for water year 2009: a) 200-member ensemble streamflows with best constructed time series and best performing ensemble members for bias closest to zero and high NSE, HBV baseline and observed flows; b) 200-member ensemble and HBV baseline snowmelt; c) observed air temperature; d) time series observed and RM-mountain catchment average precipitation; e) cumulative observed and RM-mountain catchment average precipitation.

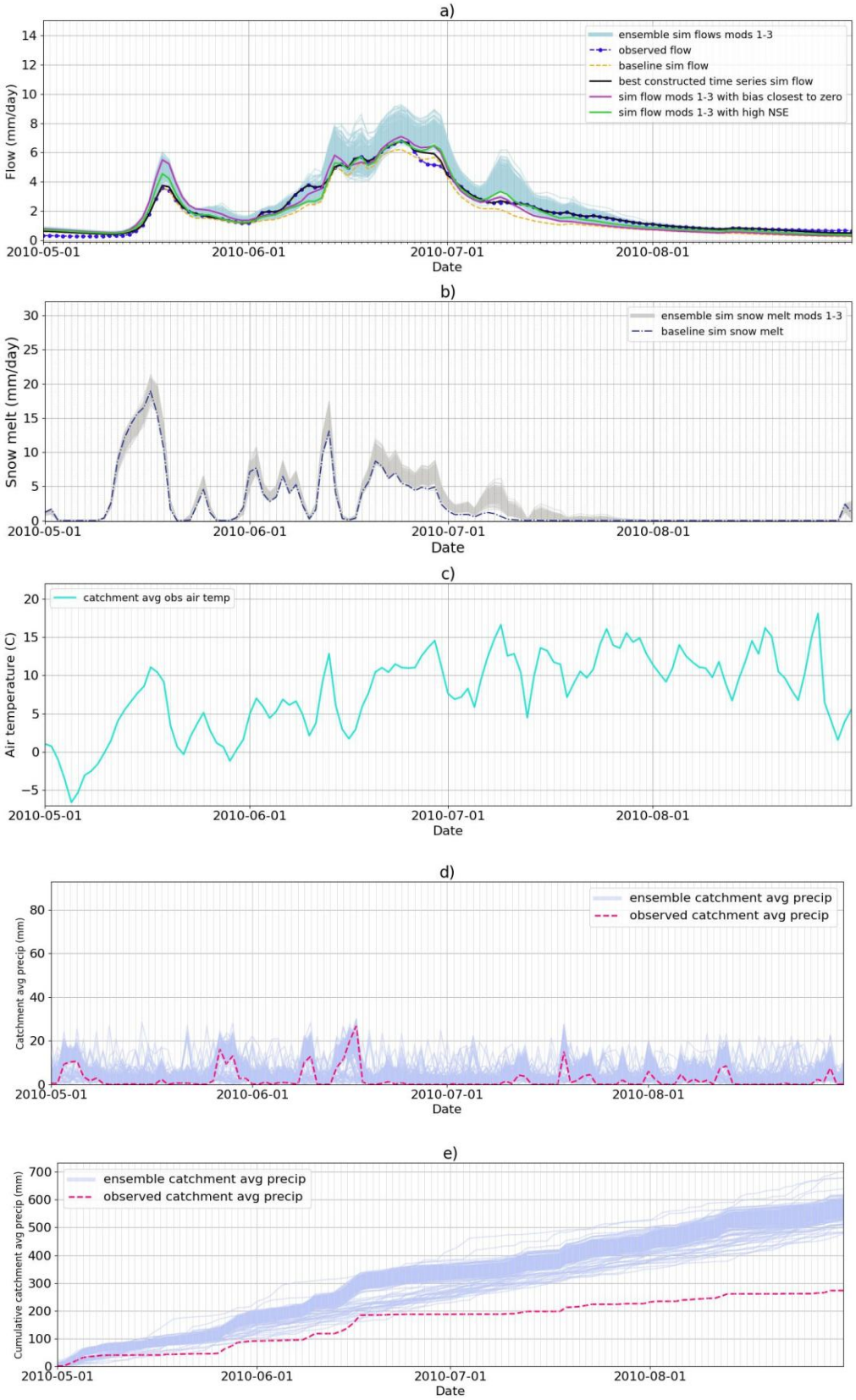

Figure B.2. As Figure B1 but for 2010

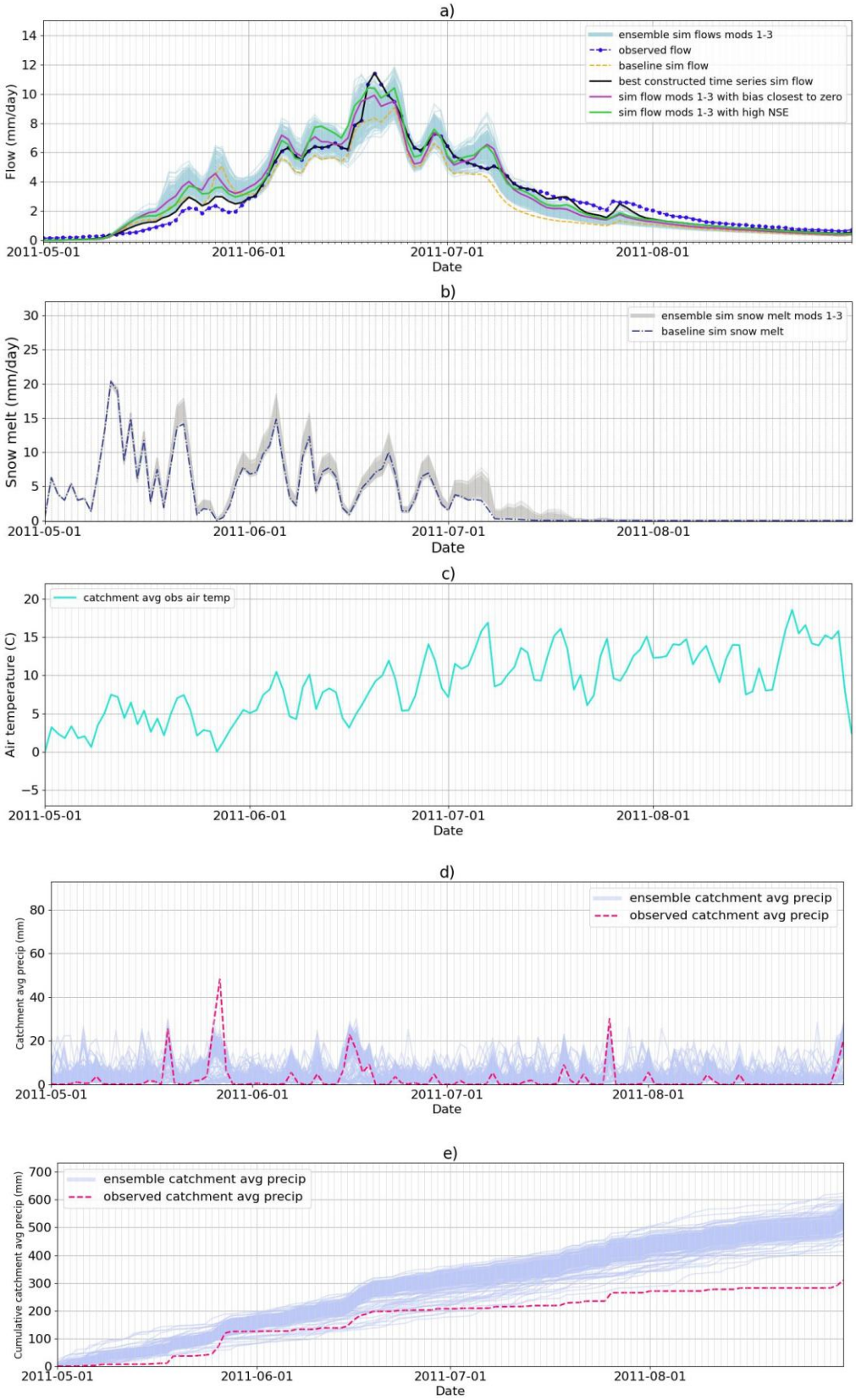

Figure B.3. As Figure B.2 but for 2011

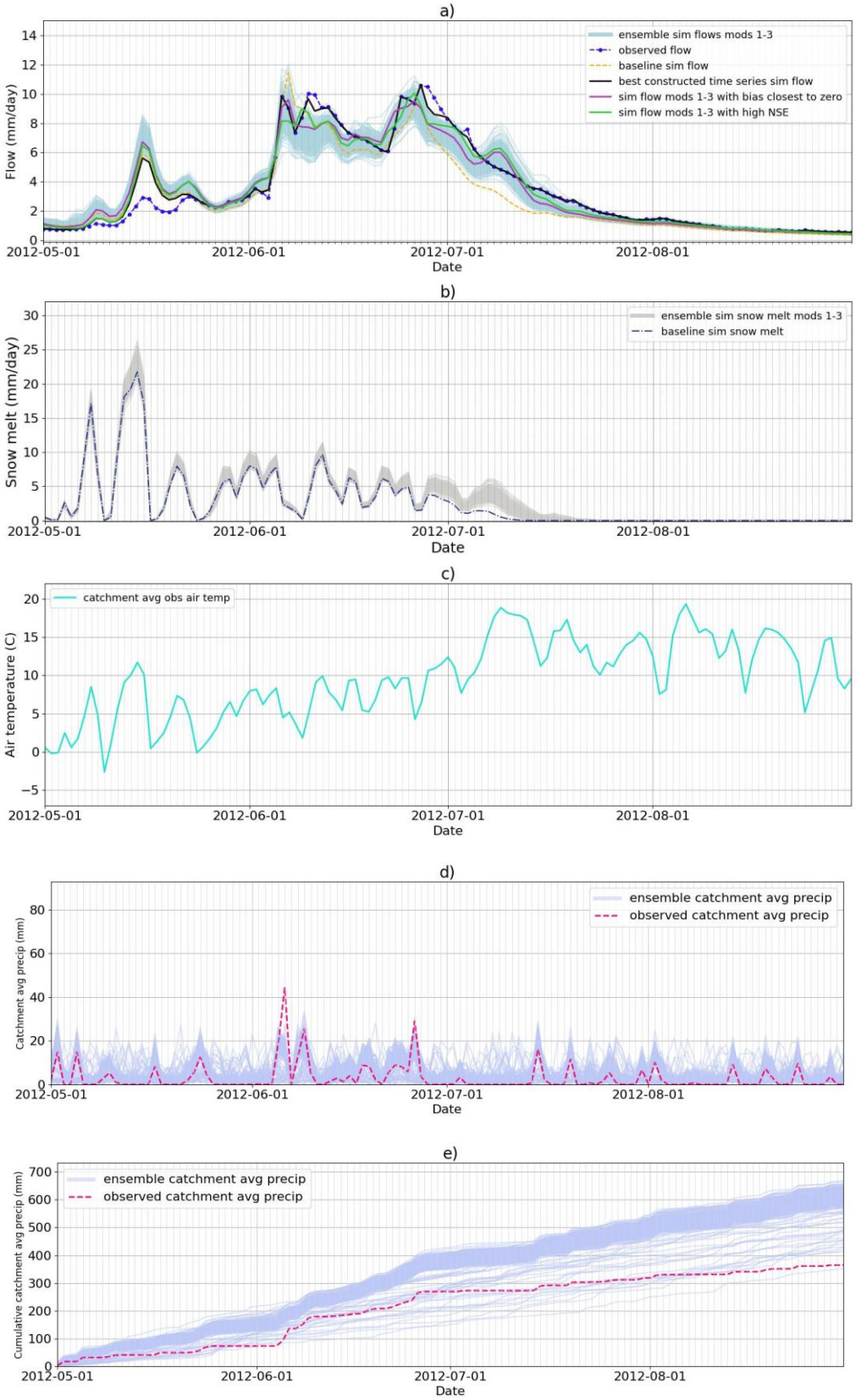

Figure B.4. As Figure B.1 but for 2012

Appendix C

A full list of CRHM modules, and the parameters in each, used in the model of MCRB are listed below.

BASIN (general model module parameters)

- basin_area (km^2) - basin area.
- hru area (km^2) - HRU area.
- hru_lat (°) - HRU latitude.
- hru_elev (m) - HRU altitude.
- hru_GSL (°) - HRU mean ground slope.
- hru_ASL (°) - HRU aspect. 0/90/180/270 - north/east/south/west facing for positive GSL.
- basin_name - basin name text string.
- hru_names - HRU name text strings.
- RUN_ID - integer number used to identify CRHM model runs. When it is positive it is appended to the log file name "CRHM_output_ID" with
- extensions .sum, .log OR .txt.
- RUN_START - run start time.
- RUN_END - run end time.
- INIT_STATE - initial state file.
- RapidAdvance_to - element[1] - date to advance to mm/dd/yyyy.
- Loop_to - element[1] - date to loop to mm/dd/yyyy and element[2] - number of loops before continuing.
- StatVars_to_Handle - state variables to allow to change.
- TraceVars - Trace these variables at end of loop.

OBS (observations module parameters)

- basin_area (km^2) - basin area.
- hru area (km^2) - HRU area.
- hru_elev (m) - HRU altitude.
- obs_elev (m) - Measurement altitude, array of values indexing measured variables: 1) t, rh and ea; 2) p and ppt.
- HRU_OBS () – array of values indexing observations to HRUs. The order is 1) t, rh and ea; 2) p and ppt; 3) u; 4) Q; and 5) for special use.
- snow_rain_determination() - snow/rain determination: 0 - air temperature, 1 - ice bulb temperature, 2 - Harder.
- tmax_allrain (°C) - precipitation is all rain when the temperature is greater or equal to this value. Not used in Harder method.
- tmax_allsnow (°C) - precipitation is all snow when the temperature is less or equal to this value. Not used in Harder method.
- catchadjust () - none - 0/Nipher - 1/MacDonald-Alter (not recommended) - 2/Smith-Alter - 3.
- ppt_daily_distrib () - 0/1 - daily precip all in first interval /equally divided over the day.
- lapse_rate (°C/100m) - temperature lapse rate correction.
- ElevChng_flag () - Elevation change control; 0 - maintain RH, 1 - keep Vp within Vsat maximum.

- precip_elev_adj (1/100m) - precipitation height adjustment {adjusted p(or ppt) = p(or ppt)*(1.0 + precip_elev_adj*elev_difference/100)}.
- ClimChng_t (°C) - Climate change additive temperature change.
- ClimChng_flag () - Climate change control; 0 - maintain RH, 1 - keep Vp within Vsat maximum
- ClimChng_precip () - Climate change multiplative p/ppt change {adjusted p(or ppt) = p(or ppt)*ClimChng_precip}.

Albedo_Richard (albedo module parameters)

- Albedo_Bare () - albedo for bare soil.
- Albedo_Snow () - albedo for snowpack.
- a1 (s) - Albedo decay time constant for dry cold snow.
- a2 (s) - Albedo decay time constant for melting snow.
- amin () - Minimum albedo for aged snow.
- amax () - Maximum albedo for fresh snow.
- smin (mm/int) - Minimum snowfall to refresh snow albedo.

Walmsley_Wind (snow transport module parameters)

- Zwind (m) - wind instrument height.
- A () - coefficient for wind speed change due to topography. Values: 0.0 – flat terrain, 2.5 – 2D escarpments, 3.0 – 2D hills, 3.5 – 2D rolling terrain, 4.0 – 3D hills, 4.4 – 3D rolling terrain.
- B () - coefficient for wind speed change due to topography. Values: 0.0 – flat terrain, 0.8 – 2D escarpments, 1.1 – 3D rolling terrain, 1.55 – 2D rolling terrain, 1.6 – 3D hills, 2.0 – 2D hills.
- L (m) - upwind half-width at half height. It is the length from the centre of a hill with height, h to the slope with half height of the hill, h/2. It is also the length from the centre of a depression with depth, h to the slope with half depth of the depression, h/2.
- Walmsley_Ht (m) - Walmsley height.

longVt (radiation module parameters)

- Vt () - terrain view factor.
- epsilon_s () - terrain emissivity.

Evap_Resist (evapotranspiration module parameters)

- evap_type () - Evaporation method for HRU, 0 - Penman-Monteith, 1 - Dalton-type bulk transfer, 2 - Priestley-Taylor.
- Ht (m) - vegetation height.
- Zwind (m) - wind measurement height.
- hru_elev (m) - altitude.
- basin_area (km^2) - basin area.
- hru_area (km^2) - HRU area.
- F_Qg () - fraction to ground flux. Qg = F_Qg*Rn.
- rcs (s/m) - minimum stomatal resistance.
- Htmax (m) - Maximum vegetation height.
- LAImax (m^2/m^2) - Maximum leaf area index.
- LAImin (m^2/m^2) - Minimum leaf area index.

- s () - Seasonal growth index.
- PM_method () - Penman-Montieth method, 0 - RC, 1 - LAI.
- inhibit_evap (flag) - flag value to inhibit evaporation, 0 - enable evaporation, 1 - inhibit evaporation.
- Soil_Depth (m) - depth of soil.
- soil_type () - 0 through 11 for water / sand / loamsand / sandloam/ loam / siltloam / sasclloam / clayloam / siclloam / sandclay / siltclay / clay.

CanopyClearingGap#3 (interception and sublimation module parameters)

- CanopyClearing () - canopy/clearing/gap - 0/1/2.
- Ht (m) - forest/vegetation height.
- hru_elev (m) - HRU mean elevation.
- basin_area (km^2) - basin area.
- hru area (km^2) - HRU area.
- Z0snow (m) - snow roughness length.
- Zref (m) - temperature measurement height.
- Zwind (m) - wind measurement height.
- LAI (m2/m2) - leaf area index.
- inhibit_evap (flag) - 0/1 enable/inhibit.
- Sbar (kg/m^2) - maximum canopy snow interception load.
- Zvent (m) - ventilation wind speed height.
- unload_t (°C) - ice-bulb temperature when canopy snow is unloaded as snow. Only use by canopy.
- unload_t _water(°C) - ice-bulb temperature when canopy snow is unloaded as water. Only use by canopy.
- Alpha_c () - canopy albedo, used for longwave-radiation enhancement estimation.
- B_canopy () - canopy enhancement parameter for long-wave radiation.
- Gap_diameter (m) - diameter of forest clearing gap. Only use by gap selection.
- Surrounding_Ht (m) - height of canopy around forest clearing gap. Only use by gap selection.

pbsmSnobal (snow transport module parameters)

- fetch (m) - fetch distance.
- Ht (m) - vegetation height.
- distrib () - distribution fractions. Value for HRU 1 controls snow transport into the basin.
- N_S ($1/m^2$) - vegetation number density.
- A_S (m) - stalk diameter.
- basin_area (km^2) - basin area.
- hru_area (km^2) - HRU area.
- inhibit_evap (flag) - an output parameter set true when the SWE is greater than zero. It is used to inhibit evaporation from the evaporation modules.
- inhibit_bs (flag) - an input inhibiting blowing snow when set equal to 1. Inhibited HRU is still able to receive drift from other HRUs.
- inhibit_subl (flag) - an input inhibiting sublimation when set equal to 1.
- u_D () - Daily windspeed correction.
- Drift_offset () - Daily windspeed drift offset correction.
- Drift_slope () - Daily windspeed drift slope correction.
- Subl_offset () - Daily windspeed sublimation offset correction.

- Subl_slope () - Daily windspeed sublimation slope correction.

snobalCRHM#1 (snow melt module parameters)

- relative_hts () - measurements heights, z_T and z_u, are relative to snow, i.e. 0 -> use (z_T), 1 -> use (z_T - z_s).
- z_g (m) - depth of soil temperature measurement.
- hru_T_g (°C) - assume constant ground temperature at depth z_g during melt when observation T_g not available.
- hru_F_g (W/m^2) - assume constant ground heat flux during melt when observation F_g not available.
- T_g_or_G_flux () - flag to decide what to do when observation T_g, F_g not available, 0 - calculate ground flux from ground temperature, 1 - use ground flux value.
- z_u (m) - height of wind measurement.
- z_T (m) - height of air temperature & vapour pressure measurements.
- z_0 (m) - roughness length.
- max_z_s_0 (m) - maximum active layer thickness.
- max_h2o_vol () - max liquid h2o content as volume ratio: V_water/(V_snow - V_ice).
- basin_area (km^2) - basin area.
- hru_area (km^2) - HRU area.
- hru_elev (m) - altitude.
- hru_rho_snow (kg/m^3) - density of snowfall.
- rain_soil_snow () - 0 - handle only snow (infiltration routine handles rain), 1 - handle snow and rain (rain is added to the snowpack).

frozenAyers (infiltration module parameters)

- basin_area (km^2) - area of watershed.
- hru_area(km^2) - area of HRUs.
- t0 (h) - Infiltration opportunity time. If < 0 - calculate opportunity time by running forward (not recommended), == 0 - calculate t0 from '0.65
- *SWE-5.0', > 0 - use as opportunity time. The values are saved in t0_var for reference.
- t0_Julian () -value > 0 - inhibit frozen algorithm till after this Julian date, 0 - enable frozen algorithm immediately when melt criteria is met.
- S0 (m^3/m^3) - surface saturation.
- Si (m^3/m^3) - initial soil saturation.
- C () - coefficient.
- hru_tsoil (ºK) - soil average temperature at start of frozen infiltration.
- t_ice_lens(ºC) - overnight minimum to cause ice lens after major melt.
- texture () - 1 through 4 for texture:- 1 - coarse/medium over coarse, 2 - medium over medium, 3 - medium/fine over fine, 4 - soil over shallow bedrock..
- groundcover () - 1 through 6 for groundcover: 1 - bare soil, 2 - row crop, 3 - poor pasture, 4 - small grains, 5 - good pasture, 6 - forested..
- soil_moist_max (mm) - Maximum available water holding capacity of soil profile. Soil profile is surface to bottom of rooting zone.

SoilDetention (soil moisture balance module parameters)

- basin_area (km^2) - basin area.
- hru_area (km^2) - HRU area.
- Sdmax (mm) - Maximum depression storage.
- Sdinit (mm) - Initial depression storage.
- soil_rechr_max (mm) - Maximum available water holding capacity of the soil recharge zone - expressed as an equivalent depth (mm3/mm2).
- Must be less than or equal to soil_moist.
- soil_rechr_init (mm) - Initial value of available water for soil recharge zone - expressed as an equivalent depth (mm^3/mm^2). Must be less than
- or equal to soil_moist_init.
- soil_moist_max (mm) - Maximum available water holding capacity of rooting zone - expressed as an equivalent depth (mm^3/mm^2).
- soil_moist_init (mm) - Initial value of available water of rooting zone - expressed as an equivalent depth (mm^3/mm^2).
- gw_max (mm) - Maximum available water holding capacity of ground water reservoir.
- gw_init (mm) - Initial value of available water in ground water reservoir.
- rechr_ssr_K (mm/d) - daily ssr drainage factor in recharge layer.
- lower_ssr_K (mm/d) - daily ssr drainage factor in lower soil layer (soil_moist - soil_rechr).
- soil_gw_K (mm/d) - The maximum amount of the excess soil water for an HRU that is routed directly to the associated groundwater reservoir
- each day- expressed as an equivalent depth (mm3/mm2).
- Sd_ssr_K (mm/d) - daily ssr drainage factor from depression storage.
- Sd_gw_K(mm/d) - daily drainage factor to groundwater from depression storage.
- gw_K (mm/d) - daily ground water drainage from gw reservoir.
- soil_withdrawal () - HRU evaporation withdrawal for soil type: 1 = sand, 2 = loam, 3 = clay, 4 = organic. soil_withdrawal[1] - rechr layer,
- soil_withdrawal[2] - lower layer. Water availability is used to limit evaporation as described below.
- cov_type () - Vegetation cover type designation for HRU: "0 = no evaporation, 1 = bare soil or shallow crops (evaporation from the recharge
- layer only), 2 = crops, grasses, shrubs and trees (evaporation from all soil moisture).
- transp_limited () - limit transpiration to recharge layer only on-1/off-0.
- inhibit_evap (flag) - flag value to inhibit evaporation, 0 - enable evaporation, 1 - inhibit evaporation.
- soil_ssr_runoff () - soil column excess to interflow(ssr)/runoff (and possibly SD) interflow-0/runoff-1
- Dts_snow_max (mm) - Maximum detention storage in snow cover period.
- Dts_organic_max (mm) - Maximum detention storage in organic layer for snow free period.
- Dts_snow_init (mm) - Initial detention storage in snow cover period.
- Dts_snow_runoff_K (mm/d) - daily detention storage of snow runoff drainage factor.
- Dts_organic_runoff_K (mm/d) - daily detention storage of organic layer runoff drainage factor.
- Dts_organic_init (mm) - Initial detention storage in organic layer for snow free period.

K_Estimate (soil moisture balance module parameters)

- Ks_lower (m/s) - saturated hydraulic conductivity for lower soil.
- Ks_upper (m/s) - saturated hydraulic conductivity for upper soil layer.
- Ks_gw (m/s) - saturated hydraulic conductivity for groundwater layer.
- hru_GSL (°) - ground slope - increasing the slope positively, tilts the plane to the north with ASL = 0.
- PSD () - pore size distribution.
- soil_rechr_max (mm) - Maximum available water holding capacity for soil recharge zone (upper portion of soil_moist where losses occur as both evaporation and transpiration). Must be less than or equal to soil_moist.
- soil_moist_max (mm) - Maximum available water holding capacity of soil profile. Soil profile is surface to bottom of rooting zone.
- inhibit_evap (flag) - 0/1 enable/inhibit. Is indicator to when there is snowcover.
- Inhibit_K_set () - Inhibit setting of rechr_ssr_K / lower_ssr_K / Sd_ssr_K / Sd_gw_K / soil_gw_K / gw_K parameters using 1/2/4/8/16/32.

Netroute_M_D (routing module parameters)

- basin_area (km^2) - basin area.
- hru_area (km^2) - HRU area.
- Lag (h) - aggregated lag for HRU.
- route_n - () Manning roughness coefficient.
- route_R - (m) hydraulic radius.
- route_S0 - () longitudinal channel slope.
- route_L - (m) routing length.
- route_X_M - () dimensionless weighting factor.
- Channel_shp - () channel cross section shape: rectangular - 0/parabolic - 1/triangular - 2.
- ssrKstorage (d) - storage constant for subsurface runoff to HRU routing.
- ssrLag (h) - Lag for subsurface runoff to HRU routing.
- runKstorage (d) - storage constant runoff to HRU routing.
- runLag (h) - Lag for runoff to HRU routing.
- distrib_Route () - route this HRU's outflow to these HRUs.
- distrib_Basin () - route this HRU's outflow to basin outlet.
- gwwhereto () - 0 - basin gw (basingw), >0 other HRU surface input. <0 other -HRU gw input, or (< -HRUmax or > +HRUmax) - surface basin outflow (basinflow),
- order () - HRU routing process order.
- Sdmax (mm) - maximum depression storage.
- soil_rechar_max (mm) - Maximum available water holding capacity for soil recharge zone.
- Sd_ByPass () - 0 - normal, 1 - Bypass Pond/Depressional storage (i.e. Sd). Also applies to redirected gw.
- soil_rechr_ByPass () - 0 - normal, 1 - Bypass recharge layer (i.e. soil_rechr). Also applies to redirected gw.
- gwKstorage (d) - storage constant for gw to HRU routing.
- gwLag (h) - Lag for gw to HRU routing.
- preferential_flow () - flag for allowing preferential flow, 0 - no preferential and remain as runoff routing to other HRU, 1 - preferential flow and
- route runoff to other HRU's gw.

- scaling_factor () - multiplies the inflow by this scaling factor, i.e. inflow += scaling_factor*(runoutflow + ssroutflow).